Tailoring nanocatalysts and reaction interfaces for water- and CO_2-electrolysis

Acknowledgements

I have always considered myself extremely fortunate in my 30 years of life, as I've had the opportunity to meet and get to know amazing people, and this good fortune extends to my professional life. Throughout my Ph.D. studies at the Laboratory of Materials for Renewable Energy (LMER), I received an abundance of help, warmth, care, kindness, and love from colleagues who later became close friends. Initially, I embarked on my Ph.D. journey with the intention of working on a scientific project that would be entirely my own. However, I ended up gaining much more than that – not only knowledge and skills but also personal qualities that have contributed to my growth, including independence, skepticism, diligence, tenacity, and confidence. I had the chance to work with and get to know people from four different laboratories from around the world, and I appreciate all the work and discussions we shared, from scientific topics to personal life. I would like to express my gratitude to these many people who contributed to shaping a better me.

Laboratory of Materials for Renewable Energy (LMER), EPFL

I would like to express my profound gratitude to **Prof. Andreas Züttel** for giving me the invaluable opportunity to pursue my PhD thesis at LMER. The exceptional working environment and access to cutting-edge equipment, made possible by his commitment to advancing scientific research, have exceeded my expectations. My four-year journey at LMER can only be described as a colorful painting, enriched with a multitude of invaluable experiences, all made possible through the kindness and support of Andreas. In my initial year, I received invaluable guidance and mentorship from him. This foundational support laid the groundwork for my growth as an independent researcher, and I am genuinely appreciative of the autonomy granted to me as my journey went on. Throughout my time at LMER, I had the chance to engage in numerous opportunities for learning, networking, and skill development, such as participating in conferences and exchange programs, all made possible by his foresight and generosity. Being a PhD student at LMER is a significant milestone in my academic and professional journey, and I am sincerely grateful for the path it has paved for my future career.

I wish to express my heartfelt gratitude to **Prof. Wen Luo**, who played a pivotal role in shaping my scientific growth and provided me with a clear vision for my research focus. His ability to explain complex concepts in a straightforward manner greatly aided my integration into the new scientific domain. Wen's exceptional patience in clarifying concepts never made me hesitant to ask questions or admit my gaps in understanding. Furthermore, I deeply appreciate his support for my ideas during my early years as a PhD student. He never discouraged me from pursuing my ideas, even when they resulted in failures. This approach allowed me to gain valuable lessons, develop resilience, and learn to think and plan more meticulously. Although I worked with him for only a year, his presence was immensely valuable during that time, particularly because I was a newcomer to the field of research. His role served as an indispensable steppingstone in my journey toward becoming an independent researcher in the future.

Laboratory of Materials for Renewable Energy (LMER)   i
Institute of Chemical Sciences and Engineering (ISIC)
Basic Science Faculty (SB)

Laboratory of Materials for Renewable Energy (LMER)
Institute of Chemical Sciences and Engineering (ISIC)
Basic Science Faculty (SB)

ii

Laboratory for in situ Nanomaterials Characterization with Electrons (INE), EPFL

I would like to express my gratitude to **Prof. Vasiliki Tileli**, who was the supervisor for my master's thesis and offered support and encouragement throughout my four-year PhD journey as my mentor. Throughout my PhD, I had the privilege of continuing to collaborate with Vaso's lab, and our discussions expanded my understanding of various scientific aspects. I learned invaluable lessons from her dedication to science, her unwavering belief in our scientific findings, and her tenacity in proving and convincing the community about our discoveries. What's most inspiring is her consistent motivation, whether it's a simple "Excellent, My" or "Very good, My," and even in the face of unexpected results, her reassuring "It's okay, My." These words of encouragement have been a driving force, pushing me to rise each time I stumble and to aim higher when I achieve my goals.

Many thanks to **Dr. Tzu-Hsien Shen**, who was not only the supervisor of my master's thesis and my collaborator during my PhD but also my great "eating buddy" in Lausanne. He served as a prime example for me of someone deeply engaged in the scientific process, evident in his perpetual state of "always thinking," constantly questioning and doubting. In addition to our discussions about electrocatalysis, we both shared a passion for food and enjoyed exploring brunch spots in Lausanne. He was my go-to resource for all things TEM-related, and this remains true even though he has since transitioned to the industry.

Additionally, I would like to express my gratitude to all the other members at INE, who are incredibly kind and welcoming.

Electrocatalysis lab (Yeo's lab), NUS

I would like to thank **Prof. Boon Siang Jason Yeo** for giving me the opportunity to undertake a 6-month exchange in his lab at NUS. During my time there, I engaged in invaluable discussions with him, covering not only our electrocatalysis topics but also the ethics of scientific research. I was deeply impressed by his commitment to electrochemistry and his emphasis on the quality of work over meeting quantity quotas. Jason frequently asked tough questions, and as a result, once we could convince him, we gain the confidence to present and defend our conclusions when engaging with the scientific community. His mentorship has had a profound impact on my approach to research and my development as a scientist.

Furthermore, I want to convey my appreciation to the rest of the members, who are exceptionally friendly and hospitable.

Horike's lab (Kyoto University)

Special thanks are due to **Prof. Horike Satoshi**, who graciously permitted me to conduct experiments in his lab at Kyoto University and extended a warm and hospitable welcome.

Laboratory of Materials for Renewable Energy (LMER)
Institute of Chemical Sciences and Engineering (ISIC)
Basic Science Faculty (SB)

iii

EPFL Valais & CIME-EPFL

My PhD journey would have been incomplete without the invaluable assistance of the EPFL Valais campus staff. In particular, I would like to extend my heartfelt gratitude to **Mr. Stéphane Voeffray** and **Mr. Robin Délèze**, engineers at the mechanical workshop, for their tremendous support in designing and creating the cells that enabled me to carry out electrochemical measurements. They also actively contributed ideas for improving these cells. I am also grateful for the support and guidance of the scientists at the ISIC platform, including **Dr. Natalia Gasilova**, **Dr. Mounir Mensi**, **Dr. Aurélien Bornet**, and **Dr. Pascal Schouwink**. They not only provided training on equipment usage but also readily addressed my questions and came to my aid when I encountered difficulties with the machinery. My gratitude also extended to **Mr. Laurent Seydoux** and **Mrs. Annabelle Coquoz** at the chemical store, and to **Mr. Cédric Passerini** and **Mr. Jean Perruchoud** from the IT platform, who provided constant assistance concerning the chemicals and the informatic issues.

I must also acknowledge the dedicated scientists at CIME who played a crucial role in maintaining the efficient operation of the microscope center. Many of my research goals would have remained unattained without the indispensable microscopes at CIME. Therefore, I am profoundly thankful to **Dr. Marco Cantoni**, **Dr. Emad Oveisi**, **Dr. Victor Boureau**, and **Dr. Rita Therisod** for their continuous efforts in ensuring the smooth functioning of the microscopes, frequent alignment updates, and, of course, their assistance whenever I encountered equipment-related challenges.

Laboratory of Materials for Renewable Energy (LMER)   iv
Institute of Chemical Sciences and Engineering (ISIC)
Basic Science Faculty (SB)

My family

Last but, most importantly, I would like to express my gratitude to my family in Vietnam, who supported me both financially and emotionally in my pursuit of higher education in Switzerland. This journey would not have been possible without my mother, **Van Nguyen**, who not only understood my dream but also allowed me to leave home at the age of 18 to pursue my studies. Even though she may not fully comprehend what I am studying, or perhaps thinks I'm trying to turn our exhaled air into something drinkable, I am certain she takes immense pride in my educational journey.

I also want to thank my aunt, **Dung Nguyen**, whom I affectionately call 'mom.' She has played a pivotal role in many significant events in my life, from orientating me to learn French and enrolling in a French high school to eventually studying in Switzerland. Despite her persistent efforts to convince me to return to Vietnam and engage in business, I know she stands behind me in every decision I make, including pursuing a Ph.D. in Switzerland. Alongside my uncle, **Minh Pham**, they shaped my path, which began with pursuing a bachelor's degree abroad, a decision I have never regretted.

I would like to extend my thanks, as well as offer my apologies, to my dearest grandma, **Hien Nguyen**, and grandpa, **Thai Nguyen**, who have cared for me since I was a child. Every year, they eagerly anticipate my return during New Year festivals or summer vacations, and I am sorry for not being able to be with them as they grow older. I hope that my academic achievements bring them pride and serve as a way to compensate for my absence.

My gratitude also goes to my aunt, **Mai Nguyen**, my uncle, **Thang Nguyen**, and my cousins, **Mi H. Nguyen** and **Mi D. Nguyen**, in Frankfurt, who always make me feel at home when I visit them during the holidays. I can feel their eagerness to see me as they consistently prepare and send me a plan in advance of my arrival, including activities and the Vietnamese food that they will prepare to welcome me. Many thanks to uncle **Thanh Nguyen** and aunt **Hoa Le** for their warm and caring welcome whenever I returned to Vietnam during my vacations.

Lastly, a special thanks to **Christine Tran**, my cousin but more like a sister, travel companion, food buddy, and my biggest fan, always insisting that we are sisters and proudly embracing the role of being my sister.

Laboratory of Materials for Renewable Energy (LMER)
Institute of Chemical Sciences and Engineering (ISIC)
Basic Science Faculty (SB)

v

Abstract

The increasing global demand for energy, coupled with rapid industrial growth, has raised critical concerns about sustainability and the contribution of CO_2 emissions to climate change. Renewable energy sources represent a particularly promising means of mitigating these issues thanks to their vast energy generation capacity. Furthermore, carbon-free fuels—such as hydrogen—can be produced via water electrolysis powered by renewable energy, creating a closed loop that is free from carbon emissions. Additionally, renewable energy can be used to power carbon capture and utilization techniques, resulting in negative carbon emissions. These solutions rely on two key electrochemical reactions: water electrolysis and CO_2 electrolysis. Water electrolysis is a promising technology that allows for hydrogen production without relying on fossil fuels. Similarly, CO_2 electrolysis aims to reduce CO_2 emissions by converting it into other carbon-containing fuels. However, both of these reactions involve multiple electron-transfer steps, most notably the anodic oxygen evolution reaction (OER) and the cathodic CO_2 reduction reaction (CO_2RR), resulting in high overpotentials and limited energy efficiencies. As such, the development of catalysts to enhance the activity and stability of these reactions is imperative for their practical application.

The primary challenge of OER research is the development of cost-effective, earth-abundant catalysts to replace expensive benchmark materials such as IrO_2 and RuO_2. In contrast, the primary challenge of enabling CO_2 reduction in aqueous environments is related to the stability of the CO_2 molecule and the complexity of its reaction pathways, resulting in low reaction efficiency and uncontrolled product selectivity. Copper-based materials have become the focus of extensive research into electrochemical CO_2 reduction (eCO_2RR) due to their unique ability to convert CO_2 into carbonaceous compounds with more than two carbon atoms (C_{2+} products). Nevertheless, further research is necessary to reduce the reaction's overpotential and refine the selectivity of copper-based catalysts toward desired products. This thesis describes a comprehensive study aimed at developing catalysts with improved activities and stabilities, as well as promoting their selectivity for specific targeted products. Furthermore, we conducted an in-depth study of the structure of the catalyst and attempted to determine the underlying mechanisms responsible for these improvements.

First, we explored the role of surface oxygen functionalization on the dispersion and activity of Co-based catalysts in the context of OER. We found that carbon supports that were rich in acidic oxygen-containing functional groups enhanced the adsorption of metal cations and the dispersion of the catalysts. The presence of carboxyl functional groups was particularly effective at facilitating O_2 spillover from the Co surface.

Second, we studied how the incorporation of Fe impacts the OER activity of Co-based catalysts. Through in situ synthesis, we found that Fe is incorporated as a solid solution, primarily through the substitution of Fe^{3+} at Co^{3+} sites. Our CoFe catalyst exhibited excellent OER performance, as evidenced by a low Tafel slope and overpotential, making it one of the top-performing CoFe-based materials.

Laboratory of Materials for Renewable Energy (LMER)
Institute of Chemical Sciences and Engineering (ISIC)
Basic Science Faculty (SB)

vi

We then focused on improving the electrocatalytic reduction of CO_2 to C_{2+} products by tuning the hydrophilicity of polymer binders used to bind powder catalysts to the carbon paper supports. We selected fluorinated ethylene propylene (FEP)—a hydrophobic, CO_2-philic polymer—and observed a significant increase in total current density and faradaic efficiency toward C_{2+} products. Operando Raman spectroscopy revealed that the hydrophobicity of FEP resulted in the retention of CO_2 and intermediate CO on the surface of the catalyst, promoting the formation of C_{2+} products.

Finally, we identified the primary degradation mechanisms of CO_2 electrolysis in acidic environments to be the flooding of gas diffusion electrodes (GDEs). By separating the inlet catholyte from the outlet liquid products, we successfully kept the pH near the catalyst below a critical value, thereby extending the carbon-based GDEs lifetime.

In summary, we implemented a range of strategies to enhance both the activity and stability of electrochemical reactions. These strategies include the design of electrocatalysts, such as the incorporation of Fe into Co oxides and the dispersion of Co nanoparticles. We also fine-tuned the reaction environment by adjusting factors such as hydrophilicity and local pH. Our research has provided insights into the mechanisms that drive these improvements, which were accomplished through structural modifications and alterations in the reaction environment.

Keywords :

Electrochemistry, catalysis, water splitting, oxygen evolution reaction, cobalt catalysts, iron incorporation, electrochemical CO_2 reduction, copper catalysts, gas diffusion electrode, reaction environment.

Laboratory of Materials for Renewable Energy (LMER)
Institute of Chemical Sciences and Engineering (ISIC)
Basic Science Faculty (SB)

vii

Résumé

La demande croissante d'énergie à l'échelle mondiale, associée à une croissance industrielle rapide, suscite des préoccupations cruciales concernant la durabilité et la contribution des émissions de CO_2 au changement climatique. Les sources d'énergie renouvelable représentent un moyen particulièrement prometteur d'atténuer ces problèmes grâce à leur vaste capacité de production d'énergie. De plus, des carburants sans carbone, tels que l'hydrogène, peuvent être produits par électrolyse de l'eau alimentée par une énergie renouvelable, créant une boucle fermée exempte d'émissions de carbone., L'énergie renouvelable peut aussi être utilisée pour alimenter des techniques de capture et d'utilisation du CO_2, entraînant des émissions négatives. Ces solutions reposent sur deux réactions électrochimiques clés : l'électrolyse de l'eau et l'électrolyse du CO_2. L'électrolyse de l'eau est une technologie prometteuse permettant la production d'hydrogène sans recourir aux combustibles fossiles. De même, l'électrolyse du CO_2 vise à réduire les émissions de CO_2 en le convertissant en d'autres carburants contenant du carbone. Cependant, ces deux réactions impliquent plusieurs étapes de transfert d'électrons, notamment la réaction d'évolution de l'oxygène anodique (OER) et la réaction de réduction du CO_2 cathodique (CO$_2$RR), entraînant des surtensions élevées et des efficacités énergétiques limitées. Ainsi, le développement de catalyseurs pour améliorer l'activité et la stabilité de ces réactions est impératif pour leur application pratique.

Le principal défi de la recherche sur l'OER est le développement de catalyseurs économiques à base de matériaux abondants sur Terre pour remplacer les matériaux de référence coûteux tels que l'IrO_2 et le RuO_2. En revanche, le principal défi de la réduction du CO_2 en milieu aqueux est lié à la stabilité de la molécule de CO_2 et à la complexité de ses voies réactionnelles, entraînant une faible efficacité de réaction et une sélectivité de produit incontrôlée. Les matériaux à base de cuivre ont fait l'objet de nombreuses recherches sur la réduction électrochimique du CO_2 (eCO$_2$RR) en raison de leur capacité unique à convertir le CO_2 en composés carbonés contenant plus de deux atomes de carbone (produits C$_{2+}$). Cependant, des recherches supplémentaires sont nécessaires pour réduire la surtension de la réaction et affiner la sélectivité des catalyseurs à base de cuivre vers les produits souhaités. Cette thèse décrit une étude approfondie visant à développer des catalyseurs avec des activités et des stabilités améliorées, ainsi qu'à promouvoir leur sélectivité pour des produits ciblés spécifiques. De plus, nous avons mené une étude approfondie de la structure du catalyseur et tenté de déterminer les mécanismes sous-jacents responsables de ces améliorations.

Tout d'abord, nous avons exploré le rôle de la fonctionnalisation de l'oxygène de surface sur la dispersion et l'activité des catalyseurs à base de Co dans le contexte de l'OER. Nous avons constaté que les supports en carbone riches en groupes fonctionnels oxygénés acides favorisaient l'adsorption des cations métalliques et la dispersion des catalyseurs. La présence de groupes fonctionnels carboxyles était particulièrement efficace pour faciliter le transfert d'oxygène depuis la surface du Co.

Ensuite, nous avons étudié comment l'incorporation de Fe affecte l'activité pour l'OER des catalyseurs à base de Co. Par une synthèse in situ, nous avons constaté que le Fe est incorporé sous forme de solution solide, principalement par substitution de Fe^{3+} aux sites Co^{3+}. Notre catalyseur CoFe a présenté d'excellentes

Laboratory of Materials for Renewable Energy (LMER)
Institute of Chemical Sciences and Engineering (ISIC)
Basic Science Faculty (SB)

viii

performances en OER, comme en témoignent une faible pente de Tafel et une surtension réduite, le plaçant parmi les meilleurs matériaux à base de CoFe.

Nous nous sommes ensuite concentrés sur l'amélioration de la réduction électrocatalytique du CO_2 en produits C_{2+} en ajustant l'hydrophilicité des liants polymères utilisés pour lier les catalyseurs en poudre aux supports en papier carbone. Nous avons choisi le polytétrafluoroéthylène (FEP), un polymère hydrophobe et CO_2-phile, et avons observé une augmentation significative de la densité de courant totale et de l'efficacité faradique vers les produits C_{2+}. La spectroscopie Raman operando a révélé que l'hydrophobicité du FEP entraînait la rétention du CO_2 et du CO intermédiaire à la surface du catalyseur, favorisant la formation de produits C_{2+}.

Finalement, nous avons identifié les mécanismes primaires de dégradation de l'électrolyse du CO_2 dans des environnements acides comme étant le phénomène d'inondation des électrodes de diffusion de gaz (GDEs). En séparant le catholyte d'entrée des produits liquides de sortie, nous avons réussi à maintenir avec succès le pH près du catalyseur en dessous d'une valeur critique, prolongeant ainsi la durée de vie des GDEs à base de carbone.

En résumé, nous avons mis en œuvre une gamme de stratégies pour améliorer à la fois l'activité et la stabilité des réactions électrochimiques. Ces stratégies comprennent la conception d'électrocatalyseurs, telle que l'incorporation de Fe dans les oxydes de Co et la dispersion des nanoparticules de Co. Nous avons également affiné l'environnement réactionnel en ajustant des facteurs tels que l'hydrophilicité et le pH local. Nos recherches ont fourni des aperçus des mécanismes qui entrainent ces améliorations, réalisées grâce à des modifications structurelles et des altérations de l'environnement réactionnel.

Mots-clés : Électrochimie, catalyse, électrolyse de l'eau, réaction d'évolution de l'oxygène, catalyseurs de cobalt, incorporation de fer, réduction électrochimique du CO_2, catalyseurs de cuivre, électrode de diffusion de gaz, environnement réactionnel.

Laboratory of Materials for Renewable Energy (LMER)
Institute of Chemical Sciences and Engineering (ISIC)
Basic Science Faculty (SB)

ix

Contents

Laboratory of Materials for Renewable Energy (LMER)
Institute of Chemical Sciences and Engineering (ISIC)
Basic Science Faculty (SB)

x

Laboratory of Materials for Renewable Energy (LMER)
Institute of Chemical Sciences and Engineering (ISIC)
Basic Science Faculty (SB)

xi

Laboratory of Materials for Renewable Energy (LMER)
Institute of Chemical Sciences and Engineering (ISIC)
Basic Science Faculty (SB)

xii

Laboratory of Materials for Renewable Energy (LMER)
Institute of Chemical Sciences and Engineering (ISIC)
Basic Science Faculty (SB)

xiii

CHAPTER 1: Introduction

The world experienced an explosion in global population over the last century; this was coupled with an exponential increase in energy demand, which increased by a factor of 80 in contrast to the 6-fold increase in world population[1]. This trend highlights an increase in the amount of energy required per capita: an unavoidable consequence of industrialization and modernization. Ever since the discovery of the steam engine by Watt during the Industrial Revolution, in which steam derived from charcoal-boiled water was transformed into mechanical work, fossil fuels have been the primary source of energy in modern civilization. In 1997, fossil fuels provided 75% of the total global energy supply, while the contributions of renewable and nuclear energy only amounted to 19% and 6%, respectively[2]. The intensive use of fossil fuels has raised two major issues: i) **Sustainability**: fossil fuels are a finite primary source, and thus finding alternative sources is vital for current and future generations; ii) **Climate change**: the burning of fossil fuels generates CO_2, which leads to global warming and other related environmental disasters. It is thus extremely important to reduce the amount of past, present, and future CO_2 emissions.

1.1. Question of sustainability

The Cambridge dictionary defines "sustainability" as "the quality of causing little or no damage to the environment and therefore able to continue for a long time". Fossil fuels, usually in the form of coal, oil, or natural gas, are hydrocarbons with varying carbon chain lengths that can be burned to generate energy. These materials are formed from the decomposition and accumulation of dead plant and animal matter over several hundreds of millions of years[3]. Due to its long formation time, fossils are non-renewable, and thus their use in modern society is highly unsustainable. According to Holdren[4], "the problem is not that we are running out of energy" but "it's that we have nearly run out of the low-cost energy". Indeed, despite their ability to provide a theoretically infinite amount of energy, renewable resources have remained relatively expensive compared to fossil fuels due to their high cost of production. With the development of photovoltaic technology, the cost of renewable energy has been significantly reduced: the price of concentrating solar power (CSP) and photovoltaic (PV) energy dropped twofold between 2010 and 2020, and now costs approximately the same amount as fossil fuel[5] .

One source of renewable energy is the Sun, which supplies an amount of energy that could theoretically meet global energy consumption: 3×10^{24} Joules a year. This reservoir has an energy capacity that is 10,000 times greater than Earth's total energy consumption[6]. Although it only ever shines on half of the Earth's surface at any one time, its capacity as an energy source remains far greater than global energy demands. However, the amount of energy generated from this source is limited due to a lack of infrastructure. Specifically, although the "raw material" available for electricity generation is more than sufficient, we are unable to collect all of the sunlight incident on the Earth's surface due to the lack of solar panel coverage, as well as the intrinsic energy inefficiencies associated with solar panels. Another problem associated with solar energy is that the Sun does not shine everywhere or at all times. Thus, the storage of solar energy is an important consideration

Laboratory of Materials for Renewable Energy (LMER)
Institute of Chemical Sciences and Engineering (ISIC)
Basic Science Faculty (SB)

14

for energy trading, transportation, and mobile applications. In general, energy can be stored within an electric field in a capacitor, as gravitational potential energy in a pumped-hydroelectric storage system, as kinetic energy in flywheels, or within chemical bonds in specific compounds[7]. In chemical energy storage, hydrogen is a particularly promising candidate due to its high gravimetric energy density of 120 kJ/g[8]. Furthermore, hydrogen is often utilized in many industries, such as the production of ammonia or carbon hydrogenation reactions. Approximately 50% of the world's hydrogen is used for ammonia production through a high-pressure reaction between hydrogen and nitrogen[9]. In the carbon hydrogenation reaction, hydrogen and carbon monoxide react at high pressures and temperatures to produce synthetic fuels such as methane, methanol, or other hydrocarbons.

Züttel et al. described a completely sustainable hydrogen energy cycle (Figure 1.1a) involving the collection, storage, and consumption of solar energy using hydrogen as an energy carrier[1]. Solar energy is first used to split water into hydrogen and oxygen. The hydrogen could then be used as an energy carrier, either to be stored for use during the night or transported to areas with low irradiation. Hydrogen can be either combusted or used in a fuel cell to release energy; these processes do not generate any CO_2 emissions, unlike fossil fuels. The limited exploitation of this significant source of renewable energy arises from inefficiencies in three specific stages: 1) the production of hydrogen from solar energy, 2) the storage efficiency of the energy carrier, and 3) the consumption of the energy carrier. During the production step, there are limitations regarding the scalability of hydrogen production from water electrolysis due to the high cost of the stack compared to the methane–steam reforming methods[10]. In the storage step, the low volumetric energy density of hydrogen at ambient pressure necessitates its compression into liquid hydrogen, which is extremely costly. Furthermore, additional safety requirements are necessary due to the highly flammable nature of hydrogen. The conversion of hydrogen in fuel cells is also relatively costly due to the high cost of the catalysts used in the stack, such as platinum[11].
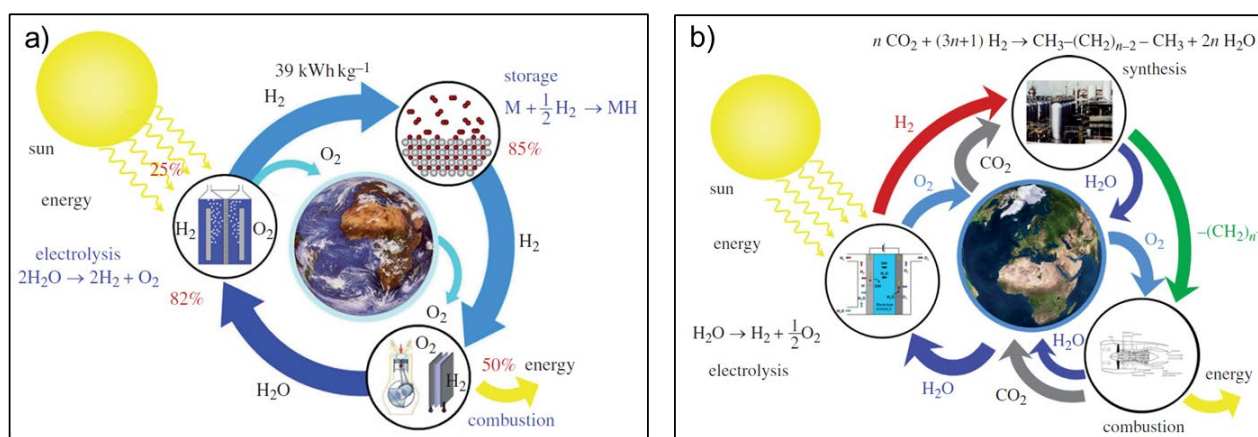
Figure 1.1. The hydrogen and carbon economies: the cycle of production, storage, and consumption. **a) Hydrogen cycle**: Solar energy is used in water electrolysis, generating oxygen and hydrogen. This reaction releases back oxygen into the atmosphere, while hydrogen is used as the energy carrier. The hydrogen can be stored for later use, shipped, or used in mobile applications. Energy is extracted from the hydrogen by combustion or by reacting the hydrogen with oxygen in a fuel cell to form water. **b) Carbon cycle**: Solar energy is used in water electrolysis, generating oxygen and hydrogen. The hydrogen is used in the CO_2 hydrogenation reaction to synthesize hydrocarbons. These hydrocarbons act as energy

Laboratory of Materials for Renewable Energy (LMER)
Institute of Chemical Sciences and Engineering (ISIC)
Basic Science Faculty (SB)

15

carriers and can be stored or transported. Energy can be extracted from the hydrocarbons using fuel cells or via combustion processes, resulting in the release of CO_2. Reprint with permission from Züttel et al.[1], copyright 2010, Royal Society.

To address these limitations, several approaches have been used to improve the efficiency and reduce the cost of each of these steps. Alternative storage materials have been studied to replace liquid hydrogen. These include porous carbon, zeolites, or metal–organic frameworks (MOFs) through physisorption as well as porous organic polymers[12], which can be used to store hydrogen. Hydrides can also be used to store hydrogen by chemisorption; these generally exhibit higher storage capacities compared to physisorption[13]. Extensive research has also been conducted on the development of catalysts that can replace expensive catalysts with non-precious, earth-abundant catalysts for electrochemical reactions in water electrolysis (i.e., catalysts for the oxygen evolution reaction (OER) and the hydrogen evolution reaction) and fuel cell (oxygen reduction reaction and hydrogen oxidation reaction)[14].

1.2. CO₂ emissions

In addition to sustainability issues, fossil fuel-based economies are well-known for their severely negative environmental impact. The drastic rise in fossil fuel consumption in the 20th century has led to a tenfold increase in CO_2 emissions[2]; these emissions are considered to be the main driver of anthropogenic climate change and can lead to other environmental complications such as acid rain and ozone depletion[15]. Carbon capture, utilization, and storage (CCUS) refer to a family of complex techniques that are used to collect and store/use the discharged CO_2, effectively recycling CO_2 emissions. CO_2 is collected from the outlet streams of industrial sources or direct-air carbon capture (DACC) before being separated and stored either biologically in plants or geologically in the deep ocean or soil. Figure 1.1b provides an example of how the captured carbon can be utilized in a closed loop in which there are net-zero carbon emissions. CO_2 reacts with the H_2-generated photo-water electrolysis to form carbon-based fuels. The energy stored in these hydrogen carbons can be extracted using a fuel cell or via combustion, releasing CO_2 back into the atmosphere. In addition to the net-zero carbon emissions promised by the utilization of carbon in closed carbon loops, carbon storage allows for net negative emissions, compensating for the over-utilization of fossil fuels over the last two centuries. In contrast to the hydrogen cycle, in which water is the only initial "raw material", CCUS requires the pure CO_2 generated from the capture and separation processes. Each of the fundamental steps—capture, separation, carbon hydrogenation reaction, and fuel consumption—has its own inefficiencies and thus requires specific materials or catalysts, significantly increasing the research complexity required to maximize their overall efficiency. Nevertheless, CCUS techniques are extremely valuable since they can help store renewable energy while removing atmospheric CO_2.

The storage of energy in the carbon cycle described above involves two major steps: the production of hydrogen by water electrolysis, and the reaction of this hydrogen with CO_2 to form hydrocarbons. The latter reaction requires high temperatures and pressures, and the overall efficiency of the process is limited by the efficiency of each sub-step. Recently, electrochemical CO_2 reduction reactions (eCO₂RRs) powered by renewable energy have been proposed as a promising means of combining water electrolysis and CO_2

Laboratory of Materials for Renewable Energy (LMER)
Institute of Chemical Sciences and Engineering (ISIC)
Basic Science Faculty (SB)

16

hydrogenation. This involves the use of CO_2 and water to reduce CO_2 to single- or multi-carbon products (depending on the catalyst). Figure 1.2 describes how this utilizes captured CO_2 and converts it into chemical feedstocks, such as hydrocarbons, alcohols, and syngas, reducing the need for fossil fuels in the chemical production industry. Notably, this process precludes the need for high temperature and pressure conditions. Consequently, this process can be used for decentralized, scalable, and mobile applications.
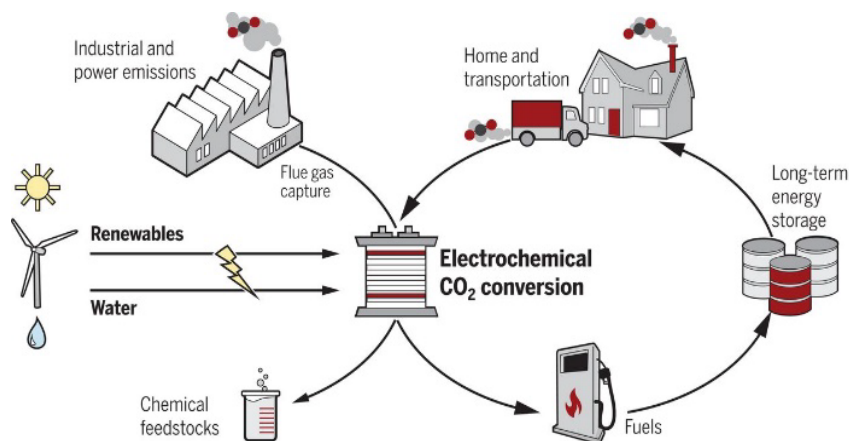
Figure 1.2. The storage of renewable energy via the reduction of CO_2 to chemical feedstocks and fuels. Reprint with permission from De Luna et al.[16], copyright 2019, American Association for the Advancement of Science.

eCO_2RR is thus a promising technology for both CO_2 sequestration and the chemical storage of renewable energy. Nevertheless, there are still several challenges that must be overcome, such as the development of catalysts that can lower the overpotential of the eCO_2RR while achieving the desired product selectivity.

This research described in this thesis aimed to design and develop catalysts for electrochemical reactions in energy conversion devices. Specifically, this study investigated the use of electrocatalysts in two key half-cell reactions: the OER and the eCO_2RR. These reactions are fundamental components of electrolysis processes that are needed to convert renewable energy into a chemical energy carrier for efficient storage. The OER takes place at the anode in water and CO_2 electrolysis, while the eCO_2RR occurs at the cathode in CO_2 electrolysis (Figure 1.3).
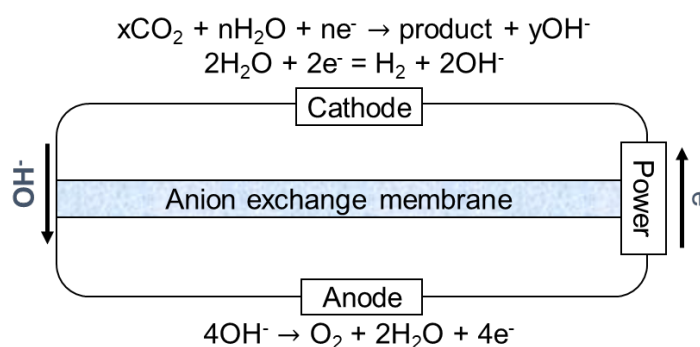
Figure 1.3. Diagram showing the two half-cell reactions in alkaline water- and CO_2- electrolysis.

Laboratory of Materials for Renewable Energy (LMER)
Institute of Chemical Sciences and Engineering (ISIC)
Basic Science Faculty (SB)

17

1.3. Water electrolysis and the oxygen evolution reaction

An electrolysis unit used to split water into hydrogen and oxygen consists of an anode, a cathode, an electrolyte, and a power supply. Water electrolysis involves the following chemical reaction: $H_2O \rightarrow 2\,H_2 + O_2$, which produces hydrogen at the cathode and oxygen at the anode[17]. In an electrolyser, the cathode and the anode are attached to the negative and positive terminals of the power supply, respectively.

The half-reactions that occur at the electrodes are:

Acidic condition:

Cathode: $2H^+ + 2e^- \rightarrow H_2$ $\hfill$ (1)

Anode: $2H_2O \rightarrow 4H^+ + 4e^- + O_2$ $\hfill$ (2)

Alkaline condition:

Cathode: $2H_2O + 2e^- \rightarrow H_2 + 2OH^-$ $\hfill$ (3)

Anode: $4OH^- \rightarrow 2H_2O + 4e^- + O_2$ $\hfill$ (4)

Applying a potential to the electrolysis cell results in the simultaneous formation of hydrogen and oxygen at both the cathode and anode, respectively. Hydrogen formation only involves two electrons, while oxygen evolution is a sluggish multi-step reaction that requires four electrons and significant activation polarization at the anode. Due to the complexity of the OER, researchers have attempted to break down the multi-step reaction into individual steps that only involve the transfer of a single electron, which would allow them to investigate the rate-determining step of the reaction in more detail[18]. Several mechanisms have been proposed such as a three-step reaction with two intermediates, M-OH and M-O[19,20], a four-step reaction with three intermediates, M-OH, M-O, and M-OOH[21–23], or a two-site mechanism[24].

The definition of a catalyst according to the Cambridge Dictionary is "something that makes a chemical reaction happen more quickly without itself being changed". Specifically, a catalyst facilitates the adsorption of the reactant followed by the desorption of the intermediate from its surface without participating in the reaction itself. The intrinsic activity of a catalyst is typically represented by the turnover frequency (TOF), which measures the number of electrons transferred per active site per second[14]. However, determining the number of active sites on a catalyst is complex; consequently, two other kinetic parameters are commonly used as an activity metric: the Tafel slope and the overpotential at a fixed geometric current density, typically 1 or 10 mA cm^{-2}.

1.3.1. Pathways and descriptions of OER activity

Man et al. describe OER activity as the difference in free energy of the two intermediates O^* and $OH^{*[25,26]}$. The binding energies of three intermediates — O^*, OH^* and OOH^* — were estimated from first principles using density-functional theory (DFT) calculations on the following four electron reaction paths:

$H_2O + {}^* \rightarrow OH^* + H^+ + e$ $\hfill$ (5)

$OH^* \rightarrow O^* + H^+ + e$ $\hfill$ (6)

Laboratory of Materials for Renewable Energy (LMER)
Institute of Chemical Sciences and Engineering (ISIC)
Basic Science Faculty (SB)

18

$$H_2O + O^* \rightarrow HOO^* + H^+ + e \qquad (7)$$

$$HOO^* \rightarrow {}^* + O_2 + H^+ + e \qquad (8)$$

By plotting the adsorption energy of HOO* as a function of that of HO* on perovskites, rutiles, anatase, Mn_xO_y, Co_3O_4, and NiO oxides, Man et al. discovered a universal scaling relationship between the binding energy of two intermediates ΔE_{OOH^*} and ΔE_{OH^*}: $\Delta E_{OOH^*} = \Delta E_{OH^*} + 3.2$ eV. The change in free energy in Equation (7) can be written as: $\Delta G_{OOH^*} - \Delta G_{O^*} = \Delta G_{OH^*} + 3.2$ eV $- \Delta G_{O^*} = 3.2$ eV $- (\Delta G_{O^*} - \Delta G_{OH^*})$. The overpotential of the reaction is determined by the two reaction steps (6) and (7) featuring the intermediate O*; specifically, the reaction with the higher change in free energy, $[\Delta G_{O^*} - \Delta G_{OH^*}]$ or $[3.2$ eV $- (\Delta G_{O^*} - \Delta G_{OH^*})]$, determines the overpotential. Consequently, $\Delta G_{O^*} - \Delta G_{OH^*}$ was chosen to be the descriptor of OER overpotential; Man et al. used this representation of OER overpotential to obtain a volcano plot for perovskites (Figure 1.4a), rutiles, anatase, Mn_xO_y, and Co_3O_4 oxides (Figure 1.4b).
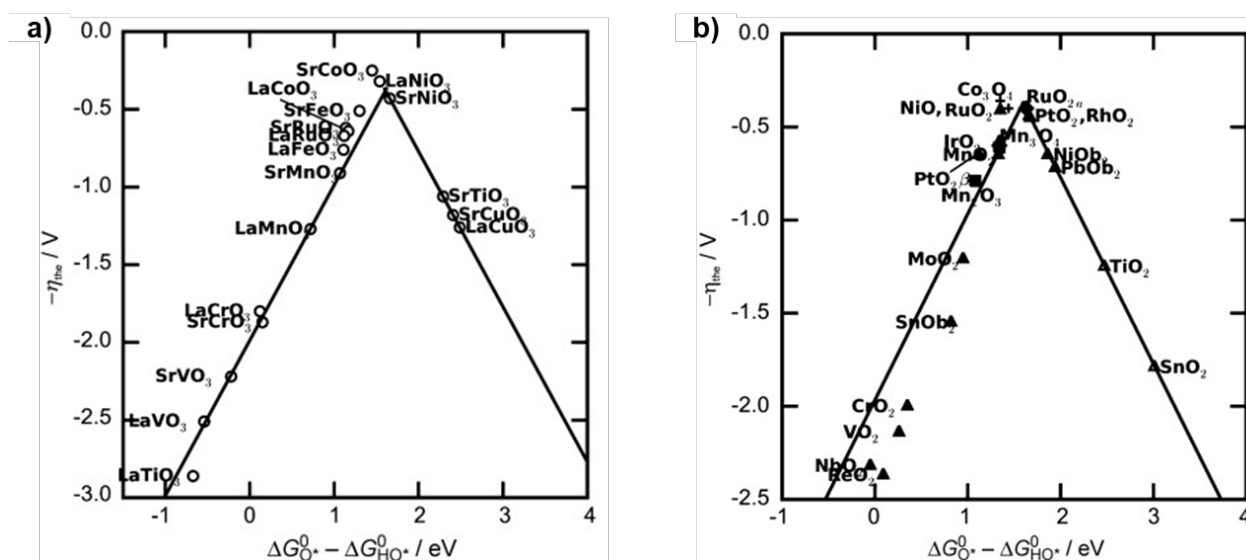
Figure 1.4. Volcano plot devired from the universal scaling relationship between the binding energy of two intermediates ΔE_{OOH^*} and ΔE_{OH^*} for **a)** perovskites and **b)** rutiles, anatase, Co_3O_4 and Mn_xO_y oxides. Reprint with permission from Man et al.[25], copyright 2011, John Wiley & Sons.

Based on the work of Hammer and Nørskov[27], who used a d-band centre to describe the reactivity of the transition metals, Suntivich et al. used the occupancy of the e_g orbital in surface transition metal ions as a descriptor of OER activity [28]. The e_g orbital of surface transition metal (i.e., B-site metal) ions is associated with the σ-bonding with the adsorbate, which affects the OER activity. Consequently, a volcano plot was obtained by plotting the potential at a fixed current of 50 µA cm$^{-2}_{ox}$ as a function of the occupancy of the e_g orbital for different double perovskites. It was found that the potential decreases with increasing e_g, reaching a minimum at $e_g = 1$ before increasing again for $e_g > 1$. The volcano-shaped nature of the plot was explained by the different rate-determining steps in each of the two branches. Suntivich et al. concluded that $Ba_{0.5}Sr_{0.5}Co_{0.8}Fe_{0.2}O_{3-\delta}$ (BSCF) was the best catalyst in terms of OER activity because it exhibited $e_g = 1.2$, which was closest to unity.

Laboratory of Materials for Renewable Energy (LMER)
Institute of Chemical Sciences and Engineering (ISIC)
Basic Science Faculty (SB)

19

Grimaud et al.[29] recently proposed another descriptor for OER activity based on the work of Lee et al.[30], who found that the oxygen (O) p-band centre measured relative to the Fermi energy was an appropriate descriptor of the oxygen reduction reaction (ORR) in SOFCs. The O p-band centre relative to the Fermi energy of perovskites was calculated and was determined to be a good descriptor for OER activity. BSCF remained the best catalyst for the OER because its O p-band centre was located relatively close to the Fermi energy. However, BSCF undergoes amorphization after a few OER cycles[31,32]. Despite possessing an O p-band centre that was further away from the Fermi energy, the double perovskite $Ln_{0.5}Ba_{0.5}CoO_{3-\delta}$ (with Ln = Pr, Sm, Gd, and Ho) exhibited comparable OER activity and a much higher stability than BSCF.

Cheng et al.[33] suggested that a network of descriptors would provide a better assessment of OER activity compared to a single descriptor; consequently, the flat band potential (E_{fb}), ex-situ electronic conductivity, and oxygen vacancy were used in their multi-descriptor system. Although the OER activity of the $La_{1-x}Sr_xCoO_{3-\delta}$, $LaMnO_{3-\delta}$ perovskite series, BSCF, and $PrBaCo_2O_{6-\delta}$ (PBCO) complex perovskites followed each single descriptor, exceptions were observed. High electronic conductivity was found to enhance OER activity, with the exception of PBCO and $LaMnO_{3-\delta}$. Unfunctionalized BSCF had a relatively high vacancy concentration but did not favour OER, deviating from the common trends observed in the rest of the samples. Furthermore, no correlation was observed between E_{fb} and OER catalytic activity. In general, a good catalyst has E_{fb} lower than 1.53 V; nevertheless, the other two parameters must be considered to explain the trends in catalytic OER activity.

Recently, evidence of an (oxy)hydroxide layer formed at the surface of the oxide catalyst during operation was revealed using ex-situ and operando characterization methods; these included the formation of CoO(OH) on top of Co_3O_4[34], Ni(Fe)OOH on top of $NiFe_2O_4$[35,36], and Co(Fe)OOH on top of BSCF[37]. The change in the electronic structure of the catalyst after OER suggested another oxygen evolution mechanism: the lattice oxygen evolution reaction (LOER)[38,39]. In this framework, the oxygen generated in the OER does not come from the electrolyte but instead comes from the lattice oxygen in the oxide catalyst[40,41] ($M^{2n+}O_n^{2-} \rightarrow M_{aq}^{2n+} + 0.5\ O_2 + 2n\ e^-$). Lattice oxygen vacancies remaining after OER are replenished by oxygen from the electrolyte[41]. The remaining M_{aq}^{2+} can either remain in the solution and become oxidized to a higher oxidation state or recombine with OH^- to form a superficial oxy(hydroxide) layer[21,38]. The proposed LOER model, which is driven by the mobility of the oxygen anion in the bulk material, provides a good explanation for catalyst corrosion as well as the evolution of oxygen and the formation of the oxy(hydroxide) layer during electrolysis operations. Another suggested model for the participation of lattice oxygen in the OER is the lattice-oxygen participation mechanism (LOM)[42–44]. The mechanism was initially proposed for $LaNiO_3$, where the oxygen from the electrolyte is first adsorbed at the transition metal site before interacting with the lattice oxygen site and displacing surface oxygen, leaving the lattice oxygen site vacant before being filled by surface oxygen. The process is thus continuously assisted by lattice oxygen: the displaced lattice oxygen generates molecular oxygen, while oxygen from the electrolyte continuously fills up the surface vacancies. DFT calculations also demonstrate that the as-described mechanism is energetically favoured compared to conventional mechanisms[39].

Laboratory of Materials for Renewable Energy (LMER)
Institute of Chemical Sciences and Engineering (ISIC)
Basic Science Faculty (SB)

20

1.3.2. Electrocatalysts for OER

OER catalyst research covers a wide range of materials, including solid-state and molecular catalysts. Solid-state catalysts comprise metals, metal oxides, perovskites, and spinels, while molecular catalysts include ruthenium polypyridine and ammine catalysts, inorganic clusters, iridium complexes, and macrocyclic OER catalysts[19]. Among these materials, metal oxides are currently preferred over metals for OER, since it is widely accepted that a surface oxide layer forms on top of the metal surface prior to OER onset potential. The most commonly used oxide catalysts for OER are RuO_2 and IrO_2, but their scarcity has motivated scientists to investigate other noble-metal-free oxides, including perovskites, spinels, and other layer-structured materials[22], with a focus on first-row transition metals such as Ni, Co, and Fe due to their abundance, low cost, and high catalytic activity[20,23,34,35,45–47]. Suen et al.[22] presents a comprehensive summary of the experimental parameters and kinetic criteria of the OER activity for different families of compounds.

1.3.2.1.   Perovskite

Perovskites are compounds with the chemical formula ABO_3, where A and B are different cations. A is typically an alkaline or rare-earth metal, while B is a transition metal that occupies the octahedral site. The combination of charges for A and B can be 1-5, 2-4, or 3-3. Some perovskites, such as $LaCoO_3$, $LaMnO_3$, and $LaFeO_3$, have been utilized as cathode materials in solid oxide fuel cells (SOFC) rather than alkaline electrolysis as catalysts for OER; this is despite them being highly promising candidates for both oxygen reduction and evolution reactions. BSCF has been identified as the most effective perovskite catalyst based on the recently proposed descriptor involving the occupancy of the e_g orbital of surface transition metal ions. Man et al. and Mefford et al. have also used DFT calculations to show that $SrCoO_3$ and $SrCoO_{0.27}$ are the best catalysts for OER[39,48].

1.3.2.2.   Spinel

The standard chemical formula for spinel is AB_2O_4, where A is a divalent cation occupying the tetrahedral site and B is a trivalent cation occupying the octahedral site[49]. Like perovskites, spinels have been extensively studied as catalysts for the OER. Cation and oxygen vacancies can be introduced by changing synthesis conditions, such as oxygen pressure, synthesis temperature, or calcination temperature[50]. The structure can also be doped to add more defects. These structural modifications can result in changes to the d-band splitting, electrical conductivity[51] or diffusion of oxygen[52].

Cobalt-based catalysts are the most commonly used spinel structure for the OER. The spinel structure of cobalt oxide is Co_3O_4, in which Co^{2+} occupies the tetrahedral site and Co^{3+} occupies the octahedral site. Replacing Co^{2+} or Co^{3+} with other transition metals is an efficient way to improve the OER activity of Co-based spinels. Wang et al. investigated the roles of Co^{2+} and Co^{3+} in Co-based spinel structures by comparing three compounds: Co_3O_4, $CoAl_2O_4$, and $ZnCo_2O_4$[53]. By replacing Co^{2+} with Zn^{2+} and Co^{3+} with Al^{3+}, the OER activity of $ZnCo_2O_4$ was much lower than that of Co_3O_4 and $CoAl_2O_4$, which exhibited similar values. It was revealed that the Co^{2+} occupying tetrahedral sites was responsible for releasing electrons at high potentials to form CoOOH, enhancing OER activity[53]. In addition, both the activity for OER and the stability of Co_3O_4

Laboratory of Materials for Renewable Energy (LMER)
Institute of Chemical Sciences and Engineering (ISIC)
Basic Science Faculty (SB)

21

were improved by Cu doping[54]. Specifically, OER activity enhancement was observed for increasing Cu concentrations from 0.1 to 0.7, peaking at 0.7 before dropping as Cu concentrations increased from 0.7 to 0.9. The occupation of octahedral sites by Cu^{2+} leads to a higher concentration of Co^{3+} in tetrahedral sites, improving OER activity. In the Co-Fe spinel system, Fe^{3+} preferentially occupies octahedral sites, lowering the symmetry of the catalyst due to the longer Fe^{3+}-O bond compared to that of Co^{3+}-O[55]. This leads to the d-orbital splitting of Co^{3+}, which modifies its electronic properties. The optimal OER activity was observed when the occupation of Fe^{3+} was maximized with $Co_{2.775}Fe_{0.225}O_4$.

Dispersing or growing Co-based spinel onto a high-surface-area support is the second most common method of improving its OER activity, as this increases the specific surface area of the active phase. Co_3O_4 grown on reduced mildly oxidized graphene oxide (rmGO) was reported to possess excellent catalytic activity for both the ORR and the OER[56]. A sub-monolayer of cobalt oxide deposited on an Au substrate also exhibited a TOF that was 45 times greater than that of a bulk phase[57]. This outstanding intrinsic activity is due to the selective growth of Co_3O_4 (111) surfaces on single Au crystal (100)[58,59].

1.3.2.3.   Layered-double hydroxides

Layered double hydroxides (LDHs) have a structure composed of a 2D positively charged brucite-like layer that is intercalated with anions[60]. The 2D layer is a series of octahedral structures connected at shared edges. These octahedral sites have a transition metal at their centre that is surrounded by oxygen. LDH families based on Co and Ni have been shown to exhibit good OER catalytic activities[46,47,61–68].

Subbaraman et al.[69] investigated the OER of four different LDH structures electrodeposited on Pt (111) surfaces; they found that a reduced Metal-OH_{ads} bond strength resulted in a lower activation barrier during the Volmer step, facilitating water dissociation. Meanwhile, stronger bonds led to an excessive amount of OH_{ads} on the surface, preventing the re-adsorption of water molecules on available sites. The highest catalytic activities were obtained with Ni, followed by Co, Fe and Mn; this was attributed to the optimal balance between the facilitation of water dissociation and the exposure of enough surface area for water re-adsorption. In Ni-based LDHs, aged $Ni(OH)_2$ was reported to exhibit an OER catalytic activity that was 20 times higher than that obtained from a freshly deposited Ni film, suggesting that ageing Ni films improve OER activity in the same way as Fe incorporation[67]. Later, it was revealed that the deposition of aged Ni film in Fe-free KOH only increases the crystallinity and that the enhanced OER activity observed in aged $Ni(OH)_2$ was mainly caused by the presence of Fe impurities in commercial KOH[47]. In pure Ni films in the presence of both TraceSelect KOH (< 36 ppb Fe) and reagent grade KOH (< 1 ppm Fe), ageing leads to the anodic shift of the redox peak (hydroxide/oxyhydroxide) and improved OER activity. Similarly, the addition of a small amount of iron to Co films lowered both the OER onset potential and the Tafel slope of Co-based LDHs[70]. Although both the Co-Fe and Ni-Fe systems exhibited exceptional catalytic OER activities, Fe is more easily incorporated into Ni films than Co films, and the activity of Ni increases by 100 times while the activity of Co only increases by a factor of 10 with the same amount of Fe impurities[70]. This stark difference was attributed to the more oxophilic nature of Co, resulting in much stronger Co-O bonds and, consequently, more stable CoOOH morphologies upon Fe incorporation[71].

Laboratory of Materials for Renewable Energy (LMER)
Institute of Chemical Sciences and Engineering (ISIC)
Basic Science Faculty (SB)

22

1.4. CO₂ electrolysis and cathodic electrochemical CO₂ reduction (eCO₂RR)

CO_2 electrolysis is relatively similar to water electrolysis, with the exception being that CO_2 is fed into the electrolyte at the cathode of the electrochemical cell. Therefore, two reduction reactions occur simultaneously at the cathode: the HER and the CO_2RR, which form different carbon-containing products. The half-cell reactions at the cathode and anode are as follows:

Cathode:

$$xCO_2 + nH^+ + ne^- \rightarrow product + yH_2O$$

$$2H_2O + 2e^- \rightarrow H_2 + 2OH^-$$

Anode:

$$4OH^- \rightarrow 2H_2O + 4e^- + O_2$$
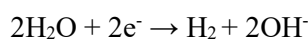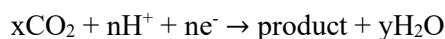
1.4.1. Pathways and descriptors of the eCO₂RR

The reduction reaction between CO_2 and H_2O produces a wide range of carbon-containing products with different reaction pathways. Table 1 presents the possible reaction pathways between CO_2 and H_2O and their equilibrium potential at standard conditions (vs RHE).

Table 1. The equilibrium potential of different half-cell eCO₂RR reactions.

Half-cell reaction	E^0 (V vs RHE)
$CO_2 + H_2O + 2e^- = CO + 2OH^-$	-0.11
$CO_2 + 2H_2O + 2e^- \rightarrow HCOOH + 2OH^-$	-0.09
$CO_2 + 6H_2O + 8e^- = CH_4 + 8OH^-$	+0.16
$2CO_2 + 8H_2O + 12e^- = C_2H_4 + 12OH^-$	+0.07
$2CO_2 + 9H_2O + 12e^- = C_2H_5OH + 12OH^-$	+0.08
$3CO_2 + 13H_2O + 18e^- = C_3H_7OH + 18OH^-$	+0.09
$2H_2O + 2e \rightarrow H_2 + 2OH^-$	0.00

In general, aqueous CO_2 reduction is performed at neutral pH ranges because HER is favoured at low pHs and CO_2 molecules do not exist under alkaline conditions. Hori et al. systematically studied the eCO₂RR performance of different metal cathodes using electrolytes at neutral pH ranges and found that the selectivity of eCO₂RR is highly correlated with the metal used for the cathode[72]. They found that electrodes could be classified into four main categories based on the primary products formed on the metal surfaces. The first group is composed of metals that favoured the formation of formate (HCOO⁻) – these include Pb, Tl, In, Sn, and Cd. The second group includes Au, Ag and Zn, which mainly favour the production of CO. The third

Laboratory of Materials for Renewable Energy (LMER)
Institute of Chemical Sciences and Engineering (ISIC)
Basic Science Faculty (SB)

23

group refers to metals that favour the HER, such as Fe, Ni, Ti, and Pt. Finally, the fourth group is comprised of Cu, which reduces CO_2 to hydrocarbons, aldehydes, and alcohols[72]. Since such trends in product selectivity are not closely related to the periodic table, there has been a significant amount of research into uncovering parameters that can be used to classify these metals. Bagger et al.[73] proposed a descriptor based on the binding energies of various intermediates for the classification of the transition metals into different categories. Here, the binding energies of H* and CO* were used to describe the ability of Cu to further reduce CO*: Cu is the only metal that possesses a negative E_{CO*} and a slightly positive E_{H*} (Figure 1.5). In addition, it was suggested that protonated formaldehyde was prone to the formation of hydrocarbons when bound to the metal surface through carbon while being prone to the formation of alcohol when bound through oxygen. Therefore, the adsorption energies of the protonated species OCH3* and CH2OH* were also used to categorize the metals into hydrocarbon- or alcohol-production groups. The binding energy of CO* intermediates was widely accepted as a descriptor for eCO2RR, since weaker CO* binding can lead to the release of CO while stronger CO* binding can block active sites, resulting in significant HER[74]. However, the CO* binding energy used in these works was based on computational studies: although they correlated well with the adsorption energies of CO on a single crystal surface in an ultrahigh vacuum, they did not consider the complexity of electrochemical interfaces. Most recently, Xu et al. revealed that CO* binding energies only partially describe C_{2+} selectivity and that an additional descriptor should be taken into account: the ratio between active Cu sites for $CO_2 \rightarrow CO$ reduction and active sites for $CO \rightarrow C_{2+}$ products.
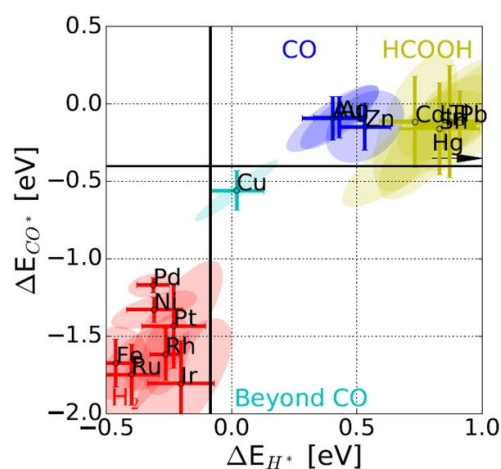
Figure 1.5. Classification of metal surfaces with respect to hydrogen and CO binding energies. Reprint with permission from Bagger et al.[73], copyright 2017, John Wiley & Sons..

Considering that Cu is the only metal capable of producing hydrocarbons and alcohols, gaining a deeper understanding of the reaction mechanisms on the Cu surface would potentially allow for the enhanced selectivity of the desired products. It is generally accepted that CO* is an intermediate in CO_2 reduction that can be further reduced due to the similarity in the product distribution of eCO2RR and eCORR on Cu surfaces[75]. Two pathways for ethylene formation from adsorbed CO* on Cu surfaces have been proposed. The first pathway was proposed by Norskov et al.[74], who suggested that the adsorbed CO* was reduced to ethylene and proved that the limiting factor of this pathway was controlled by CO* protonation. The second pathway was suggested by Koper et al., who showed that two adjacent CO* could interact to form a CO dimer,

Laboratory of Materials for Renewable Energy (LMER)
Institute of Chemical Sciences and Engineering (ISIC)
Basic Science Faculty (SB)

24

which subsequently hydrogenated and bonded to the surface through an enediol or oxametallacycle intermediates. The rate-determining step in this pathway was suggested to be the dimerization of CO and its subsequent electron transfer.

In summary, different computational studies have shown that there are two possible pathways for the reduction of CO_2 to ethylene:

- At low overpotentials (-0.4 V vs RHE), CO dimerization is the primary pathway. This pathway is specific to Cu (100) surfaces and selective to ethylene formation.
- At high overpotentials (-0.8 vs RHE), CO hydrogenation is the primary pathway. This pathway has a common intermediate with the production of methane and can take place on both Cu (111) and Cu (100) surfaces.

1.4.2. Electrocatalysts for the eCO$_2$RR to C$_{2+}$ products

The unique selectivity of Cu for the formation of C_{2+} products has motivated researchers to modify it for enhanced selectivity. The selectivity of eCO$_2$RR on Cu surfaces depends strongly on the overpotential. Hori and Kuhl reported that the selectivity of the reaction towards hydrocarbons and alcohols reaches a maximum at a relatively high overpotential of approximately -1.05 V vs RHE. At low overpotentials, hydrogen and CO are still the main products. Consequently, the main goal of many researchers is the lowering of the overpotential while still maintaining the selectivity of eCO$_2$RR.

In recent years, several experiments have been conducted to improve the eCO$_2$RR performance of Cu[76–83]. These studies have shown that the activity and selectivity of Cu catalysts can be tuned by increasing the number of active sites or by boosting the intrinsic catalytic performance of the materials. More active sites are introduced in structures with large surface areas such as nanoparticles, nanowires, or porous materials. In addition, the use of high-surface-area supports such as graphene or carbon nanotubes can help better disperse active sites. Since reactions can preferentially occur at specific sites (e.g., kinks, steps, edges, and specific crystalline planes), it is important to control the shape of the catalyst to maximise the number of active sites. The following section presents the three most representative material classes used to significantly enhance selectivity towards C_{2+} products: Cu nanoparticles, oxide-derived Cu, and Cu alloys.

1.4.2.1. Cu nanoparticles (Cu-NP)

The synthesis of nanoparticles is the preferred method of increasing the number of active sites on a catalyst per unit mass, which improves its overall activity. The effect of the Cu particle size on the eCO$_2$RR activity and selectivity was assessed by measuring the increase in faradaic current when particle sizes were reduced to the nanometre scale[84]. However, it was found that the selectivity of the catalyst towards CO and H_2 increased and its selectivity towards CH_4 and C_2H_4 decreased when the particles were smaller than 15 nm. These selectivity values remain constant for particle sizes between 2–15 nm, but particles smaller than 2 nm were found to produce almost no C_{2+} products. This size–selectivity correlation was attributed to an increased number of atoms with a coordination number of less than 8. In order to achieve high activities while retaining

Laboratory of Materials for Renewable Energy (LMER)
Institute of Chemical Sciences and Engineering (ISIC)
Basic Science Faculty (SB)

25

a high selectivity towards ethylene on a Cu (100) surface, Cu nanocubes were synthesized to maximise the surface area to volume ratio while maintaining the (100) facet; the performance of these nanocubes was then compared to polycrystalline Cu[85]. 44-nm Cu nanocubes were found to exhibit an eCO_2RR faradaic efficiency (FE) of 80% and a 25% selectivity towards ethylene; size-dependent selectivity was found to be associated with the ratio between the number of edge-sites to plane-sites in the (100) plane[86].

Ex situ studies on the structural evolution of Cu nanocubes were conducted to identify links between the electrochemical performance and the morphology of the catalysts. Ex situ transmission electron microscopy (TEM) tracking was used to monitor the Cu nanocubes at different reaction times, revealing that the nanocubes progressed through three stages of evolution[87]. First, there is a pitting process during which the corners and edges of the cubes dissolve, followed by the formation of Cu nanoclusters in the neighbourhood of the initial cube. Over time, the clusters grow in size and coalesce between the nanocubes, resulting in nanocluster formation up to 12 hours after the start of the reaction. The degradation of Cu nanocubes explains the increase in H_2 selectivity and the decrease in CO selectivity over time. Ex situ TEM was also used to show that the morphology of the Cu_2O nanocubes changed after the reaction: the initial cubes were found to have fragmented into 2–4 nm particles that were stacked on top of each other. The enhanced selectivity towards C_{2+} products was thus attributed to the combination of fragmentation and stacked geometry because isolated 2-nm nanocubes only resulted in increased HER activities[88].

1.4.2.2.   Oxide-derived Cu catalysts (OD-Cu)

In addition to Cu nanoparticles, OD-Cu catalysts also exhibit excellent activities with respect to eCO_2RR[89–93]. Annealed Cu_2O nanowires[91], galvanostatically deposited Cu_2O[90], electrochemically oxidized Cu_2O[92] were found to be capable of generating 40%, 50%, and 60% C_{2+} products, respectively; in addition, oxygen plasma-treated treated duplex CuO–Cu_2O exhibited a 60% faradaic selectivity towards C_2H_4[89]. Ex situ characterizations are commonly used to examine the catalysts before and after eCO_2RR[94–96]. However, the surface of Cu is sensitive to the presence of oxygen; consequently, Cu catalysts may be oxidized between the end of the electrochemical measurements and the start of the characterization. The complete reduction of copper oxides under eCO_2RR conditions was supported by operando Raman spectroscopy[90] as well as ex-situ secondary ion mass spectroscopy (SIMS)[92]. Furthermore, the presence of a significant amount of oxides was reported by a combination of EDX and quasi-in-situ XPS[93,97]. Ex situ electron energy loss spectroscopy (EELS) also demonstrated that, although the surface of the reduced catalyst is composed of a pure metallic phase, there is a subsurface layer of oxygen that increases the CO binding energy and aids the formation of C-C bonds[98]. Consequently, the structure and chemistry of CO_2RR-active catalytic surfaces have remained the subject of further investigations.

1.4.2.3.   Cu-based bimetallic catalysts

Since it is widely accepted that CO is the key reaction intermediate in the electroreduction of CO_2 to C_{2+} products, the combination of Cu and a CO-producing metal has attracted a significant amount of attention in the context of boosting the selectivity of C_{2+} products. In such a catalytic system, the guest metal (such as Ag, Au, or Zn) can produce CO more effectively than pure Cu; consequently, if the distance between the guest

Laboratory of Materials for Renewable Energy (LMER)
Institute of Chemical Sciences and Engineering (ISIC)
Basic Science Faculty (SB)

26

metal site and the Cu is sufficiently small (i.e., lower than the diffusion length of CO), the CO formed at the guest metal can diffuse onto an active Cu site, allowing it to be adsorbed and transforming the CO more reduced products.

The stability and selectivity of Cu-based bimetallic catalysts can be tuned by varying the composition of the alloyed metals or by designing specific bimetallic structures and interfaces. Ag-decorated Cu nanowires have been shown to boost the FE of C_2H_4 to 52% compared to the 33% obtained on bare Cu nanowires[99], while the Ag@C@Cu core-shell structure is known to promote the formation of ethanol over ethylene[100]. In addition, the stability of the core-shell structure and the selectivity of the catalyst towards C_{2+} products were significantly improved when Ag was replaced with Pd, which produces CO at a lower rate[101].

1.5. Objectives and outline of the research work

Given the aforementioned challenges of dealing with sustainability and CO_2 emissions, it is clear that water electrolysis remains a promising solution for the fossil fuel-free production of hydrogen, and that eCO2RR can address the problems associated with the discharge of CO_2 by capturing and reducing it to other carbon-containing fuels. However, both reactions involve multiple electrons; these reactions involve different intermediate steps, leading to high overpotentials and low energy efficiencies. Consequently, it is vital to identify **catalysts** that can enhance the activity and stability of the reaction, allowing these reactions to be used daily. In addition, the reduction of CO_2 in aqueous media could produce a wide range of carbon-containing compounds; it is therefore necessary to develop catalysts that can enhance its selectivity towards a targeted product. In the context of the OER, the challenge is less reliant on product selectivity and has more to do with the development of earth-abundant catalysts that can replace the current benchmark catalysts, which generally include precious oxides such as IrO_2 and RuO_2.

In a practical electrochemical reactor, the activity and stability of a reaction not only depends on the catalyst but also the **reaction environment**; this includes parameters such as reactant concentrations, pH, and ions in the electrolyte. Thus, improving the performance of the reaction can be accomplished either by modifying the catalyst[102] or by tuning the reaction environment[103]. Modifications to catalysts include strategies that aim to increase the intrinsic activity of the material by modifying the electronic structure and interfaces of the catalysts via alloying, interactions, and confinement[83]. The number of active sites on the catalyst can be also tuned by growing nanostructures or by dispersing the nanocatalysts onto a high-surface-area support[83]. In contrast, tuning the reaction environment consists of adjusting the local hydrophilicity, local pH, and local concentrations of the reactants. In the context of the OER and eCO2RR, which produce and consume O_2 and CO_2 in an aqueous electrolyte aided by a catalyst surface, the reaction site refers to the interface between the solid, liquid, and gaseous components. Therefore, controlling the hydrophilicity of the local environment around the catalyst can change the ability of the gas and liquid phase to access the surface, which would result in changes in the catalyst's activity and product selectivity. Furthermore, changes to the local pH might affect the coverage of certain reaction intermediates, such as the known low coverage of CO at low pHs, resulting in

Laboratory of Materials for Renewable Energy (LMER)
Institute of Chemical Sciences and Engineering (ISIC)
Basic Science Faculty (SB)

27

the depletion of C_{2+} products in eCO_2RR[104]. Finally, increasing the mass transport of the reactants to the catalyst surface enhances reaction activity; for example, higher OH^- concentrations are known to result in lower Tafel slopes in the OER[105], while using a flow-cell reactor to promote the diffusion of CO_2 to the catalyst surface allows for a much higher CO_2RR current density compared to a conventional H-cell[103].

In this thesis, we synthesized a highly active catalyst and adjusted its reaction environment to optimize its activity and stability while also maximizing its selectivity towards the desired products. The work is divided into four chapters, each describing a distinct aspect of the research:

Chapter 2: Understanding the role of surface oxygen-containing functional groups on carbon-supported cobalt catalysts for oxygen evolution reaction

In this chapter, we investigated the impact of surface oxygen functionalization on the dispersion of Co-based catalysts and their catalytic activity towards the OER. Our research focused on different oxygen species present on the surface of various carbon supports. We specifically highlight the crucial role played by surface oxygen-containing functional groups (s-OFGs) in enhancing the adsorption of metal cations onto the carbon surface. We revealed that the carbon support with the highest acidic s-OFGs content exhibited a superior dispersion of sub-nano- and nano-sized Co particles, as well as the highest mass activity and TOF for OER at a Co loading of 0.5 wt.%. Furthermore, our research revealed evidence of a strong interaction between the support and small Co nanoparticles, particularly in the formation of additional s-OFGs. In particular, carboxyl functional groups (COOH) were found to be particularly effective in facilitating O_2 spillover from the Co surface, thereby aiding the removal of O_2.

Chapter 3: Elucidating the mechanism of Fe incorporation in in situ synthesized Co–Fe oxygen-evolving nanocatalysts

This chapter describes our attempt to understand the incorporation mechanisms, local structure, placement, and mechanistic role of Fe in enhancing the OER activity of Co-based catalysts. The in situ synthesis method described in this research allows for the investigation of the structure of the catalyst at its most native state. TEM and sensitive surface characterization techniques revealed that the in situ catalyst is composed of a mixture of amorphous $CoFeO_x$ and crystalline CoO and Co_3O_4, with Fe incorporated as a solid solution. Electron diffraction and operando electrochemical quartz-crystal microbalance (EQCM) analyses revealed that the incorporation of Fe into the Co-host structure occurred through the substitution of Fe^{3+} at Co^{3+} sites. The CoFe catalyst exhibited a Tafel slope of 28.3 mV dec^{-1} and an overpotential at 10 mA cm^{-2} of 319 mV, which ranks among the best CoFe-based catalysts for OER. Operando Raman spectroscopy and electrochemical microbalance measurements showed that Fe reduces the transition potential from the in situ deposited catalyst to the OER-active phase.

Chapter 4: Enhanced electrocatalytic CO_2 reduction to C_{2+} products by adjusting the local reaction environment with polymer binders

Here, we aimed to regulate the local access of the liquid and gas phases to the catalyst surface by tuning the hydrophilicity of the polymer binder, which is usually used to bind the catalyst to the carbon paper support.

Laboratory of Materials for Renewable Energy (LMER)
Institute of Chemical Sciences and Engineering (ISIC)
Basic Science Faculty (SB)

28

The powder catalyst can be effectively coated with a thin layer (~1.2 nm) of polymer binder through a combination of physical mixing and sonication. The utilization of three polymer binders with different hydrophilicity revealed that the most hydrophobic/CO_2-philic polymer, FEP, significantly enhanced the total current density as well as the selectivity of the catalyst towards CO_2RR products. We also observed a significant increase in selectivity towards C_{2+} products. Such trends were explained by operando Raman spectroscopy, which showed that the hydrophobicity of the FEP not only retains CO_2, which promotes the formation of CO_2RR products but also retains the important intermediate CO, which is subsequently reduced to C_{2+} products.

Chapter 5: Unveiling degradation mechanisms in gas diffusion electrodes towards enhancing the stability of CO_2 electrolysis in acidic environments.

This chapter investigates the activity and stability of OD-Cu in low-pH environments. A reasonably low pH allows for the production of C_{2+} products while also allowing for the improved utilization of CO_2; this is because the acid electrolyte can convert bicarbonate (formed due to high local pH) back into CO_2. Although an acidic solution could generate a significant amount of hydrogen, additional cations reduced proton access and resulted in an FE of 70% towards C_{2+} products; this was similar to the yield obtained in alkaline conditions (pH 14). Operando Raman spectroscopy revealed that even at a bulk pH of 2, the local pH at the catalyst surface remained alkaline due to the presence of surface hydroxide species. We also found that the dynamic reconstruction of OD-Cu catalyst in acid was not the only reason for electrode deactivation since the potential-induced metallic Cu surface was stable under the reaction conditions; instead, it was the change in bulk pH and the flooding of the gas diffusion electrode (GDE) that led to the depletion of C_{2+} products. To mitigate this issue, we suggested the separation of the inlet catholyte from the outlet liquid products. This strategy aims to uphold a consistent pH level upon entering the cell. By maintaining a continuous flow of the solution, we effectively regulated the pH in close proximity to the catalyst, ensuring it remains below a critical threshold, thus preventing flooding.

The final chapter concludes the research and discusses the potential of future research projects.

Laboratory of Materials for Renewable Energy (LMER)
Institute of Chemical Sciences and Engineering (ISIC)
Basic Science Faculty (SB)

29

References

[1]   A. Züttel, A. Remhof, A. Borgschulte, O. Friedrichs, *Philos. Trans. R. Soc. A Math. Phys. Eng. Sci.* **2010**, *368*, 3329.

[2]   C. Song, in *Catal. Today*, **2002**, pp. 17–49.

[3]   M. K. Hubbert, *Science (80-.).* **1949**, *109*, 103.

[4]   J. P. Holdren, *Popul. Environ.* **1991**, *12*, 231.

[5]   International Renewable Energy Agency, *Renewable Power Generation Costs in 2017*, **2018**.

[6]   M. Grätzel, *Nature* **2001**, *414*, 338.

[7]   L. Schlapbach, A. Züttel, *Nature* **2001**, *414*, 353.

[8]   K. T. Møller, T. R. Jensen, E. Akiba, H. wen Li, *Prog. Nat. Sci. Mater. Int.* **2017**, *27*, 34.

[9]   R. Ramachandran, R. K. Menon, *Int. J. Hydrogen Energy* **1998**, *23*, 593.

[10]   L. B. Bertuccioli, A. Chan, D. Hart, F. Lehner, B. Madden, E. Standen, *Study on Development of Water Electrolysis in the EU*, **2014**.

[11]   S. T. Thompson, B. D. James, J. M. Huya-Kouadio, C. Houchins, D. A. DeSantis, R. Ahluwalia, A. R. Wilson, G. Kleen, D. Papageorgopoulos, *J. Power Sources* **2018**, *399*, 304.

[12]   D. P. Broom, C. J. Webb, K. E. Hurst, P. A. Parilla, T. Gennett, C. M. Brown, R. Zacharia, E. Tylianakis, E. Klontzas, G. E. Froudakis, T. A. Steriotis, P. N. Trikalitis, D. L. Anton, B. Hardy, D. Tamburello, C. Corgnale, B. A. van Hassel, D. Cossement, R. Chahine, M. Hirscher, *Appl. Phys. A Mater. Sci. Process.* **2016**, *122*, 1.

[13]   J. Ren, N. M. Musyoka, H. W. Langmi, M. Mathe, S. Liao, *Int. J. Hydrogen Energy* **2017**, *42*, 289.

[14]   C. Wei, R. R. Rao, J. Peng, B. Huang, I. E. L. Stephens, M. Risch, Z. J. Xu, Y. Shao-Horn, *Adv. Mater.* **2019**, *31*, 1.

[15]   O. Z. Sharaf, M. F. Orhan, *Renew. Sustain. Energy Rev.* **2014**, *32*, 810.

[16]   P. De Luna, C. Hahn, D. Higgins, S. A. Jaffer, T. F. Jaramillo, E. H. Sargent, *Science (80-.).* **2019**, *364*, DOI 10.1126/science.aav3506.

[17]   P. Nikolaidis, A. Poullikkas, *Renew. Sustain. Energy Rev.* **2017**, *67*, 597.

[18]   W. T. Hong, M. Risch, K. A. Stoerzinger, A. Grimaud, J. Suntivich, Y. Shao-Horn, *Energy Environ. Sci.* **2015**, *8*, 1404.

[19]   T. R. Cook, D. K. Dogutan, S. Y. Reece, Y. Surendranath, T. S. Teets, D. G. Nocera, *Chem. Rev.* **2010**, *110*, 6474.

[20]   Y. Yan, B. Y. Xia, B. Zhao, X. Wang, *J. Mater. Chem. A* **2016**, *4*, 17587.

[21]   E. Fabbri, T. J. Schmidt, *ACS Catal.* **2018**, *8*, 9765.

Laboratory of Materials for Renewable Energy (LMER)
Institute of Chemical Sciences and Engineering (ISIC)
Basic Science Faculty (SB)

30

[22]   N. T. Suen, S. F. Hung, Q. Quan, N. Zhang, Y. J. Xu, H. M. Chen, *Chem. Soc. Rev.* **2017**, *46*, 337.

[23]   F. Song, L. Bai, A. Moysiadou, S. Lee, C. Hu, L. Liardet, X. Hu, *J. Am. Chem. Soc.* **2018**, *140*, 7748.

[24]   N. B. Halck, V. Petrykin, P. Krtil, J. Rossmeisl, *Phys. Chem. Chem. Phys.* **2014**, *16*, 13682.

[25]   I. C. Man, H. Su, F. Calle-Vallejo, H. A. Hansen, J. I. Martínez, N. G. Inoglu, J. Kitchin, T. F. Jaramillo, J. K. Nørskov, J. Rossmeisl, *ChemCatChem* **2011**, *3*, 1159.

[26]   J. Rossmeisl, Z. W. Qu, H. Zhu, G. J. Kroes, J. K. Nørskov, *J. Electroanal. Chem.* **2007**, *607*, 83.

[27]   B. Hammer, J. K. Nørskov, *Adv. Catal.* **2000**, *45*, 71.

[28]   J. Suntivich, K. J. May, H. A. Gasteiger, J. B. Goodenough, Y. Shao-Horn, *Science (80-.).* **2011**, *334*, 1383.

[29]   A. Grimaud, K. J. May, C. E. Carlton, Y. L. Lee, M. Risch, W. T. Hong, J. Zhou, Y. Shao-Horn, *Nat. Commun.* **2013**, *4*, DOI 10.1038/ncomms3439.

[30]   Y. L. Lee, J. Kleis, J. Rossmeisl, S. H. Yang, D. Morgan, *Energy Environ. Sci.* **2011**, *4*, 3966.

[31]   K. J. May, C. E. Carlton, K. A. Stoerzinger, M. Risch, J. Suntivich, Y. L. Lee, A. Grimaud, Y. Shao-Horn, *J. Phys. Chem. Lett.* **2012**, *3*, 3264.

[32]   C. Zhang, C. P. Berlinguette, S. Trudel, *Chem. Commun.* **2016**, *52*, 1513.

[33]   X. Cheng, E. Fabbri, Y. Yamashita, I. E. Castelli, B. Kim, M. Uchida, R. Haumont, I. Puente-Orench, T. J. Schmidt, *ACS Catal.* **2018**, *8*, 9567.

[34]   M. Favaro, J. Yang, S. Nappini, E. Magnano, F. M. Toma, E. J. Crumlin, J. Yano, I. D. Sharp, *J. Am. Chem. Soc.* **2017**, *139*, 8960.

[35]   L. Calvillo, F. Carraro, O. Vozniuk, V. Celorrio, L. Nodari, A. E. Russell, D. Debellis, D. Fermin, F. Cavani, S. Agnoli, G. Granozzi, *J. Mater. Chem. A* **2018**, *6*, 7034.

[36]   C. S. Hsu, N. T. Suen, Y. Y. Hsu, H. Y. Lin, C. W. Tung, Y. F. Liao, T. S. Chan, H. S. Sheu, S. Y. Chen, H. M. Chen, *Phys. Chem. Chem. Phys.* **2017**, *19*, 8681.

[37]   E. Fabbri, M. Nachtegaal, T. Binninger, X. Cheng, B. J. Kim, J. Durst, F. Bozza, T. Graule, R. Schäublin, L. Wiles, M. Pertoso, N. Danilovic, K. E. Ayers, T. J. Schmidt, *Nat. Mater. 2017 169* **2017**, *16*, 925.

[38]   T. Binninger, R. Mohamed, K. Waltar, E. Fabbri, P. Levecque, R. Kötz, T. J. Schmidt, *Sci. Rep.* **2015**, *5*, DOI 10.1038/srep12167.

[39]   J. T. Mefford, X. Rong, A. M. Abakumov, W. G. Hardin, S. Dai, A. M. Kolpak, K. P. Johnston, K. J. Stevenson, *Nat. Commun.* **2016**, *7*, DOI 10.1038/ncomms11053.

[40]   C. Spöri, J. T. H. Kwan, A. Bonakdarpour, D. P. Wilkinson, P. Strasser, *Angew. Chemie Int. Ed.* **2017**, *56*, 5994.

Laboratory of Materials for Renewable Energy (LMER)
Institute of Chemical Sciences and Engineering (ISIC)
Basic Science Faculty (SB)

31

[41] B. Han, K. A. Stoerzinger, V. Tileli, A. D. Gamalski, E. A. Stach, Y. Shao-Horn, *Nat. Mater.* **2017**, *16*, 121.

[42] X. Rong, J. Parolin, A. M. Kolpak, *ACS Catal.* **2016**, *6*, 1153.

[43] J. S. Yoo, X. Rong, Y. Liu, A. M. Kolpak, *ACS Catal.* **2018**, *8*, 4628.

[44] J. S. Yoo, Y. Liu, X. Rong, A. M. Kolpak, *J. Phys. Chem. Lett.* **2018**, *9*, 1473.

[45] M. Gong, H. Dai, *Nano Res.* **2014**, *8*, 23.

[46] D. Friebel, M. W. Louie, M. Bajdich, K. E. Sanwald, Y. Cai, A. M. Wise, M. J. Cheng, D. Sokaras, T. C. Weng, R. Alonso-Mori, R. C. Davis, J. R. Bargar, J. K. Nørskov, A. Nilsson, A. T. Bell, *J. Am. Chem. Soc.* **2015**, *137*, 1305.

[47] L. Trotochaud, S. L. Young, J. K. Ranney, S. W. Boettcher, *J. Am. Chem. Soc.* **2014**, *136*, 6744.

[48] I. C. Man, H. Su, F. Calle-Vallejo, H. A. Hansen, J. I. Martínez, N. G. Inoglu, J. Kitchin, T. F. Jaramillo, J. K. Nørskov, J. Rossmeisl, *ChemCatChem* **2011**, *3*, 1159.

[49] W. H. Bragg, *Nature* **1915**, *95*, 561.

[50] K. Uusi-Esko, E.-L. Rautama, M. Laitinen, T. Sajavaara, M. Karppinen, *Chem. Mater.* **2010**, *22*, 6297.

[51] J. Du, T. Zhang, F. Cheng, W. Chu, Z. Wu, J. Chen, *Inorg. Chem.* **2014**, *53*, 9106.

[52] T. Nakamura, M. Misono, Y. Yoneda, *Bull. Chem. Soc. Jpn.* **1982**, *55*, 394.

[53] H. Y. Wang, S. F. Hung, H. Y. Chen, T. S. Chan, H. M. Chen, B. Liu, *J. Am. Chem. Soc.* **2016**, *138*, 36.

[54] X. Wu, K. Scott, *J. Mater. Chem.* **2011**, *21*, 12344.

[55] X. Gao, J. Liu, Y. Sun, X. Wang, Z. Geng, F. Shi, X. Wang, W. Zhang, S. Feng, Y. Wang, K. Huang, *Inorg. Chem. Front.* **2019**, *6*, 3295.

[56] Y. Liang, Y. Li, H. Wang, J. Zhou, J. Wang, T. Regier, H. Dai, *Nat. Mater.* **2011**, *10*, 780.

[57] B. S. Yeo, A. T. Bell, *J. Am. Chem. Soc.* **2011**, *133*, 5587.

[58] J. A. Koza, Z. He, A. S. Miller, J. A. Switzer, *Chem. Mater.* **2012**, *24*, 3567.

[59] Z. Chen, C. X. Kronawitter, B. E. Koel, *Phys. Chem. Chem. Phys.* **2015**, *17*, 29387.

[60] Q. Wang, D. Ohare, *Chem. Rev.* **2012**, *112*, 4124.

[61] F. Song, X. Hu, *J. Am. Chem. Soc.* **2014**, *136*, 16481.

[62] F. Song, X. Hu, *Nat. Commun.* **2014**, *5*, 4477.

[63] J. Ping, Y. Wang, Q. Lu, B. Chen, J. Chen, Y. Huang, Q. Ma, C. Tan, J. Yang, X. Cao, Z. Wang, J. Wu, Y. Ying, H. Zhang, *Adv. Mater.* **2016**, *28*, 7640.

[64] R. Ma, Z. Liu, K. Takada, N. Iyi, Y. Bando, T. Sasaki, *J. Am. Chem. Soc.* **2007**, *129*, 5257.

Laboratory of Materials for Renewable Energy (LMER)
Institute of Chemical Sciences and Engineering (ISIC)
Basic Science Faculty (SB)

32

[65] Z. Qiu, C. W. Tai, G. A. Niklasson, T. Edvinsson, *Energy Environ. Sci.* **2019**, *12*, 572.

[66] M. Gong, Y. Li, H. Wang, Y. Liang, J. Z. Wu, J. Zhou, J. Wang, T. Regier, F. Wei, H. Dai, *J. Am. Chem. Soc.* **2013**, *135*, 8452.

[67] M. W. Louie, A. T. Bell, *J. Am. Chem. Soc.* **2013**, *135*, 12329.

[68] F. Dionigi, P. Strasser, *Adv. Energy Mater.* **2016**, *6*, 1600621.

[69] R. Subbaraman, D. Tripkovic, K. C. Chang, D. Strmcnik, A. P. Paulikas, P. Hirunsit, M. Chan, J. Greeley, V. Stamenkovic, N. M. Markovic, *Nat. Mater.* **2012**, *11*, 550.

[70] M. S. Burke, M. G. Kast, L. Trotochaud, A. M. Smith, S. W. Boettcher, *J. Am. Chem. Soc.* **2015**, *137*, 3638.

[71] T. Zhang, M. R. Nellist, L. J. Enman, J. Xiang, S. W. Boettcher, *ChemSusChem* **2019**, *12*, 2015.

[72] Y. Hori, *Mod. Asp. Electrochem.* **2008**, *42*, 89.

[73] A. Bagger, W. Ju, A. S. Varela, P. Strasser, J. Rossmeisl, *ChemPhysChem* **2017**, *18*, 3266.

[74] A. A. Peterson, F. Abild-Pedersen, F. Studt, J. Rossmeisl, J. K. Nørskov, *Energy Environ. Sci.* **2010**, *3*, 1311.

[75] Y. Hori, A. Murata, R. Takahashi, S. Suzuki, *J. Am. Chem. Soc.* **1987**, *109*, 5022.

[76] L. Gong, X. Y. E. Chng, Y. Du, S. Xi, B. S. Yeo, *ACS Catal.* **2018**, *8*, 807.

[77] D. Kim, J. Resasco, Y. Yu, A. M. Asiri, P. Yang, *Nat. Commun.* **2014**, *5*, 1.

[78] C. G. Morales-Guio, E. R. Cave, S. A. Nitopi, J. T. Feaster, L. Wang, K. P. Kuhl, A. Jackson, N. C. Johnson, D. N. Abram, T. Hatsukade, C. Hahn, T. F. Jaramillo, *Nat. Catal.* **2018**, *1*, 764.

[79] Y. Lum, J. W. Ager, *Energy Environ. Sci.* **2018**, *11*, 2935.

[80] J. Huang, M. Mensi, E. Oveisi, V. Mantella, R. Buonsanti, *J. Am. Chem. Soc.* **2019**, *141*, 2490.

[81] D. Ren, B. S. H. Ang, B. S. Yeo, *ACS Catal.* **2016**, *6*, 8239.

[82] M. B. Ross, P. De Luna, Y. Li, C. T. Dinh, D. Kim, P. Yang, E. H. Sargent, *Nat. Catal.* **2019**, *2*, 648.

[83] Z. W. Seh, J. Kibsgaard, C. F. Dickens, I. Chorkendorff, J. K. Nørskov, T. F. Jaramillo, *Science (80-.).* **2017**, *355*, eaad4998.

[84] R. Reske, H. Mistry, F. Behafarid, B. Roldan Cuenya, P. Strasser, *J. Am. Chem. Soc.* **2014**, *136*, 6978.

[85] F. S. Roberts, K. P. Kuhl, A. Nilsson, *Angew. Chemie Int. Ed.* **2015**, *54*, 5179.

[86] A. Loiudice, P. Lobaccaro, E. A. Kamali, T. Thao, B. H. Huang, J. W. Ager, R. Buonsanti, *Angew. Chemie Int. Ed.* **2016**, *55*, 5789.

[87] J. Huang, N. Hörmann, E. Oveisi, A. Loiudice, G. L. De Gregorio, O. Andreussi, N. Marzari, R. Buonsanti, *Nat. Commun.* **2018**, *9*, 1.

Laboratory of Materials for Renewable Energy (LMER)
Institute of Chemical Sciences and Engineering (ISIC)
Basic Science Faculty (SB)

33

[88] H. Jung, S. Y. Lee, C. W. Lee, M. K. Cho, D. H. Won, C. Kim, H. S. Oh, B. K. Min, Y. J. Hwang, *J. Am. Chem. Soc.* **2019**, *141*, 4624.

[89] H. Mistry, A. S. Varela, C. S. Bonifacio, I. Zegkinoglou, I. Sinev, Y. W. Choi, K. Kisslinger, E. A. Stach, J. C. Yang, P. Strasser, B. R. Cuenya, *Nat. Commun.* **2016**, *7*, 1.

[90] D. Ren, Y. Deng, D. Handoko, C. S. Chen, S. Malkhandi, B. S. Yeo, **2015**, DOI 10.1021/cs502128q.

[91] M. Ma, K. Djanashvili, W. A. Smith, *Angew. Chemie Int. Ed.* **2016**, *55*, 6680.

[92] Y. Lum, J. W. Ager, *Angew. Chemie Int. Ed.* **2018**, *57*, 551.

[93] D. Gao, I. Zegkinoglou, N. J. Divins, F. Scholten, I. Sinev, P. Grosse, B. Roldan Cuenya, *ACS Nano* **2017**, *11*, 4825.

[94] K. Manthiram, B. J. Beberwyck, A. P. Alivisatos, *J. Am. Chem. Soc.* **2014**, *136*, 13319.

[95] X. Cheng, B. J. Kim, E. Fabbri, T. J. Schmidt, *ACS Appl. Mater. Interfaces* **2019**, *11*, 34787.

[96] W. T. Osowiecki, J. J. Nussbaum, G. A. Kamat, G. Katsoukis, M. Ledendecker, H. Frei, A. T. Bell, A. P. Alivisatos, *ACS Appl. Energy Mater.* **2019**, *2*, 7744.

[97] R. M. Arán-Ais, F. Scholten, S. Kunze, R. Rizo, B. Roldan Cuenya, *Nat. Energy* **2020**, *5*, 317.

[98] A. Eilert, F. Cavalca, F. S. Roberts, J. Osterwalder, C. Liu, M. Favaro, E. J. Crumlin, H. Ogasawara, D. Friebel, L. G. M. Pettersson, A. Nilsson, *J. Phys. Chem. Lett.* **2017**, *8*, 285.

[99] J. Gao, H. Zhang, X. Guo, J. Luo, S. M. Zakeeruddin, D. Ren, M. Grätzel, *J. Am. Chem. Soc.* **2019**, *141*, 18704.

[100] J. Zhang, T. H. M. Pham, Y. Ko, M. Li, S. Yang, C. D. Koolen, L. Zhong, W. Luo, A. Züttel, *Cell Reports Phys. Sci.* **2022**, *3*, 100949.

[101] P. Wilde, P. B. O'Mara, J. R. C. Junqueira, T. Tarnev, T. M. Benedetti, C. Andronescu, Y.-T. Chen, R. D. Tilley, W. Schuhmann, J. J. Gooding, *Chem. Sci.* **2021**, DOI 10.1039/d0sc05990k.

[102] W. Luo, W. Xie, R. Mutschler, E. Oveisi, G. L. De Gregorio, R. Buonsanti, A. Züttel, *ACS Catal.* **2018**, *8*, 6571.

[103] F. P. García de Arquer, C. T. Dinh, A. Ozden, J. Wicks, C. McCallum, A. R. Kirmani, D. H. Nam, C. Gabardo, A. Seifitokaldani, X. Wang, Y. C. Li, F. Li, J. Edwards, L. J. Richter, S. J. Thorpe, D. Sinton, E. H. Sargent, *Science (80-.).* **2020**, *367*, 661.

[104] X. Liu, P. Schlexer, J. Xiao, Y. Ji, L. Wang, R. B. Sandberg, M. Tang, K. S. Brown, H. Peng, S. Ringe, C. Hahn, T. F. Jaramillo, J. K. Nørskov, K. Chan, *Nat. Commun. 2019 101* **2019**, *10*, 1.

[105] G. F. Li, M. Divinagracia, M. F. Labata, J. D. Ocon, P. Y. Abel Chuang, *ACS Appl. Mater. Interfaces* **2019**, *11*, 33748.

Laboratory of Materials for Renewable Energy (LMER)
Institute of Chemical Sciences and Engineering (ISIC)
Basic Science Faculty (SB)

34

CHAPTER 2:

Understanding the role of surface oxygen-containing functional groups on carbon-supported cobalt catalysts for oxygen evolution reaction

Thi Ha My Pham[a,b], Youngdon Ko[a,b], Manhui Wei[a,b,c], Kangning Zhao[d], Liping Zhong[a,b,*], Andreas Züttel[a,b]

[a]Laboratory of Materials for Renewable Energy (LMER), Institute of Chemical Sciences and Engineering (ISIC), Basic Science Faculty (SB), École Polytechnique Fedérale de Lausanne (EPFL) Valais/Wallis, Energypolis, Rue de l'Industrie 17, CH-1951 Sion, Switzerland.

[b] Empa Materials Science & Technology, CH-8600 Dübendorf, Switzerland

[c] School of Mechanical Engineering, Beijing Institute of Technology, Beijing 100081, P. R. China

[d]Laboratory of Advanced Separations, Ecole Polytechnique Federale de Lausanne, Sion, Switzerland

*Corresponding author: liping.zhong@epfl.ch

Chapter 2 is reproduced with permission from the Royal Society of Chemistry

Edit: caption numbers of figures, tables, and equations were edited to match the thesis chapter number, and typos have been corrected according to the examiner's comments.

Summary: A high content of acidic surface OFGs on a carbon support enables the fine dispersion of Co-based nanocatalysts, enhancing its OER mass activity, while also inducing additional COOH surface groups that act as O_2 spillover sites.

Laboratory of Materials for Renewable Energy (LMER)
Institute of Chemical Sciences and Engineering (ISIC)
Basic Science Faculty (SB)

35
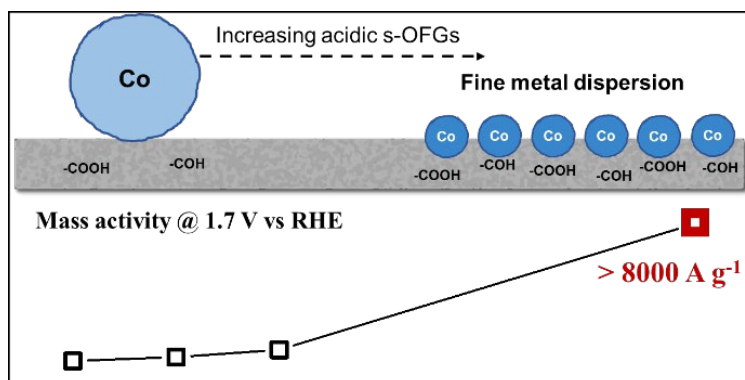
Abstract

Supported Co-based catalysts exhibit promising catalytic activities in oxygen evolution reaction (OER) during alkaline water electrolysis. Surface functionalization of the support modulates the dispersion of the catalysts and their interaction with the support, consequently tuning their catalytic properties. This study thoroughly investigates the role of surface oxygen-containing groups (OFGs) during the synthesis of carbon-supported Co-based catalysts and their contribution to the OER catalytic activity of the material. Following the dispersion of Co onto four different carbon supports, X-ray photoelectron spectroscopy, N_2 adsorption-desorption, and transmission electron microscopy were used to analyze the dispersion degree of cobalt and the concentration of surface OFGs. The results reveal that high concentrations of acidic OFGs over the surface of carbon support lead to the fine dispersion of Co nanoparticles. Raman spectroscopy further demonstrates that the homogeneous dispersion of Co nanoparticles results in the formation of additional surface OFGs and defects in the carbon structure. By adjusting the Co loading onto support, it is verified that the small and finely-dispersed Co nanoparticles, rather than the large agglomerates, contribute significantly to the introduction of additional surface carboxyl groups (COOH) resulting from strong metal-support interaction. The excellent mass activities that exceeded 8 A mg^{-1} can be predominantly attributed to these small and finely-dispersed Co nanoparticles and their corresponding high surface concentration of COOH groups, which were found to participate directly in OER by serving as O_2 spillover sites.

Laboratory of Materials for Renewable Energy (LMER)
Institute of Chemical Sciences and Engineering (ISIC)
Basic Science Faculty (SB)

36

1   Introduction

Of the many transition metals that are non-precious, Co-based materials exhibit the most promising catalytic activity for oxygen evolution reactions (OERs) in alkaline water electrolysis[1–3]. Indeed, Co-based materials from several different structural families exhibit excellent catalytic activities for OERs, including spinels[4], perovskites[5,6], or layer-structured type materials[7,8]. Despite exhibiting a high geometric current density in OERs, the mass activity of these bulk Co-based catalysts is relatively low due to the limited surface area that is exposed to the electrolyte. Consequently, the catalysts are typically dispersed onto an inert support, a protocol that allows for the prevention of agglomerations, maximizes the surface area exposed to the electrolyte and enhances their stability[9]. Carbon-based materials are commonly used as supports for OER-active catalysts due to their inertness and electrical conductivity[10,11]. Catalyst surface areas can be further enhanced using a variety of different methods, including the synthesis of single-atom catalysts or by anchoring the catalysts to clusters of nanoparticles[12,13]. For example, one approach aimed at maximizing the atomic efficiency of a transition metal catalyst and achieving high current densities at low metal loading is the synthesis of single-atom cobalt-based catalysts, such as Co-N-C, which increases their turnover frequency (TOF)[14]. Co_3O_4 nanocrystals grown on mildly reduced graphene oxide exhibited higher geometric current densities for OER and a lower Tafel slope compared to bulk Co_3O_4 subjected to the same degree of surface loading. This suggests that this approach not only increases the active surface area of the catalyst but enhances metal-support interactions (MSIs), which synergistically improve the OER catalytic activity[15]. In general, the catalytic activity of a metal-supported catalyst is strongly dependent on the dispersion, particle size, and loading of the metal[16]. These parameters can be tuned by selecting suitable carbon supports or employing different treatments during the synthesis process[17].

Oxygen-containing functional groups (OFGs) have been widely studied due to their strong influence on the reactivity of carbon surfaces[12,18–22]. Introducing surface OFGs (s-OFGs) or shifting their distribution towards specific functional groups allows the activity of specific reactions to be tuned towards certain desired products. OFGs have been used to regulate reactivity in applications such as heavy metal adsorption as well as several electrochemical applications. Different OFGs have exhibited different activities with regards to the adsorption of different heavy metals[23]; for example, acidic OFGs enhance the adsorption of Pb^{2+} onto carbon surfaces[24,25], while increasing the amount of carboxyl and phenol groups has a positive effect on capacitance in supercapacitor applications[26,27]. Hydroxyl groups help anchor CoP particles to biomass-carbonized carbon microtubes in applications that exploit the hydrogen evolution reaction (HER), facilitating electron transfer from the catalyst to the carbon support and consequently enhancing HER activity[28]. An excess number of carboxylic groups has been shown to intrinsically boost CO_2RR activity due to their synergistic effect with other surficial functional groups, while also enhancing the dispersion of Ag nanoparticles on CNT, increasing surface area and geometric current density[29,30]. Oxygen reduction reaction (ORR) to hydrogen peroxide is aided by the presence of quinone functional groups on the carbon surface[31]. Despite the extensive amount of research conducted on ORRs, few studies have examined the impact of OFGs on OERs[32,33]. Previous studies have shown that s-OFGs directly influence the intrinsic OER activity of defective graphene[33] and may also

Laboratory of Materials for Renewable Energy (LMER)   37
Institute of Chemical Sciences and Engineering (ISIC)
Basic Science Faculty (SB)

indirectly by influencing the dispersion of the active metal phase[32]. Nonetheless, a more comprehensive understanding about the influence of s-OFGs on factors such as metal dispersion, metal-support interactions, and on OER activity, is strongly required.

In this study, we aim not only to understand the influence of surface oxygen-containing functional groups (s-OFGs) on carbon-supported cobalt with regards to OER reactivity but also intend to discuss their role in the modulation of Co nanoparticle size and metal-support interactions during synthesis. Four different carbon materials were used as inert supports for a Co-based catalyst, with each material possessing an inherently different surface concentration of s-OFGs. Using X-ray photoelectron spectroscopy (XPS), N_2 adsorption-desorption and transmission electron microscopy (TEM), we reveal that a carbon support with a high content of acidic groups (e.g., COH and COOH) leads to the formation of highly dispersed nano- and sub-nano-sized Co-based nanoparticles. The results of Raman spectroscopic analysis further demonstrate that the introduction of nano-sized Co results in the formation of more defects on the carbon surface while also generating additional s-OFGs. Catalytic performance tests show that this increase in s-OFGs enhances OER activity. Accordingly, we propose a mechanism that explains the role of s-OFGs in the synthesis of carbon-supported cobalt catalysts and discuss their potential OER applications.

2 Materials and methods

2.1 Synthesis of carbon-supported Co-based catalyst

Four commercial carbon materials were used to synthesize the cobalt-based catalysts used in this study: graphene nanoplatelets (GNPs; Sigma-Aldrich), carbon nanotubes (CNT; Jiangsu Cnano Technology), carbon black (CB; Vulcan XC-72R, Fuelcellstore) and acetylene carbon black (ACB; 100% compressed, abcr). Cobalt (II) oxide (CoO, Sigma-Aldrich) and cobalt (II,III) oxide (Co_3O_4, Sigma-Aldrich) were used as control samples. The carbon-supported cobalt catalysts were synthesized using the incipient wetness method. Cobalt nitrate ($Co(NO)_3.6H_2O$) from Alfa Aesar was used as the cobalt precursor. To synthesize each catalyst, cobalt nitrate salt was first dissolved in a mixture of deionized water and ethanol (1:1, vol%) to form a Co solution with a concentration of 83 mg mL^{-1}. The prepared solution was then applied to a 2 g sample of each carbon material by dry impregnation multiple times until the target loading percentage was obtained. Following the impregnation step, the samples were dried in air at 80°C for 12 h. After drying, each sample was calcined at 400°C for 3h in N_2.

Throughout the rest of the manuscript, the Co-based catalysts will be referred to using the following notation: [support-mass loading of Co]. For example, a GNP support with a Co mass loading of 0.5 wt.% will be referred to as GNP-0.5.

2.2 Preparation of the electrolyte

A 1M KOH solution was prepared by diluting potassium hydroxide (KOH; 50%, Carl Roth) in 1 L of milli-Q water. The Fe impurities were removed from the electrolyte through the addition of 1 g of nickel(II) hydroxide

Laboratory of Materials for Renewable Energy (LMER)
Institute of Chemical Sciences and Engineering (ISIC)
Basic Science Faculty (SB)

38

(Ni(OH)$_2$; Fluka) per litre of KOH solution; the resulting solution was stirred overnight. The solution was subsequently filtered using filter paper (Cytiva, pore size 50 µm) to obtain a Fe-free 1M KOH solution.

2.3   Preparation of the electrode

A 3-mm diameter disk of glassy carbon electrode (ALS) was polished using silicon carbide grinding paper with two different grit numbers. The disks were initially polished using P500 paper, followed by P100 (VSM). The electrode was further polished using a 0.05 µm polishing alumina suspension (BASi) on a polishing cloth (MicroCloth, Buehler) until the reflective surface resembled a mirror finish. The electrode was rinsed with milli-Q water and dried using a hot-air gun. The reference electrode used in this study was Ag/AgCl, while the counter electrode was a Pt spring.

The catalyst ink for drop-casting was prepared using 10 mg of as-synthesized catalyst, 1 mL of IPA, and 100 µL of Nafion. The ink was sonicated for 30 min. 1 µL of the as-prepared ink was drop-casted onto the glassy carbon working electrode. The surface dose of the catalyst was 0.143 mg cm^{-2}.

2.4   Electrochemical characterization

A potentiostat (Metrohm Autolab PGSTAT204) was used for electrochemical measurements. Cyclic voltammetry (CV) was performed using a conventional three-electrode chemical setup in the Fe-free 1M KOH solution (pH 14). The potential was swept between 1.0 and 1.7 and back to obtain V vs RHE (reversible hydrogen electrode) data at a scan rate of 10 mV s^{-1}. A rotating disk electrode system (RDE; RRDE-3A, ALS) was used to ensure that no bubbles were present during the CV scan. The rotating speed of the RDE was fixed at 1600 revolutions per minute (rpm). For electrochemical measurements extending to high overpotentials between 1.5 to 2.2 V vs RHE, linear sweep voltammetry (LSV) was performed at the same scan rate and RDE rotation speed.

To estimate the electrochemical surface area (ECSA), CVs were performed in a non-Faradaic region over a 100-mV interval at seven different scan rates. The scan rates used for the GNP support were 50, 75, 100, 150, 200, 300, and 400 mV s^{-1}, while the scan rates used for the CNT, CB, and AB supports were 100, 200, 300, 400, 600, 800, and 1000 mV s^{-1} due to the noise observed at lower scan rates. The double-layer capacitance (C_{dl}) can be calculated from the measured charging current (i_c) and the scan rate (θ) using the following equation:

$$i_c = C_{dl} \times \theta$$

The TOF was then calculated as follows:

$$TOF = i / (z \times F \times n_{catalyst})$$

With i the measured current at a fixed overpotential, z the number of electrons involved in the reaction, F the Faraday constant and n the number of moles of Co in the catalyst.

The electrochemical impedance spectroscopy (EIS) was conducted by applying 1.5 V vs RHE ± 10 mV to the working electrode. The frequency for the EIS ranges from 10^5 to 0.1 Hz.

Laboratory of Materials for Renewable Energy (LMER)
Institute of Chemical Sciences and Engineering (ISIC)
Basic Science Faculty (SB)

39

2.5   Materials characterization

Scanning electron microscopy (SEM) images and their corresponding elemental maps obtained by energy dispersive X-ray spectroscopy (EDX) were acquired using a Thermo Fisher Teneo FE-SEM. High-angle annular dark-field (HAADF) images and the corresponding EDX elemental maps were obtained using a Thermo Fisher Tecnai Osiris 200kV transmission electron microscope (TEM). X-ray diffraction (XRD) patterns were obtained using a Bruker D8 Advance system using Cu Kα (λ = 1.54 Å) radiation. Inductively coupled plasma optical emission spectrometry (ICP-OES) was performed using an Agilent 5110 instrument. Raman spectroscopy was conducted between 1000–3800 cm^{-1} using a Raman microscope (Renishaw, inVia confocal Raman microscope) with a green light source with a wavelength of 532 nm. The surface area of the supports was determined using the N_2 adsorption-desorption method on a BELSORP MAX II analyzer (Microtract MRB) following the Brunauer-Emmett-Teller (BET) technique. C 1s and O 1s X-ray photoelectron spectroscopy (XPS) spectra were obtained using a Kratos Axis Supra XPS system in an ultra-high-vacuum (UHV) environment, utilizing the monochromatic Kα line of an aluminium X-ray source (1486.6 eV), with the analyser set to a pass energy of 20 eV. The deconvolution of the C 1s and O 1s peaks was performed using the CasaXPS software.

3   Results & Discussion

3.1   Cobalt dispersion modulated by surface oxygen-containing functional groups

The XRD patterns of the four supports (Figure 2.1a) revealed that the GNP support had a graphite structure with a sharper primary peak, suggesting that it possessed a higher degree of crystallinity compared to the other three samples. The Raman spectra of the supports acquired in the range of wavelengths containing the D and G peaks are presented in Figure 2.1b. In general, the ratio of I_d to I_g provides information about the crystallite size as well as the nature of the defects in a material[34,35]. The decreasing I_d to I_g ratios of the supports (ACB > CB > CNT > GNP) suggested that the supports exhibited the following degree of graphitization: GNP > CNT > CB > ACB, indicating that the GNP support exhibits the greatest electrical conductivity[36]. Figures S2.1 and 2.1c present the adsorption-desorption isotherm and the specific surface area of the supports determined with the BET method, respectively. The CNT support exhibited the highest BET surface area, followed by GNP, ACB, and CB (Table S2.1). The two most graphitized carbon supports (GNP and CNT) exhibited specific surface areas that were almost triple those observed in the two amorphous carbons.

The ECSA, typically dependent of the surface area[37], was determined by investigating the double-layer capacitance of the four supports under identical surface loading conditions (Figure S2.2). Interestingly, the ECSA of the supports exhibited a different trend compared to their specific surface area (Figure 2.1c): although the carbon nanotubes (CNT) and the graphene nanoplatelets (GNP) exhibited the greatest specific surface areas, GNP displayed a C_{dl} that was 20 times higher than the others (Figure S2.3). One of the factors contributing to the disparity between BET surface area and ECSA was proved to be the distinct electrical conductivity exhibited by various materials[38]. Since carbon-based materials are recognized for their high electrical

Laboratory of Materials for Renewable Energy (LMER)   40
Institute of Chemical Sciences and Engineering (ISIC)
Basic Science Faculty (SB)

conductivity[39,40], there must be factors beyond electrical conductivity that contribute to this discrepancy. Previous studies have shown that the surface chemistry of carbon materials, particularly the presence of OFGs, plays a crucial role in their double-layer capacitance[26]. To this end, the C 1s and O 1s XPS spectra were examined to compare the differences between the carbon and oxygen species on the surfaces of these supports.
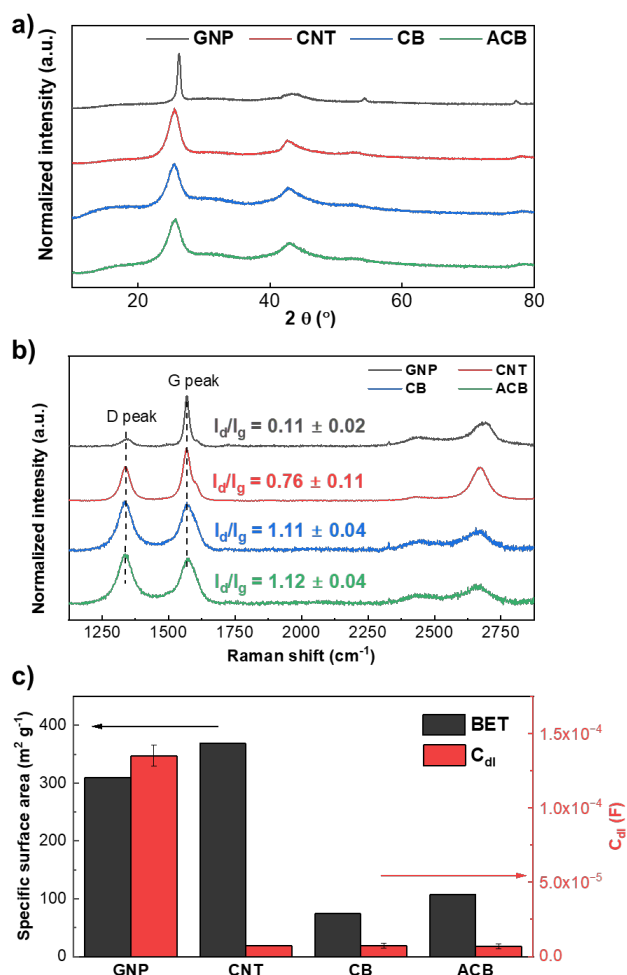
Figure 2.1. The structural characterizations of the four carbon supports investigated. a) XRD patterns acquired at 2θ between 10–80°. b) Raman spectroscopy including the peaks of the D band (1300–1500 cm^{-1}) and the G band (1500–1700 cm^{-1}), which are associated with carbon. c) Specific surface area of the four supports as measured by N$_2$-adsorption measurements as well as their double-layer capacitance as determined by electrochemical methods.

The XPS O 1s and C 1s spectra of the four supports and their corresponding peak deconvolutions are presented in Figure 2.2 and S2.4, respectively. The deconvoluted peaks revealed different s-OFGs on the carbon supports, including acidic surface species such as phenol (COH) and carboxyl (COOH) groups as well as basic species such as quinone and carbonyl (C=O) groups[22,41]. Figure 2.2 shows that four oxygen surface species were identified in all four supports, fitted to the following peak positions: C=O (532.2–532.7 eV), COH (533.4–533.9 eV), COOH (534.2–535.0 eV), and gas-phase water/surface carbon oxygenates (536.1–537 eV)[42]. The C 1s spectra and their deconvoluted peaks are presented in Figure S2.4, indicating the presence of the following six surface carbon species: C=C (284.81–284.84 eV), C-C (285.03–285.25 eV), COH (285.83–286.41 eV), C=O (288 eV), COOH (289.62–390 eV), and surface carbon oxygenates (291.55–291.69 eV)[42,43]. There was a significant difference between the surface oxygen concentrations observed in each support. GNP and CB

Laboratory of Materials for Renewable Energy (LMER)
Institute of Chemical Sciences and Engineering (ISIC)
Basic Science Faculty (SB)

41

possessed the highest surface oxygen concentrations exceeding 3% (Table S2.2), while ACB and CNT only exhibited surface oxygen concentrations of approximately 1% and 0.6%, respectively.

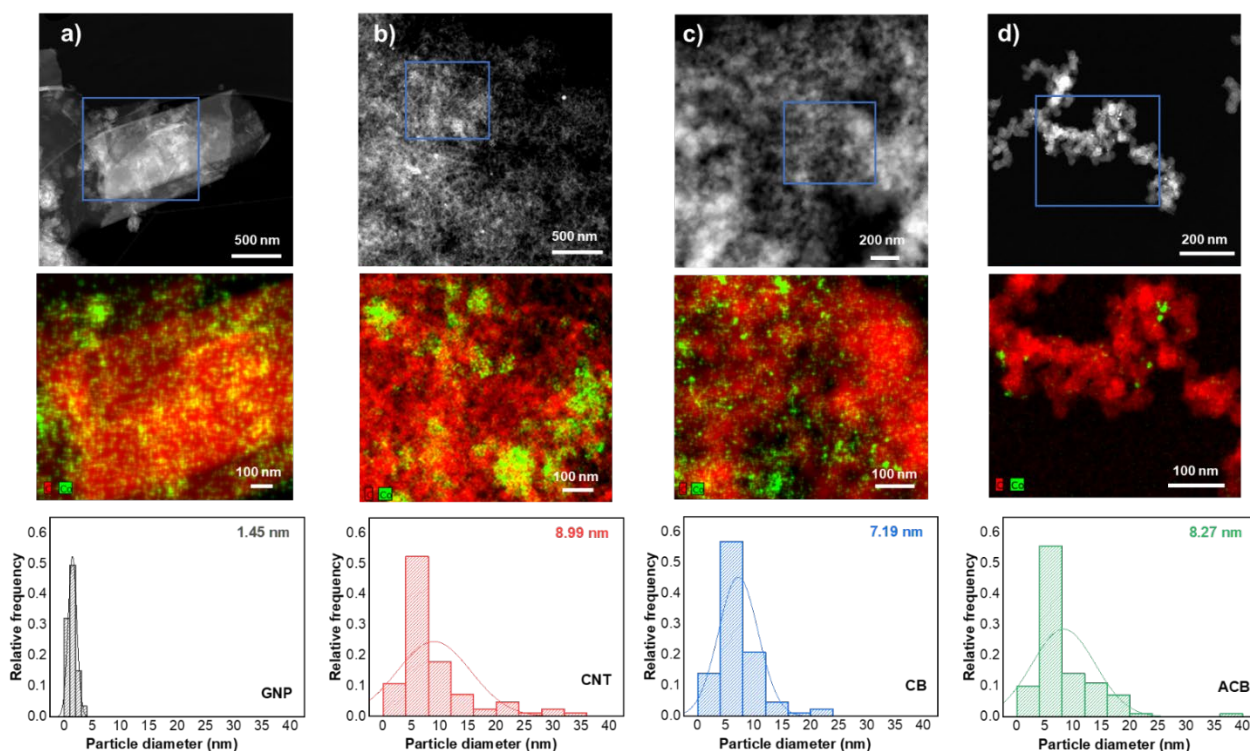Furthermore, we observed a significant variation in the distribution of s-OFGs. To assess the composition of the various s-OFGs across the four supports, the surface concentration of each s-OFG was determined by dividing the corrected area obtained from the O 1s spectra by the corresponding carbon area obtained from the C1s spectra. The distribution of s-OFG surface concentrations, obtained via the peak deconvolution of all four supports using defined deconvolution parameters, is summarized in Table S2.2. We found that there was a slight disparity in the distribution of s-OFGs between the two supports that exhibited the highest surface oxygen concentrations (GNP and CB): the GNP support exhibited a higher concentration of acidic groups, while CB exhibited a greater abundance of basic groups (Table S2.2).
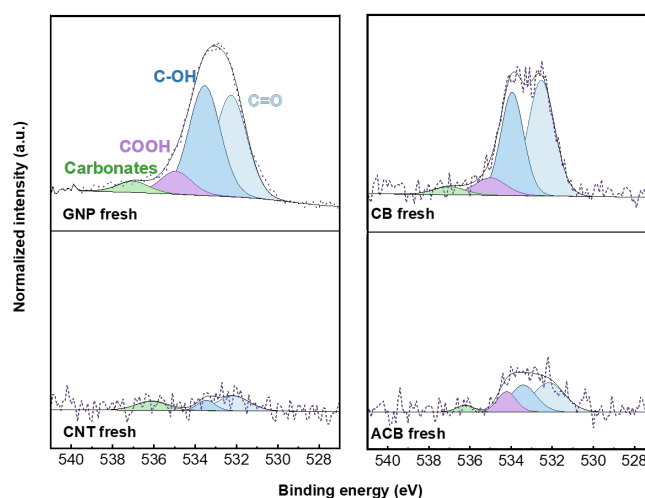
Figure 2.2. The XPS O 1s spectra of the four supports and the fitted peaks for the following s-OFGs: O=C, O-C, O-C=O (in COOH), and surface carbon oxygenates. The intensity of the O 1s spectra is normalized to the carbon intensity of the C 1s spectra to illustrate the oxygen concentration relative to the total amount of surface carbon.

After wet impregnation, drying, and calcination, the Co content of the Co-catalyst supported on carbon support (GNP-0.5, CNT-0.5, CB-0.5, ACB-0.5) was assessed with ICP-OES (Table S2.3). GNP-0.5 exhibited a Co content of 0.51 ± 0.005 wt.%; this uncertainty is approximately 1% of the average value, suggesting that the Co was homogeneously distributed across the calcined powder. The CNT-0.5, CB-0.5, and ACB-0.5 samples also had an average Co content close to 0.5 wt.%, but the variation between the two sets of measurements conducted in all three samples revealed the heterogenous distribution of Co within these samples.

Laboratory of Materials for Renewable Energy (LMER)
Institute of Chemical Sciences and Engineering (ISIC)
Basic Science Faculty (SB)

42

Figure 2.3. The distribution of the Co-catalyst on the carbon support. From left to right: HAADF-STEM images, elemental maps of carbon and cobalt (blue rectangle), and the particle size distribution of the Co-catalyst supported on a) GNP-0.5, b) CNT-0.5, c) CB-0.5, and d) ACB-0.5

The distribution of the Co-catalyst on the four carbon supports was further visualized using scanning transmission electron microscopy (STEM; Figure 2.3). The HAADF-STEM images of the Co-catalyst supported on carbon highlight the mass differences between cobalt and carbon, with the bright area corresponding to cobalt. The elemental maps of carbon and cobalt showed that the cobalt was most homogeneous dispersed on the GNP support (Figure 2.3a), while the agglomeration of cobalt can be clearly seen in the other three supports (Figure 2.3b–d). HAADF-STEM images and elemental maps of other areas are presented in Figures S2.5–8; the particle size distribution of cobalt on the carbon support was also measured in those areas. While the Co-catalyst dispersed on GNP has an average particle size of 1.45 nm, the other carbon supports exhibited an average Co particle size between 7–9 nm, with the largest particle sizes approaching 40 nm. Since the same synthesis protocol was used for all supports, these differences in Co particle size and dispersion must be attributed to the differences in the specific surface area and/or the surface-active sites for metal nucleation and growth in each carbon support.

We observed two trends concerning the average size of Co nanoparticles supported on carbon materials. First, the CNT and GNP supports exhibited similar BET surface areas (368 and 310 m^2 g^{-1}, respectively). However, the GNP support had a more homogenous Co dispersion with smaller nanoparticle sizes, indicating a reduced degree of agglomeration. Based on the discussion above, the more homogenous Co dispersion observed can be attributed to the higher concentration of surface oxygen on the GNP support. Second, although CB and GNP had similar surface oxygen concentrations (3.51% and 3.32%, respectively), CB had a much lower surface area, and thus less well-dispersed cobalt. We noticed that there is a tradeoff between the surface

Laboratory of Materials for Renewable Energy (LMER)
Institute of Chemical Sciences and Engineering (ISIC)
Basic Science Faculty (SB)

43

concentration of acidic groups and the specific surface area. For instance, CB with a low specific area but a high concentration of s-OFGs shows a similar average Co-particle size compared to CNT, which possesses a high surface area but a much lower s-OFGs concentration. Hence, the dispersion of Co nanoparticles depends strongly on both the specific surface area and the surface oxygen concentration of the porous carbon support. In other words, maximizing both factors is necessary to provide sufficient nucleation sites for the Co nanoparticles.

To investigate the extent of the effects of specific surface area, we calculated the total surface content of each s-OFG by multiplying their surface concentrations with their corresponding specific surface area on each of the carbon supports. Figure 2.4 presents the total surface content of three s-OFGs in conjunction with the average size of Co nanoparticles on each of the four supports. We found that fresh supports with lower total surface concentrations of phenol and carboxyl groups led to the formation of larger particles. However, the total surface concentration of the carbonyl groups did not exhibit the same trends. It is important to note that the presence of both COH and COOH groups results in a slightly acidic surface, which lowers the pH of the point of zero charge and imparts a negative charge to the carbon surface[24]. This improves the adsorption of the metal cation to the carbon surface, resulting in a more even dispersion of the supported metal particles[25,44].
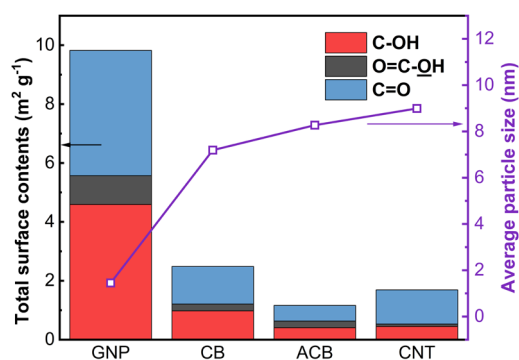
Figure 2.4. The total surface content of COH, COOH, and C=O groups across each of the four supports, as well as the average size of the supported Co nanoparticles in each support.

These results further emphasize the fact that GNP is a promising carbon support that allows for an ideal degree of Co dispersion, which can be attributed to its high surface concentration of acidic groups and its relatively large specific area. Based on these observations, we propose that the total surface content of acidic groups can be used as a valuable indicator for optimizing the dispersion of metals on carbon-based supports. This parameter has the potential to be utilized in other applications that require highly dispersed nanoparticles, allowing users to choose the most suitable supports for their applications.

Figure 2.5a presents the geometric current density as a function of potential for a catalyst with a Co mass loading of 0.5 wt.% (denoted as Co0.5) at a surface loading of 0.14 mg cm^{-2}. The geometric current density at a fixed overpotential of 450 mV (Figure 2.5b) increases across the four supports as follows: ACB-0.5 < CB-0.5 < CNT-0.5 < GNP-0.5. Interestingly, the mass activity of GNP-0.5 exceeds 8 A mg^{-1}, which is much higher than the values obtained for the CNT-0.5, CB-0.5, and ACB-0.5 catalysts (1.0, 0.6, and 0.3 A mg^{-1}, respectively; Figure 2.5c). The mass activity obtained on our GNP-0.5 was among the highest values that were previously

Laboratory of Materials for Renewable Energy (LMER)
Institute of Chemical Sciences and Engineering (ISIC)
Basic Science Faculty (SB)

44

reported for Co-based catalysts[45–54] (Figure 2.5d). Similarly, the TOF obtained for the GNP-0.5 catalyst was 12, 15 and 19 times higher than that obtained for CNT-0.5, CB-0.5, and ACB-0.5 respectively. The fitted Nyquist plot reveals that the charge-transfer resistance of GNP-0.5 is notably lower compared to the other three supported catalysts (Figure S2.9). Besides, the Tafel slope exhibits a remarkable similarity among GNP-0.5, CNT-0.5, and CB-0.5, with a slightly elevated value for ACB-0.5 (Figure S2.10). However, this variation in Tafel slope is not as significant as the differences observed in mass activity and TOF. In brief, the high geometric current density, ECSA, and TOF values, obtained for GNP reflect an abundance of active sites to the electrolyte, and are most likely attributable to the homogeneous dispersion of the Co-catalyst on GNP. This similarity in Tafel slope further confirms that the enhanced OER activity of GNP arises from the fine dispersion of Co catalysts, rather than from a difference in intrinsic activity.
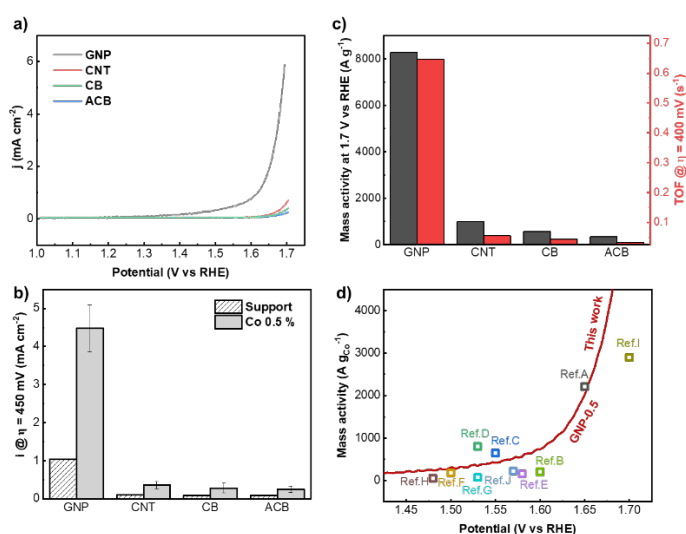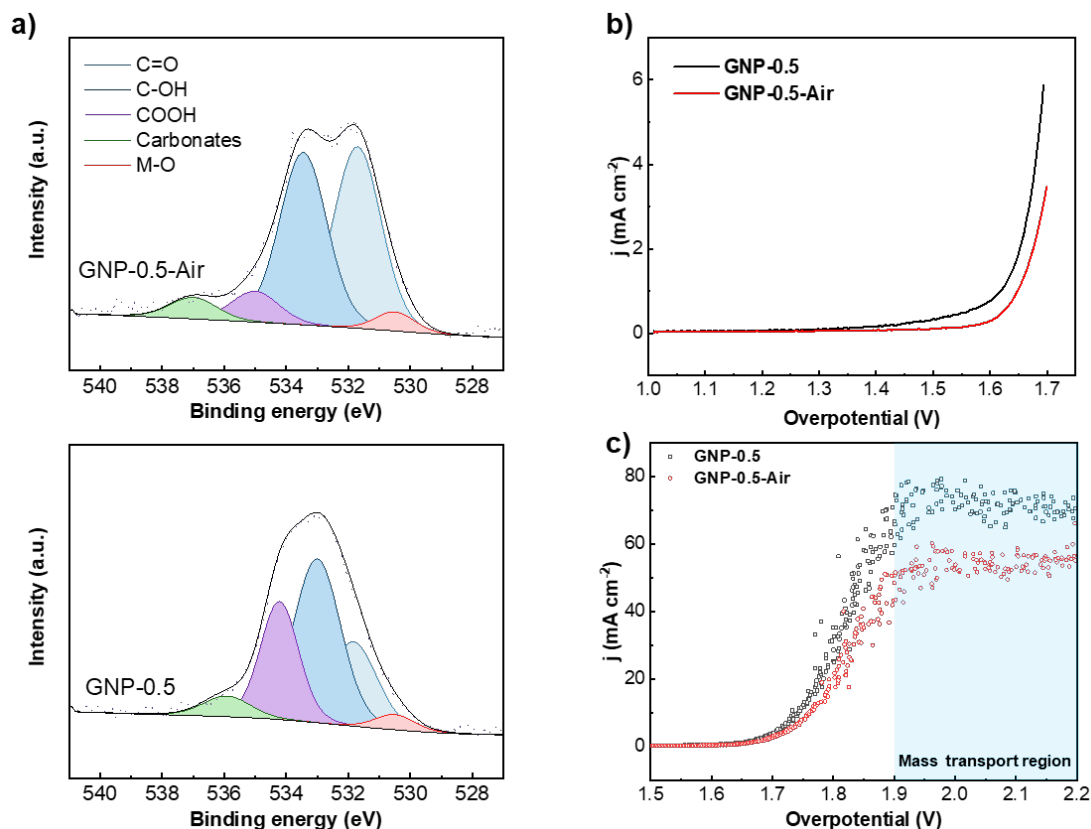

Figure 2.5. The OER activity of the Co-catalyst supported on each of the four carbon materials. a) The geometric current density of GNP-Co, CNT-Co, CB-Co, and ACB-Co in Fe-free 1M KOH solution, scanned from 1.0–1.7 V vs RHE at a scan rate of 10 mV s^{-1}. CV curves were iR-corrected (85% iR drop compensation) and averaged across the forward and backward scans. b) A summary of the geometric current density at an overpotential of 450 mV, measured on a fresh carbon support and Co0.5 supported on the four carbon materials. c) Mass activity and TOF of the carbon-supported Co0.5 catalyst. d) Mass activity for OER of the GNP-0.5 catalyst compared with those of other reported Co-based catalyst (summarized in Table S2.4).

3.2   The role of surface oxygen-containing functional groups in enhancing OER activity

Although the dispersion of the Co catalyst on the GNP support was attributed to the adsorption of metal cations onto acidic s-OFGs, the concentration of s-OFGs did not decrease following the wet impregnation process. Instead, the total oxygen surface concentration increased from 3.32% to 4.37% in conjunction with a change in the distribution of s-OFGs. This suggests that the Co doping process introduced additional surface oxygen groups. We also observed an increase in the I_d/I_g ratio following the doping process (Table S2.5). The I_d/I_g ratio, as determined through Raman spectra, exhibited the highest increase following Co doping (a 29% increase in the GNP-0.5 sample compared to fresh GNP), indicating that the incorporation of Co introduced more defects to the carbon support (Figure S2.11).

Laboratory of Materials for Renewable Energy (LMER)
Institute of Chemical Sciences and Engineering (ISIC)
Basic Science Faculty (SB)

45

To investigate the contribution of s-OFGs to oxygen generation, we conducted experiments using the same GNP support with varying oxygen surface concentrations and s-OFGs distributions. After impregnation and drying, the GNP-0.5 sample was subjected to two different thermal treatments: calcination in N_2 at 400°C (GNP-0.5) and calcination in air at 300°C (GNP-0.5-Air). The XPS peak deconvolutions for O 1s (Figure 2.6a) and C 1s (Figure S2.12) were performed with similar deconvolution parameters as with the four fresh carbon supports, but a peak at 530.5 eV in the O 1s spectra was added for the metal-oxygen bond. The calculated s-OFGs surface concentrations are summarized in Table S2.6. Although the oxygen content of GNP-0.5-Air was found to be slightly greater than that of the fresh support, both samples exhibited very similar s-OFG distributions. In contrast, GNP-0.5 had a much higher oxygen content while also possessing a significantly different s-OFG distribution. Specifically, the concentration of C=O groups decreased slightly, while there was a slight increase in the concentration of COH groups. Most notably, the surface concentration of carboxylic groups (COOH) increased fivefold, suggesting that the surface chemistry of the GNP support had been significantly altered following the impregnation of the Co catalyst and the subsequent calcination process in N_2. Although the s-OFGs of the fresh support serve as adsorption sites for metal cations, the increase in s-OFGs following Co impregnation could be attributed to MSI[55]. These interactions, which typically involve encapsulation or interphase interactions[56], introduce additional surface functional groups. In addition, the strong interaction between the Co catalyst and the carbon support may distort the graphene network, resulting in the formation of sp^2 defects and consequently creating more edges for the generation of carboxylic groups[12].

The iR-corrected and averaged CV curves of GNP-Co and GNP-0.5-Air were plotted in Figure 2.6b. The geometric current densities at an overpotential of 450 mV were found to be higher for the N_2-calcined samples compared to the air-calcined samples (Figure S2.13). Indeed, DFT calculations have shown that the combination of defects and COOH groups elevates the adsorption energies of ΔG_{Oads} - ΔG_{OHads} to the top of the volcano descriptor plot, reducing the overpotential of the OER[33]. The presence of surface COOH groups facilitates the deprotonation reaction at the carbon surface[57], which has been shown to contribute significantly to the additional overpotential required for OERs[58]. These s-OFGs can also participate in the reaction by serving as sites for the spillover of oxygen molecules generated from OERs, providing additional active sites on the surface of the catalyst[59] and improving OER kinetics[60]. The Raman spectra acquired over the wavelength range containing Co_3O_4 for GNP-0.5, GNP-0.5-Air and commercial Co_3O_4 were plotted in Figure S2.14a. It is widely accepted that the presence of oxygen vacancies contributes to a blue-shift in the Raman peak[61,62]. In our study, since the peak corresponding to Co_3O_4 of the two samples is located at the same position as that of the commercial reference, it can be deduced that there were no oxygen defects induced to the supported Co-catalyst during the calcination. The similarity in Tafel slope between GNP-0.5 and GNP-0.5-Air, as illustrated in Figure S2.14b, further supports that the primary distinction arising from the two calcination procedures is mainly the surface content of COOH groups rather than the catalysts themselves.

Laboratory of Materials for Renewable Energy (LMER)
Institute of Chemical Sciences and Engineering (ISIC)
Basic Science Faculty (SB)

46

Figure 2.6. A comparison of the impregnated, dried Co-catalyst supported on GNP calcined in air and in nitrogen. a) XPS O 1s spectra of GNP-0.5-air and GNP-0.5 and their corresponding deconvoluted peaks. b) CV of GNP-0.5-Air and GNP-0.5 in Fe-free 1M KOH solution, scanned from 1.0–1.7 V vs RHE at a scan rate of 10 mV s^{-1}. CV curves were iR-corrected (85% iR drop compensation) and averaged across the forward and backward scans. c) LSV of GNP-0.5-Air and GNP-0.5 in Fe-free 1M KOH solution, scanned from 1.5–2.2 V vs RHE at a scan rate of 10 mV s^{-1}. The potentials were iR-corrected (85% iR drop compensation).

To investigate the extent to which the COOH groups facilitate O_2 spillover, we collected LSV measurements in the high overpotential range between 1.5–2.2 V vs RHE. Across this range, the measured current density is no longer predominantly governed by the kinetics of the OER and is instead influenced by the mass transport of hydroxide ions and generated oxygen. As we increased the potential beyond 1.9 V vs RHE, the current density plateaued and ceased to increase (Figure 2.6c). Notably, the limit of the current density was higher for GNP-0.5 compared to GNP-0.5-Air despite both samples being subjected to the same degree of catalyst surface loading (Figure S2.15). This suggests that the mass transport of released O_2 from the active Co sites is more efficient in GNP-0.5, which — as previously shown — possesses a higher abundance of COOH groups. Thus, our measurements of the limiting current densities in the mass-transport region suggest that O_2 spillover is enhanced by the presence of COOH groups.

3.3   Additional s-OFGs modulated by metal-support interactions

A range of Co loads on GNP was investigated to examine the balance between the abundance of metal cations and the amount of available acidic s-OFGs. The following Co mass concentrations (mass of Co/ total mass) were used for sample preparation and loading: 0.05, 0.1, 0.5, 4.8, 9.1, 17, and 29; the loaded samples are

Laboratory of Materials for Renewable Energy (LMER)
Institute of Chemical Sciences and Engineering (ISIC)
Basic Science Faculty (SB)

47

henceforth denoted as GNP-0.05, GNP-0.1, GNP-0.5, GNP-4.8, GNP-9.1, GNP-17, and GNP-29, respectively. At the two lowest Co mass loading, there was almost no enhancement in OER activity (Figure S2.16). This can be primarily attributed to the insufficient Co content for achieving a uniform impregnation through wet-impregnation synthesis. As a result, a concentration of 0.5 wt.% was set to be the minimum threshold for our study. The weight percentages of the Co-catalyst supported on GNP were measured using ICP and confirmed that the prepared catalysts (produced via the wet-impregnation method) had Co loadings similar to the theoretical values calculated for synthesis (Table S2.7).

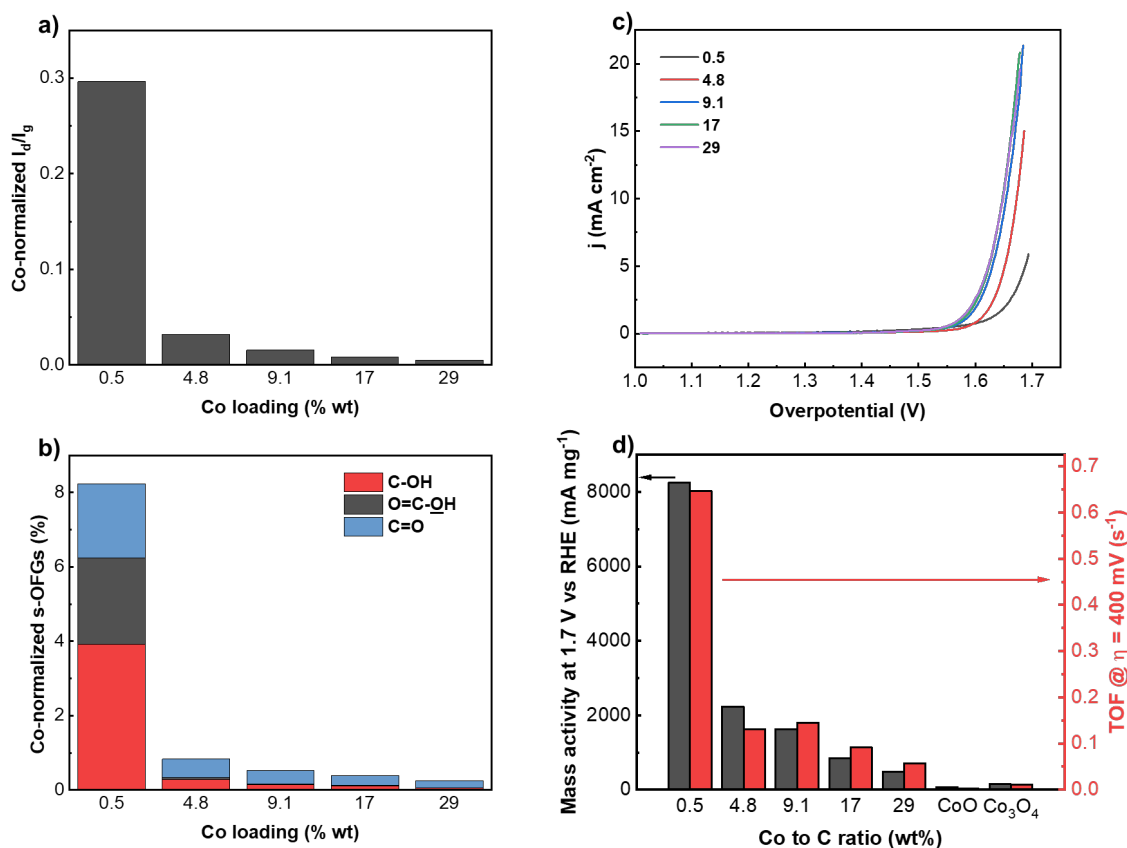As shown previously in Figure 2.2, GNP-0.5 possessed well-dispersed Co-catalyst particles with sizes ranging from the sub-nanometer scale to a maximum of 5 nm. Figures 2.7 and S2.17–20 present the HAADF-STEM images of the four GNP samples with Co loadings higher than 0.5 wt.%. At a loading of 4.8 wt.%, the Co particles remained relatively well-distributed on the carbon support; however, some regions with higher Co concentrations exhibited metal agglomeration, leading to the formation of larger metal particles. While Co nanoparticles were still observed both on the surface and in between the nanoplatelets, the majority of Co formed a separate bulk phase. This phase separation became more evident at higher Co loadings, as shown by the elemental maps (Figure 2.7c,d). These results suggest that when there is an excess of Co^{2+} cations compared to acidic s-OFGs, only a small portion of the cations can be adsorbed onto the surface via the action of s-OFGs. Previous studies have reported that, upon calcination at low Co concentrations, inner-sphere complexes can form on the surface of the GNP support, while an excess of Co at high concentrations results in the formation of outer-sphere complexes[63]. Upon calcination, inner-sphere complexes tend to transform into well-anchored CoO on the support, while outer-sphere complexes form more loosely attached Co_3O_4 crystallites[64]. This would explain the mixed oxides observed in the XRD patterns of Co-catalysts supported on GNP samples at loadings higher than 4.8 wt.% (Figure S2.21). Again, the absence of a blue-shift in the Raman spectra when comparing the samples to the commercial reference indicates that the calcination process did not induce any oxygen defects (Figure S2.22).

Laboratory of Materials for Renewable Energy (LMER)
Institute of Chemical Sciences and Engineering (ISIC)
Basic Science Faculty (SB)

48
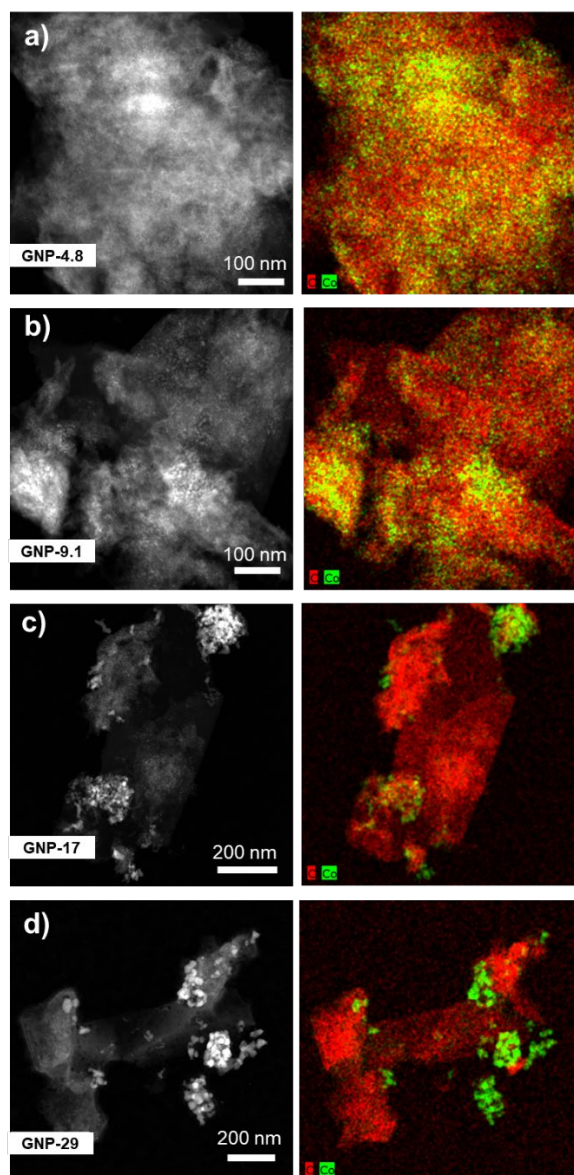
Figure 2.7. Co distribution of Co-catalysts supported on GNP at different Co loadings. a–d) HAADF-STEM images and elemental maps of GNP with Co loadings of 0.5, 4.8, 9.1, 17, and 29 wt.%.

The increased I_d/I_g ratio of GNP-0.5 compared to fresh GNP (Table S2.5) can be attributed to the increased number of defects in the carbon support caused by Co-doping, suggesting that the well-dispersed Co nanoparticles directly interact with the carbon support. When the Co loading was increased, the I_d/I_g ratio remained relatively stable (Table S2.8), suggesting that excessive Co doping does not result in additional defects in the carbon support. Furthermore, agglomerations only formed when Co loading exceeded 0.5 wt.% (Figure 2.7). We can thus conclude that the finely dispersed nanoparticles can directly interact with the carbon supports, leading to the generation of additional defects. Furthermore, the formation of large agglomerates does not contribute to this interaction. These observations are consistent with the results of previous studies that demonstrated that the fine dispersion of nanoparticles exhibited strong MSIs[65,66].

Laboratory of Materials for Renewable Energy (LMER)
Institute of Chemical Sciences and Engineering (ISIC)
Basic Science Faculty (SB)

49

Figure 2.8. The quantification of defect levels, surface functional groups, and OER activity normalized to Co-loading. a) I_d/I_g ratio normalized to Co-loading. b) Surface concentration of COH, COOH, and C=O group normalized to Co-loading. c) CV of GNP-supported Co at different Co loadings in Fe-free 1M KOH solution, scanned from 1.0–1.7 V vs RHE at a scan rate of 10 mV s^{-1}. CV curves were iR-corrected (85% iR drop compensation) and averaged across the forward and backward scans. d) Summary of the mass activity at 1.7 V vs RHE and the TOF at an overpotential of 450 mV acquired on GNP-supported Co with different Co loadings and on commercial bulk CoO and Co$_3$O$_4$.

The peak deconvolution of XPS O 1s and C1s spectra (Figure S2.23) was used to calculate the surface concentration of s-OFGs at different Co loadings. As the Co loading increased, the surface concentration of oxygen (i.e., the concentration of COH, COOH, and C=O groups) also increased (Figure S2.24). The surface oxygen concentrations of the five Co-doped GNP samples were all higher than that of a fresh GNP support, providing further support for the suggestion that Co-doping leads to an increase in s-OFGs; however, no linear correlations were observed between these two parameters. Indeed, despite an almost 20-fold increase in Co loading, the surface concentration of s-OFGs only slightly increased from 4.37% to 4.85%. Similarly, an almost 60-fold increase in Co loading resulted in less than a twofold increase in s-OFG concentration (Table S2.9). Furthermore, the Co-normalized I_d/I_g ratios and s-OFG concentrations (Table S2.10) were found to decrease with increasing Co loading (Figure 2.8a and 2.8b, respectively). These observations suggest that the presence of s-OFGs in the Co-doped GNP can be primarily attributed to the presence of small, finely dispersed nanoparticles rather than large, agglomerated Co oxides, which have an insignificant contribution by comparison. The evaluated OER activity of the Co-doped GNP at different Co loadings is

Laboratory of Materials for Renewable Energy (LMER)
Institute of Chemical Sciences and Engineering (ISIC)
Basic Science Faculty (SB)

50

presented in Figure 2.8c and 8d. The geometric current density increased from GNP-0.5 to GNP-4.8 to GNP-9.1 but remained unchanged at higher Co loadings (Figure 2.8c). In contrast, both the mass activity and the TOF decreased as the Co loading increased (Figure 2.8d). Modulating the surface loading of the catalyst reveals that an optimal mass activity was achieved across all Co loading values when the loading is set at 0.143 mg cm^{-2} (Figure S2.25), which was consistently used throughout the entirety of this study. OER activity was also measured on two unsupported commercial oxides: CoO and Co$_3$O$_4$ (Figure S2.26) that were subjected to the same degree of catalyst surface loading. Despite being subjected to higher Co loadings, the bulk oxides did not exhibit higher geometric current densities compared to the carbon-supported oxides. The increase in Co loading resulted in a consistent decrease in both mass activity and TOF, consistent with the trends observed in the Co-normalized I$_d$/I$_g$ ratios and s-OFGs surface concentrations. This suggests that the finely dispersed nanoparticles primarily function as active sites, where strong MSIs facilitate the generation of OFGs such as COOH on the surface of the catalyst. The formation of these OFGs plays a crucial role in enhancing the intrinsic activity of the supported catalyst, particularly in terms of facilitating O$_2$ spillover, as previously demonstrated. In conclusion, the presence of small, well-dispersed nanoparticles with robust MSIs is vital for maximizing the mass activity of the Co-doped GNP catalyst. This can be achieved by promoting the formation of OFGs that contribute to the overall OER activity of the catalysts.

3.4   Proposed mechanism for s-OFGs promoted OER activity
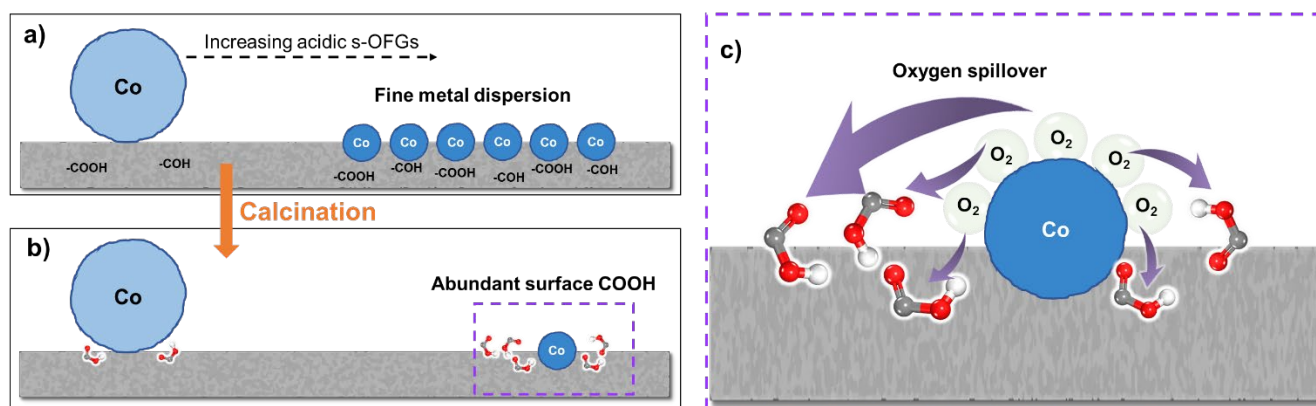
Figure 2.9. The proposed mechanism for the contribution of s-OFGs at different stages of the synthesis process. a) High concentrations of acidic groups enhance the dispersion of small nanoparticles. b) Strong interaction between the anchored nanoparticles resulting in an abundance of additional surface COOH. c) COOH facilitates the generation of O$_2$ spillover sites under OER conditions.

Laboratory of Materials for Renewable Energy (LMER)
Institute of Chemical Sciences and Engineering (ISIC)
Basic Science Faculty (SB)

51

s-OFGs play a crucial role in determining the dispersion and size distribution of carbon-supported Co-based catalysts. In this study, we suggest that the specific surface concentration of acidic s-OFGs is a key factor in metal cation adsorption. A high surface concentration of acidic s-OFGs, in conjunction with a large specific surface area, results in a higher overall concentration of acidic groups. The abundance of acidic groups creates more sites for the adsorption of Co cations (Figure 2.9a). These acidic s-OFGs serve as anchoring sites, enabling the fine dispersion of Co nanoparticles and reducing the potential formation of agglomerations during heating or electrochemical reactions. Supports with a high concentration of acidic s-OFGs but low specific surface areas, or vice versa, do not generate a sufficient number of adsorption sites for the optimal dispersion of nanoparticles. In the absence of adequate adsorption sites, excess cations form outer-sphere complexes, leading to weakly attached nanoparticles that are more prone to agglomeration[64].

The process of doping the Co catalysts introduces a significant number of active sites for OERs. These active sites consist of finely dispersed nano- and sub-nanoparticles that are firmly anchored onto the carbon support. Their strong interactions with the support lead to an increased number of structural defects within the carbon structure and facilitate the formation of high concentrations of s-OFGs; specifically, additional edge sites for COOH groups can be created through the generation of additional sp^2 defects in the structure[12] (Figure 2.9b). In contrast, large, agglomerated particles that are weakly bound to the surface do not generate a substantial amount of s-OFGs. Under OER conditions, the abundant COOH groups generated by the small Co nanoparticles function as spillover sites for the O_2 generated at the Co surface. This continuous release of occupied active sites enables the reaction to proceed more effectively (Figure 2.9c). It can thus be concluded that small Co nanoparticles that are firmly anchored to the surface serve as primary active sites for OERs, and are consequently the greatest contributors to the samples with the highest mass activity and TOF.

4   Conclusions

This study demonstrated that adjusting the surface functionalization and the specific surface area of a support can be a promising approach to control the size and distribution of supported metal catalysts, which in turn, can have a significant impact on the activity of electrochemical reactions that occur at gas-solid-liquid interfaces. Of the different surface oxygen species investigated, we found that the acidic s-OFGs of C-OH and COOH played a significant role in serving as active sites for the mounting of Co phases on the carbon surface. The GNP support exhibited the greatest specific surface area, the highest surface concentration of acidic OFGs, and the best dispersion of Co phases across the four carbon supports investigated. Consequently, GNP was found to have a superior dispersion of sub-nano- and nano-sized Co particles, as well as the highest mass activity and TOF for OER when loaded with Co0.5. Our findings offer insights into the overall surface content of acidic groups, which can be applied in diverse applications requiring well-dispersed nanoparticles, enabling the selection of the most suitable supports for specific applications.

In addition, our research has provided evidence for strong interactions between the support and the Co particles, especially in the case of small nanoparticles, which can lead to the formation of additional oxygen

Laboratory of Materials for Renewable Energy (LMER)   52
Institute of Chemical Sciences and Engineering (ISIC)
Basic Science Faculty (SB)

functional groups. Among these groups, the carboxyl functional groups (COOH) are particularly efficient in facilitating O_2 spillover, which helps remove O_2 from the Co surface. Based on these findings, we can conclude that small, well-dispersed Co nanoparticles can strongly interact with carbon, in contrast to large, agglomerated Co particles, and can serve as active sites for OERs due to the formation of more COOH groups.

Conflicts of interest

There are no conflicts to declare.

Acknowledgements

References

[1]   A. Boucly, L. Artiglia, E. Fabbri, D. Palagin, D. Aegerter, D. Pergolesi, Z. Novotny, N. Comini, J. T. Diulus, T. Huthwelker, M. Ammann, T. J. Schmidt, *J. Mater. Chem. A* **2022**, *10*, 2434.

[2]   F. T. Haase, A. Bergmann, T. E. Jones, J. Timoshenko, A. Herzog, H. S. Jeon, C. Rettenmaier, B. R. Cuenya, *Nat. Energy* **2022**, *7*, 765.

[3]   T. H. Shen, L. Spillane, J. Vavra, T. H. M. Pham, J. Peng, Y. Shao-Horn, V. Tileli, *J. Am. Chem. Soc.* **2020**, *142*, 15876.

[4]   S. Saddeler, G. Bendt, S. Salamon, F. T. Haase, J. Landers, J. Timoshenko, C. Rettenmaier, H. S. Jeon, A. Bergmann, H. Wende, B. Roldan Cuenya, S. Schulz, *J. Mater. Chem. A* **2021**, *9*, 25381.

[5]   J. Suntivich, K. J. May, H. A. Gasteiger, J. B. Goodenough, Y. Shao-Horn, *Science (80-.).* **2011**, *334*, 1383.

[6]   X. Li, J. Zhang, Q. Feng, C. Pu, L. Zhang, M. Hu, X. Zhou, X. Zhong, W. Yi, J. Tang, Z. Li, X. Zhao, H. Li, B. Xu, *J. Mater. Chem. A* **2018**, *6*, 17288.

[7]   S. Lee, A. Moysiadou, Y. C. Chu, H. M. Chen, X. Hu, *Energy Environ. Sci.* **2022**, *15*, 206.

[8]   F. Le Formal, N. Guijarro, W. S. Bourée, A. Gopakumar, M. S. Prévot, A. Daubry, L. Lombardo, C. Sornay, J. Voit, A. Magrez, P. J. Dyson, K. Sivula, *Energy Environ. Sci.* **2016**, *9*, 3448.

[9]   T. Reier, M. Oezaslan, P. Strasser, *ACS Catal.* **2012**, *2*, 1765.

[10]   C. E. Beall, E. Fabbri, A. H. Clark, N. S. Yüzbasi, T. Graule, T. J. Schmidt, *EcoMat* **2023**, 1.

[11]   T. Poux, F. S. Napolskiy, T. Dintzer, G. Kéranguéven, S. Y. Istomin, G. A. Tsirlina, E. V. Antipov, E. R. Savinova, *Catal. Today* **2012**, *189*, 83.

[12]   I. C. Gerber, P. Serp, *Chem. Rev.* **2020**, *120*, 1250.

[13]   T. He, A. R. Puente-Santiago, S. Xia, M. A. Ahsan, G. Xu, R. Luque, *Adv. Energy Mater.* **2022**, *12*,

Laboratory of Materials for Renewable Energy (LMER)
Institute of Chemical Sciences and Engineering (ISIC)
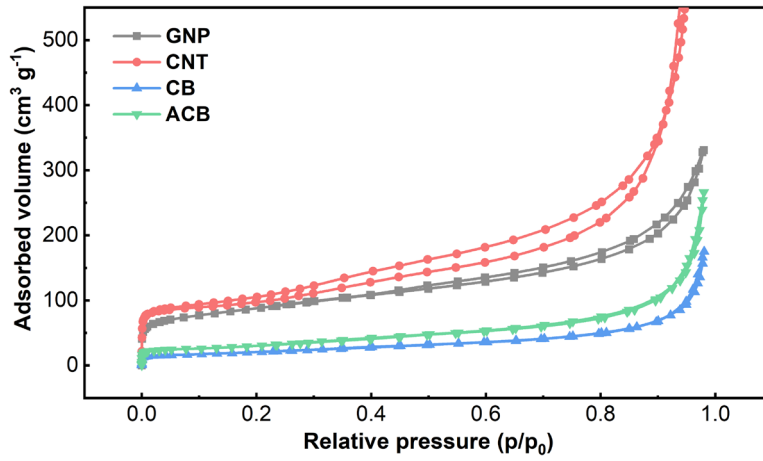Basic Science Faculty (SB)

53

2200493.

[14]   L. Bai, C. S. Hsu, D. T. L. Alexander, H. M. Chen, X. Hu, *J. Am. Chem. Soc.* **2019**, *141*, 14190.

[15]   Y. Liang, Y. Li, H. Wang, J. Zhou, J. Wang, T. Regier, H. Dai, *Nat. Mater.* **2011**, *10*, 780.

[16]   E. Antolini, *Appl. Catal. B Environ.* **2016**, *181*, 298.

[17]   P. Mäki-Arvela, D. Y. Murzin, *Appl. Catal. A Gen.* **2013**, *451*, 251.

[18]   M. Jerigová, M. Odziomek, N. López-Salas, *ACS Omega* **2022**, *7*, 11544.

[19]   C. Qiu, L. Jiang, Y. Gao, L. Sheng, *Mater. Des.* **2023**, *230*, 111952.

[20]   F. Zoller, S. Häringer, D. Böhm, J. Luxa, D. Fattakhova-Rohlfing, F. Zoller, D. Böhm, D. Fattakhova-Rohlfing, S. Häringer, J. Luxa, Z. Sofer, *Small* **2021**, *17*, 2007484.

[21]   Z. Li, B. Li, Y. Hu, S. Wang, C. Yu, *Mater. Adv.* **2022**, *3*, 779.

[22]   J. E. Zuliani, S. Tong, C. Q. Jia, D. W. Kirk, *J. Power Sources* **2018**, *395*, 271.

[23]   X. Yang, Y. Wan, Y. Zheng, F. He, Z. Yu, J. Huang, H. Wang, Y. S. Ok, Y. Jiang, B. Gao, *Chem. Eng. J.* **2019**, *366*, 608.

[24]   X. Song, H. Liu, L. Cheng, Y. Qu, *Desalination* **2010**, *255*, 78.

[25]   N. Xie, H. Wang, C. You, *J. Hazard. Mater.* **2021**, *405*, 124221.

[26]   M. J. Bleda-Martínez, J. A. Maciá-Agulló, D. Lozano-Castelló, E. Morallón, D. Cazorla-Amorós, A. Linares-Solano, *Carbon N. Y.* **2005**, *43*, 2677.

[27]   J. E. Zuliani, S. Tong, C. Q. Jia, D. W. Kirk, *J. Power Sources* **2018**, *395*, 271.

[28]   X. Zhang, L. Song, L. Tong, M. Zeng, Y. Wang, *Chem. Eng. J.* **2022**, *440*, 135884.

[29]   F. Yang, X. Ma, W. Bin Cai, P. Song, W. Xu, *J. Am. Chem. Soc.* **2019**, *141*, 20451.

[30]   J. Sun, J. Xu, H. Jiang, X. Zhang, D. Niu, *ChemElectroChem* **2020**, 1869.

[31]   G. F. Han, F. Li, W. Zou, M. Karamad, J. P. Jeon, S. W. Kim, S. J. Kim, Y. Bu, Z. Fu, Y. Lu, S. Siahrostami, J. B. Baek, *Nat. Commun.* **2020**, *11*, 2209.

[32]   A. Ejsmont, K. Kadela, G. Grzybek, T. Darvishzad, G. Słowik, M. Lofek, J. Goscianska, A. Kotarba, P. Stelmachowski, *ACS Appl. Mater. Interfaces* **2023**, *15*, 5148.

[33]   Z. Liu, Z. Zhao, Y. Wang, S. Dou, D. Yan, D. Liu, Z. Xia, S. Wang, *Adv. Mater.* **2017**, *29*, 1606207.

[34]   TUINSTRA F, KOENIG JL, *J. Chem. Phys.* **1970**, *53*, 1126.

[35]   L. G. Cançado, A. Jorio, E. H. M. Ferreira, F. Stavale, C. A. Achete, R. B. Capaz, M. V. O. Moutinho, A. Lombardo, T. S. Kulmala, A. C. Ferrari, *Nano Lett.* **2011**, *11*, 3190.

[36]   G. Moon, H. Tu, *ACS Appl. Energy Mater.* **2019**, *2*, 6672.

[37]   D. Lozano-Castelló, D. Cazorla-Amorós, A. Linares-Solano, S. Shiraishi, H. Kurihara, A. Oya, *Carbon N. Y.* **2003**, *41*, 1765.

Laboratory of Materials for Renewable Energy (LMER)   54
Institute of Chemical Sciences and Engineering (ISIC)
Basic Science Faculty (SB)

[38] S. Jung, C. C. L. McCrory, I. M. Ferrer, J. C. Peters, T. F. Jaramillo, *J. Mater. Chem. A* **2016**, *4*, 3068.

[39] D. Z. Khater, R. S. Amin, M. Mahmoud, K. M. El-Khatib, *RSC Adv.* **2022**, *12*, 2207.

[40] X. X. Fernández Sánchez-Romate, A. del Bosque García, M. Sánchez, A. Ureña, *ACS Appl. Mater. Interfaces* **2023**, *15*, 22377.

[41] J. Zhou, P. Yang, P. A. Kots, M. Cohen, Y. Chen, C. M. Quinn, M. D. de Mello, J. Anibal Boscoboinik, W. J. Shaw, S. Caratzoulas, W. Zheng, D. G. Vlachos, *Nat. Commun.* **2023**, *14*, 2293.

[42] A. Fujimoto, Y. Yamada, M. Koinuma, S. Sato, *Anal. Chem.* **2016**, *88*, 6110.

[43] A. Aarva, V. L. Deringer, S. Sainio, T. Laurila, M. A. Caro, *Chem. Mater.* **2019**, *31*, 9256.

[44] J. Wu, T. Wang, Y. Zhang, W. P. Pan, *Bioresour. Technol.* **2019**, *291*, 121859.

[45] P. Kumar, K. Kannimuthu, A. S. Zeraati, S. Roy, X. Wang, X. Wang, S. Samanta, K. A. Miller, M. Molina, D. Trivedi, J. Abed, M. A. Campos Mata, H. Al-Mahayni, J. Baltrusaitis, G. Shimizu, Y. A. Wu, A. Seifitokaldani, E. H. Sargent, P. M. Ajayan, J. Hu, M. G. Kibria, *J. Am. Chem. Soc.* **2023**, *145*, 8052.

[46] R. Lu, D. K. Sam, W. Wang, S. Gong, J. Liu, A. Durairaj, M. Li, X. Lv, *J. Colloid Interface Sci.* **2022**, *613*, 126.

[47] L. Yang, H. Liu, H. Shen, Y. Huang, S. Wang, L. Zheng, D. Cao, *Adv. Funct. Mater.* **2020**, *30*, 1.

[48] A. W. Jensen, G. W. Sievers, K. D. Jensen, J. Quinson, J. A. Arminio-Ravelo, V. Brüser, M. Arenz, M. Escudero-Escribano, *J. Mater. Chem. A* **2020**, *8*, 1066.

[49] P. Jash, P. Srivastava, A. Paul, *Chem. Commun.* **2019**, *55*, 2230.

[50] C. Cai, S. Han, X. Zhang, J. Yu, X. Xiang, J. Yang, L. Qiao, X. Zu, Y. Chen, S. Li, *RSC Adv.* **2022**, *12*, 6205.

[51] J. Huang, J. Chen, T. Yao, J. He, S. Jiang, Z. Sun, Q. Liu, W. Cheng, F. Hu, Y. Jiang, Z. Pan, S. Wei, *Angew. Chemie - Int. Ed.* **2015**, *54*, 8722.

[52] M. Kim, B. Lee, H. Ju, S. W. Lee, J. Kim, *Adv. Mater.* **2019**, *31*, 1.

[53] A. Bähr, H. Petersen, H. Tüysüz, *ChemCatChem* **2021**, *13*, 3824.

[54] Y. R. Hong, S. Mhin, K. M. Kim, W. S. Han, H. Choi, G. Ali, K. Y. Chung, H. J. Lee, S. I. Moon, S. Dutta, S. Sun, Y. G. Jung, T. Song, H. S. Han, *J. Mater. Chem. A* **2019**, *7*, 3592.

[55] B. Zhang, L. Shao, W. Zhang, X. Sun, X. Pan, D. S. Su, *ChemCatChem* **2014**, *6*, 2607.

[56] B. Zhang, D. S. Su, *ChemCatChem* **2015**, *7*, 3639.

[57] Y. Lu, L. Huang, Y. Guo, X. Yang, *Carbon N. Y.* **2021**, *183*, 355.

[58] I. C. Man, H. Su, F. Calle-Vallejo, H. A. Hansen, J. I. Martínez, N. G. Inoglu, J. Kitchin, T. F. Jaramillo, J. K. Nørskov, J. Rossmeisl, *ChemCatChem* **2011**, *3*, 1159.

Laboratory of Materials for Renewable Energy (LMER)
Institute of Chemical Sciences and Engineering (ISIC)
Basic Science Faculty (SB)

55

[59]   Y. Zhu, W. Zhou, Z. Shao, *Small* **2017**, *13*, 1.

[60]   P. Wang, M. Yan, J. Meng, G. Jiang, L. Qu, X. Pan, J. Z. Liu, L. Mai, *Nat. Commun.* **2017**, *8*, 1.

[61]   X. Wang, X. Li, J. Mu, S. Fan, X. Chen, L. Wang, Z. Yin, M. Tadé, S. Liu, *ACS Appl. Mater. Interfaces* **2019**, *11*, 41988.

[62]   K. Xiang, Z. Xu, T. Qu, Z. Tian, Y. Zhang, Y. Wang, M. Xie, X. Guo, W. Ding, X. Guo, *Chem. Commun.* **2017**, *53*, 12410.

[63]   K. Morimoto, S. Anraku, J. Hoshino, T. Yoneda, T. Sato, *J. Colloid Interface Sci.* **2012**, *384*, 99.

[64]   T. Ataloglou, J. Vakros, K. Bourikas, C. Fountzoula, C. Kordulis, A. Lycourghiotis, *Appl. Catal. B Environ.* **2005**, *57*, 299.

[65]   A. Parastaev, V. Muravev, E. Huertas Osta, A. J. F. van Hoof, T. F. Kimpel, N. Kosinov, E. J. M. Hensen, *Nat. Catal.* **2020**, *3*, 526.

[66]   H. Tang, F. Liu, J. Wei, B. Qiao, K. Zhao, Y. Su, C. Jin, L. Li, J. J. Liu, J. Wang, T. Zhang, *Angew. Chemie - Int. Ed.* **2016**, *55*, 10606.
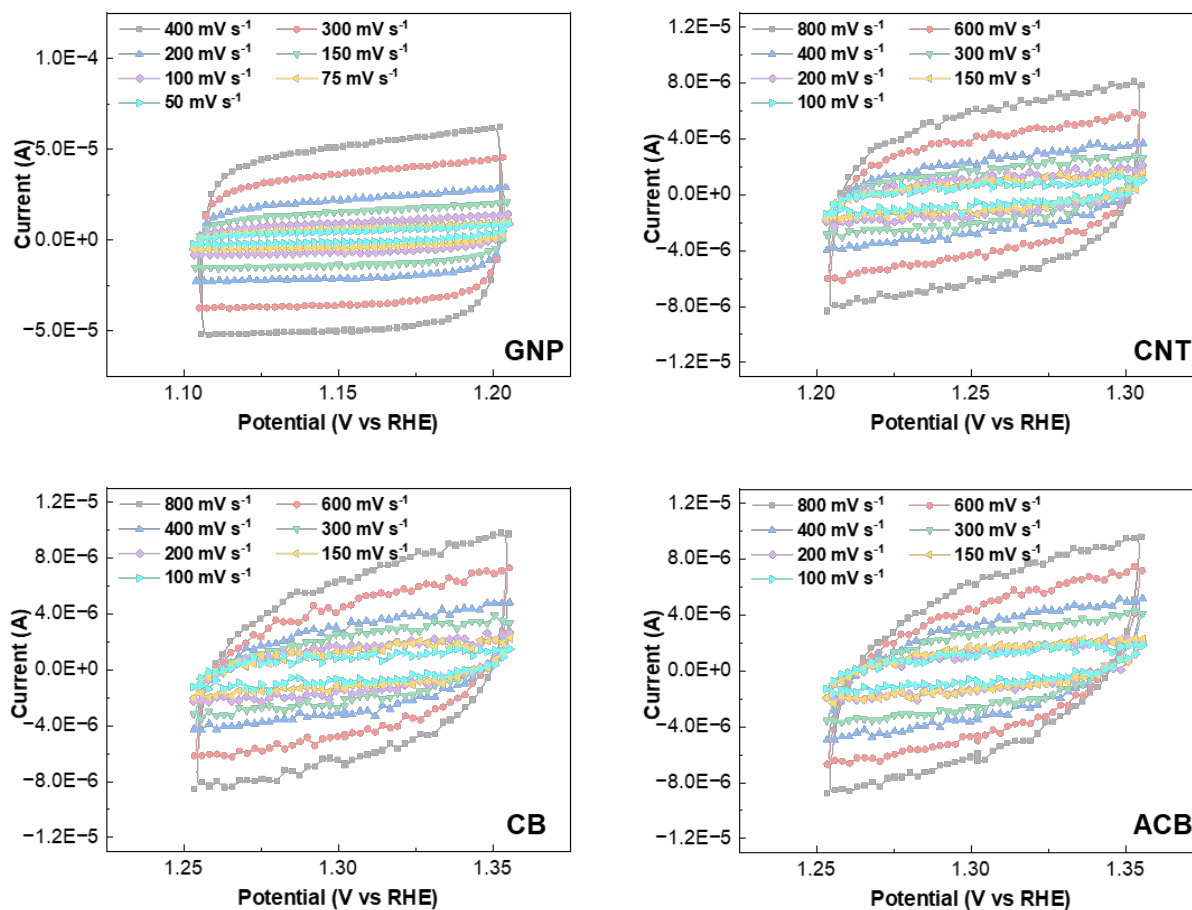
Laboratory of Materials for Renewable Energy (LMER)   56
Institute of Chemical Sciences and Engineering (ISIC)
Basic Science Faculty (SB)
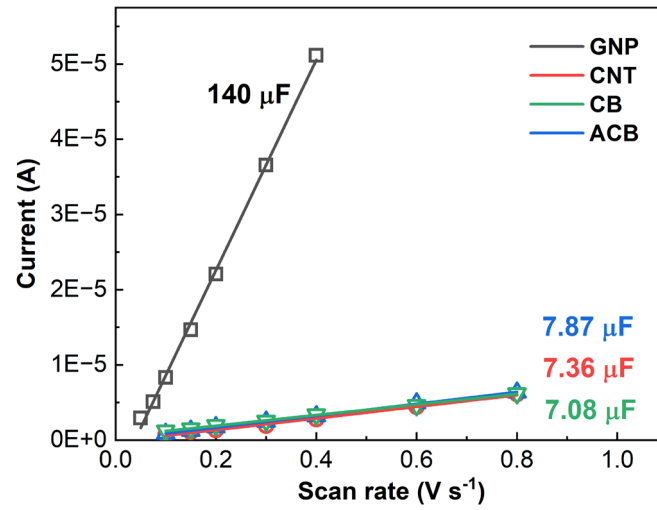
5 Supporting information

Figure S2.1. N_2 adsorption-desorption as a function of relative pressure, acquired by N_2-adsorption measurements on the four fresh supports.

Laboratory of Materials for Renewable Energy (LMER)
Institute of Chemical Sciences and Engineering (ISIC)
Basic Science Faculty (SB)

57

Table S2.1. Summary of the BET surface area of the four fresh supports, derived from the N_2 adsorption-desorption measurements using BET method.
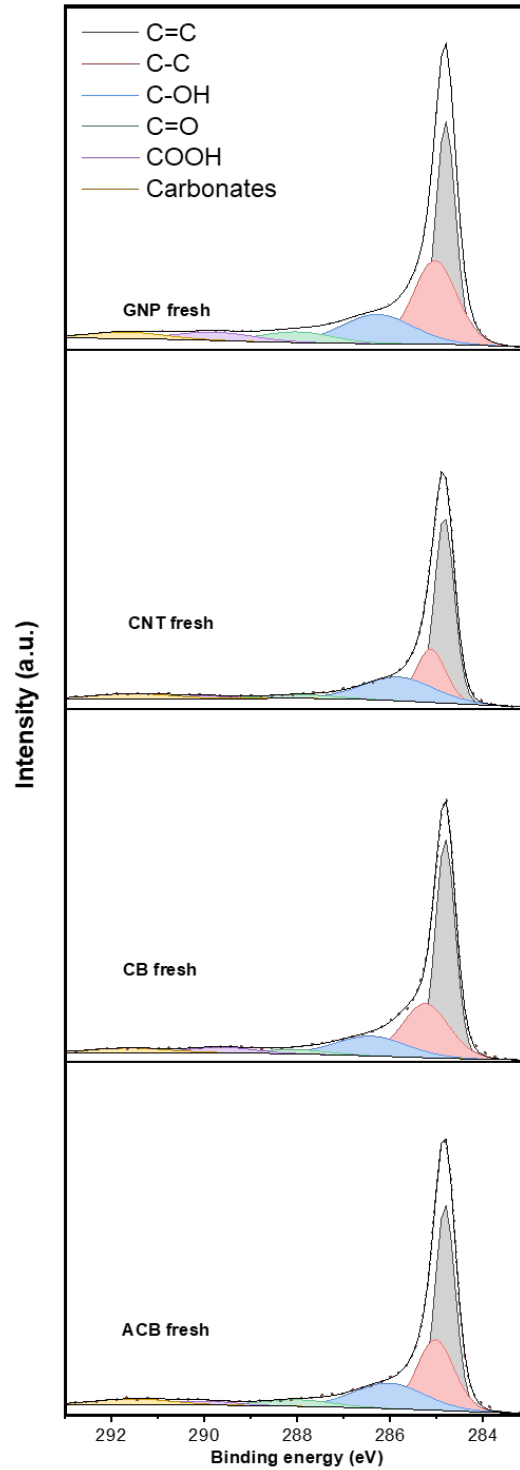
Support	BET surface area ($m^2\,g^{-1}$)
CNT	368
ACB	107
CB	74
GNP	310

Laboratory of Materials for Renewable Energy (LMER)
Institute of Chemical Sciences and Engineering (ISIC)
Basic Science Faculty (SB)

58

Figure S2.2. Double-layer capacitance measurements for different carbon supports. The sub-figures plot the current as a function different scan rate.

Laboratory of Materials for Renewable Energy (LMER)
Institute of Chemical Sciences and Engineering (ISIC)
Basic Science Faculty (SB)

59

Figure S2.3. Linear regression of the measured charging currents as a function of the scan rate. The slope of the line corresponds to the double-layer capacitance.

Laboratory of Materials for Renewable Energy (LMER)
Institute of Chemical Sciences and Engineering (ISIC)
Basic Science Faculty (SB)

60

Figure S2.4. XPS C 1s spectra of the four supports, and the fitted peaks for carbon (C=C and C-C), surface oxygen containing groups (COH, COOH and C=O), and surface carbon oxygenates
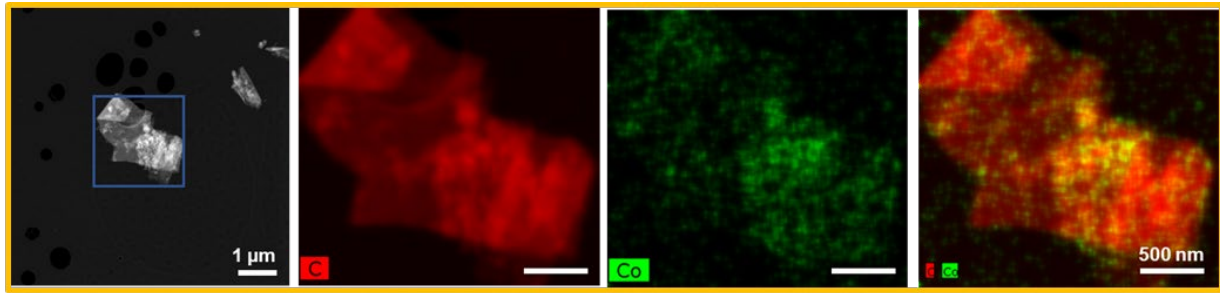
Laboratory of Materials for Renewable Energy (LMER)
Institute of Chemical Sciences and Engineering (ISIC)
Basic Science Faculty (SB)

61

Table S2.2. Summary of the surface concentration of oxygen and s-OFGs, measured on the four fresh supports.

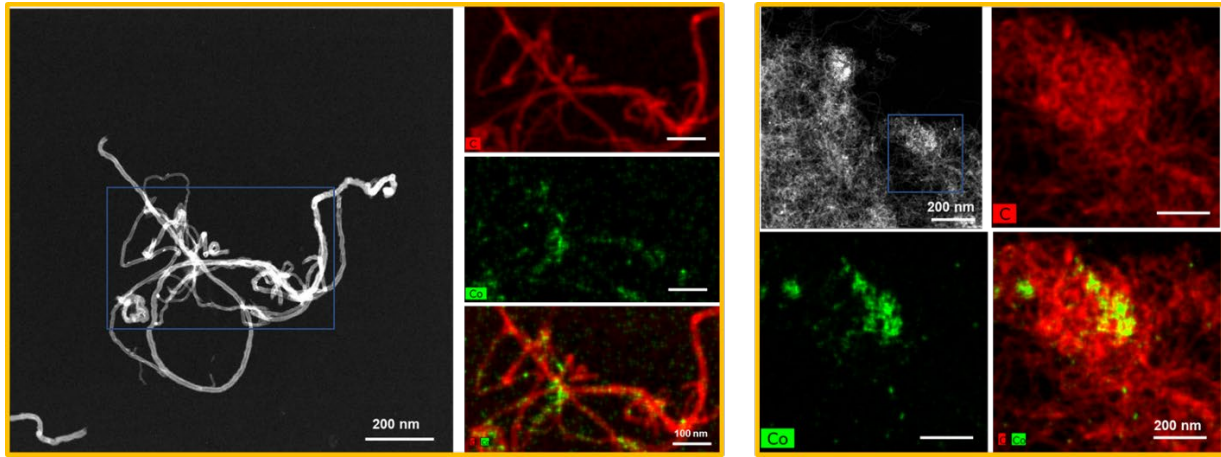|	Oxygen (%)	COH (%)	COOH (%)	C=O (%)
GNP	3.32	1.48	0.32	1.37
CB	3.51	1.32	0.32	1.72
ACB	1.15	0.38	0.21	0.49
CNT	0.65	0.12	0.23	0.31

Laboratory of Materials for Renewable Energy (LMER)
Institute of Chemical Sciences and Engineering (ISIC)
Basic Science Faculty (SB)

62

Table S2.3. Co contents in the synthesized catalysts: GNP-0.5, CNT-0.5, CB-0.5 and ACB-0.5, averaged from 2 sets of measurements

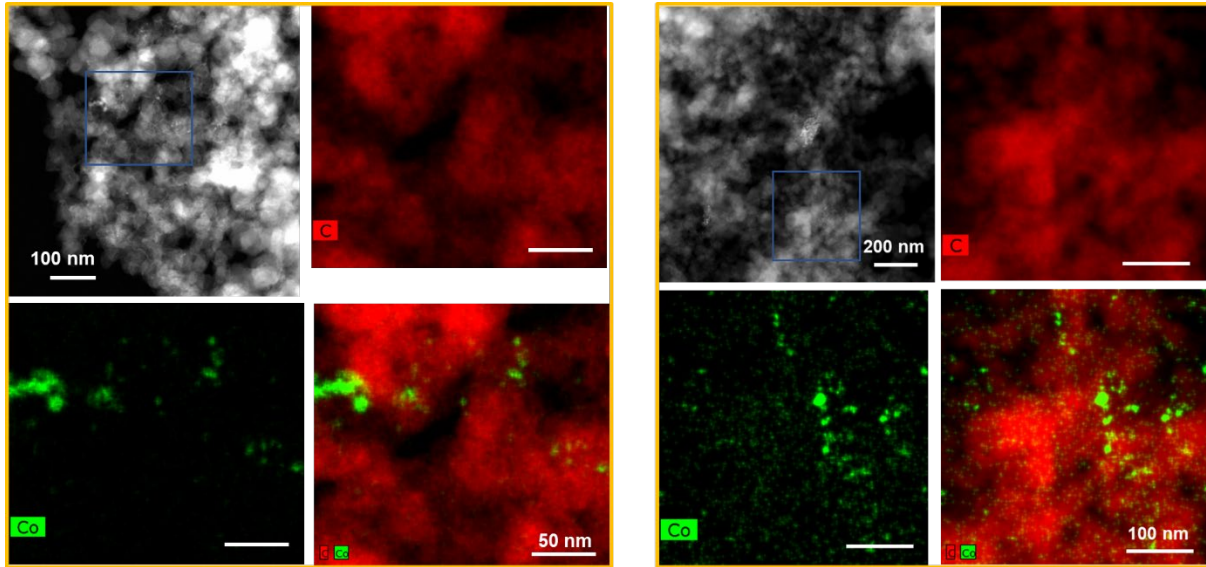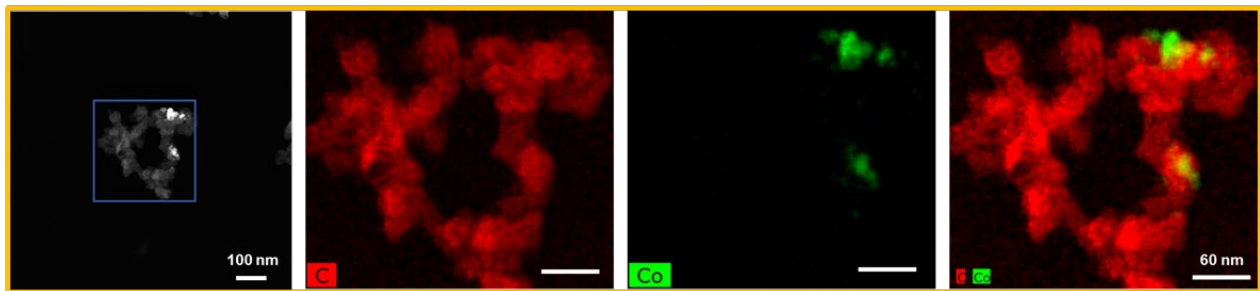|	Co concentration (%)
GNP	0.51 ± 0.01
CNT	0.57 ± 0.23
CB	0.46 ± 0.23
ACB	0.53 ± 0.10

Laboratory of Materials for Renewable Energy (LMER)
Institute of Chemical Sciences and Engineering (ISIC)
Basic Science Faculty (SB)

63
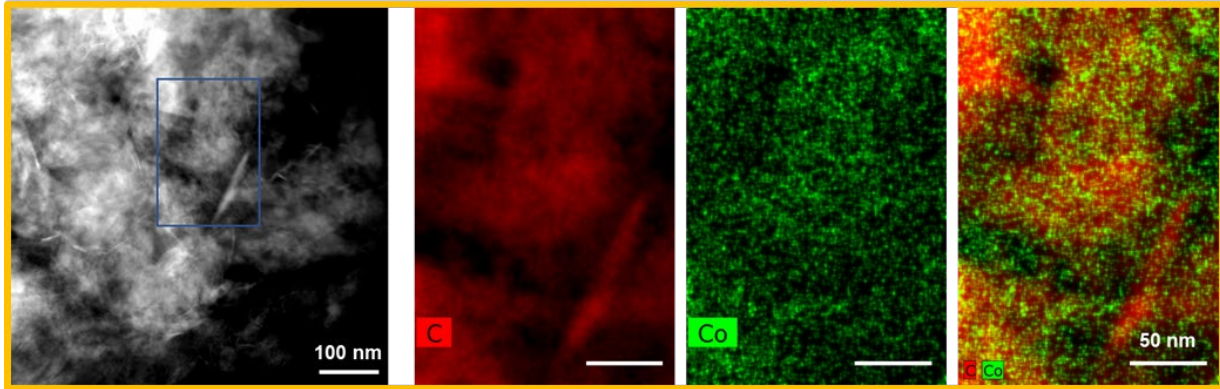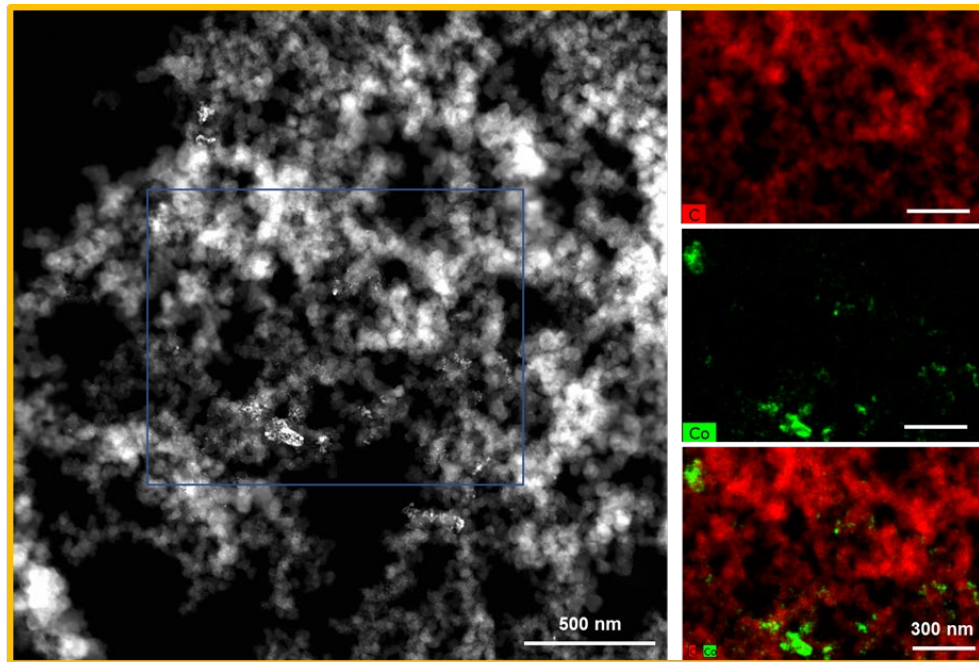
Figure S2.5. HAADF-STEM images and the corresponding elemental maps for C and Co, obtained at two different regions on GNP-0.5.

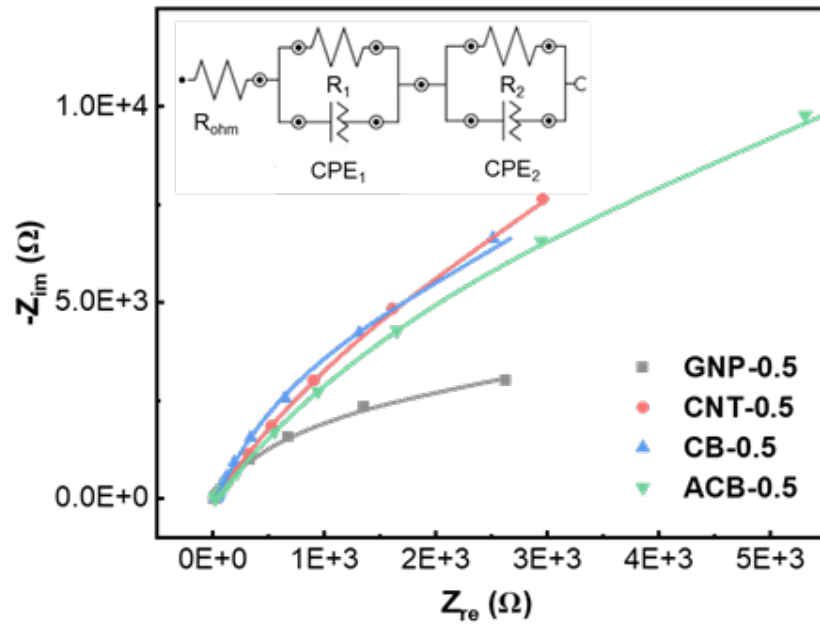Laboratory of Materials for Renewable Energy (LMER)
Institute of Chemical Sciences and Engineering (ISIC)
Basic Science Faculty (SB)

64

Figure S2.6. HAADF-STEM images and the corresponding elemental maps for C and Co, obtained at two different regions on CNT-0.5.

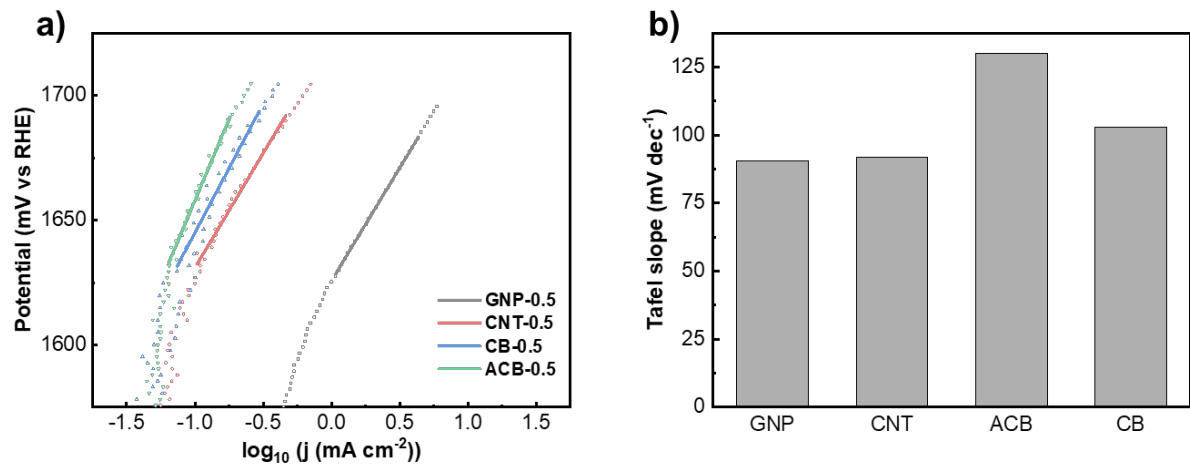Laboratory of Materials for Renewable Energy (LMER)
Institute of Chemical Sciences and Engineering (ISIC)
Basic Science Faculty (SB)

65

Figure S2.7. HAADF-STEM images and the corresponding elemental maps for C and Co, obtained at two different regions on CB-0.5.

Laboratory of Materials for Renewable Energy (LMER)
Institute of Chemical Sciences and Engineering (ISIC)
Basic Science Faculty (SB)

66

Figure S2.8. HAADF-STEM images and the corresponding elemental maps for C and Co, obtained at two different regions on ACB-0.5.

Laboratory of Materials for Renewable Energy (LMER)
Institute of Chemical Sciences and Engineering (ISIC)
Basic Science Faculty (SB)

67

Figure S2.9. Nyquist plot and the fitted curve according to the corresponding equivalent circuit. The EIS was acquired at 1.5 V vs RHE, with a perturbation amplitude of ±10 mV, from 100 kHz to 0.1 Hz.

Laboratory of Materials for Renewable Energy (LMER)
Institute of Chemical Sciences and Engineering (ISIC)
Basic Science Faculty (SB)

68

a)

b)

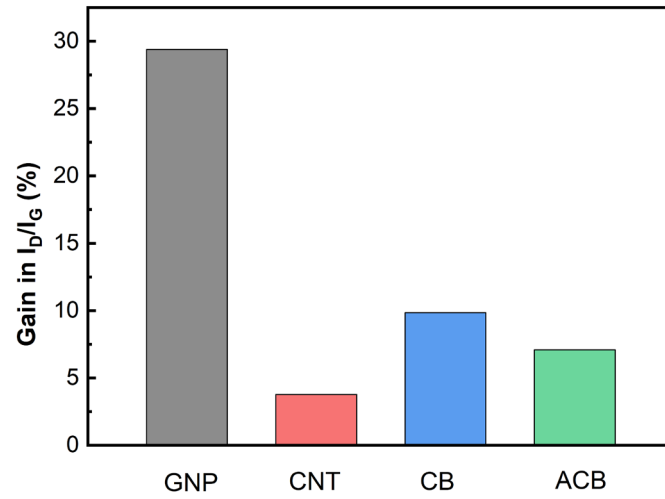**Figure S2.10.** a) Tafel plots and b) the corresponding Tafel slopes of Co- catalyst supported on four different carbons.

Laboratory of Materials for Renewable Energy (LMER)
Institute of Chemical Sciences and Engineering (ISIC)
Basic Science Faculty (SB)

69

Table S2.4. Mass activities of previously reported Co-based catalysts.

References	Samples	Overpotential (V vs RHE)	Mass activity (A g^{-1})
A[1]	Co SAC	1.65	2209
B[2]	BN/CA-NiCoFe-600	1.6	201
C[3]	$Co_{0.7}Fe_{0.3}CB$	1.55	643
D[4]	Ir-networks (Ir:Co = 1:55)	1.53	800
E[5]	$SL-Co(OH)_2$	1.58	153.8
F[6]	$Au–Co(OH)_2$	1.5	177
G[7]	γ-CoOOH nanosheets	1.53	66.6
H[8]	YRCO-560	1.48	49.75
I[9]	EtOH-CoO	1.7	2900
J[10]	$ECA-Co_xNi_{1-x}S_2$	1.57	217

Laboratory of Materials for Renewable Energy (LMER)
Institute of Chemical Sciences and Engineering (ISIC)
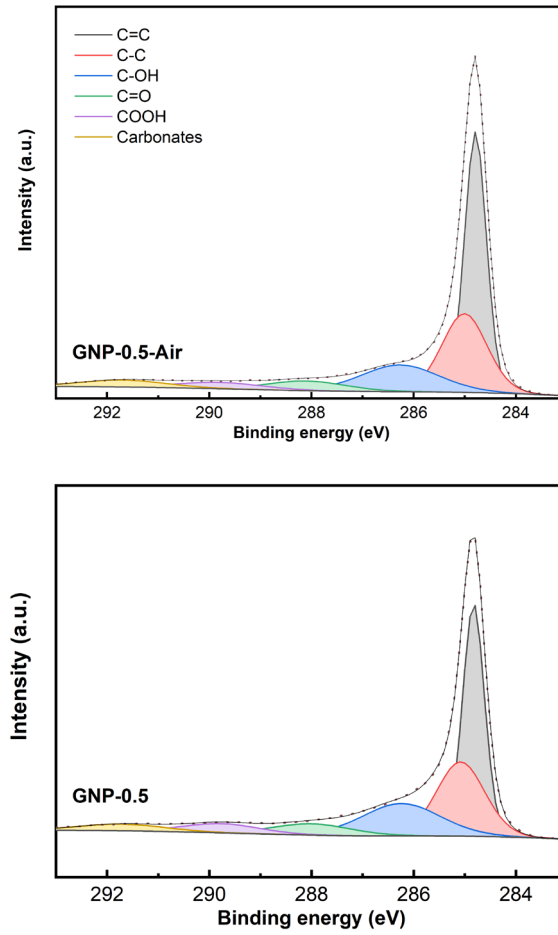Basic Science Faculty (SB)

70

Table S2.5. Summary of I_d/I_g ratio of the fresh- and doped- carbon, determined with Raman spectroscopy. The presented value was obtained from at least 10 different regions.

Support	Fresh	With Co doping
GNP	0.11 ± 0.02	0.15 ± 0.06
CNT	0.76 ± 0.11	0.79 ± 0.09
CB	1.11 ± 0.04	1.22 ± 0.04
ACB	1.12 ± 0.03	1.20 ± 0.04

Laboratory of Materials for Renewable Energy (LMER)
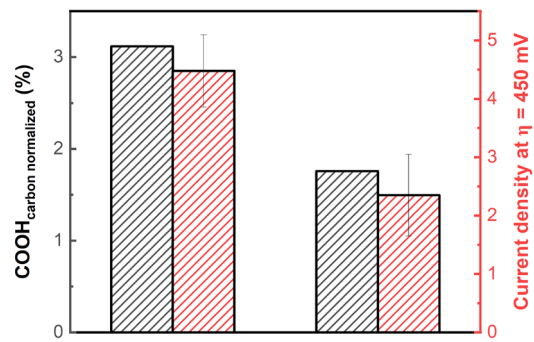Institute of Chemical Sciences and Engineering (ISIC)
Basic Science Faculty (SB)

71

Figure S2.11. The gain in I_d/I_g between before and after Co-incorporation. This value is calculated as the quotient between $[I_d/I_{g[Co-doped]} - I_d/I_{g[fresh\ support]}]$ and $[I_d/I_{g[fresh\ support]}]$.
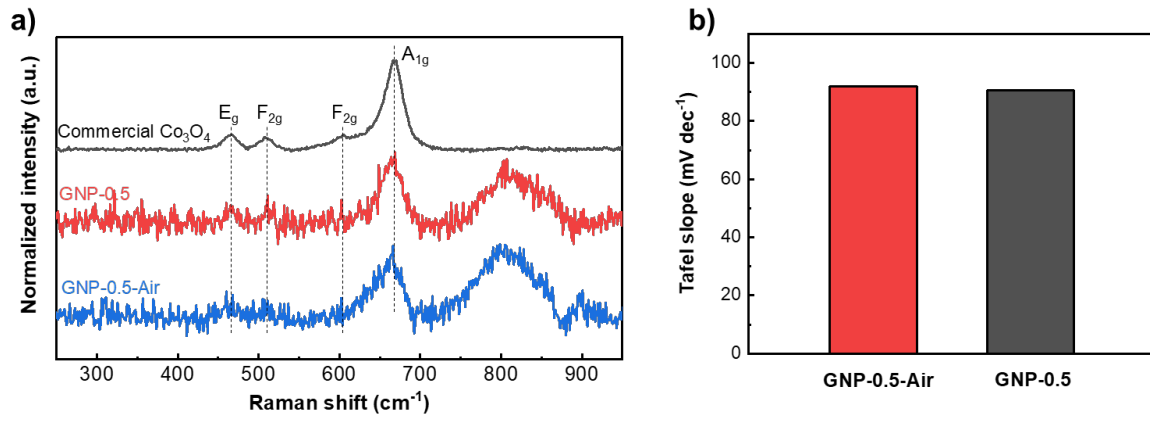
Laboratory of Materials for Renewable Energy (LMER)
Institute of Chemical Sciences and Engineering (ISIC)
Basic Science Faculty (SB)

72

Figure S2.12. XPS C 1s spectra of GNP-0.5-Air and GNP-0.5 and the corresponding deconvoluted peaks.

Laboratory of Materials for Renewable Energy (LMER)
Institute of Chemical Sciences and Engineering (ISIC)
Basic Science Faculty (SB)

73

Table S2.6. Summary of the s-OFGs surface concentration on the fresh GNP support, GNP-0.5-Air and GNP-0.5. The s-OFGs surface concentration is the ratio [area of s-OFGs fitted in O 1s spectra] to [total area of carbon in C 1s spectra].
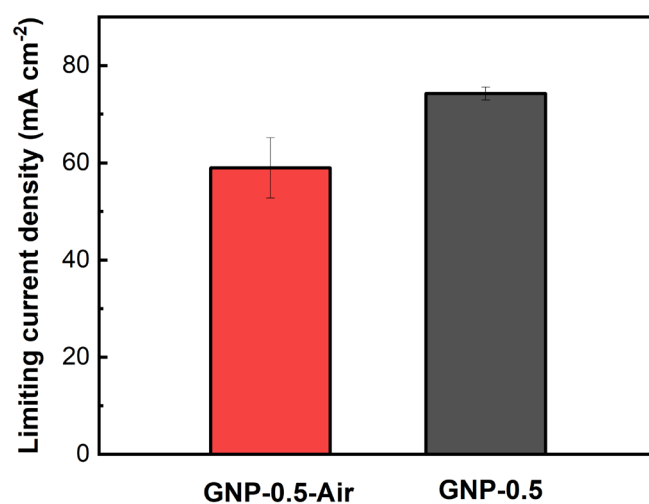
	GNP support	GNP-0.5-Air	GNP-0.5
Oxygen surface contents (%)	3.21	3.47	4.37
C=O surface concentration (%)	1.37	1.53	1.00
COH surface concentration (%)	1.48	1.49	1.96
COOH surface concentration (%)	0.32	0.27	1.15

Laboratory of Materials for Renewable Energy (LMER)
Institute of Chemical Sciences and Engineering (ISIC)
Basic Science Faculty (SB)

74
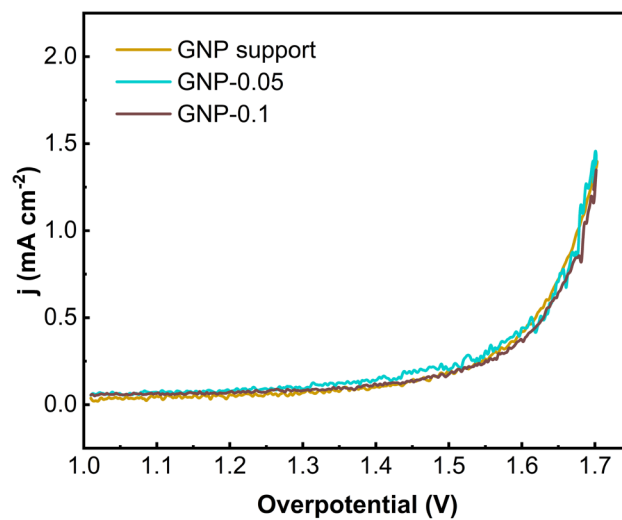
Figure S2.13. Specific COOH surface concentration and geometric current density at an overpotential of 450 mV of GNP-0.5-Air and GNP-0.5.

Laboratory of Materials for Renewable Energy (LMER)
Institute of Chemical Sciences and Engineering (ISIC)
Basic Science Faculty (SB)

75

Figure S2.14. a) Raman spectroscopy including the peaks of Co_3O_4, acquired on GNP-0.5, GNP-0.5-Air and on commercial Co_3O_4. b) the Tafel slopes of GNP-0.5 and GNP-0.5-Air

Laboratory of Materials for Renewable Energy (LMER)
Institute of Chemical Sciences and Engineering (ISIC)
Basic Science Faculty (SB)

76

Figure S2.15. Summary of the limiting current density, calculated from LSV of GNP-0.5-Air and GNP-0.5, in Fe-free KOH 1M, scanned from 1.5 to 2.2 V vs RHE at a scan rate of 10 mV s^{-1}. The potential was corrected with 85% of iR-drop.

Laboratory of Materials for Renewable Energy (LMER)
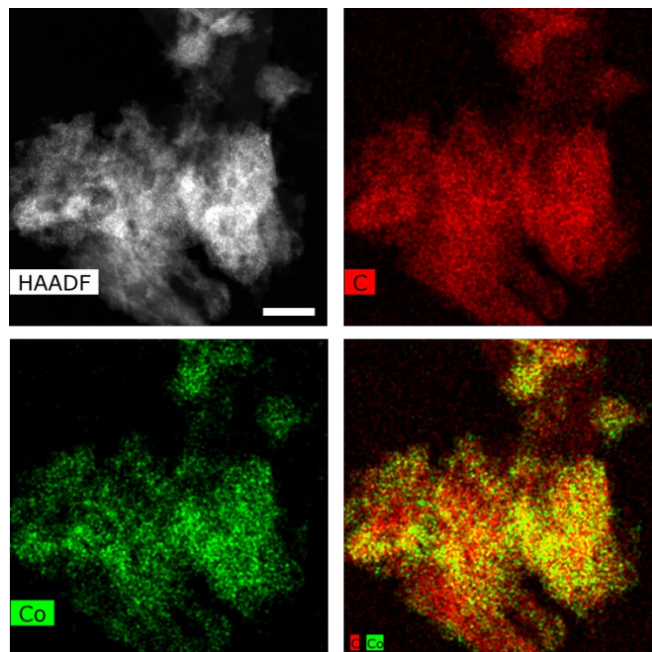Institute of Chemical Sciences and Engineering (ISIC)
Basic Science Faculty (SB)

77

Figure S2.16. CVs of GNP, GNP-0.05 and GNP-0.1 loadings in Fe-free 1M KOH solution, scanned from 1.0–1.7 V vs RHE at a scan rate of 10 mV s^{-1}. CV curves were iR-corrected (85% iR drop compensation) and averaged across the forward and backward scans.

Laboratory of Materials for Renewable Energy (LMER)
Institute of Chemical Sciences and Engineering (ISIC)
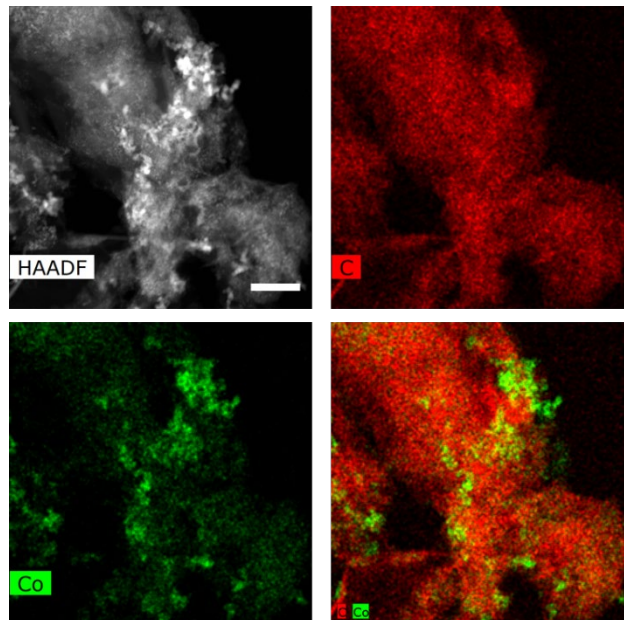Basic Science Faculty (SB)

78

Table S2.7. Co contents in the synthesized catalysts with different Co loadings: GNP-0.5, GNP-4.8, GNP-9.1, GNP-17 and GNP-29, averaged from 3 sets of measurements

Theoretical loading	Co concentration by ICP-OES
0.5	0.51 ± 0.01
4.8	4.67 ± 0.71
9.1	10.88 ± 0.21
17	17.72 ± 4.33
29	29.62 ± 6.81

Laboratory of Materials for Renewable Energy (LMER)
Institute of Chemical Sciences and Engineering (ISIC)
Basic Science Faculty (SB)

79

Figure S2.17. HAADF-STEM images and the corresponding elemental maps for C and Co of GNP-4.8. Scale bar: 100 nm.

Laboratory of Materials for Renewable Energy (LMER)
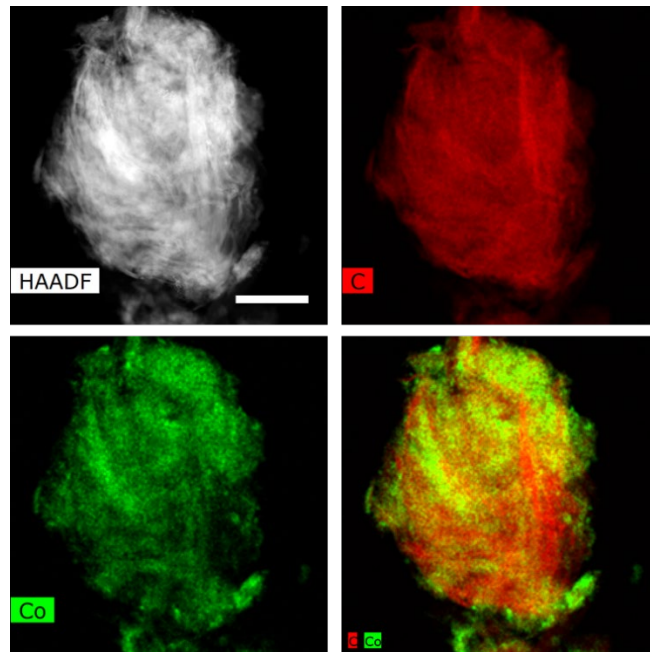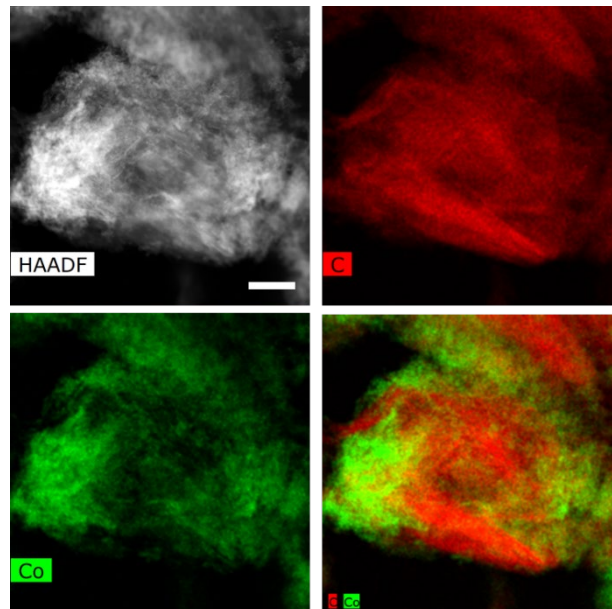Institute of Chemical Sciences and Engineering (ISIC)
Basic Science Faculty (SB)

80

Figure S2.18. HAADF-STEM images and the corresponding elemental maps for C and Co of GNP-9.1. Scale bar: 100 nm.

Laboratory of Materials for Renewable Energy (LMER)
Institute of Chemical Sciences and Engineering (ISIC)
Basic Science Faculty (SB)

81

Figure S2.19. HAADF-STEM images and the corresponding elemental maps for C and Co of GNP-17. Scale bar: 1 µm.

Laboratory of Materials for Renewable Energy (LMER)
Institute of Chemical Sciences and Engineering (ISIC)
Basic Science Faculty (SB)

82

Figure S2.20. HAADF-STEM images and the corresponding elemental maps for C and Co of GNP-29. Scale bar: 200 nm.

Laboratory of Materials for Renewable Energy (LMER)
Institute of Chemical Sciences and Engineering (ISIC)
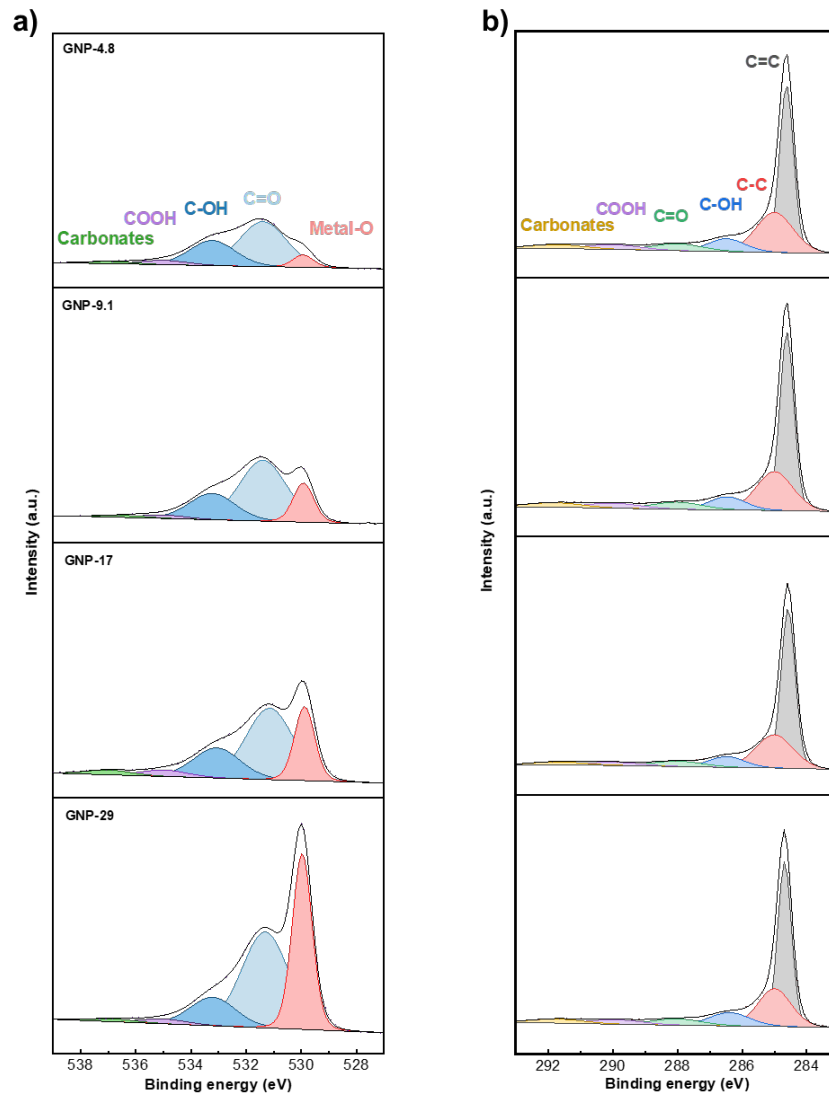Basic Science Faculty (SB)

83
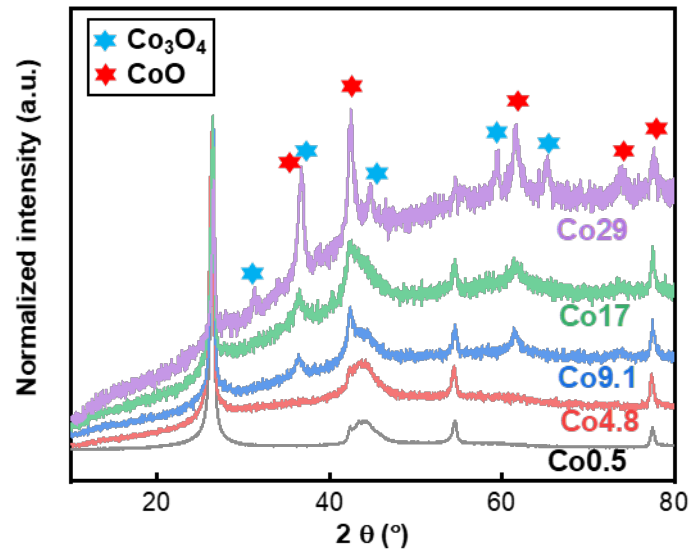
Figure S2.21. XRD patterns of the Co-based catalysts supported on GNP at different Co loadings and the reference bulk oxide phases (CoO PDF 1541662, Co_3O_4 PDF 1548531)

Laboratory of Materials for Renewable Energy (LMER)
Institute of Chemical Sciences and Engineering (ISIC)
Basic Science Faculty (SB)

84
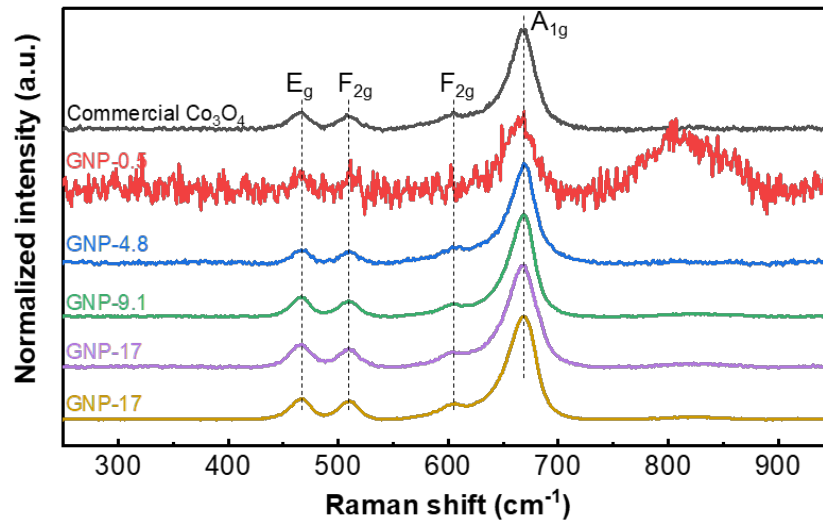
Figure S2.22. Raman spectroscopy including the peaks of Co_3O_4, acquired on Co-catalyst supported on GNP at various Co loadings and on commercial Co_3O_4.

Laboratory of Materials for Renewable Energy (LMER)
Institute of Chemical Sciences and Engineering (ISIC)
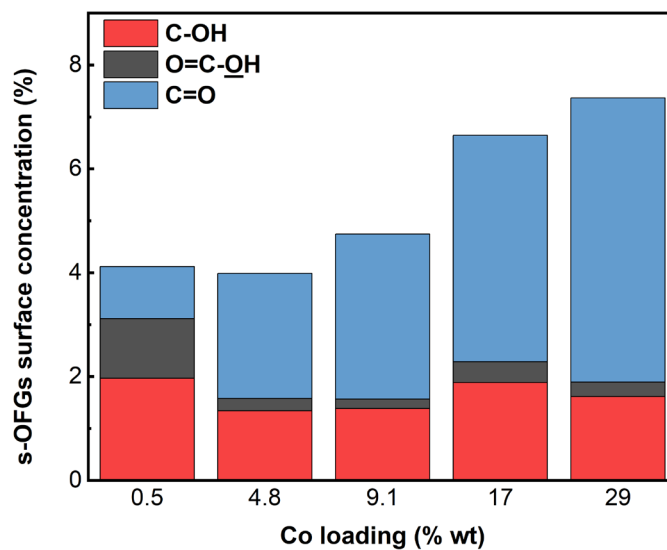Basic Science Faculty (SB)

85

Table S2.8. Summary of I_d/I_g ratio of the Co-based catalysts supported on GNP at different Co loadings, determined with Raman spectroscopy. The presented value was obtained from at least 10 different regions. The gain in I_d/I_g between before and after Co-incorporation is calculated as the quotient between $[I_d/I_{g[Co\text{-doped}]} - I_d/I_{g[fresh\ GNP]}]$ and $[I_d/I_{g[fresh\ GNP]}]$.

Co loading	I_d/I_g	Gain in I_d/I_g (%)
0	0.114 ± 0.023	
0.5	0.148 ± 0.056	29.410
4.8	0.154 ± 0.085	34.586
9.1	0.141 ± 0.034	23.434
17	0.140 ± 0.023	22.065
29	0.154 ± 0.051	34.250

Laboratory of Materials for Renewable Energy (LMER)
Institute of Chemical Sciences and Engineering (ISIC)
Basic Science Faculty (SB)

86

Figure S2.23. XPS spectra of different Co-catalyst supported on GNP, at various Co loadings. a) XPS O 1s spectra and b) XPS C 1s spectra and the corresponding deconvoluted peaks.

Laboratory of Materials for Renewable Energy (LMER)
Institute of Chemical Sciences and Engineering (ISIC)
Basic Science Faculty (SB)

87
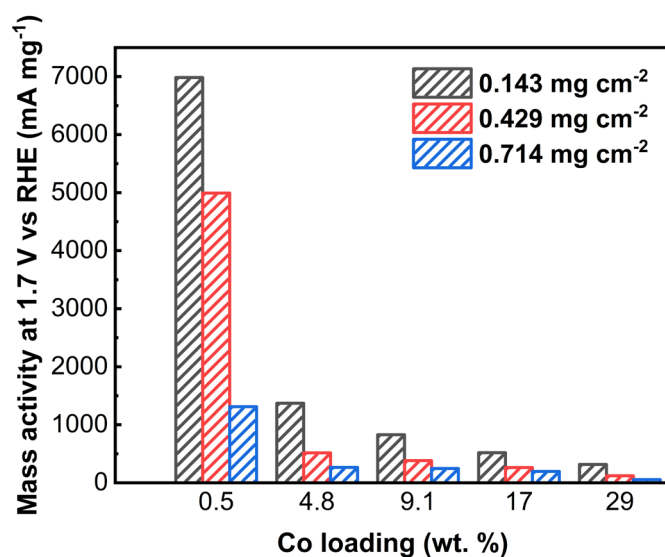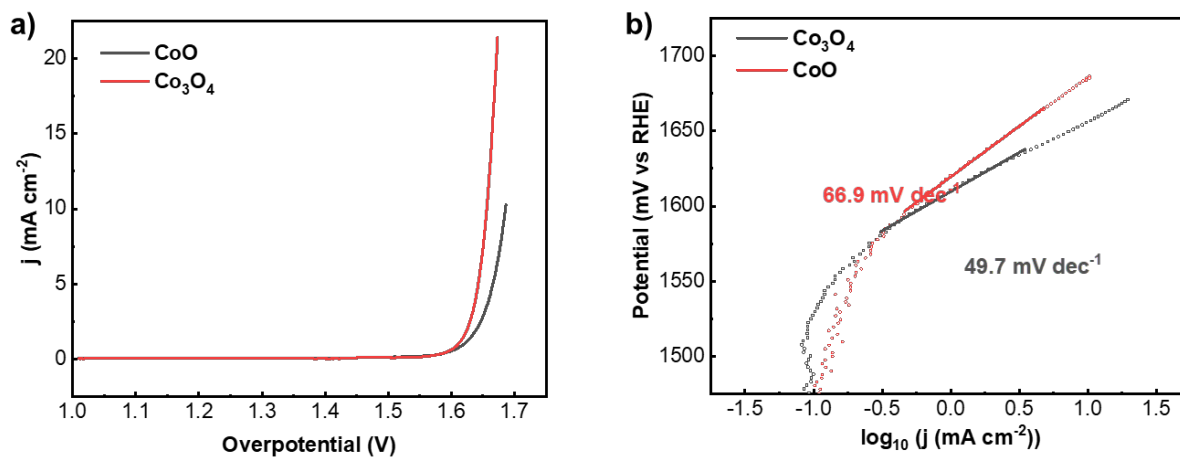
Figure S2.24. Surface concentration of COH, COOH and C=O, measured on Co-based catalysts supported on GNP at different Co loadings.

Laboratory of Materials for Renewable Energy (LMER)
Institute of Chemical Sciences and Engineering (ISIC)
Basic Science Faculty (SB)

88

Table S2.9. Summary of the surface concentration of COH, COOH and C=O, measured on Co-based catalysts supported on GNP at different Co loadings.

Co loading (%)	C-OH	O=C-OH	C=O
0.5	1.96	1.15	1.00
4.8	1.34	0.24	2.41
9.1	1.39	0.18	3.18
17	1.89	0.40	4.36
29	1.62	0.28	5.47

Laboratory of Materials for Renewable Energy (LMER)
Institute of Chemical Sciences and Engineering (ISIC)
Basic Science Faculty (SB)

89

Figure S2.25. Summary of the mass activities at 1.7 V vs RHE of GNP-0.5, GNP-4.8, GNP-9.1, GNP-17 and GNP-29 in Fe-free 1M KOH solution, at various surface loadings.

Laboratory of Materials for Renewable Energy (LMER)
Institute of Chemical Sciences and Engineering (ISIC)
Basic Science Faculty (SB)

90

Figure S2.26. OER activity of commercial CoO and Co₃O₄. a) CV in Fe-free KOH 1M, scanned from 1.0 to 1.7 V vs RHE at a scan rate of 10 mV s^{-1}. The curves were corrected with 85% of iR-drop, and averaged from onward and backward scans. b) The corresponding Tafel slopes.

Laboratory of Materials for Renewable Energy (LMER)
Institute of Chemical Sciences and Engineering (ISIC)
Basic Science Faculty (SB)

91

Table S2.10. Summary of the surface concentration of COH, COOH and C=O, measured on Co-based catalysts supported on GNP at different Co loadings, normalized by the Co mass loading of the samples.

Co loading (%)	Co-normalized C-OH (%)	Co-normalized O=C-OH (%)	Co-normalized C=O (%)	Co-normalized I_d/I_g
0.5	3.929	2.305	1.998	0.296
4.8	0.279	0.050	0.502	0.032
9.1	0.152	0.020	0.349	0.016
17	0.111	0.023	0.257	0.008
29	0.056	0.010	0.189	0.005

Laboratory of Materials for Renewable Energy (LMER)
Institute of Chemical Sciences and Engineering (ISIC)
Basic Science Faculty (SB)

92

REFERENCES

[1] P. Kumar, K. Kannimuthu, A. S. Zeraati, S. Roy, X. Wang, X. Wang, S. Samanta, K. A. Miller, M. Molina, D. Trivedi, J. Abed, M. A. Campos Mata, H. Al-Mahayni, J. Baltrusaitis, G. Shimizu, Y. A. Wu, A. Seifitokaldani, E. H. Sargent, P. M. Ajayan, J. Hu, M. G. Kibria, *J. Am. Chem. Soc.* **2023**, *145*, 8052.

[2] R. Lu, D. K. Sam, W. Wang, S. Gong, J. Liu, A. Durairaj, M. Li, X. Lv, *J. Colloid Interface Sci.* **2022**, *613*, 126.

[3] L. Yang, H. Liu, H. Shen, Y. Huang, S. Wang, L. Zheng, D. Cao, *Adv. Funct. Mater.* **2020**, *30*, 1.

[4] A. W. Jensen, G. W. Sievers, K. D. Jensen, J. Quinson, J. A. Arminio-Ravelo, V. Brüser, M. Arenz, M. Escudero-Escribano, *J. Mater. Chem. A* **2020**, *8*, 1066.

[5] P. Jash, P. Srivastava, A. Paul, *Chem. Commun.* **2019**, *55*, 2230.

[6] C. Cai, S. Han, X. Zhang, J. Yu, X. Xiang, J. Yang, L. Qiao, X. Zu, Y. Chen, S. Li, *RSC Adv.* **2022**, *12*, 6205.

[7] J. Huang, J. Chen, T. Yao, J. He, S. Jiang, Z. Sun, Q. Liu, W. Cheng, F. Hu, Y. Jiang, Z. Pan, S. Wei, *Angew. Chemie - Int. Ed.* **2015**, *54*, 8722.

[8] M. Kim, B. Lee, H. Ju, S. W. Lee, J. Kim, *Adv. Mater.* **2019**, *31*, 1.

[9] A. Bähr, H. Petersen, H. Tüysüz, *ChemCatChem* **2021**, *13*, 3824.

[10] Y. R. Hong, S. Mhin, K. M. Kim, W. S. Han, H. Choi, G. Ali, K. Y. Chung, H. J. Lee, S. I. Moon, S. Dutta, S. Sun, Y. G. Jung, T. Song, H. S. Han, *J. Mater. Chem. A* **2019**, *7*, 3592.

Laboratory of Materials for Renewable Energy (LMER)
Institute of Chemical Sciences and Engineering (ISIC)
Basic Science Faculty (SB)

93

CHAPTER 3:
Elucidating the mechanism of Fe incorporation in in situ synthesized Co-Fe oxygen-evolving nanocatalysts

Thi Ha My Pham,[a,b] Tzu-Hsien Shen,[c] Youngdon Ko,[a,b] Liping Zhong,[a,b] Loris Lombardo,[d] Wen Luo,[e] Satoshi Horike,[d] Vasiliki Tileli,[c,*] Andreas Züttel[a,b]

[a]Laboratory of Materials for Renewable Energy (LMER), Institute of Chemical Sciences and Engineering (ISIC), Basic Science Faculty (SB), École Polytechnique Fédérale de Lausanne (EPFL) Valais/Wallis, Energypolis, CH-1951 Sion, Switzerland

[b]Empa Materials Science & Technology, CH-8600 Dübendorf, Switzerland

[c]Institute of Materials, Ecole Polytechnique Fédérale de Lausanne (EPFL), CH-1015 Lausanne, Switzerland

[d]Department of Chemistry, Graduate School of Science, Kyoto University, Kitashirakawa-Oiwakecho, Sakyo-ku, Kyoto 606-8502, Japan

[e]School of Environmental and Chemical Engineering, Shanghai University, 99 Shangda Road, Shanghai 200444, China
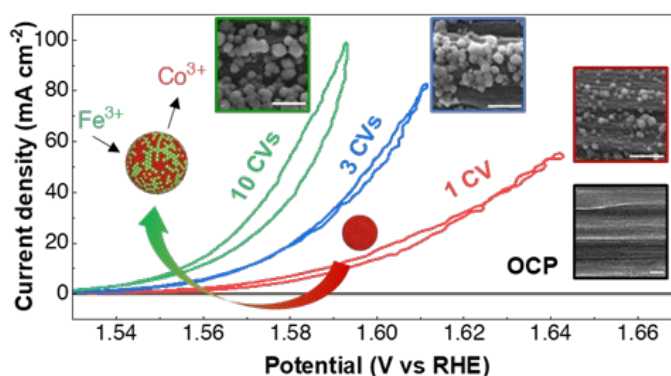
*Corresponding author: vasiliki.tileli@epfl.ch

Edit: caption numbers of figures, tables, and equations were edited to match the thesis chapter number, and typos have been corrected according to the examiner's comments.

Summary: OER highly-active CoFe nanocatalysts was formed by anodic deposition of a Co mixed oxides host-structure, followed by continuous incorporation of Fe. The Fe was incorporated by replacement of Fe^{3+} onto the Co^{3+} sites, reducing the transition potential of the Co-Fe catalyst to the OER-active phase of CoO_2.

Laboratory of Materials for Renewable Energy (LMER)
Institute of Chemical Sciences and Engineering (ISIC)
Basic Science Faculty (SB)

94

Abstract

Ni- and Co-based catalysts with Fe as a dopant demonstrate promising activity in the oxygen evolution reaction (OER) during alkaline water electrolysis, with the presence of Fe in a certain quantity being crucial for their enhanced performance. The mode of incorporation, local placement, and structure of Fe ions in the host catalyst, as well as their direct/indirect contribution to enhancing the OER activity, remain under active investigation. Herein, the mechanism of Fe incorporation into a Co-based host was investigated using an in situ synthesized Co-Fe catalyst in an alkaline electrolyte containing Co^{2+} and Fe^{3+}. Fe was found to be uniformly incorporated as a dopant element rather than as a separate phase, which occurs solely after the anodic deposition of the Co host structure, and results in exceptional OER activity with an overpotential of 319 mV at 10 mA cm^{-2} and a Tafel slope of 28.3 mV dec^{-1}. Studies on lattice structure, chemical oxidation states, and mass changes indicated that Fe is doped into the Co host structure by replacing the Co^{3+} sites with Fe^{3+} from the electrolyte. Operando Raman measurements revealed that the presence of doped Fe in the Co host structure reduces the transition potential of the in situ Co-Fe catalyst to the OER-active phase of CoO_2. The findings of our facile synthesis of highly active and stable Co-Fe particle catalysts provide a comprehensive understanding of the role of Fe doping in Co-based electrocatalysts, covering aspects that include the incorporation mode, local structure, placement, and their mechanistic role in enhancing OER activity.

Laboratory of Materials for Renewable Energy (LMER)
Institute of Chemical Sciences and Engineering (ISIC)
Basic Science Faculty (SB)

95

1   Introduction

In alkaline water electrolysis, the oxygen evolution reaction (OER) is the sluggish multistep reaction involving four electrons that results in a considerable anode activation polarization. First-row transition metals such as Ni and Co have been demonstrated as promising candidates due to their low-cost, abundance, and high OER catalytic activity in alkaline conditions[1–4]. The presence of Fe in the structure has been reported to play a crucial role in enhancing the OER activity of Ni-based and Co-based catalysts, regardless of their structure, for example $Ba_{0.5}Sr_{0.5}Co_{0.2}Fe_{0.2}O_{3-\delta}$ (BSCF) of the perovskite family[5], $Co_{3-x}Fe_xO_4$ with spinel structure[6], or $Ni_{0.75}Fe_{0.25}OOH$[7] and $Co_{0.46}Fe_{0.54}OOH$[8] of the layer-structure type catalysts.

Extensive research has been conducted on the mechanism of Fe incorporation into Ni- and Co-based catalysts and its role in enhancing the OER activity. Conventionally, Fe is intentionally doped in the Ni-and Co-catalysts during the synthesis step by adjusting the composition of the precursor solution for wet-chemical routes[9,10], or that of the electrolyte bath for electrodeposition[8,11]. Trotochaud et al. utilized grazing-incident X-ray diffraction (GIXRD) patterns to confirm that the cathodically deposited $Ni_{0.75}Fe_{0.25}(OH)_2$ aged thin films in commercial KOH has a layered double hydroxide structure of Ni-Fe fougèrites[12]. These minerals featured an extended c-axis compared to β-$Ni(OH)_2$. The lattice change was attributed to the substitution of Ni^{2+} ions by Fe^{3+}, resulting in an increased concentration of intercalated anions. Furthermore, Friebel et al., using operando X-ray absorption spectroscopy (XAS), found that Fe^{3+} cations do not intercalate between the γ-NiOOH sheets at Fe concentrations inferior to 25%[7]. Instead, they tend to replace Ni^{3+} within a sheet due to the shorter Fe-O bond length in $Ni_{1-x}Fe_xOOH$ compared to γ-FeOOH and similar to that of Ni-O. Computational calculations also indicated that Fe is the active site in $Ni_{1-x}Fe_xOOH$ since it exhibits stronger adsorption of the OER intermediates compared to Ni. For the Co-Fe system, Burke et al. have demonstrated that CoOOH provides an electrically conductive and stable host for the OER-active but poorly conductive FeOOH[8].

Recently, an electrochemical approach using cyclic voltammetry (CV) in a Fe-containing electrolyte has been reported as an efficient way for doping the Ni- and Co-based catalysts with Fe[13,14]. Compared to the cathodic co-deposition of the bulk Ni-Fe or Co-Fe catalyst, the incorporation of Fe directly via the OER alkaline electrolyte is usually referred as incidental doping or Fe-spiking. For this doping method, many studies have agreed that the presence of Fe in the catalyst structure is an irreversible process, as confirmed by Fe detection in the final catalyst. Deng et al. have shown, using operando atomic force microscopy (AFM), that exfoliated $Ni(OH)_2$ transforms into NiOOH nanoparticles with a high surface area upon anodic oxidation, with FeOOH deposited as a separate phase in this porous structure[15]. For Co-based catalysts spiked with Fe, Zhang et al. have demonstrated that intentional Fe incorporation has a stronger interaction with the CoOOH sheet compared to incidental Fe ions, which mainly localize at the edge of the hexagonal sheet and do not incorporate into the bulk structure, by analyzing their electrochemical profile[16]. However, the lattice-scale structural modifications of the Ni- and Co-based catalysts induced by Fe have not been "visualized", and the role of Fe in enhancing OER activity remains elusive.

Here, we first synthesized a Co-Fe catalyst directly on top of the carbon rotating-disk electrode (RDE) by electrochemical cycling in a KOH electrolyte containing Co^{2+} and Fe^{3+} (in situ Co-Fe catalyst). This in situ

Laboratory of Materials for Renewable Energy (LMER)
Institute of Chemical Sciences and Engineering (ISIC)
Basic Science Faculty (SB)

96

synthesis enables the characterization of catalysts in their most natural state without the need for a polymer binder, which could potentially diminish surface hydrophilicity, hindering the electrolyte's access to the catalyst or the release of oxygen. Moreover, it offers valuable insights into the preparation of nanostructures without the need of an additional exfoliation process[15] or the use of organic agents[17], holding potential for applications in operando nanoscale characterizations TEM or AFM. In comparison to the highly inert bare glassy carbon, the in situ deposited Co-Fe catalyst exhibits an overpotential at 10 mA cm^{-2} of 319 mV and a Tafel slope of 28.3 mV dec^{-1}. The electron microscopy and X-ray spectroscopy measurements reveal that the deposited Co-Fe catalyst has a Co-based host-structure with slightly larger lattice spacing compared to the deposited Co catalyst, induced by the Fe^{3+} substitution onto Co^{3+} sites. Moreover, operando optical spectroscopy and quartz-crystal microbalance measurements demonstrate that the substituted Fe^{3+} cations reduce the transition potential from the CoOOH phase to the OER-active CoO_2 phase.

2 Methodology

2.1 Preparation of the electrolyte

The electrolyte was diluted from potassium hydroxide 50% (KOH, Carl Roth) with deionized water, in order to obtain a 1 M KOH solution. To remove Fe contamination from the commercial KOH[7,12,14], the electrolyte was treated with nickel(II) hydroxide ($Ni(OH)_2$, Fluka). 1 g of $Ni(OH)_2$ was added to 1 L of 1 M KOH and the solution was stirred overnight. After sedimentation of $Ni(OH)_2$, the top solution was decanted and filtered through filter paper (Cytiva).

Neutral and acidic electrolytes were also prepared at a concentration of 1 M from potassium nitrate (KNO_3, Alfa Aesar) and nitric acid 65% (HNO_3, Sigma-Aldrich), respectively.

Different nitrate salts were prepared for addition to the treated KOH electrolyte. Cobalt(II) nitrate hexahydrate ($Co(NO_3)_2.6H_2O$, Sigma-Aldrich), iron(III) nitrate nonahydrate ($Fe(NO_3)_3.9H_2O$, Sigma-Aldrich), copper(II) nitrate trihydrate ($Cu(NO_3)_2.3H_2O$, Sigma-Aldrich), nickel(II) nitrate hexahydrate ($Ni(NO_3)_2.6H_2O$, Sigma-Aldrich) and silver nitrate ($AgNO_3$, Sigma-Aldrich) were prepared as 0.05 M solutions.

2.2 Preparation of the electrode

For the activity test, the glassy carbon - rotating disk electrode (GC-RDE) was polished with sandpaper of two different grit numbers, first with P500 and then with P1000 (VSM). After being rinsed thoroughly, the GC-RDE was polished again with 0.05 μm polishing alumina suspension (BASi) on a polishing cloth (MicroCloth, Buehler). The RDE was rinsed again with Milli-Q grade water and dried in air. The reference was a Ag/AgCl electrode, and the counter electrode was a Pt spring. Before use, the Pt counter electrode was soaked in HNO_3 25% and then a blowtorch flame applied to remove all contaminants or depositions from previous electrochemical reactions. Reference catalysts (IrO$_2$||C and RuO$_2$||C) were prepared by adding 10 mg of oxide catalysts (IrO$_2$ (Sigma-Aldrich), or RuO$_2$ (Sigma-Aldrich)), 15 mg of carbon black (Vulcan XC 72R, Fuel Cell Store) and 40 μL of Nafion (Nafion 117 containing solution, Sigma-Aldrich) into 1 mL

Laboratory of Materials for Renewable Energy (LMER)
Institute of Chemical Sciences and Engineering (ISIC)
Basic Science Faculty (SB)

97

of isopropanol. The mixture was then sonicated and drop-casted onto the GC-RDE with a surface loading of 0.3 mg cm^{-2} of oxide catalyst, 0.45 mg cm^{-2} of carbon black, and 0.06 mg cm^{-2} of Nafion.

For surface characterization, glassy carbon plates (Sigradur, HTW) and carbon papers (Toray, Alfa Aesar and Sigracet 29 AA, FuelCellStore) were used. The electrochemical measurements were performed in an H-cell which was composed of two compartments separated by a Nafion membrane. The working electrode was positioned close to the magnetic bar to reduce the effect of mass transport.

2.3   Electrochemical characterization

A potentiostat (Metrohm Autolab PGSTAT204) was used for electrochemical measurements. Cyclic voltammetry (CV) was performed with the conventional three-electrode chemical set-up in 1 M KOH, with a pH of 14. We noted that interaction between Co- and Ni-based catalysts and Fe contamination in commercial KOH was previously reported in many works[7,12,14]. Thus, to avoid crossover-effects created by the added $Co(NO_3)_2.6H_2O$ and the Fe in KOH solution, the KOH used in this work, denoted as Fe-free KOH, was treated with $Ni(OH)_2$. After treatment, the amount of Fe in commercial KOH was reduced from 55 ppb to 5 ppb (Table S3.1).

Next, the potential was swept from 1.0 to 1.7 V, then back to 1.0 V, vs RHE with a scan rate of 10 mV s^{-1}. A rotating disk electrode system (RRDE-3A, ALS) was used to thoroughly degas the electrode surface during the CV cycle. The rotating speed of the RDE was fixed at 1600 revolutions per minute (rpm).

The electrochemically active surface area (ECSA) was estimated by performing CV cycles in a non-faradaic region over an interval of 100 mV at 9 scan rates: 10, 25, 50, 75, 100, 150, 200, 300 and 400 mV s^{-1}. The charging current, i_c, is related to the scan rate, θ, following the equation:

$$i_c = C_{dl} \times \theta$$

The ECSA is proportional to the double layer capacitance, C_{dl}, by C_s^{-1}, in which C_s is the specific capacitance of the sample.

$$ECSA = C_{dl} \times C_s^{-1}$$

The typical value of C_s of a metal electrode in NaOH is reported to be 0.040 mF cm^{-2}[1,18]. The unit of ECSA is cm^2.

2.4   Materials characterization

Scanning electron microscopy (SEM) images and corresponding energy dispersive X-ray spectroscopy (EDX) elemental mapping were acquired on a ThermoFisher Teneo FE-SEM. High-resolution transmission electron microscopy (HR-TEM) images, high angle annular dark field (HAADF) images and the corresponding EDX maps were obtained with a ThermoFisher Tecnai Osiris 200kV TEM. Selected area electron diffraction (SAED) analyses were performed on a JEOL 2200FS 200 kV TEM. Electron energy-loss spectroscopy (EELS) characterizations were performed on Titan Themis TEM (ThermoFisher Scientific, USA) equipped with post column GIF Quantum ERS EELS spectrometer (Gatan, USA). The

Laboratory of Materials for Renewable Energy (LMER)
Institute of Chemical Sciences and Engineering (ISIC)
Basic Science Faculty (SB)   98

microscopy conditions for EELS acquisition were 300 kV, with a probe current 0.07 nA, under scanning TEM mode. The convergent and collection angles for EELS acquisition were 20 mrad and 19.8 mrad, respectively. Energy resolution of the EELS data is determined by full width half maximum of the zero-loss peak with the value 1.1 eV using the dispersion condition 0.1 eVch^{-1}. Spectrum-Imaging (SI) was applied with the pixel time set at 0.1s. DualEELS were performed for all the EELS acquisitions. Both low-loss and core-loss range were acquired to align zero-loss peak position in the SI datasets and deconvolve plural scattering in the core-loss spectra using Gatan Microscopy Suite (GMS).

X-ray diffraction (XRD) spectra were acquired with a Bruker D8 Advance system using Cu Kα (λ = 1.54 Å) radiation. Inductively coupled plasma optical emission spectrometry (ICP-OES) was performed with an Agilent 5110 instrument.

X-ray photoelectron spectroscopy was performed in an ultrahigh vacuum (UHV) spectrometer equipped with a VSW Class WA hemispherical electron analyzer. A Mg Kα X-ray source (1253.6 eV) was used as incident radiation beam. The high-resolution spectroscopy was conducted with a constant pass energy of 22eV, while survey scan was collected with a pass energy of 90eV. The deconvolution of Co 2p and Fe 2p spectra was completed with CasaXPS software, while the attribution of binding energy to a specific metal phase was based on previous literatures[19–21].

Operando Raman spectroscopy was performed with our home-built Raman cell, also composed of three conventional electrodes. A glassy carbon plate was used as the working electrode for the electrochemical measurements. An immersion objective (Leica, 63x) was used to send an incident beam and collect the scattered beam. Acquisition for low wavenumbers from 300 to 1200 cm^{-1} used a blue light with a wavelength of 457 nm, and that for high wavenumbers between 3000 and 4000 cm^{-1} used a red light of 633 nm. A constant potential between 1.1 and 1.7 V vs RHE was applied and held for 2 minutes before launching the Raman acquisition.

Operando electrochemical quartz-crystal microbalance (EQCM) measurements were performed with QCM922A (Seiko EG&G). Toray carbon paper was ground and mixed with isopropanol and Nafion, then drop-cast onto a Pt-quartz electrode. Ag/AgCl and Pt wire were used as the reference and counter electrodes, respectively. The standard resonance frequency of the Pt-quartz oscillator is 8.99 ± 0.03 MHz.

3   Results & Discussion

3.1   In situ synthesis of CoFe-based catalysts on carbon electrode and their characterization

The in situ synthesis of the CoFe-based catalysts, schematically demonstrated in Figure 3.1a, was performed in a RDE system. Co-Fe catalysts were precipitated on carbon electrodes by performing cyclic voltammetry (CV) in an alkaline solution of 1M KOH with 0.5 mM Co(NO$_3$)$_2$.6H$_2$O and 0.2 mM Fe(NO$_3$)$_3$.9H$_2$O (labeled as KOH-CoFe). The electrochemical cycling was done between 1.0 and 1.7 V vs RHE at a scan rate of 10 mV s^{-1} for 10 cycles, where an increase in OER current density was observed from the 1st to the 10th cycle (Figure 3.1b). Compared to the fresh glassy carbon (GC) electrode, deposition of Co-Fe catalyst was clearly observed after 10 CV cycles as shown in the photographs of the electrodes in Figure 3.1b. We note that

Laboratory of Materials for Renewable Energy (LMER)   99
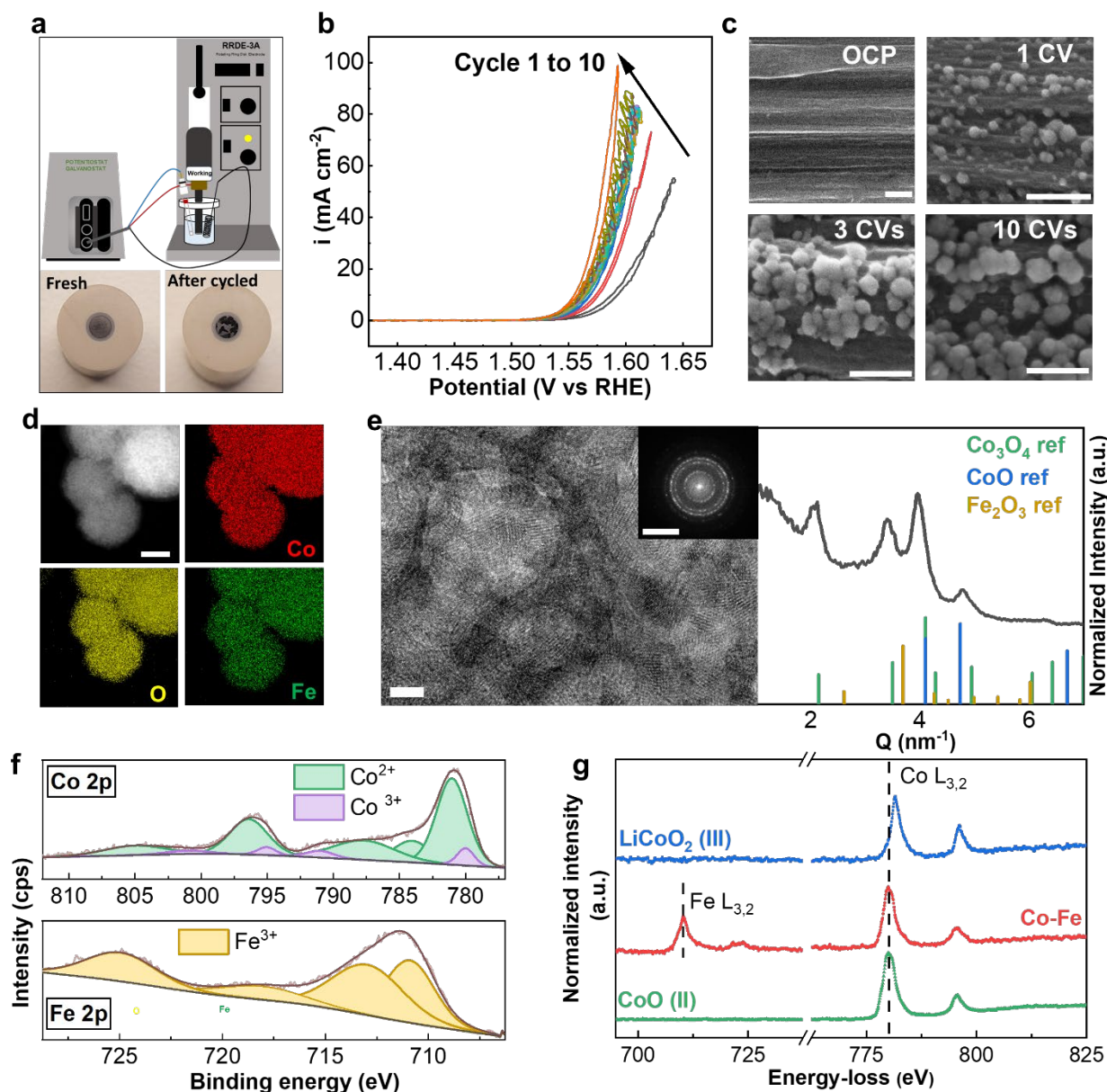Institute of Chemical Sciences and Engineering (ISIC)
Basic Science Faculty (SB)

similar catalyst deposition could be performed on various carbon paper supports (Figure S3.1). The surface of the carbon paper during the deposition process was investigated using SEM imaging. From a bare surface at open circuit potential (OCP, shown in Figure S3.2), spherical Co-Fe nanoparticles were formed after the first cycle (Figure 3.1c). The average size of these spherical catalysts was measured and found to be approximately 40 nm (Figures S3.3 and S3.4). From the 3rd to the 10th cycle, the newly-formed Co-Fe particles increased both in size and population, as also demonstrated by the size distribution analysis in Figures S3.3-S3.4. After 10 cycles, the carbon surface was almost fully covered by these Co-Fe particles (Figure 3.1c). Control experiments showed that Co-Fe catalysts with similar morphology were also deposited by applying a constant current density (chronopotentiometry (CP) at a current of 20 mA cm^{-2}) as shown in Figure S3.5, indicating that the in situ synthesis is an anodic deposition process. Unlike other transition metals such as Cu, Fe, Ag and Ni, which do not show deposition upon application of anodic potential and consequently do not exhibit enhanced OER activity (Figure S3.6), the Co-based catalyst was the only one showing notable OER activity. When synthesizing by cycling the Co-catalyst alongside with other transition metals in KOH-CoCu, KOH-CoAg, KOH-CoNi and KOH CoFe, we observed a decrease in overpotential at 10 mA cm^{-2} and a change in Tafel slope only when using KOH-CoFe (Figure 3.1 and Figure S3.7). Additionally, no enhanced OER activity was observed when the GC electrode was cycled in KOH-NiFe, under similar experimental conditions as KOH-CoFe (Figure S3.8). This suggests that the CoFe-catalyst, deposited in situ, shows excellent OER activity, and is particularly interesting for understanding the effects of Fe incorporation in this structure.

We further investigated the influence of pH on in situ synthesis of the CoFe-based catalysts through CP activation in acidic and neutral environments. A constant current density of 20 mA cm^{-2} was first applied for 600 seconds on the GC electrode in KNO$_3$-CoFe, followed by 10 CV cycles in 1M Fe-free KOH. No activity enhancement was observed for the neutral solution (Figure S3.9a). Correspondingly, no particle deposition (or other change) was noticed on the carbon surface after the activation in neutral medium, except for the residual salt (Figure S3.9b). An activation process in 1 M HNO$_3$, similarly, did not modify the OER activity of the GC electrode (Figure S3.10), demonstrating that the deposition occurs only in alkaline solution.

The chemical composition and elemental distribution of the Co-Fe catalysts obtained from the deposited layer on carbon paper were further investigated using STEM-EDX. Within a single Co-Fe catalyst particle, as shown in the HAADF-STEM image in Figure 3.1d, the EDX elemental maps reveal a homogeneous distribution of Co and Fe. STEM-EDX quantification indicates an overall 29 at% of Fe in the Co-Fe catalyst particle. We also note that the content of Fe in the Co-Fe catalyst particles can be adjusted by changing the concentration of Fe^{3+} in the electrolyte (Figure S3.11). The X-ray diffraction (XRD) analysis of the Co-Fe catalyst did not exhibit any characteristic peaks corresponding to Co or Fe-based phases. Instead, only graphite-related features were observed, which can be attributed to the significant thickness of the carbon support material (Figure S3.12). As a result, the crystal structure of the Co-Fe catalyst was examined by analyzing the micro-diffraction pattern obtained through electron diffraction in TEM. Figure 3.1e depicts a high resolution bright-field TEM image of the Co-Fe catalyst after 10 CVs. The corresponding fast Fourier transform (FFT) pattern of Co-Fe catalysts shows features of polycrystalline phases CoO and Co$_3$O$_4$ (Figure

Laboratory of Materials for Renewable Energy (LMER)
Institute of Chemical Sciences and Engineering (ISIC)
Basic Science Faculty (SB)

100

3.1e), and no additional peaks associated with Fe-rich phase are detected. Rotational average intensity of the selected area electron diffraction (SAED) pattern shows that the Co-Fe catalysts are predominantly composed of polycrystalline CoO, Co_3O_4 and amorphous $CoFeO_x$ (Figure S3.13). We note that the peak corresponding to Co_3O_4 at 2.15 nm^{-1} was insignificant in the SAED patterns of the in situ Co-Fe catalyst but clearly observable in those of the Co catalyst (Figure S3.14), suggesting a weaker presence of Co^{3+} in the Co-Fe structure.

Moreover, XPS spectra indicate that Co in the Co-Fe catalyst is predominantly in a mixed oxidation state of Co^{2+} and Co^{3+}, with Co^{2+} being the major component[19,20], while Fe is in the Fe^{3+} oxidation state[21] (Figure 3.1f). Co $L_{3,2}$ edge EEL spectra of the in situ Co-Fe catalysts are shown in Figure 3.1g. The Co $L_{3,2}$ peak position matches the EELS of CoO (II) reference, indicating that the valence of Co is predominantly +2 in the Co-Fe-based catalyst. The contribution of the +3 oxidation state with respect to the $LiCoO_2$ (III) reference was almost unnoticeable for the Co-Fe catalyst in the EEL spectrum. To conclude, the in situ Co-Fe catalyst is composed of amorphous $CoFeO_x$ and polycrystalline CoO and Co_3O_4 with mixed Co oxidation states (predominantly +2).

Laboratory of Materials for Renewable Energy (LMER)
Institute of Chemical Sciences and Engineering (ISIC)
Basic Science Faculty (SB)

101

Figure 3.1. a, Schematic of rotating disk electrode (RDE) setup. **b,** Evolution of the polarization curves of glassy carbon electrode during 10 CV cycles in KOH-CoFe. The scan rate is 10 mV s^{-1} and the iR was corrected at 85 %. **c,** SEM images of the carbon paper at OCP, and after 1, 3, 10 cycles of CV in KOH-CoFe. Scale bar: 500 nm. **d,** HAADF-STEM image of in situ Co-Fe catalyst (after 10 CVs) and the corresponding elemental maps of Co and Fe. Scale bar: 50 nm **e,** BF-HRTEM image of the in situ Co-Fe catalyst (after 10 CVs), scale bar: 5 nm. Inset: corresponding FFT pattern, scale bar: 5 nm^{-1}. Right: corresponding rotational average intensity. **f,** XPS spectra for Co 2p and Fe 2p of in situ Co-Fe after 100 CVs (extended cycling is needed to collect sufficient signal from the catalyst layer). **g,** EEL spectra for Co L$_{3,2}$ and Fe L$_{3,2}$ of the in situ Co-Fe after 10 CVs. The spectra of CoO (II) and LiCoO$_2$ (III) references are also shown.

3.2 Identifying the structural phase of Fe in the Co-Fe catalyst

To better understand the structural form of Co and Fe in the Co-Fe catalyst, we performed identical in situ synthesis separately in 1 M KOH + Co^{2+} (denoted as KOH-Co), or in 1 M KOH + Fe^{3+} (denoted as KOH-Fe) on GC electrodes. Interestingly, only the GC electrode cycled in KOH-Co showed an enhancement of OER current after 10 CV cycles (Figure 3.2a). The GC electrode cycled in KOH-Fe showed no activity

Laboratory of Materials for Renewable Energy (LMER)
Institute of Chemical Sciences and Engineering (ISIC)
Basic Science Faculty (SB)

102

enhancement compared to that cycled in Fe-free KOH. SEM images of the GC electrode showed that there was anodic deposition of Co particles after cycling in KOH-Co electrolyte (Figure S3.15a), while no deposition occurred in KOH-Fe electrolyte (Figure S3.15b). These results reveal that the anodic deposition takes place only with the presence of Co^{2+} in the electrolyte, and there is no deposited Fe-based phase in Fe^{3+}-containing electrolyte. It suggests that the in situ Co-Fe catalyst has a Co host-structure, and Fe^{3+} incorporation occurs solely after the anodic deposition of Co host-phase.

To this point, the route by which Fe is doped into the host-structure remains unclear, whether it forms a separate second phase on the deposited scaffold or exists as a solid solution. Additionally, the specific location of Fe within the host-structure is yet to be determined. With electrochemical QCM, we first evaluated the change in mass of the GC electrode by CV in KOH-Co and KOH-Fe electrolytes, in sequence. When a current density of 25 mA cm^{-2} was applied to the carbon electrode in KOH-Co, we observed a gain in mass of the electrode corresponding to the anodic deposition of Co (Figure 3.2b). The potential recorded was 1.59 V vs RHE in KOH-Co. The electrode was then immersed in KOH-Fe and the same geometric current density was applied. In KOH-Fe, the recorded potential dropped from 1.59 V vs RHE in KOH-Co to 1.50 V vs RHE in KOH-Fe, confirming again the positive effect of Fe incorporation in enhancing OER activity of Co catalyst. Interestingly, there was no change in the mass of the deposited Co catalyst, indicating that no additional anodic deposition or insertion of an Fe-based phase onto the Co-host structure occurred during cycling in KOH-Fe. The experimental design, along with the electrochemical quartz crystal microbalance (QCM), suggests that Fe is incorporated into the Co host-structure by replacing Fe at specific Co sites. Furthermore, the concentrations of Co^{2+} in the KOH-Fe solution were measured after performing cyclic voltammetry (CV) or anodic constant potential (CP) experiments (Table S3.2). Following 10 CV cycles of the in situ Co in KOH-Fe, the Co^{2+} concentration in the KOH-Fe electrolyte rose from 15 ppb to 65 ppb, demonstrating that Co is being released from the deposited catalyst into the solution. Similarly, after subjecting the in situ Co catalyst in KOH-Fe to 30 minutes of CP at 25 mA cm^{-2}, we observed an increase in the Co^{2+} concentration in the KOH-Fe electrolyte from 20 to 50 ppb. The change in Co^{2+} concentration in KOH-Fe following CV and anodic constant potential CP can be attributed to the leaching of Co from the deposited Co-catalyst. These results provide additional evidence supporting the hypothesis of Fe-to-Co exchange.

Additionally, we compared the structure of Co and Co-Fe particles to further understand the specific location of Fe in the Co-Fe catalysts. The FFT pattern shows that the reflections of Co catalysts are similar to the ones in the Co-Fe catalysts (Figure S3.14) with mixed Co oxide phases that include amorphous CoO_x and crystalline phases of rock salt CoO and spinel Co_3O_4. Bright-field TEM images show that both catalysts exhibit spherical morphology (Figure 3.2c). HR-TEM images and the corresponding FFT patterns of the catalysts are shown in Figure S3.16. The crystal structure of Co-Fe catalysts resembles that of the Co-catalysts, as suggested by the reflections in the FFT patterns occurring at similar spatial frequency (Figure 3.2d). However, when overlapping the rotational average intensity of the two FFT patterns, we observed a slight shift of every peak to smaller Q-value, indicating a larger lattice parameter of approximately 3% in the case of Co-Fe (Table S3.3). The alteration in the lattice constant suggests the formation of a uniform solid solution consisting of Fe incorporated within the deposited Co-catalysts. Additionally, at a particle

Laboratory of Materials for Renewable Energy (LMER)
Institute of Chemical Sciences and Engineering (ISIC)
Basic Science Faculty (SB)

103

level, we observed that the average size of Co-Fe spheres was larger than that of Co spheres following an equivalent number of cycles (Figures S3.3-3.4,3.17-3.18). This observation aligns with the prior discovery made through operando AFM, which revealed a significant increase in particle height with the incorporation of Fe[15]. Deconvolution of XPS spectra reveals that the ratios of Co^{2+} to Co^{3+} in in situ Co and Co-Fe catalysts are 4.83 and 8.62 respectively, meaning that there is less Co^{3+} in the Co-Fe catalyst (Figure 3.2e). This indicates that Fe^{3+} replaces Co^{3+} in the mixed oxide structure, therefore lowering the numbers of Co^{3+} site. No shift in the main peaks of Co 2p was observed, suggesting that no change in coordination of Co sites takes place upon addition of Fe. In the EEL spectra, despite the +2 oxidation state in both catalysts, the Co $L_{3,2}$ fine structure of Co-Fe particles differs slightly from pure Co particles, as shown in Figure 3.2f. This is attributed to the modification of the electronic structure due to Fe incorporation in the cobalt host structure.
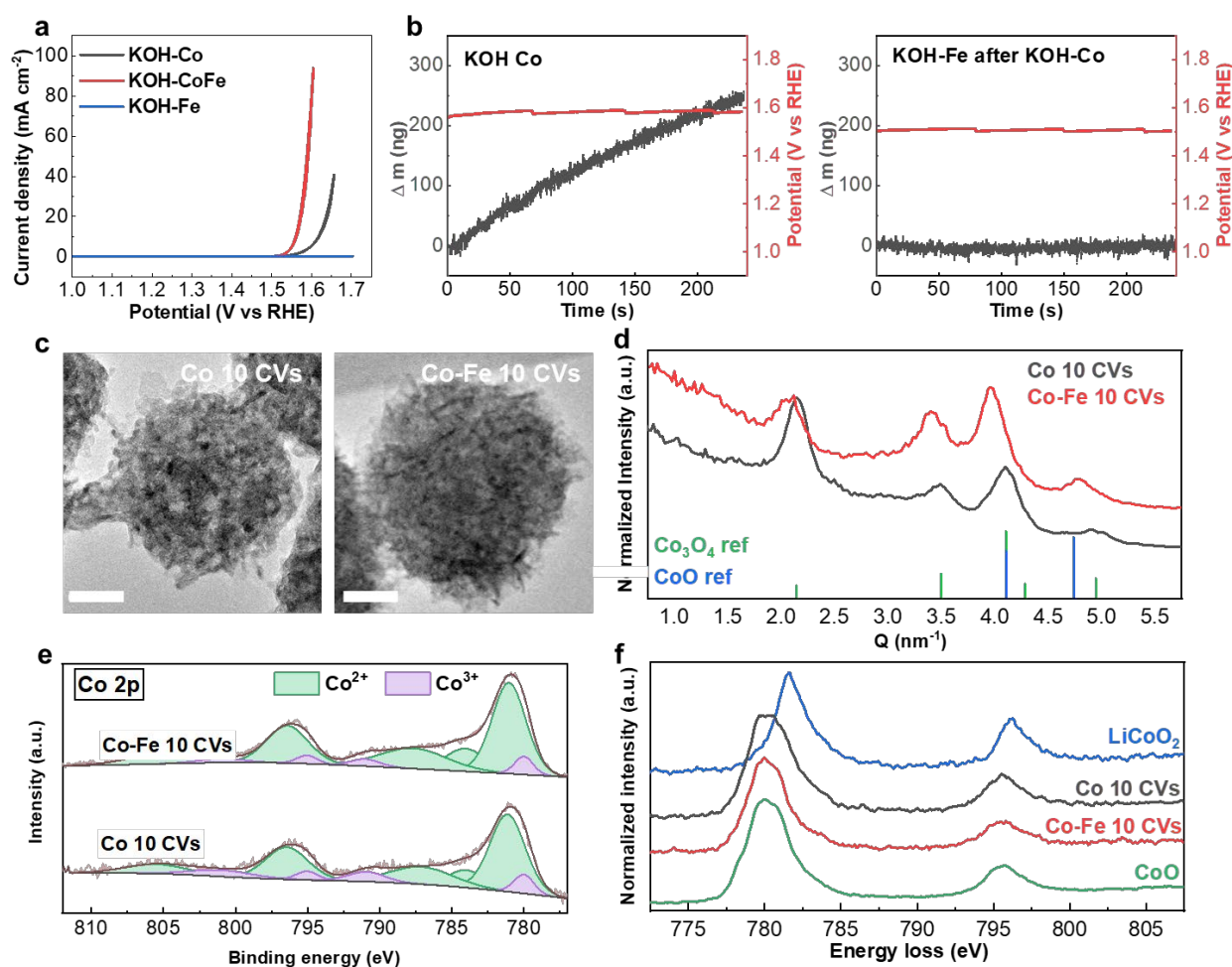
Figure 3.2. Comparison of in situ Co and Co-Fe catalysts. **a,** CV curves of the in situ CoFe, in situ Co catalysts, and glassy carbon cycled in KOH-Fe. The 10th cycle is plotted, with 85 % of iR correction. The scan rate is 10 mV s^{-1}. **b,** Mass gain recorded during anodic polarization of carbon electrode in KOH-CO, at a current density of 25 mA cm^{-2}. After that, no change in mass was observed during anodic polarization of the electrodeposited Co in KOH-Fe, at a current density of 25 mA cm^{-2}. **c,** TEM images of in situ Co and in situ Co-Fe catalyst formed after 10 CVs in KOH-Co and KOH-CoFe respectively. Scale bar 20 nm. **d,** Integrated intensity of the FFT pattern of in situ Co and in situ Co-Fe after 10 CVs (corresponding HR-TEM images in Figure S3.14). **e,** XPS spectra for Co 2p of in situ Co-Fe and in situ Co catalysts formed after 100 CVs (extended cycling is needed to collect sufficient signal from the catalyst layer), with the corresponding peak deconvolution to Co^{2+} and Co^{3+}. **f,** EEL spectra for Co $L_{3,2}$ of the in situ Co and Co-Fe catalysts after10 CVs. The spectra of CoO (II) and LiCoO$_2$ (III) references are also shown.

Laboratory of Materials for Renewable Energy (LMER)
Institute of Chemical Sciences and Engineering (ISIC)
Basic Science Faculty (SB)

104

3.3 OER activity and stability of Co-Fe catalysts

Next, the OER activity of the in situ Co-Fe catalyst was evaluated (Figure 3.3a). The in situ synthesis was considered to be complete after 10 CV cycles, with full coverage of the carbon surface by the deposited Co-Fe catalyst (Figure 3.1c). The bare GC cycled in Fe-free KOH showed that it was inactive for OER with only 0.23 mA cm^{-2} at 1.7 V vs RHE. Compared to the bare carbon surface, the in situ Co-Fe catalyst showed an overpotential at 10 mA cm^{-2} of 319 mV. Correspondingly, the Tafel slope dropped from 306 mV dec^{-1} for bare carbon to 28.3 mV dec^{-1} for the Co-Fe catalyst. The values were averaged from 10 sets of measurements, as summarized in Table S3.4. A variation range of ±10% for both the overpotential at 10 mA cm^{-2} and the Tafel slope emphasizes the high repeatability of our in situ synthesis method. The evolution of the OER activity of the in situ Co-Fe catalyst over 50 CV cycles at a scan rate of 10 mV s^{-1} is shown in Figures S3.19 and S3.20. The two kinetic parameters reached their stable value range after only 10 cycles, and they remained relatively stable from 10 cycles onwards: between 315 and 328 mV for the overpotential at 10 mA cm^{-2} and between 28 and 32 mV dec^{-1} for the Tafel slope. Therefore, we emphasize the rapidity and practicality of the proposed in situ synthesis method to produce an OER-active catalyst.

The ECSA measurements of the in situ Co-Fe catalyst were performed after 10 CV cycles. The cycles at different scan rates in the non-faradaic region showed that the double layer capacitance rose from 0.011 to 0.269 mF, corresponding to an increase of ECSA from 0.28 to 6.7 cm^2 after only 10 CVs in KOH-CoFe, as shown in Figure 3.3b. To further evaluate the influence of Fe/Co ratio on the OER activity, we gradually increased the concentration of Fe^{3+} and fixed the concentration of Co^{2+} at 0.5 mM (Figure S3.21). The content of Fe quantified by EDX represented as a function of the concentration of Fe^{3+} precursor followed a linear relationship with a slope of 1.03 (Figure S3.11). This demonstrated that, with our in situ synthesis method, the content of Fe can be easily tuned by adjusting the ratio of Co^{2+} to Fe^{3+} in the KOH-CoFe solution. Figure 3.3c showed that both the overpotential at 10 mA cm^{-2} and the Tafel slope changed depending on the amount of Fe in the in situ synthesized Co-Fe catalyst. The two parameters followed an inversed volcano shape where the lowest values were obtained at an Fe^{3+} concentration of 0.2 mM, corresponding to approximately 28.6 at% in the CoFe mixture (a trend obtained from 2 sets of measurements, Figure S3.22). This reverse volcano shape is very similar to previous findings for Ni-Fe bimetallic catalysts, in which the Ni-Fe film was prepared by cathodic electrodeposition in a mixed salt bath[7,22].

The stability of the in situ Co-Fe catalyst was also evaluated in the same electrolyte where in situ synthesis occurs. The in situ Co-Fe catalyst was first formed with 10 CV cycles in KOH-CoFe with a scan rate of 10 mA s^{-1}, then underwent an accelerated stability test at a scan rate of 400 mA s^{-1}. After 2000 accelerated CV cycles, the change of overpotential at 10 mA cm^{-2} was only 3 mV, from 313 to 310 mV, and the Tafel slope showed an increase 0.1 mV dec^{-1} (Figure 3.3d). Even though the CV curve remains stable after 2000 accelerated cycles, we observed a change in size and distribution of the catalyst. Both the average size and the size distribution increased with the number of cycles, indicating a continuous nucleation of new particles, in parallel with the growth of the previously formed particles (Figures S3.3-3.4). The ECSA, on the other hand, primarily undergoes changes between the 1st and 10th cycle, with negligible evolution observed within the stability test range from the 10th to the 2000th cycle (Figure S3.23). The marginal 3 mV decrease of the overpotential agrees with the slight increase in ECSA between the 10th and 2000th cycle, which

Laboratory of Materials for Renewable Energy (LMER)
Institute of Chemical Sciences and Engineering (ISIC)
Basic Science Faculty (SB)

105

enhances the overall OER activity. In summary, the stability in OER activity can be assigned to the full geometrical coverage and the dynamic nucleation and growth of the in situ Co-Fe catalyst.
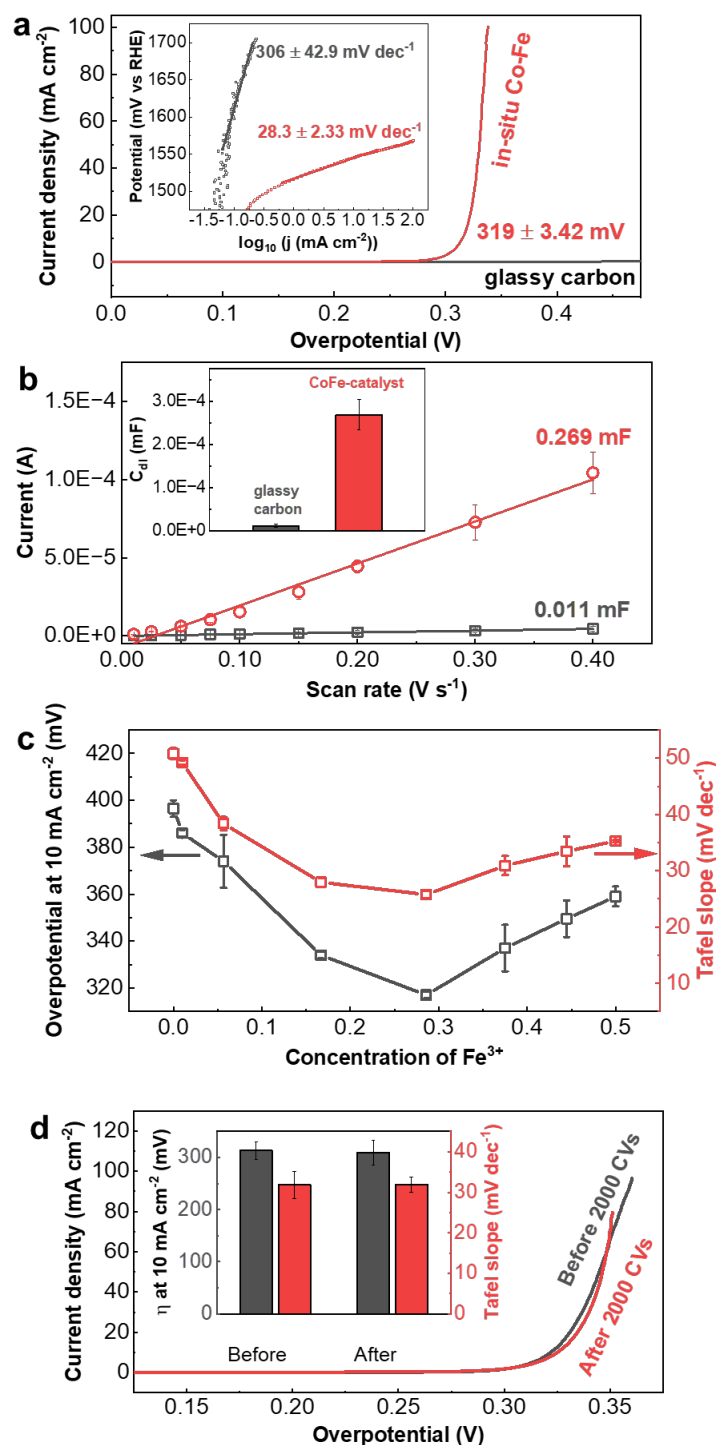

Figure 3.3. Activity for OER of the in situ synthesized Co- and CoFe-based catalysts. **a,** Cyclic voltammetry (CV) curves of glassy carbon (GC) in Fe-free KOH and in KOH-CoFe after 10 cycles. Inset: Tafel slopes. The scan range of the CVs were 1.0 to 1.7 V vs RHE and the scan rate was 10 mV s^{-1}. The CV curves and Tafel slopes were averaged over 10 individual measurements (Table S3.2). All the CV curves were corrected with 85% of iR-drop. **b,** Electrochemically Active Surface Are (ECSA) of the glassy carbon, in situ Co-Fe catalyst, acquired after 10 CVs in the electrolyte for synthesis. **c,** Overpotential at 10 mA cm^{-2} and Tafel slope as a function of the Fe^{3+} concentration in the electrolyte (mM), obtained from 2 sets of measurements. **d,** Activity for OER before and after 2000 accelerated CVs in KOH-CoFe at 400 mV s^{-1} scan rate. The curve was plotted with CV measurements (10 CVs at 10 mA cm^{-2}) before and after the accelerated stability test.

Laboratory of Materials for Renewable Energy (LMER)
Institute of Chemical Sciences and Engineering (ISIC)
Basic Science Faculty (SB)

106

Similar measurements were performed on the in situ Co catalyst to evaluate its electrochemical performance for OER. We noticed an anodic shift of the Co^{2+}/Co^{3+} redox peak of Co catalyst induced by doped-Fe (Figure S3.24), which was previously assigned to the strong electronic interaction between Co and Fe[8]. The overpotential at 10 mA cm^{-2}, Tafel slope, ECSA and stability of the in situ Co catalyst are presented in Table S3.5 and Figures S3.25-3.29. The Co catalyst exhibits an overpotential at 10 mA cm^{-2} of 395 mV and a Tafel slope of 51.4 mV dec^{-1}, with a stability up to 2000 CV cycles. Its ECSA was 16-fold higher than bare glassy carbon yet only half that of the Co-Fe catalyst. The OER activity of the Co catalyst synthesized by our in situ method was among the best of Co-based compounds[6,14,31,23–30], as presented in Figure S3.30 and Table S3.6.

3.4   Operando characterization of Co-Fe catalyst at anodic polarization

Operando Raman measurements were performed to track the evolution of the surface structure of in situ Co-Fe and Co catalysts, at different applied potentials from 1.1 to 1.7 V vs RHE. In the in situ Co catalyst (Figure S3.31), we observed peaks at 503 and 686 cm^{-1} which have been previously reported to be characteristic for the E_g and A_{1g} vibrational modes of CoOOH[11,23,32,33] (reference for peak positions summarized in Table S3.7). The small peak at 487 cm^{-1} is assigned to the glassy carbon surface, as observed in the Raman spectrum of the bare glassy carbon (Figure S3.32). For the in situ Co-Fe catalyst (Figure 3.4a), the similar phase of Co(Fe)OOH was observed in the entire range of applied potential, with the main peak at 503 cm^{-1} red-shifted to 497 cm^{-1} (Figure 3.4a). We also noticed a broad shoulder ranging from 600 to 700 cm^{-1} in the Co-Fe catalyst, instead of a sharp and intense peak at 686.5 cm^{-1} as observed in pure Co catalyst. The presence of this shoulder and the red shift of the main peak might be induced from a change in electronic structure due to the replacement of doped Fe^{3+} at Co^{3+}sites[34]. Starting from 1.4 and 1.6 V vs RHE for Co-Fe and Co catalysts, respectively, new peaks at 465 and 580 cm^{-1} were observed. Previous studies have assigned these peaks to the E_g and A_{1g} vibrational modes of the OER-active phase CoO_2, prior to OER, which was formed after the redox reaction from Co^{3+} to Co^{4+}, as summarized in Table S3.7[23,33,35,36]. In order to understand the phase transition from CoOOH to the OER-active phase CoO_2 , we deconvoluted the Raman spectra (Figure 3.4a,b for Co-Fe and Co catalysts) and plotted the ratio between their areas in Figure 3.4c. For the in situ Co catalyst, CoOOH is the only surface species from 1.1 to 1.5 V vs RHE, and the phase transition occurs only after 1.5 V vs RHE. In Co-Fe catalyst, the OER-active phase CoO_2 appeared at 1.4 V vs RHE, and the area ratio between OER-active phase CoO_2 and CoOOH increased from 1.4 to 1.7 V vs RHE, indicating that CoOOH is gradually replaced by the OER-active phase CoO_2. This phase transition from CoOOH to OER-active phase CoO_2 was also observed with electrochemical QCM. During the forward scan from 1.4 to 1.7 V vs RHE, we observed a decrease in mass of the Co-Fe catalyst which corresponds to a phase transition, as shown in Figure 3.4d. The change in mass was reversible when the potential was scanned backwards from 1.7 to 1.4 V vs RHE. This transition was observed only between 1.55 and 1.7 V vs RHE in in situ Co catalyst (Figure S3.33). At the potential range where the OER-active phase CoO_2 was present, we also observed an increase in noise, which can be attributed to the generation of oxygen bubbles on the surface. The potential of transition from CoOOH to OER-active phase CoO_2 identified by EQCM match those determined by operando Raman spectroscopy (red for CoOOH and green for OER-active phase

Laboratory of Materials for Renewable Energy (LMER)
Institute of Chemical Sciences and Engineering (ISIC)
Basic Science Faculty (SB)

107

CoO$_2$ in Figure 3.4d). Therefore, operando Raman spectroscopy and electrochemical QCM demonstrated that the formation of OER-active phase CoO$_2$ takes place at 1.4 V vs RHE in Co-Fe catalyst and at 1.6 V vs RHE in Co catalyst.
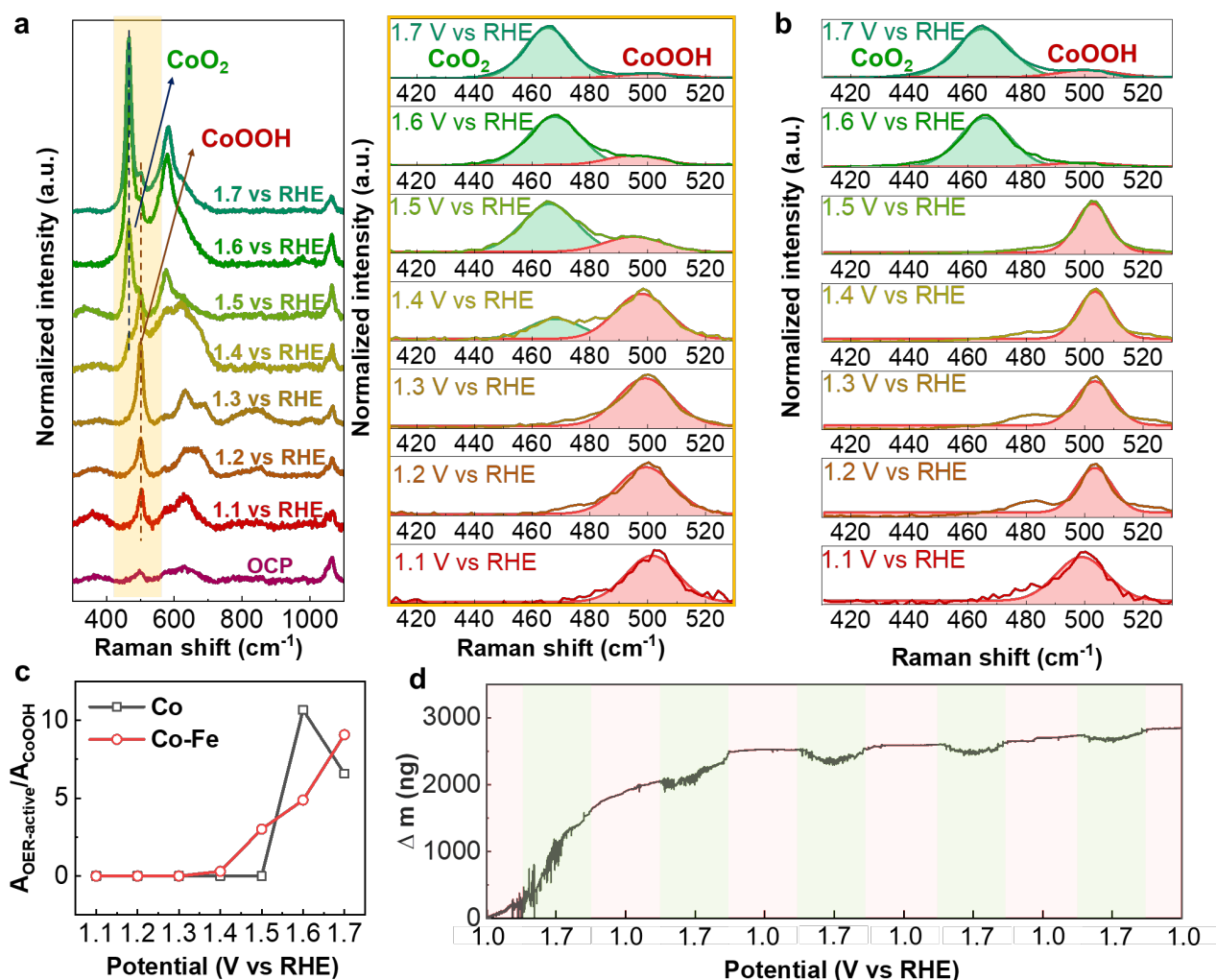
Figure 3.4. Tracking the catalyst evolution during OER. **a,** Operando Raman measurements acquired on in situ Co-Fe catalysts at different applied potential and the corresponding spectra deconvolution from 410 to 530 cm^{-1}. Each spectrum was acquired 60s after the application of the potential. **b,** Operando Raman spectra of in situ Co catalyst and its deconvolution. **c,** Ratio of the area of OER-active phase CoO$_2$ to that of CoOOH for in situ Co-Fe and Co, determined with Raman spectra deconvolution. **d,** Change in mass of in situ Co-Fe catalyst over 5 CVs. The drop of mass occurred when the potential went up from 1.4 to 1.7 then down to 1.4 vs RHE. The red and green colors correspond to the phases plotted in (a).

With Raman spectroscopy, we further investigated the hydroxyl stretching mode located between 3000 and 4000 cm^{-1} for in situ Co-Fe and Co catalysts (Figures S3.34 and S3.35). The broad peak between 3100 and 3700 cm^{-1} was deconvoluted to three peaks. The first two peaks at low Raman shift were assigned to the two stretching vibrational modes of the OH band[37], and the third peak at the highest shift to the M-OH bond[38,39]. We observed a blue shift in the M-OH peak of Co-Fe compared to the pure Co catalyst at all applied potentials, indicating that the M-OH bond is stronger in Co-Fe than Co (Figure S3.36). According to the volcano plot of the intrinsic activity as a function of M-OH bond strength proposed by Morales-Guio

Laboratory of Materials for Renewable Energy (LMER)
Institute of Chemical Sciences and Engineering (ISIC)
Basic Science Faculty (SB)

108

et al., the CoO_x is on the left branch while the FeO_x is on the right branch[40]. For OER, since OH^- adsorption is necessary in each single step, it must bind sufficiently strong to the metal to reach low overpotential[41]. However, when the OH^- adsorption is too strong, the oxygenated species cannot be desorbed from the surface, leading to high overpotential[42]. Thus, an intermediate M-OH bond strength is optimal for OER catalytic activity. In our in situ Co-Fe catalyst, the substitution of Fe^{3+} at Co^{3+} site helps increase the OH^- adsorption strength of Co, bringing the M-OH bond strength closer to the optimal value corresponding to the top of the volcano plot.

3.5 Incorporation mechanism and role of Fe in in situ Co-Fe catalyst

Based on the observations discussed in Section 3.2, it can be inferred that Fe^{3+} ions replace Co^{3+} ions within the Co-rich lattice, indicating a homogeneous Fe doping through Fe-to-Co exchange rather than the formation of a separate phase. Therefore, the in situ synthesized Co-Fe catalyst can be defined as a Co-based structure that is uniformly doped with Fe through Fe-to-Co exchange. The catalyst retains the primary characteristics of anodically deposited Co oxides, with a slightly enlarged lattice plane due to the incorporation of Fe.

By examining the electrochemical characteristics of the Co and Co-Fe catalyst, it it possible to predict the specific placement of Fe within the Co-host structure. Previous studies of Fe-spiked NiOOH have shown that the incorporation of Fe at the edge of the NiOOH sheet was reflected in an increase in activity without any change in the redox properties of the host phase. Upon cycling, the anodic shift in the redox peak suggests a gradual incorporation of Fe from the edge or defect sites into the bulk structure[13]. During the cycling process in KOH-Co, we observed a gradual improvement in OER activity (Figure 3.5a), which can be attributed to the anodic deposition of the Co-catalyst. At the same time, the area underneath the redox peak at -185 mV, corresponding to the $Co^{2+/3+}$ redox wave[16], also increased, indicating a higher amount of deposited Co-catalyst (Figure S3.37). The position of this peak remained unchanged throughout the process. Subsequently, when the deposited Co-catalyst (10 CVs anodic deposition) was cycled in KOH-Fe, we noticed an increase in activity and an anodic shift of the redox peak by 25 mV, occurring spontaneously after the first cycle. This observation suggests an immediate incorporation of Fe into the bulk of the Co-host structure rather than at the edges. Throughout 10 CVs in KOH-Fe, both the OER activity (Figure 3.5a) and the redox peak (Figure S3.37) remained unchanged, indicating that the Fe remained stable within the bulk structure and there was no gradual evolution in its specific location during cycling. Based on the above discussion, we conclude that the in situ synthesis of the Co-Fe catalyst from an alkaline electrolyte containing Co^{2+} and Fe^{3+} ions involves a continuous process of Co deposition and Fe substitution onto the bulk Co host-structure. During the 1st cycle, Co^{2+} is anodically deposited onto the carbon support to form a Co oxide host structure. This deposited structure is composed of amorphous CoO_x, with crystalline nanoparticles of Co_3O_4 and CoO. After this 1st cycle, Fe^{3+} in the electrolyte is incorporated into the bulk structure of deposited Co oxides via substitution into a solid solution where Co^{3+} sites in the Co oxides host-structure are replaced by Fe^{3+}. With increased number of CV cycles, Co^{2+} continues to deposit, resulting in nucleation of new Co oxide nanoparticles on available carbon surface and growth in size of previously

Laboratory of Materials for Renewable Energy (LMER)
Institute of Chemical Sciences and Engineering (ISIC)
Basic Science Faculty (SB)

109

formed Co mixed-oxide nanoparticles. Simultaneously, Fe^{3+} keeps substituting Co^{3+} in the deposited Co-based host-structure to form the final structure of Co-Fe catalyst with uniform Fe distribution in the Co host-structure with larger lattice spacing (Figure 3.5a).

The resulting in situ Co-Fe catalyst is highly active for OER due to an increase in both intrinsic and extrinsic activities. The enhanced extrinsic activity can be assigned to the increased ECSA of the in situ Co-Fe catalyst, compared to that of in situ Co catalyst. With the presence of doped-Fe in the Co-based structure, the ECSA was boosted by a factor of two (Figure S3.28). The enhanced intrinsic activity with Fe-doping is revealed by the lower Tafel slope of Co-Fe catalyst in ECSA-normalized current density (Figure S3.38). Indeed, operando Raman spectra and QCM data support the fact that incorporation of Fe^{3+} in the mixed Co oxides reduces the formation potential for OER-active phase CoO_2 (Figure 3.5a), resulting to an enhancement of the intrinsic activity of the Co-Fe catalyst.

Figure 3.5b presents the overpotential at 10 mA cm^{-2} and the Tafel of previously reported CoFe-based compounds and our in situ Co-Fe catalyst[5,6,44–50,8,14,24,25,27,28,30,43].The in situ catalyst synthesized herein outperforms a wide range of other CoFe-based catalysts and was among the best with other Co-Fe oxy-hydroxides. Thus, with a simple method of adding Co^{2+} and Fe^{3+} into the electrolyte, we directly synthesized an in situ Fe-doped Co-based catalyst on glassy carbon RDE, with high intrinsic catalytic performance and high active surface area.
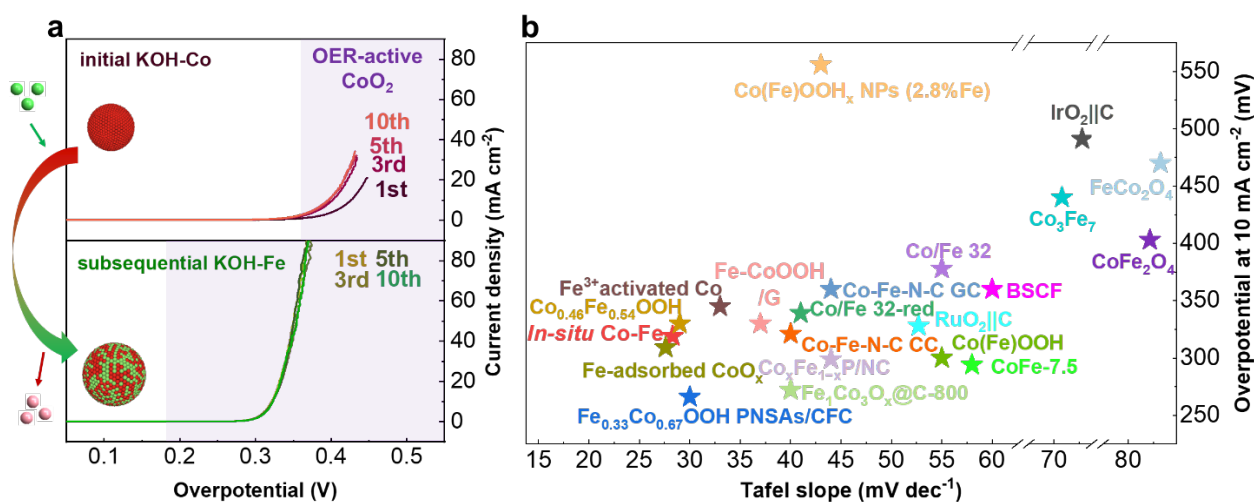
Figure 3.5. a, Schematic of the proposed Fe^{3+} substituted on Co^{3+} site for enhanced OER activity in in situ Co-Fe catalyst. **b,** Activity for OER of the in situ Co-Fe catalyst compared with other reported CoFe-based catalyst. The details of the catalysts and electrolyte are summarized in Table S3.8.

4   Conclusions

In conclusion, we have demonstrated the mechanism of Fe incorporation onto a Co host-structure via the in situ synthesis of a highly active Fe-doped Co-based catalyst for OER. The in situ Co-Fe catalyst comprises of a Fe solid solution phase within a Co host-phase that is formed via anodic electrodeposition of Co^{2+} from the electrolyte. The Co base phase is composed of crystalline Co_3O_4, crystalline CoO and amorphous CoO_x, and exhibited an overpotential at 10 mA cm^{-2} of 395 mV and a Tafel slope of 54.1 mV dec^{-1}. Our

Laboratory of Materials for Renewable Energy (LMER)   110
Institute of Chemical Sciences and Engineering (ISIC)
Basic Science Faculty (SB)

investigation reveals that the incorporation of Fe into the host structure occurred through the substitution of Fe^{3+} ions at Co^{3+} sites within the mixed Co oxides. This conclusion is supported by our analysis of the lattice structure and oxidation states of the Co-Fe catalyst, as well as by in situ electrochemical QCM measurements carried out using a specific experimental design. The Fe-doped Co catalyst further enhanced the activity for OER: the overpotential at 10 mA cm^{-2} and the Tafel slope were reduced to 319 mV and 28.3 mV dec^{-1}, respectively. This is due to the strengthened metal-OH bond in the Co base phase and increased electrochemically active surface area resulting from the doped Fe. In addition to providing valuable insights into the mechanism and impact of Fe incorporation on enhancing the OER activity of Co-based catalysts, our research emphasizes the significance of in situ synthesis, which enables the characterization of the catalyst in its most natural state. This approach can be extended to other operando characterizations of Co-Fe-based electrocatalysts, opening up possibilities for further exploration and understanding in this field.

Acknowledgements

Author Information Notes

Corresponding author: *Vasiliki Tileli

Email: vasiliki.tileli@epfl.ch

Note: The authors declare no competing financial interests.

References

[1]   C. C. L. McCrory, S. Jung, J. C. Peters, T. F. Jaramillo, *J. Am. Chem. Soc.* **2013**, *135*, 16977.

[2]   C. Wei, R. R. Rao, J. Peng, B. Huang, I. E. L. Stephens, M. Risch, Z. J. Xu, Y. Shao-Horn, *Adv. Mater.* **2019**, *31*, 1.

[3]   M. Gong, H. Dai, *Nano Res.* **2014**, *8*, 23.

[4]   E. Fabbri, T. J. Schmidt, *ACS Catal.* **2018**, *8*, 9765.

[5]   J. Suntivich, K. J. May, H. A. Gasteiger, J. B. Goodenough, Y. Shao-Horn, *Science (80-.).* **2011**, *334*, 1383.

[6]   X. Gao, J. Liu, Y. Sun, X. Wang, Z. Geng, F. Shi, X. Wang, W. Zhang, S. Feng, Y. Wang, K. Huang, *Inorg. Chem. Front.* **2019**, *6*, 3295.

[7]   D. Friebel, M. W. Louie, M. Bajdich, K. E. Sanwald, Y. Cai, A. M. Wise, M. J. Cheng, D. Sokaras, T. C. Weng, R. Alonso-Mori, R. C. Davis, J. R. Bargar, J. K. Nørskov, A. Nilsson, A. T. Bell, *J. Am. Chem. Soc.* **2015**, *137*, 1305.

[8]   M. S. Burke, M. G. Kast, L. Trotochaud, A. M. Smith, S. W. Boettcher, *J. Am. Chem. Soc.* **2015**, *137*, 3638.
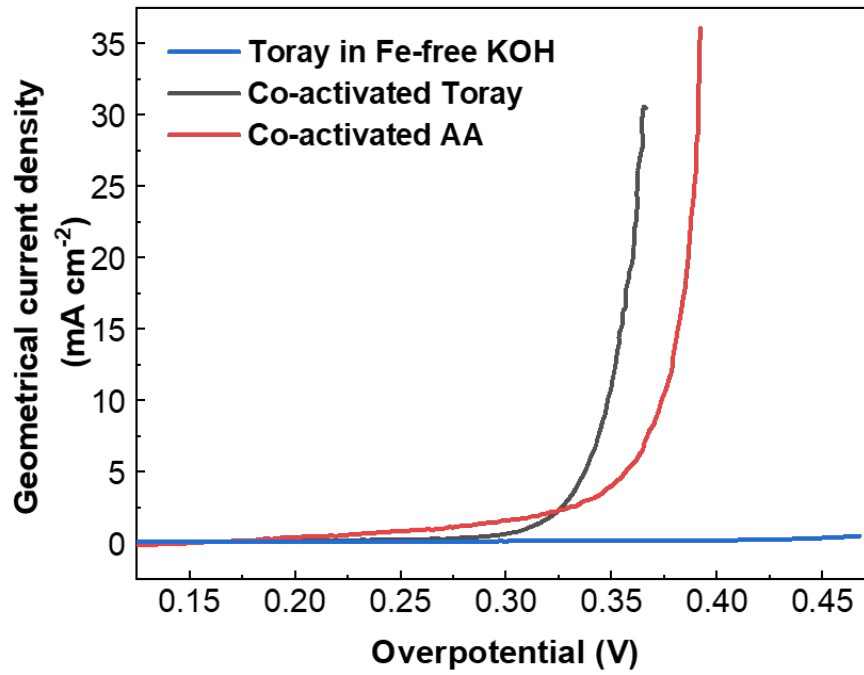
Laboratory of Materials for Renewable Energy (LMER)
Institute of Chemical Sciences and Engineering (ISIC)
Basic Science Faculty (SB)

111

[9]   S. Jung, C. C. L. McCrory, I. M. Ferrer, J. C. Peters, T. F. Jaramillo, *J. Mater. Chem. A* **2016**, *4*, 3068.

[10]   W. H. Lee, M. H. Han, Y. J. Ko, B. K. Min, K. H. Chae, H. S. Oh, *Nat. Commun.* **2022**, *13*, 1.

[11]   B. S. Yeo, A. T. Bell, *J. Am. Chem. Soc.* **2011**, *133*, 5587.

[12]   L. Trotochaud, S. L. Young, J. K. Ranney, S. W. Boettcher, *J. Am. Chem. Soc.* **2014**, *136*, 6744.

[13]   M. B. Stevens, C. D. M. Trang, L. J. Enman, J. Deng, S. W. Boettcher, *J. Am. Chem. Soc.* **2017**, *139*, 11361.

[14]   L. Bai, C.-S. Hsu, D. T. L. Alexander, H. M. Chen, X. Hu, *J. Am. Chem. Soc.* **2019**, *141*, 14190.

[15]   J. Deng, M. R. Nellist, M. B. Stevens, C. Dette, Y. Wang, S. W. Boettcher, *Nano Lett.* **2017**, *17*, 6922.

[16]   T. Zhang, M. R. Nellist, L. J. Enman, J. Xiang, S. W. Boettcher, *ChemSusChem* **2019**, *12*, 2015.

[17]   J. T. Mefford, A. R. Akbashev, M. Kang, C. L. Bentley, W. E. Gent, H. D. Deng, D. H. Alsem, Y. S. Yu, N. J. Salmon, D. A. Shapiro, P. R. Unwin, W. C. Chueh, *Nature* **2021**, *593*, 67.

[18]   S. Jung, C. C. L. McCrory, I. M. Ferrer, J. C. Peters, T. F. Jaramillo, *J. Mater. Chem. A* **2016**, *4*, 3068.

[19]   L. Zhong, M. Barreau, D. Chen, V. Caps, M. Haevecker, D. Teschner, D. H. Simonne, E. Borfecchia, W. Baaziz, B. Šmíd, S. Zafeiratos, *Appl. Catal. B Environ.* **2021**, *297*, DOI 10.1016/j.apcatb.2021.120397.

[20]   L. Zhong, M. Barreau, V. Caps, V. Papaefthimiou, M. Haevecker, D. Teschner, W. Baaziz, E. Borfecchia, L. Braglia, S. Zafeiratos, *ACS Catal.* **2021**, *11*, 5369.

[21]   H. Yu, Y. Wang, C. Zhu, Y. Jing, Q. Song, C. Guan, C.-F. Du, H. Yu, Y. Wang, Y. Jing, Q. Song, C. Du, C. Zhu, C. Guan, *Adv. Mater. Interfaces* **2021**, *8*, 2001310.

[22]   M. W. Louie, A. T. Bell, *J. Am. Chem. Soc.* **2013**, *135*, 12329.

[23]   A. Moysiadou, S. Lee, C. S. Hsu, H. M. Chen, X. Hu, *J. Am. Chem. Soc.* **2020**, *142*, 11901.

[24]   X. Cheng, B. J. Kim, E. Fabbri, T. J. Schmidt, *ACS Appl. Mater. Interfaces* **2019**, *11*, 34787.

[25]   E. Budiyanto, M. Yu, M. Chen, S. Debeer, O. Rüdiger, H. Tüysüz, *ACS Appl. Energy Mater.* **2020**, *3*, 8583.

[26]   Y. Liang, Y. Li, H. Wang, J. Zhou, J. Wang, T. Regier, H. Dai, *Nat. Mater.* **2011**, *10*, 780.

[27]   J. Meng, Z. Cui, X. Yang, S. Zhu, Z. Li, K. Qi, L. Zheng, Y. Liang, *J. Catal.* **2018**, *365*, 227.

[28]   S. H. Ye, Z. X. Shi, J. X. Feng, Y. X. Tong, G. R. Li, *Angew. Chemie - Int. Ed.* **2018**, *57*, 2672.

[29]   C. Alex, S. C. Sarma, S. C. Peter, N. S. John, *ACS Appl. Energy Mater.* **2020**, *3*, 5439.

[30]   L. Bai, C. S. Hsu, D. T. L. Alexander, H. M. Chen, X. Hu, *Nat. Energy* **2021**, *6*, 1054.

[31]   F. Song, X. Hu, *Nat. Commun.* **2014**, *5*, 4477.

Laboratory of Materials for Renewable Energy (LMER)
Institute of Chemical Sciences and Engineering (ISIC)
Basic Science Faculty (SB)

112

[32]   S. Ye, J. Wang, J. Hu, Z. Chen, L. Zheng, Y. Fu, Y. Lei, X. Ren, C. He, Q. Zhang, J. Liu, *ACS Catal.* **2021**, *11*, 6104.

[33]   X. Deng, G. Y. Xu, Y. J. Zhang, L. Wang, J. Zhang, J. F. Li, X. Z. Fu, J. L. Luo, *Angew. Chemie - Int. Ed.* **2021**, *60*, 20535.

[34]   J. Li, G. Lu, G. Wu, D. Mao, Y. Guo, Y. Wang, Y. Guo, *RSC Adv.* **2013**, *3*, 12409.

[35]   Z. Chen, L. Cai, X. Yang, C. Kronawitter, L. Guo, S. Shen, B. E. Koel, *ACS Catal.* **2018**, *8*, 1238.

[36]   M. Inaba, Y. Iriyama, Z. Ogumi, Y. Todzuka, A. Tasaka, **1997**, *28*, 613.

[37]   J. Quiño, T. Hellwig, M. Griesing, W. Pauer, H. U. Moritz, S. Will, A. Braeuer, *Int. J. Heat Mass Transf.* **2015**, *89*, 406.

[38]   J.-W. Zhao, C.-F. Li, Z.-X. Shi, J.-L. Guan, G.-R. Li, *Research* **2020**, *2020*, 1.

[39]   R. L. Frost, M. L. Weier, J. T. Kloprogge, *J. Raman Spectrosc.* **2003**, *34*, 760.

[40]   C. G. Morales-Guio, L. Liardet, X. Hu, *J. Am. Chem. Soc.* **2016**, *138*, 8946.

[41]   P. Rüetschi, P. Delahay, *J. Chem. Phys.* **1955**, *23*, 556.

[42]   S. Trasatti, *J. Electroanal. Chem.* **1980**, *111*, 125.

[43]   L. Gong, X. Y. E. Chng, Y. Du, S. Xi, B. S. Yeo, *ACS Catal.* **2017**, *8*, 807.

[44]   X. Han, C. Yu, S. Zhou, C. Zhao, H. Huang, J. Yang, Z. Liu, J. Zhao, J. Qiu, *Adv. Energy Mater.* **2017**, *7*, 1602148.

[45]   M. Harada, F. Kotegawa, M. Kuwa, *ACS Appl. Energy Mater.* **2022**, *5*, 278.

[46]   Z. Sun, A. Curto, J. Rodríguez-Fernández, Z. Wang, A. Parikh, J. Fester, M. Dong, A. Vojvodic, J. V. Lauritsen, *ACS Nano* **2021**, *15*, 18226.

[47]   J. Chen, Y. Zhang, H. Ye, J. Q. Xie, Y. Li, C. Yan, R. Sun, C. P. Wong, *ACS Appl. Energy Mater.* **2019**, *2*, 2734.

[48]   M. Li, Y. Xiong, X. Liu, X. Bo, Y. Zhang, C. Han, L. Guo, *Nanoscale* **2015**, *7*, 8920.

[49]   L. Gong, J. Koh, B. S. Yeo, *ChemSusChem* **2018**, *11*, 3790.

[50]   E. Budiyanto, S. Salamon, Y. Wang, H. Wende, H. Tüysüz, *JACS Au* **2022**, *2*, 697.

Laboratory of Materials for Renewable Energy (LMER)
Institute of Chemical Sciences and Engineering (ISIC)
Basic Science Faculty (SB)

113

5   Supporting Information

Table S3.1. Fe concentration of the commercial and treated KOH, determined by ICP-OES at different wavelengths.

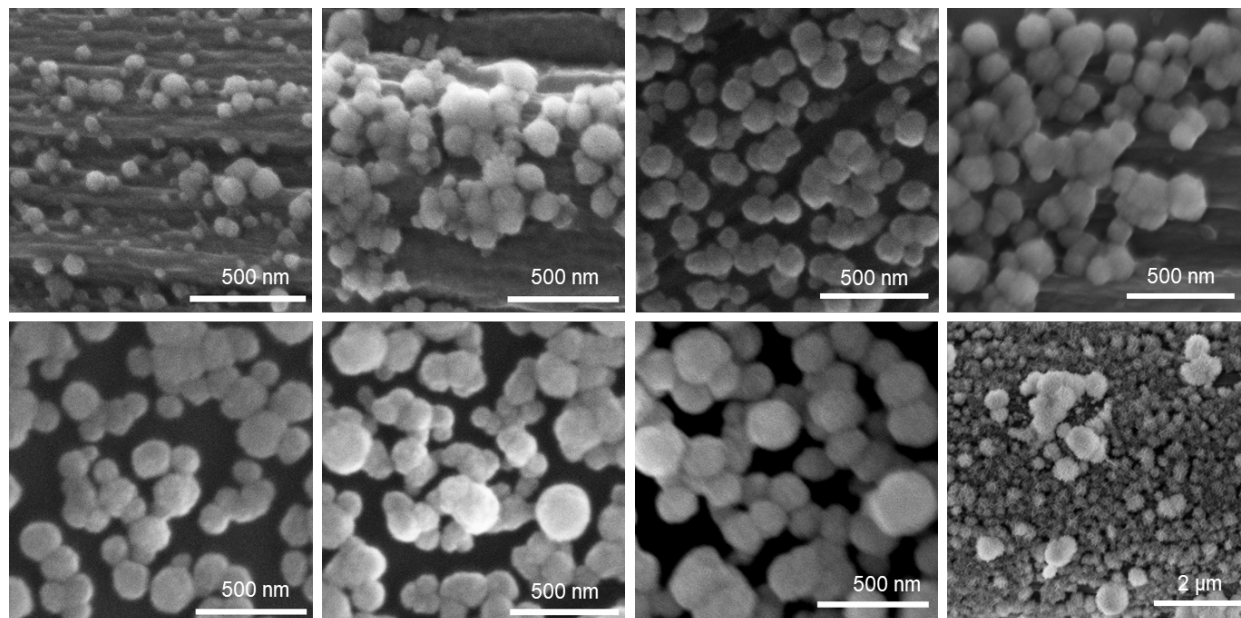|	Fe 234.350 nm (ppm)	Fe 238.204 nm (ppm)	Fe 239.563 nm (ppm)	Fe 259.940 nm (ppm)	Average
Commercial KOH 1 M	0.06	0.06	0.06	0.04	0.055
Treated KOH 1 M	0.00	0.00	0.02	0.00	0.005

Laboratory of Materials for Renewable Energy (LMER)
Institute of Chemical Sciences and Engineering (ISIC)
Basic Science Faculty (SB)

114

Figure S3.1. Geometrical current density as a function of overpotential of two carbon papers Toray and Sigracet 29

AA activated in KOH-Co.

Laboratory of Materials for Renewable Energy (LMER)
Institute of Chemical Sciences and Engineering (ISIC)
Basic Science Faculty (SB)

115
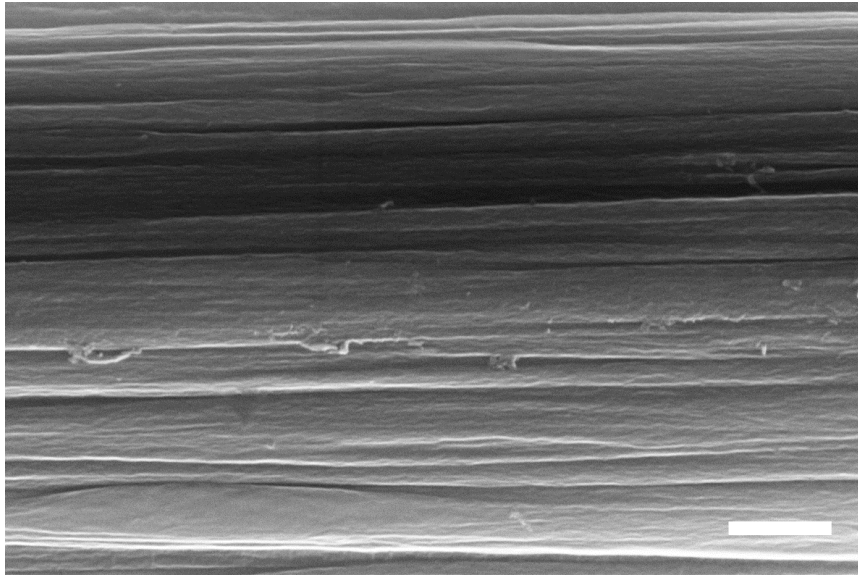
Figure S3.2. SEM image of the carbon paper after 10 CVs in Fe-free KOH. No deposited catalyst has been observed.

Scale bar: 1 μm.

Laboratory of Materials for Renewable Energy (LMER)
Institute of Chemical Sciences and Engineering (ISIC)
Basic Science Faculty (SB)

116

Figure S3.3. SEM images of the spherical particles formed on Toray carbon paper after different number of cycles in KOH-CoFe (from left to right): 1, 5, 10, 30, 50, 100, 300 and 3000 cycles.

Laboratory of Materials for Renewable Energy (LMER)
Institute of Chemical Sciences and Engineering (ISIC)
Basic Science Faculty (SB)

117
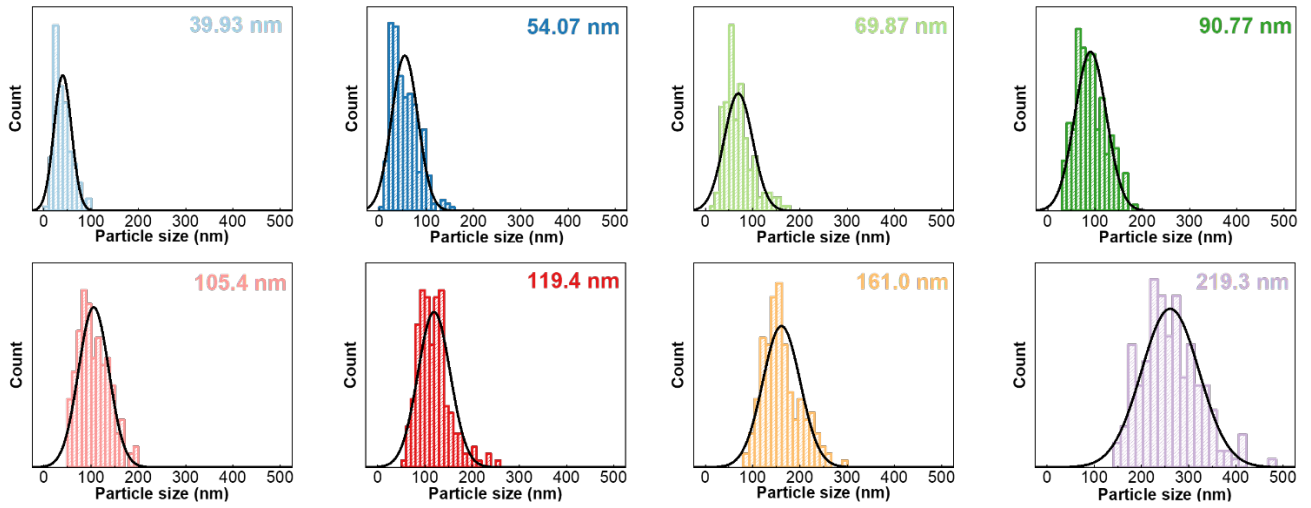
Figure S3.4. Size distribution of the spherical particles formed on Toray carbon paper after different number of cycles in KOH-CoFe (from left to right): 1, 5, 10, 30, 50, 100, 300 and 3000 cycles.

Laboratory of Materials for Renewable Energy (LMER)
Institute of Chemical Sciences and Engineering (ISIC)
Basic Science Faculty (SB)

118
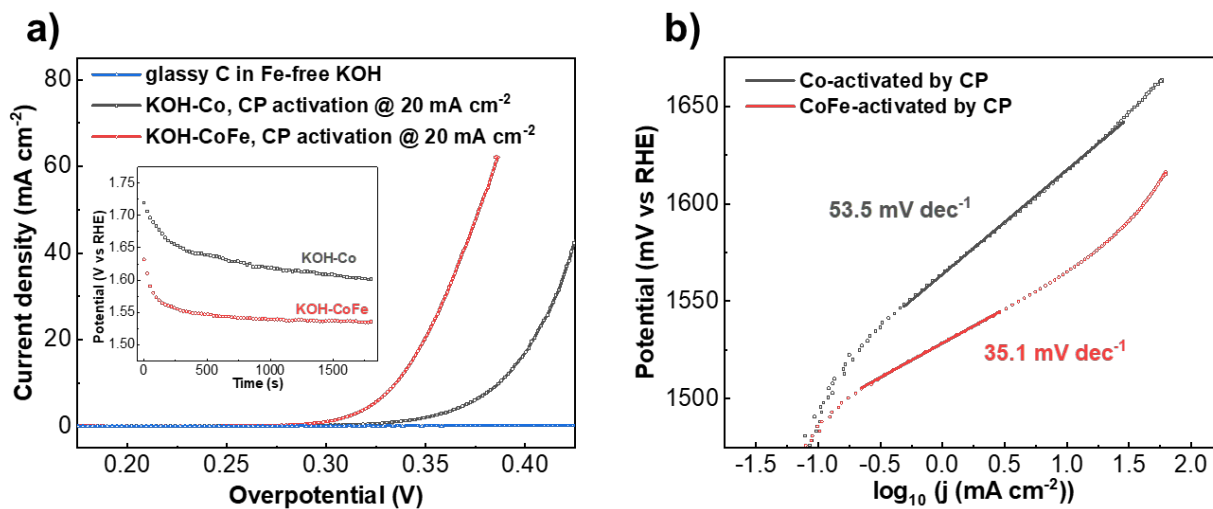
Figure S3.5. Activity for OER of different CP activation of GC-RDE in KOH-Co and in KOH-CoFe **a)** Current density as a function of overpotential. Inset: Evolution of the potential as a function of time at 20 mA cm^{-2}. **b)** corresponding Tafel slopes.

Laboratory of Materials for Renewable Energy (LMER)
Institute of Chemical Sciences and Engineering (ISIC)
Basic Science Faculty (SB)

119
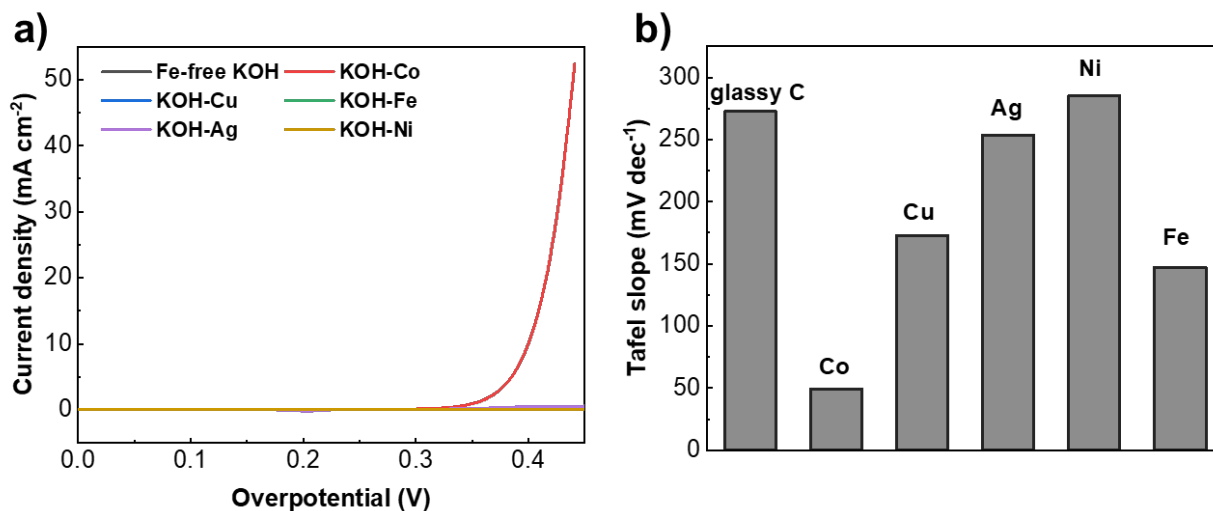
Figure S3.6. GC-RDE electrode cycled in different electrolytes: Fe-free KOH, KOH-Co, KOH-Cu, KOH-Fe, KOH-Ag and KOH-Ni, at a scan rate of 10 mV s^{-1}. a) Current density as a function of overpotential. b) Summary of the Tafel slopes.

Laboratory of Materials for Renewable Energy (LMER)
Institute of Chemical Sciences and Engineering (ISIC)
Basic Science Faculty (SB)

120
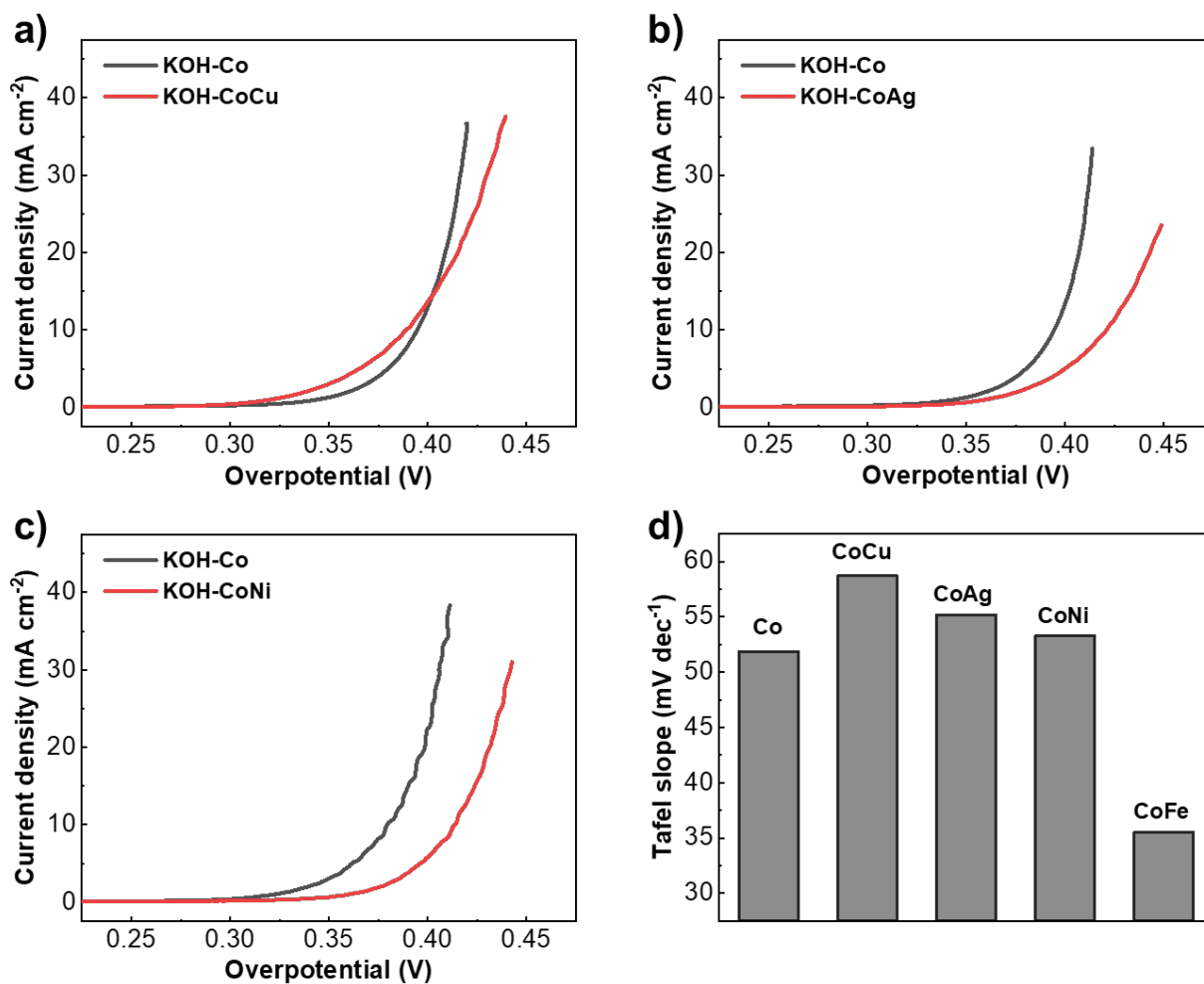
Figure S3.7. Deposited Co-catalyst cycled in different electrolytes, at a scan rate of 10 mA s^{-1}. a) KOH-CoCu, b) KOH-CoAg, c) KOH-CoNi. d) Summary of the Tafel slopes.

Laboratory of Materials for Renewable Energy (LMER)
Institute of Chemical Sciences and Engineering (ISIC)
Basic Science Faculty (SB)

121
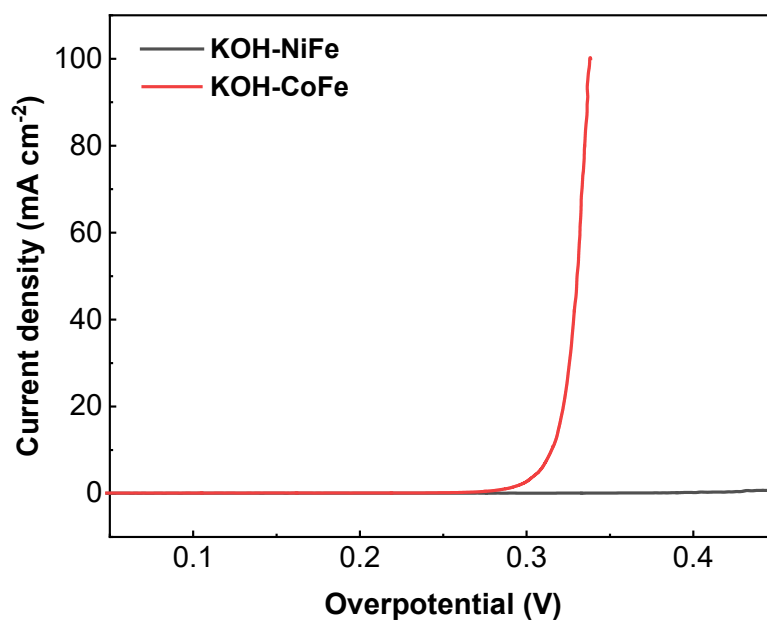
Figure S3.8. GC-RDE electrode cycled in KOH-NiFe, composed of Fe-free KOH + 0.5 mM Ni^{2+} + 0.2 mM Fe^{3+}, under similar electrochemical conditions as KOH-CoFe.

Laboratory of Materials for Renewable Energy (LMER)
Institute of Chemical Sciences and Engineering (ISIC)
Basic Science Faculty (SB)

122
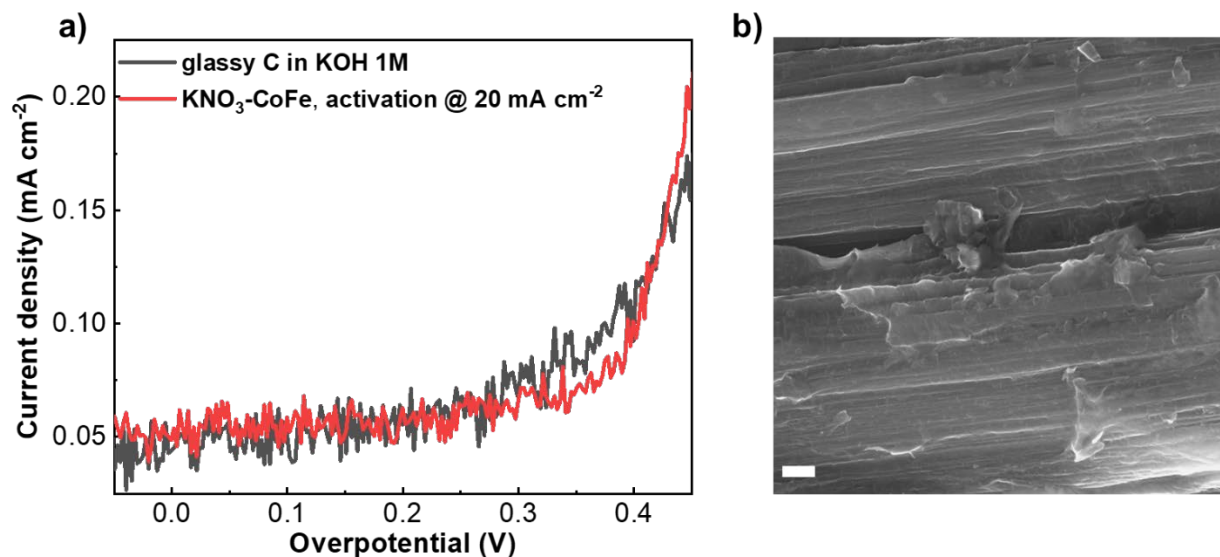
Figure S3.9. Anodic CP activation of the GC-RDE in KNO_3 1 M with the presence Co^{2+} and Fe $^{3+}$. a) Current density as a function of overpotential. b) SEM image of the Toray carbon paper after CP activation in neutral conditions. Scale bar: 1 μm.

Laboratory of Materials for Renewable Energy (LMER)
Institute of Chemical Sciences and Engineering (ISIC)
Basic Science Faculty (SB)

123
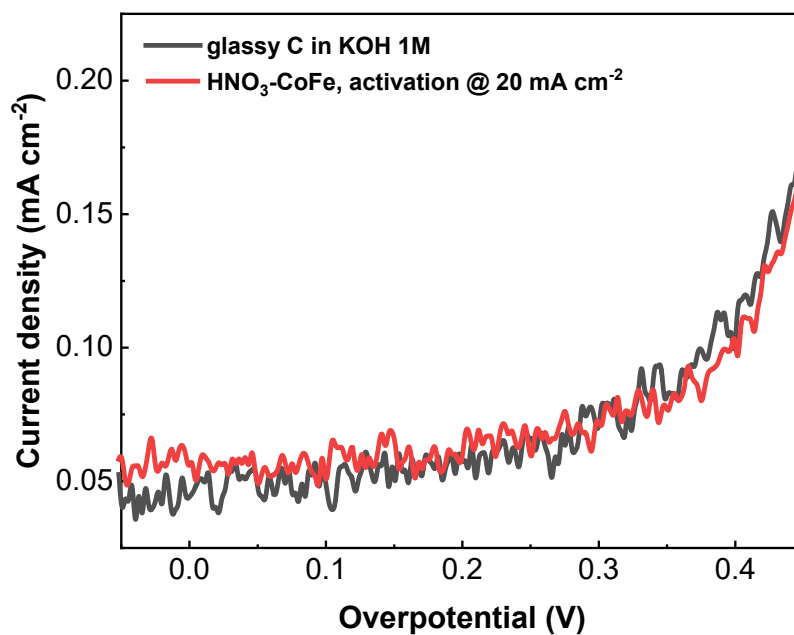
Figure S3.10. Anodic CP activation of the GC-RDE in HNO_3 1 M with the presence of $Co^{2+} + Fe^{3+}$.

Laboratory of Materials for Renewable Energy (LMER)
Institute of Chemical Sciences and Engineering (ISIC)
Basic Science Faculty (SB)

124
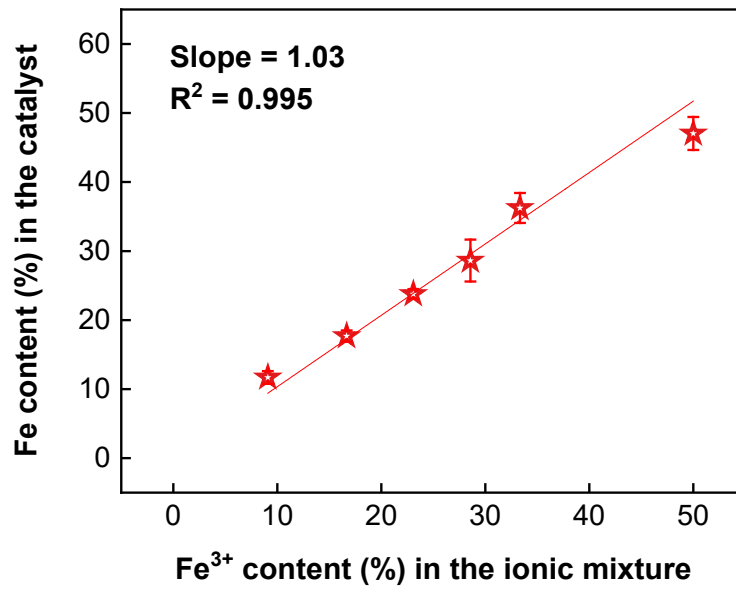
Figure S3.11. The correlation curve between the content of Fe in the catalyst determined by EDX and the concentration of Fe^{3+} in the ionic mixture.

Laboratory of Materials for Renewable Energy (LMER)
Institute of Chemical Sciences and Engineering (ISIC)
Basic Science Faculty (SB)

125
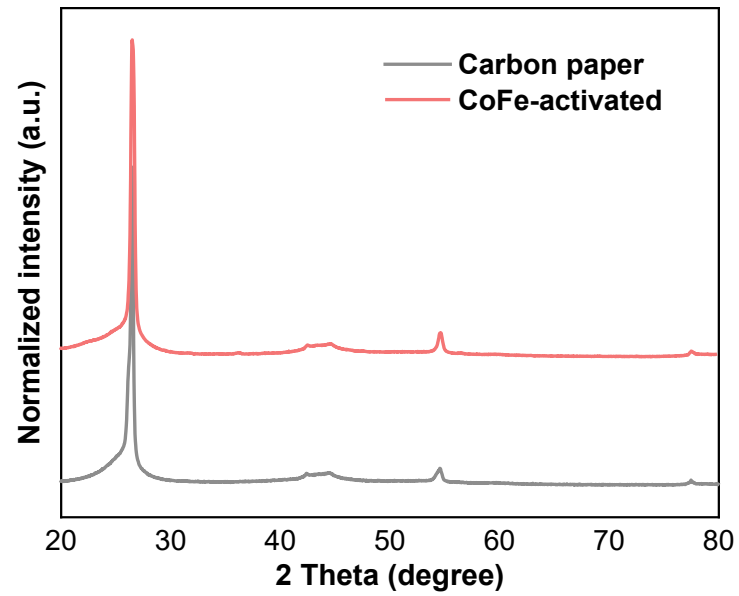
Figure S3.12. XRD pattern of the dry Toray carbon paper and that activated in KOH-CoFe.

Laboratory of Materials for Renewable Energy (LMER)
Institute of Chemical Sciences and Engineering (ISIC)
Basic Science Faculty (SB)

126
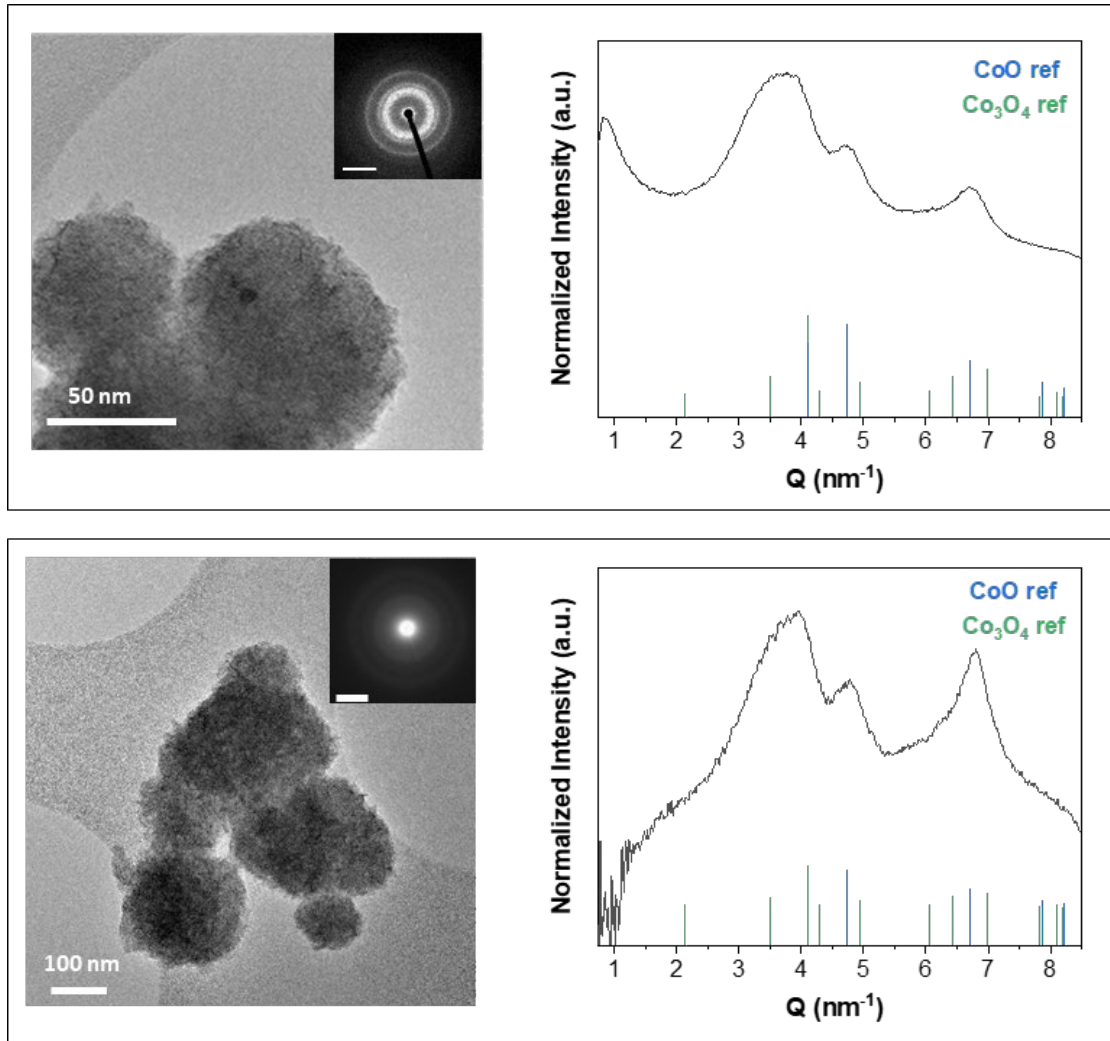
Figure S3.13. BF-TEM image, SAED patterns (scale bar: 5 nm^{-1}) and the corresponding integrated intensity of in situ Co-Fe catalyst, acquired at two different regions.

Laboratory of Materials for Renewable Energy (LMER)
Institute of Chemical Sciences and Engineering (ISIC)
Basic Science Faculty (SB)

127
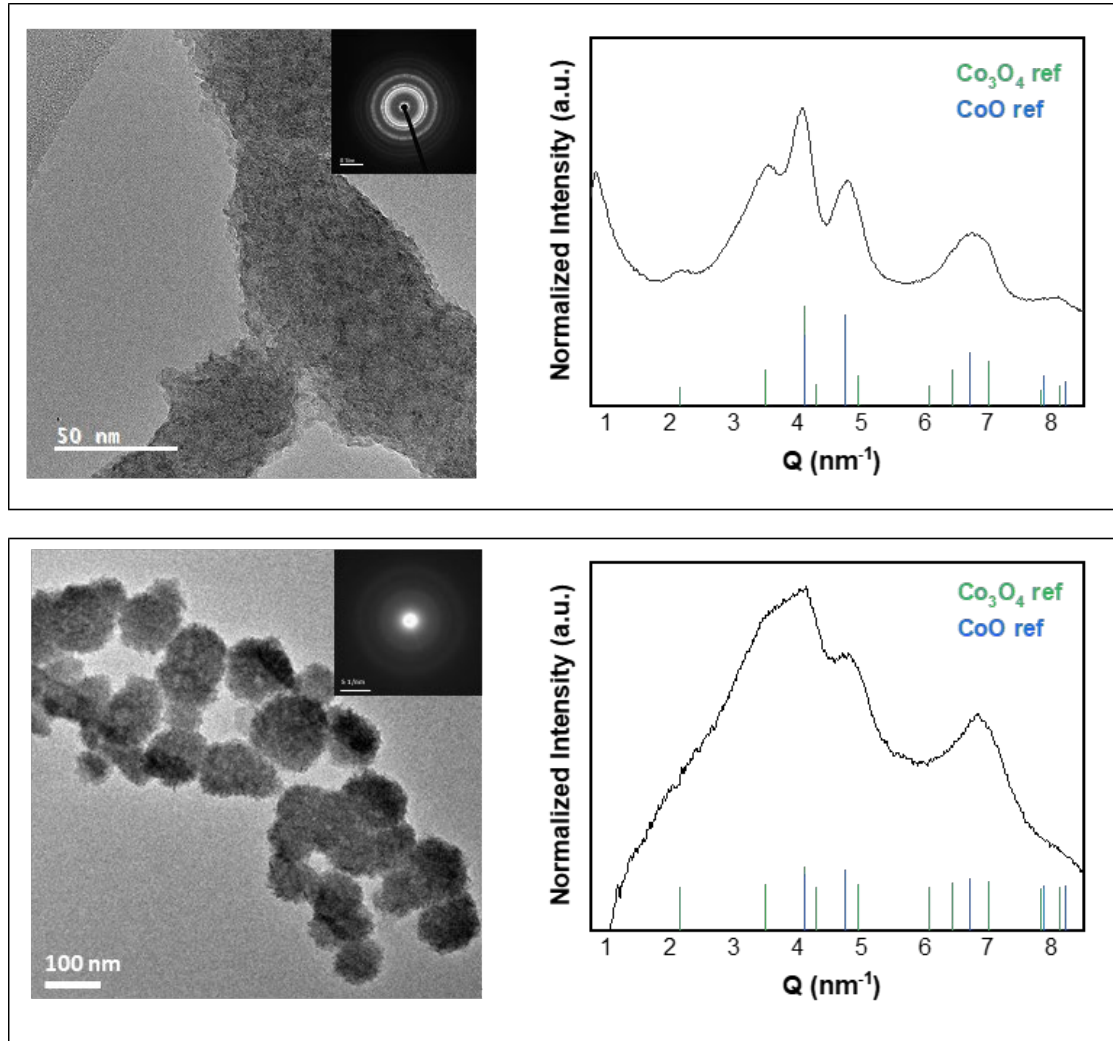
Figure S3.14. BF-TEM image, SAED patterns and the corresponding integrated intensity of in situ Co catalyst, acquired at two different regions.

Laboratory of Materials for Renewable Energy (LMER)
Institute of Chemical Sciences and Engineering (ISIC)
Basic Science Faculty (SB)

128
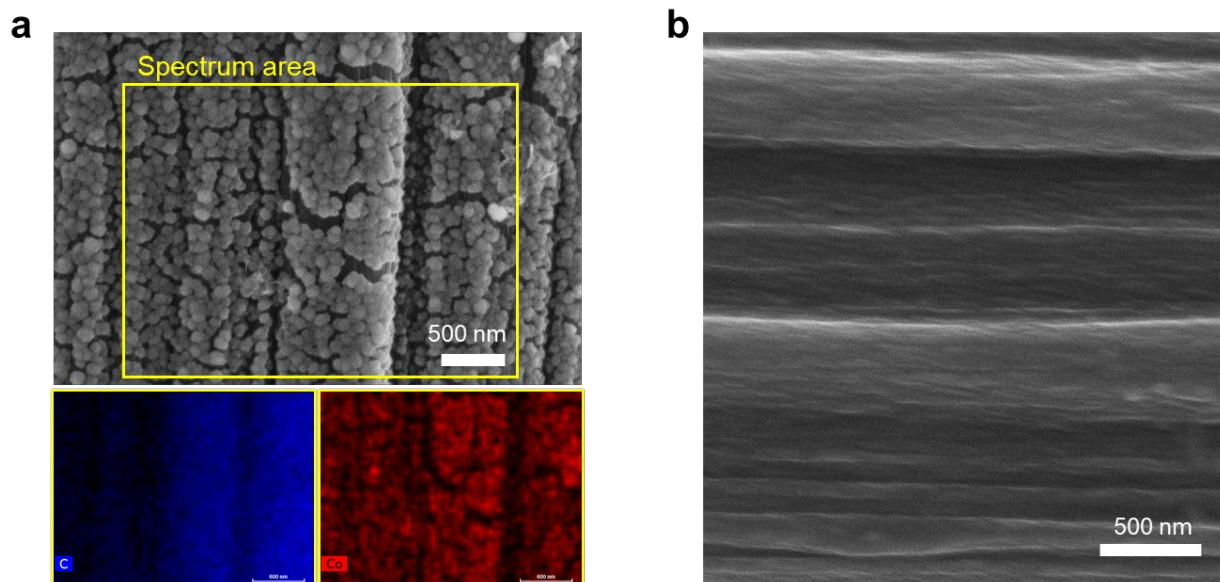
Figure S3.15. a) SEM image and the corresponding EDX of the in situ Co catalyst, formed after 10 CVs of Toray carbon paper in KOH-Co. b) SEM image of Toray carbon paper after 10 CVs in KOH-Fe. No deposition was observed.

Laboratory of Materials for Renewable Energy (LMER)
Institute of Chemical Sciences and Engineering (ISIC)
Basic Science Faculty (SB)

129

Table S3.2. Concentration of Co in KOH-Co and subsequential KOH-Fe, determined with ICP-OES. The in situ Co catalyst was first deposited in KOH, by 10 CVs and by 30 minutes of CP at 25 mA cm^{-2}. After deposition, the Co-catalyst underwent similar CV and anodic CP tests in KOH-Fe. Upper line = initial concentration in Co, lower line = Co concentration after the electrochemical tests.

Co concentration (ppm)	10 CVs	CP 30 min at 25 mA cm^{-2}
Deposition in KOH-Co	10.79476	12.61379
	6.109813	10.10931
Subsequential cycling in KOH-Fe	0.017138	0.019824
	0.064708	0.050088

Laboratory of Materials for Renewable Energy (LMER)
Institute of Chemical Sciences and Engineering (ISIC)
Basic Science Faculty (SB)

130
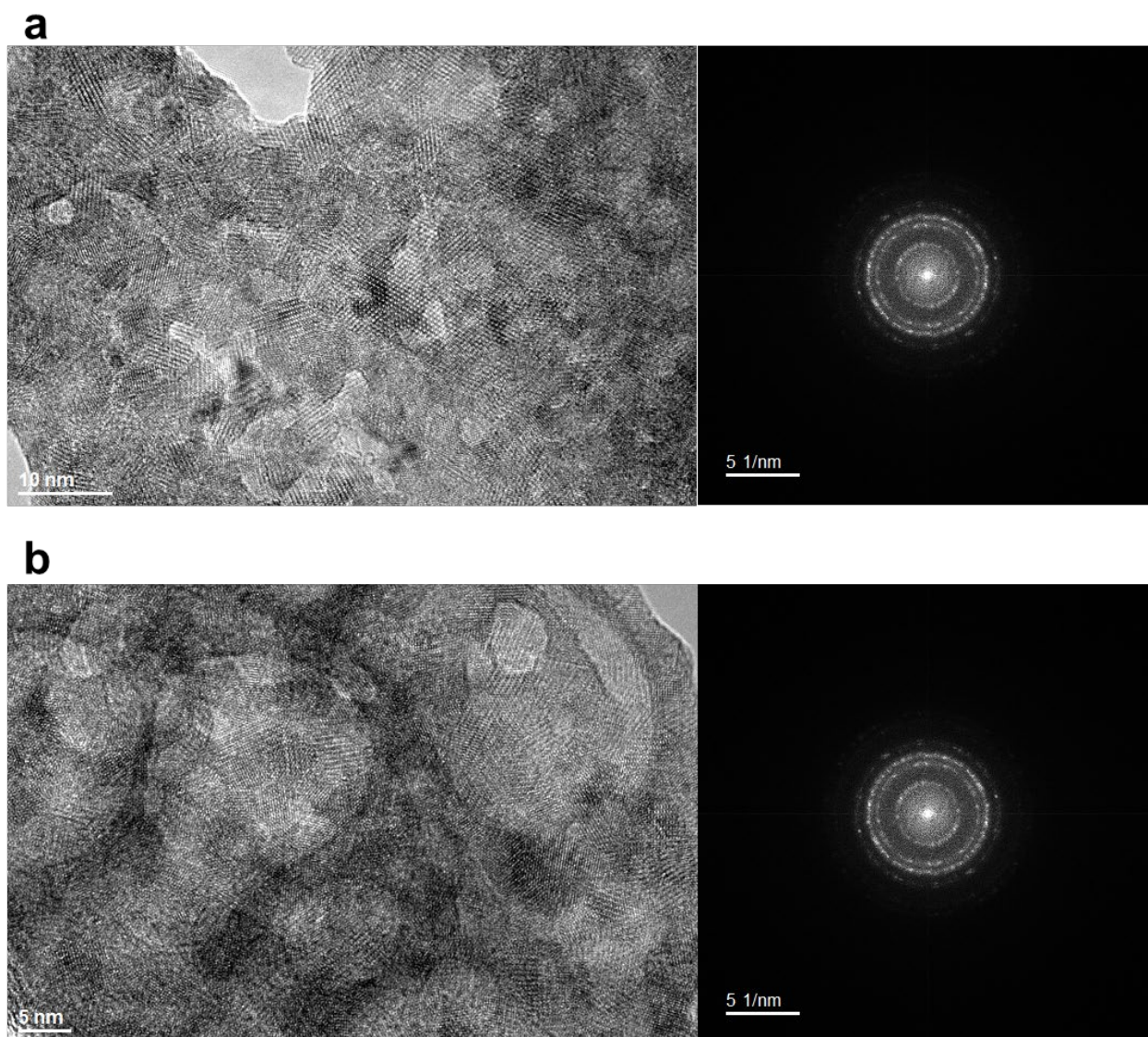
Figure S3.16. HR-TEM images and the corresponding FFT of a) in situ Co catalyst. b) in situ Co-Fe catalyst.

Laboratory of Materials for Renewable Energy (LMER)
Institute of Chemical Sciences and Engineering (ISIC)
Basic Science Faculty (SB)

131

Table S3.3. Q-value and corresponding lattice parameters of in situ Co and Co-Fe catalyst, extracted from integrated intensity of the FFT in Figure S3.16. In the last column: calculated expansion of the lattice parameter in Co-Fe with respect to that of Co catalyst.

a_{Co} (nm^{-1})	a_{Co-Fe}(nm^{-1})	d_{Co}(Å)	d_{Co-Fe}(Å)	Expansion (%)
2.148	2.089	4.656	4.786	2.805
3.489	3.407	2.866	2.935	2.422
4.096	3.964	2.442	2.523	3.330
4.941	4.790	2.024	2.088	3.172

Laboratory of Materials for Renewable Energy (LMER)
Institute of Chemical Sciences and Engineering (ISIC)
Basic Science Faculty (SB)

132
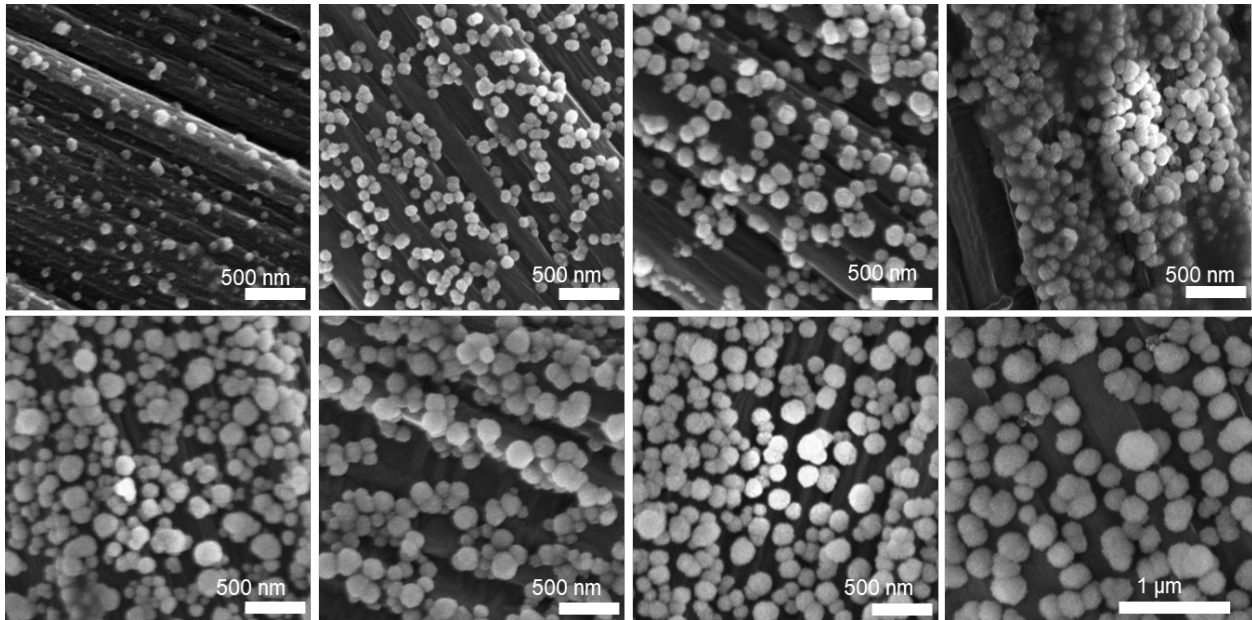
Figure S3.17. SEM images of the spherical particles formed on Toray carbon paper after different number of cycles in KOH-Co (from left to right): 1, 5, 10, 30, 50, 100, 300 and 3000 cycles.
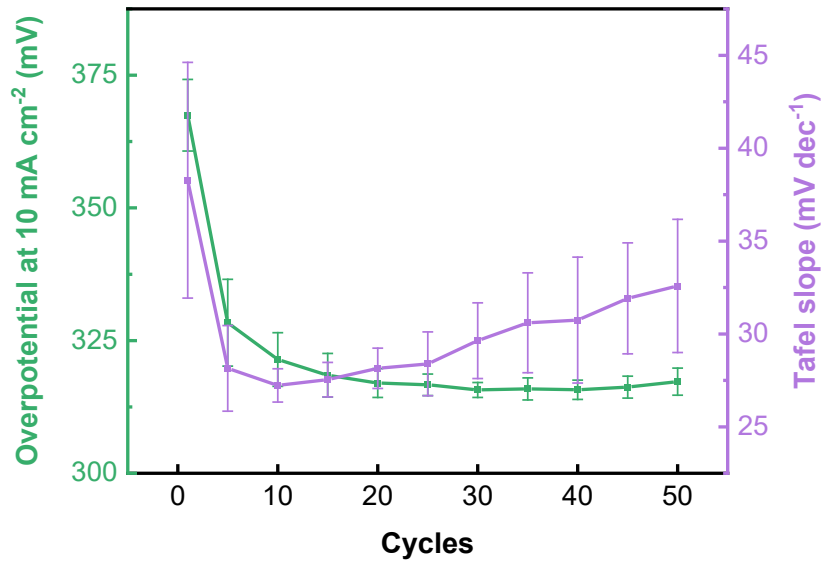
Laboratory of Materials for Renewable Energy (LMER)
Institute of Chemical Sciences and Engineering (ISIC)
Basic Science Faculty (SB)

133
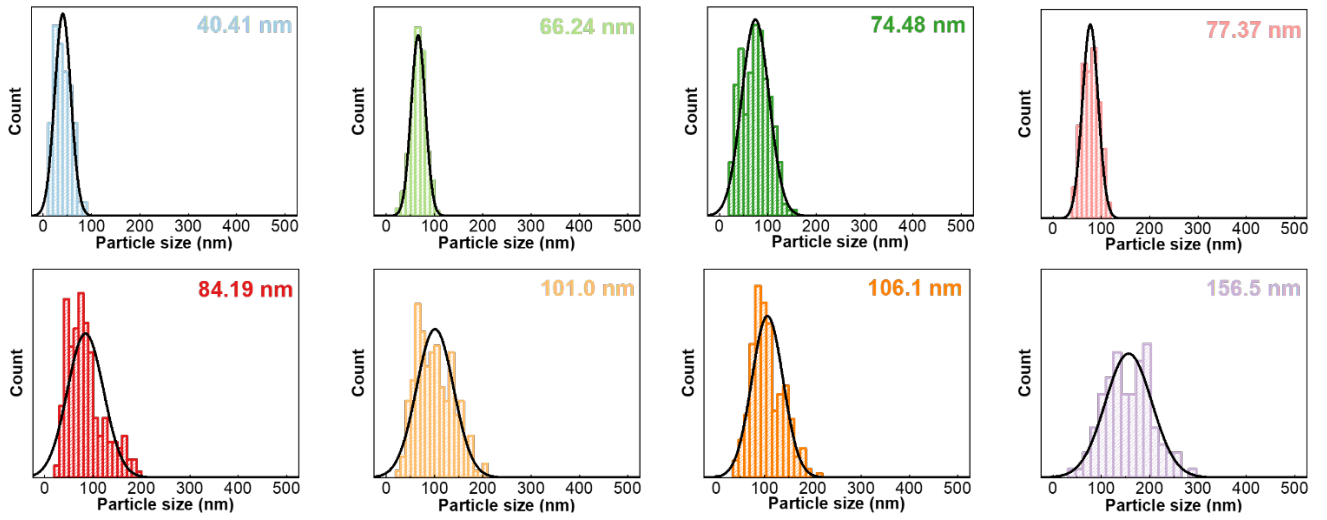
Figure S3.18. Size distribution of the spherical particles formed on Toray carbon paper after different number of cycles in KOH-Co (from left to right): 1, 5, 10, 30, 50, 100, 300 and 3000 cycles.

Laboratory of Materials for Renewable Energy (LMER)
Institute of Chemical Sciences and Engineering (ISIC)
Basic Science Faculty (SB)

134

Table S3.4. Summary of the overpotential at 10 mA cm^{-2} and the Tafel slope of 10 different samples, measured after 10 CVs in KOH Co-Fe.

	Overpotential at 10 mA cm^{-2} (mV)	Tafel slope (mV dec^{-1})
1	316	26.2
2	319	26.72
3	320	28.33
4	322	28.4
5	326	33.5
6	319	27.5
7	315.5	27.3
8	322.6	28.46
9	315.5	30.37
10	318	25.3
Average	319.4 ± 3.42	28.2 ± 2.33

Laboratory of Materials for Renewable Energy (LMER)
Institute of Chemical Sciences and Engineering (ISIC)
Basic Science Faculty (SB)

135
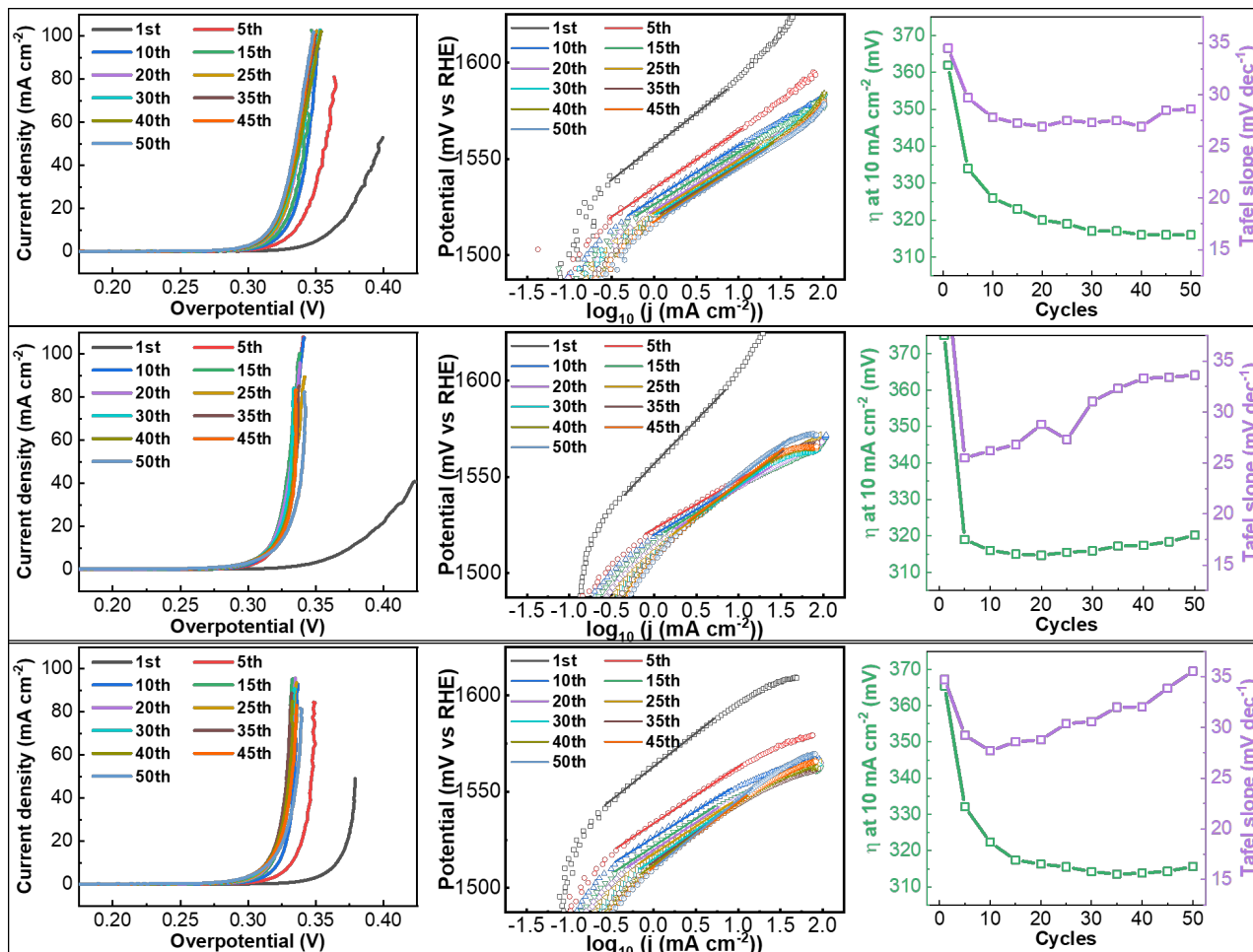
Figure S3.19. Evolution of the CV scan at 10 mV s^{-1} over 50 cycles in KOH-CoFe. Each sub-figure presented a set of measurements. From left to right: current density as a function of overpotential, Tafel slope, overpotential at 10 mA cm^{-2} and Tafel slope over as a function of number of cycles.
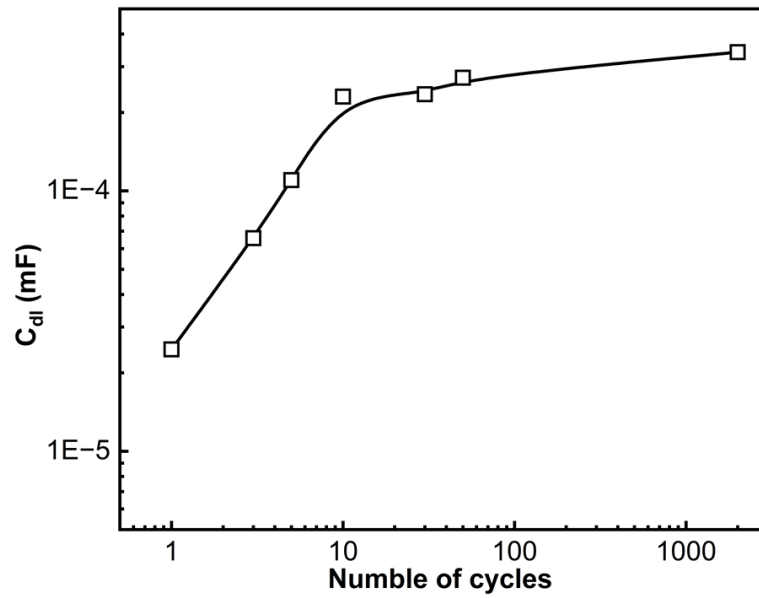
Laboratory of Materials for Renewable Energy (LMER)
Institute of Chemical Sciences and Engineering (ISIC)
Basic Science Faculty (SB)

136

Figure S3.20. Evolution of the overpotential at 10 mA cm^{-2} and the Tafel slope over 50 CVs in KOH-CoFe. The scan rate was 10 mV s^{-1}. The error bar was averaged from 3 sets of measurements in Figure S3.19.

Laboratory of Materials for Renewable Energy (LMER)   137
Institute of Chemical Sciences and Engineering (ISIC)
Basic Science Faculty (SB)
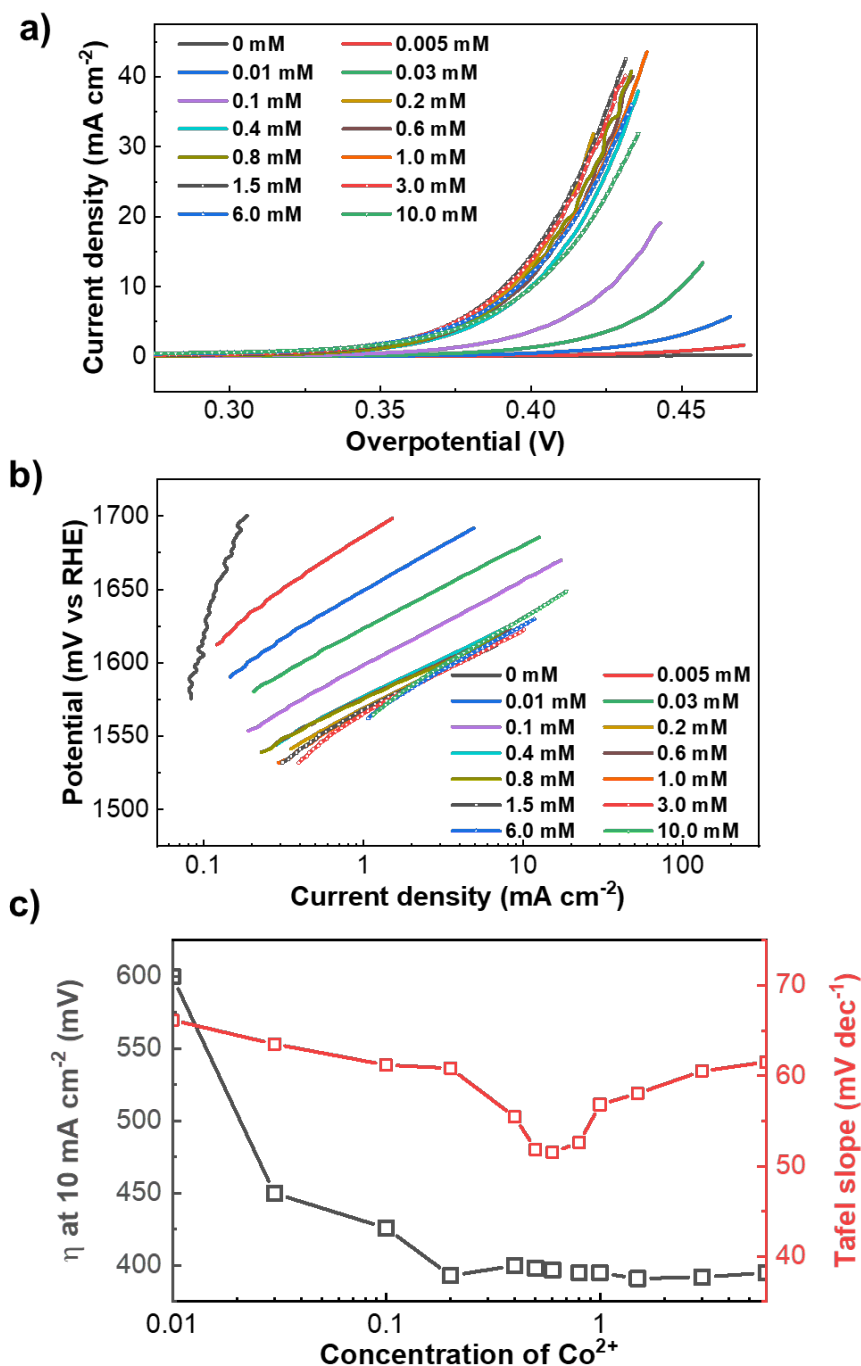
Figure S3.21. Activity for OER at different concentration of Co^{2+} in the solution **a)** Current density as a function of overpotential. **b)** Tafel slope. **c)** Summary of the overpotential at 10 mA cm^{-2} and the Tafel slope with respect to the concentration of Co^{2+}.

Laboratory of Materials for Renewable Energy (LMER)
Institute of Chemical Sciences and Engineering (ISIC)
Basic Science Faculty (SB)

138
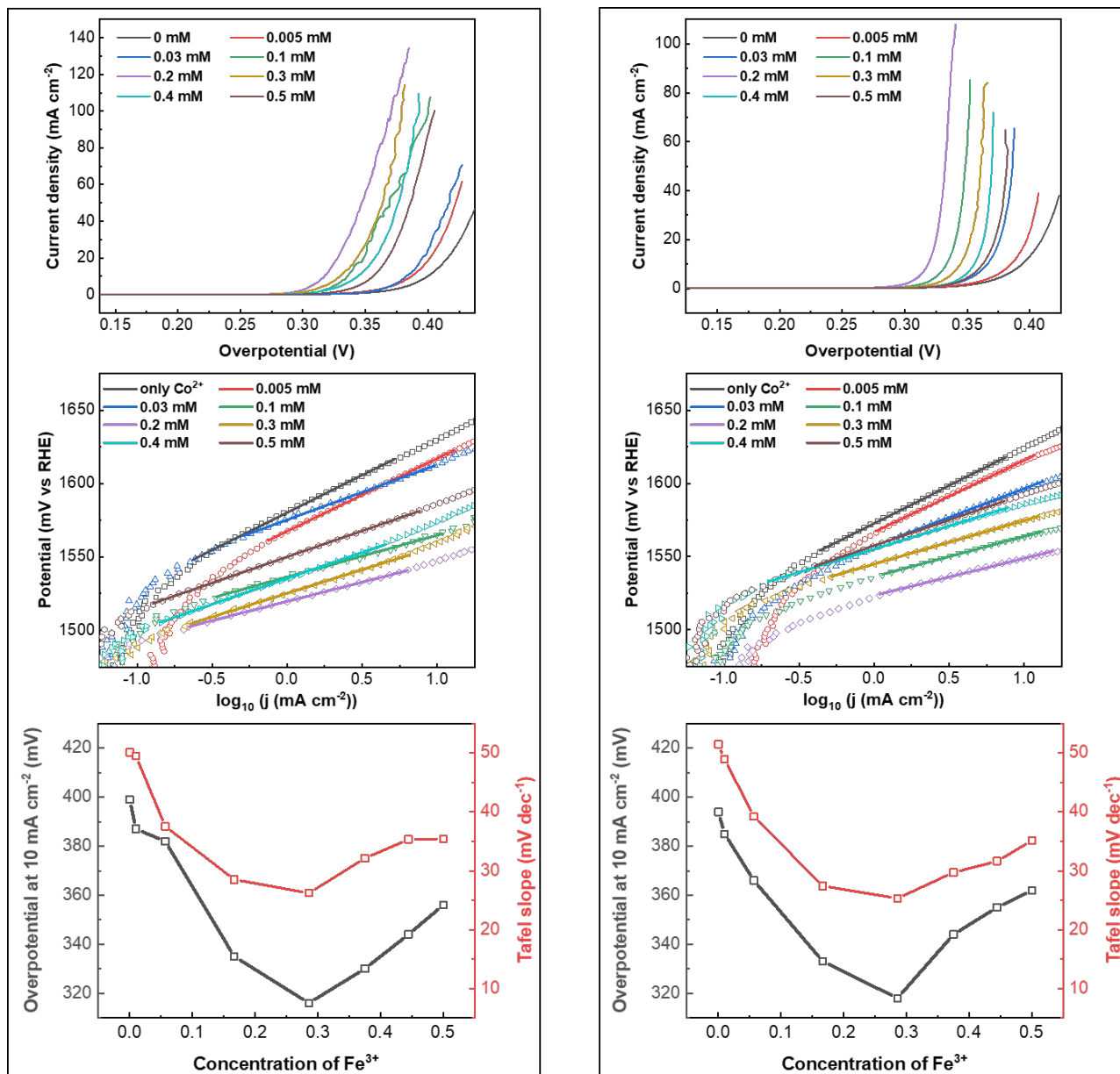
Figure S3.22. Evolution of the CV scan at 10 mV s^{-1} for various concentration of Fe^{3+} in the electrolyte, with a fixed concentration of Co^{2+} of 0.5 mM. Each sub-figure presented a set of measurements. From top to bottom: current density as a function of overpotential, Tafel slope, overpotential at 10 mA cm^{-2} and Tafel slope over, as a function Fe^{3+} concentration.

Laboratory of Materials for Renewable Energy (LMER)
Institute of Chemical Sciences and Engineering (ISIC)
Basic Science Faculty (SB)

139

Figure S3.23. Evolution of the C_{dl} with respect to the number of cycles in KOH-CoFe. The C_{dl} was evaluated after 1, 3, 5, 10, 50, 300 and 2000 cycles.

Laboratory of Materials for Renewable Energy (LMER)
Institute of Chemical Sciences and Engineering (ISIC)
Basic Science Faculty (SB)

140
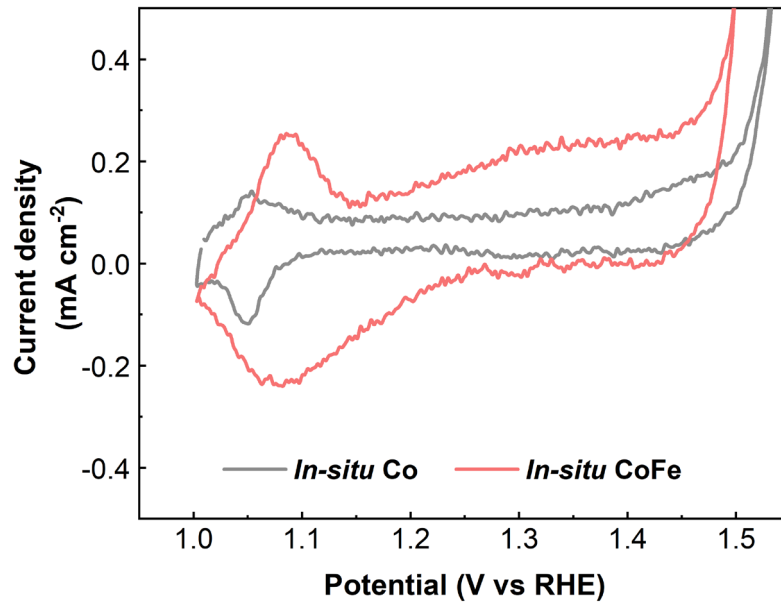
Figure S3.24. CV curves of in situ Co and in situ Co-Fe in the potential range prior to OER.

Laboratory of Materials for Renewable Energy (LMER)
Institute of Chemical Sciences and Engineering (ISIC)
Basic Science Faculty (SB)

141

Table S3.5. Summary of the overpotential at 10 mA cm^{-2} and the Tafel slope of 10 different samples, measured after 10 CVs in KOH-Co.

	Overpotential at 10 mA cm^{-2} (mV)	Tafel slope (mV dec^{-1})
1	389	51.4
2	394	50.6
3	412	56.3
4	398	49.1
5	401	50.7
6	395	52.2
7	389.4	49.6
8	393	51.7
9	392	51.6
10	390	51.3
Average	395 ± 6.99	51.5 ± 1.96

Laboratory of Materials for Renewable Energy (LMER)
Institute of Chemical Sciences and Engineering (ISIC)
Basic Science Faculty (SB)

142
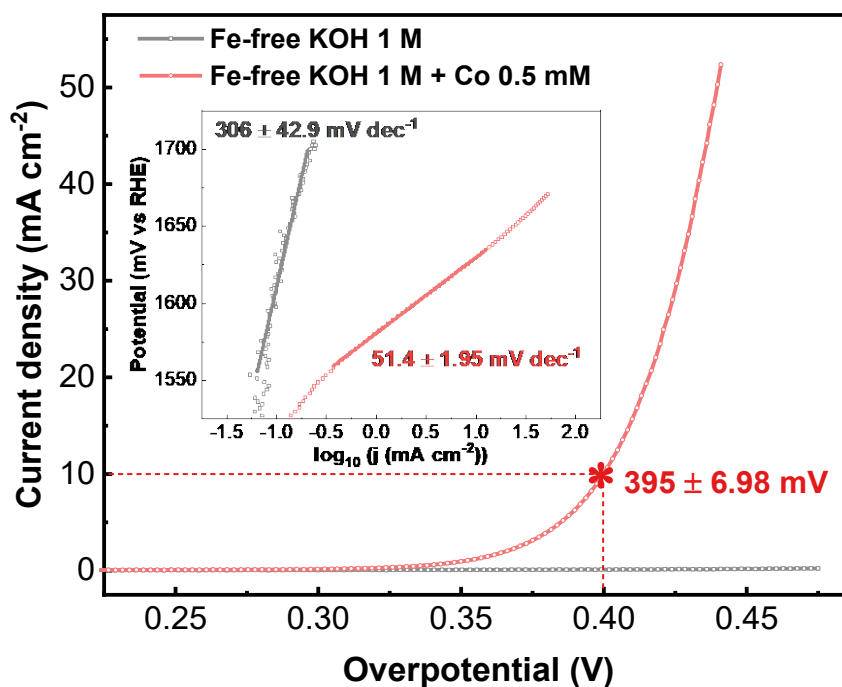
Figure S3.25. CV curves of GC-RDE in Fe-free KOH and in KOH-Co after 10 cycles. Inset: Tafel slopes. The scan range of the CVs were 1.0 to 1.7 V vs RHE and the scan rate was 10 mV s^{-1}. The CV curves and Tafel slopes were averaged over 10 individual measurements (Table S3.5). All the CV curves were corrected with 85% of iR-drop.
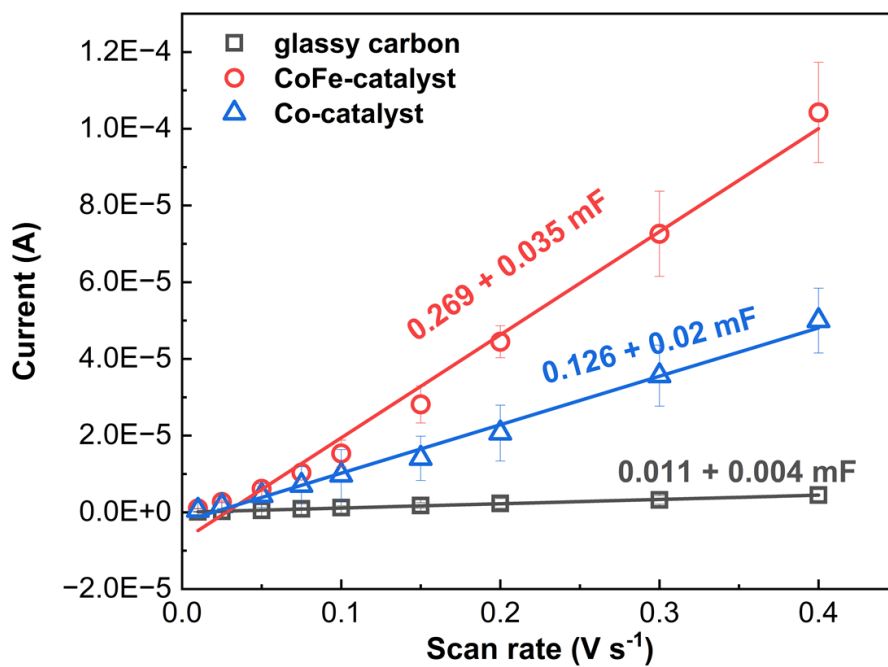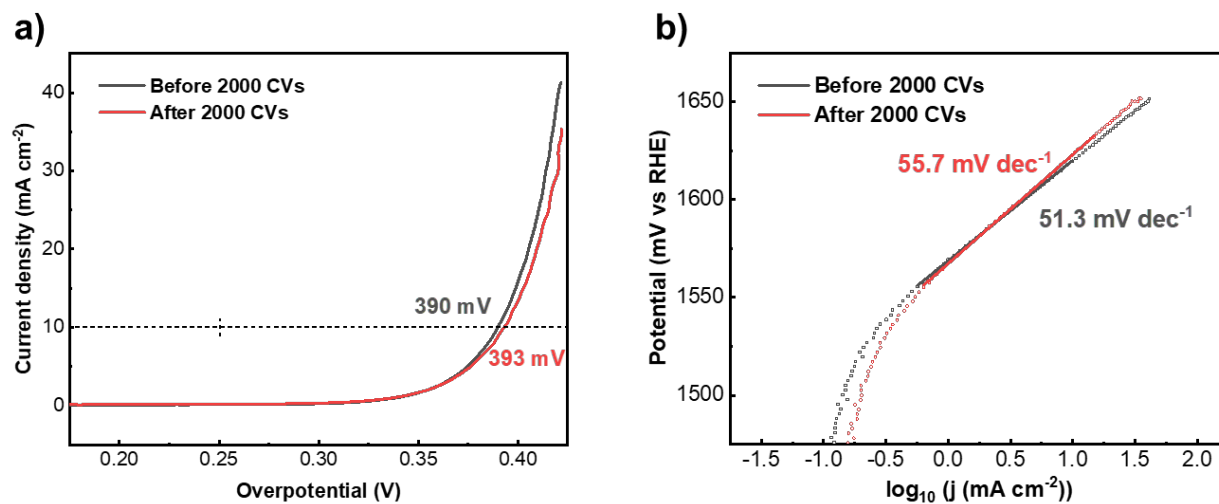
Laboratory of Materials for Renewable Energy (LMER)
Institute of Chemical Sciences and Engineering (ISIC)
Basic Science Faculty (SB)

143
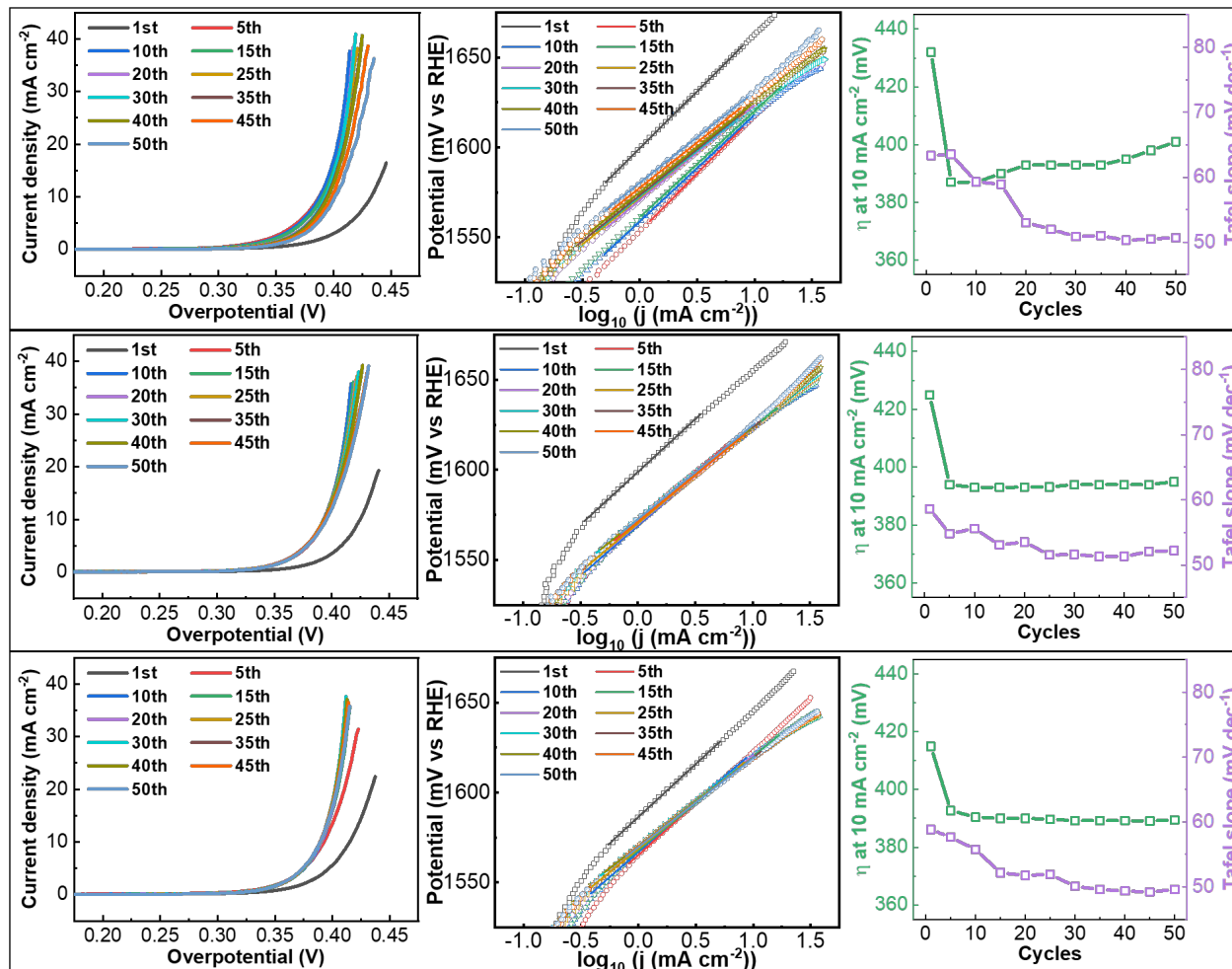
Figure S3.26. Evolution of the CV scan at 10 mV s^{-1} over 50 cycles in KOH-Co. Each sub-figure presented a set of measurements. From left to right: current density as a function of overpotential, Tafel slope, overpotential at 10 mA cm^{-2} and Tafel slope over as a function of number of cycles.

Laboratory of Materials for Renewable Energy (LMER)
Institute of Chemical Sciences and Engineering (ISIC)
Basic Science Faculty (SB)

144
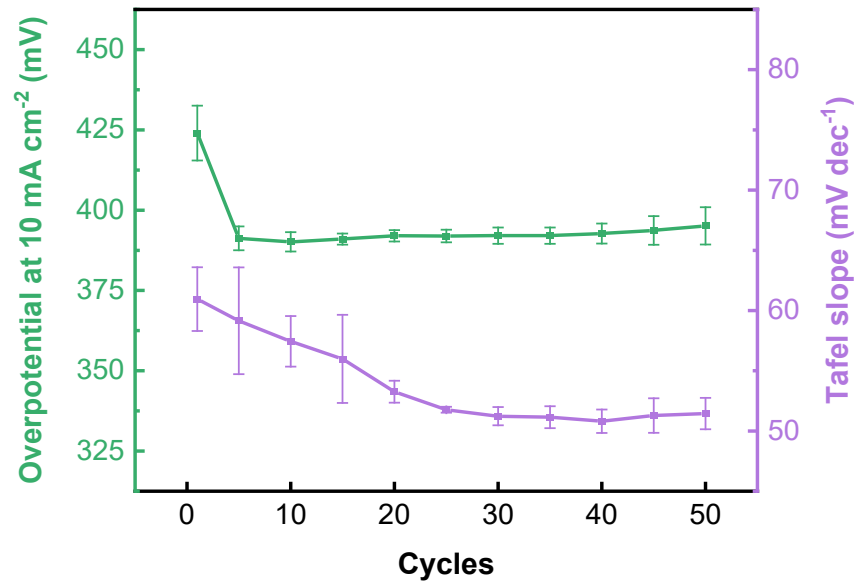
Figure S3.27. Evolution of the overpotential at 10 mA cm^{-2} and the Tafel slope over 50 CVs in KOH-Co. The scan rate was 10 mV s^{-1}. The error bar was averaged from 3 sets of measurements in Figure S3.26.
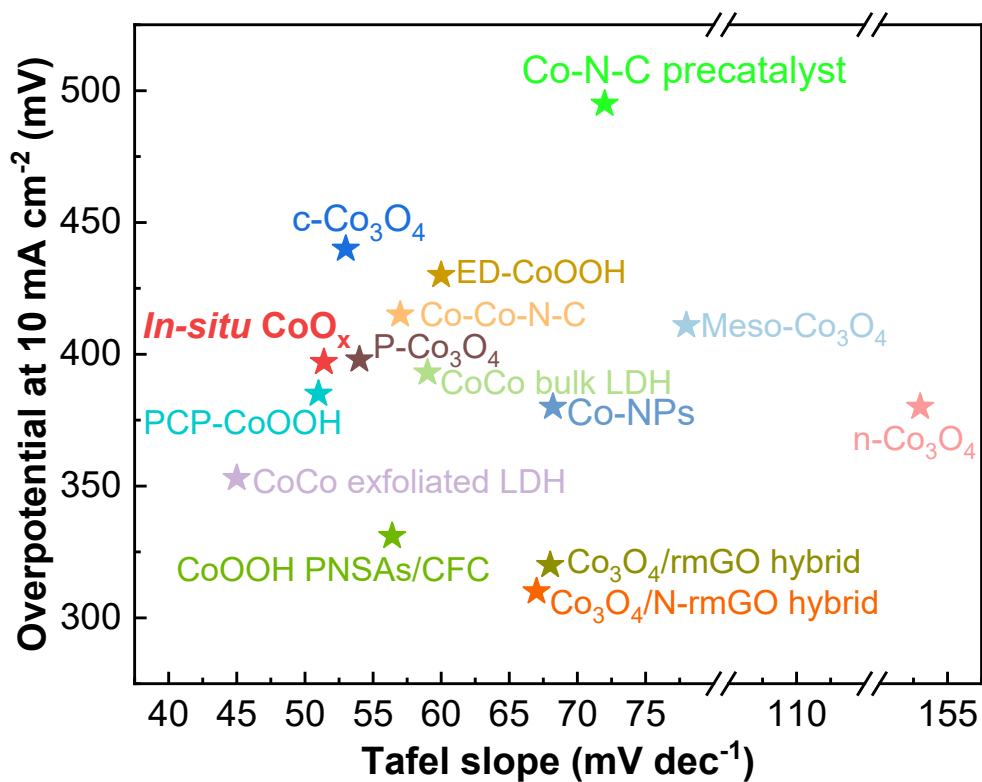
Laboratory of Materials for Renewable Energy (LMER)
Institute of Chemical Sciences and Engineering (ISIC)
Basic Science Faculty (SB)

145

Figure S3.28. ECSA of the bare GC-RDE, in situ Co and Co-Fe catalysts, acquired after 10 CVs in their corresponding electrolyte for synthesis.

Laboratory of Materials for Renewable Energy (LMER)
Institute of Chemical Sciences and Engineering (ISIC)
Basic Science Faculty (SB)

146

Figure S3.29. Activity for OER before and after 2000 accelerated CVs in KOH-Co at 400 mV s^{-1} scan rate.

Laboratory of Materials for Renewable Energy (LMER)
Institute of Chemical Sciences and Engineering (ISIC)
Basic Science Faculty (SB)

147

Table S3.6. Summary of Tafel slope, overpotential at 10 mA cm^{-2} and concentration of KOH from a variety of Co-based catalyst.

Co-based catalysts	Tafel slope (mV dec^{-1})	Overpotential at 10 mA cm^{-2} (mV)	c_{KOH}	References
In situ Co	51.4	397	1 M	This work
ED-CoOOH	60	430	0.1 M	Ref [23]
PCP-CoOOH	51	385	0.1 M	Ref [24]
Pristine Co$_3$O$_4$	54	398	1 M	Ref [25]
Co$_3$O$_4$/rmGO hybrid	68	320	1 M	Ref [26]
Co$_3$O$_4$/N-rmGO hybrid	67	310	1 M	Ref [26]
Co NPs	68.2	380	0.1 M	Ref [27]
CoOOH PNSAs/CFC	56.4	331	1 M	Ref [28]
c-Co$_3$O$_4$	53	440	1 M	Ref [29]
n-Co$_3$O$_4$	153	380	1 M	Ref [29]
Meso-Co$_3$O$_4$	78	411	1 M	Ref [6]
Co-Co-N-C	57	415	1 M	Ref [30]
Co-Co bulk LDH	59	393	1 M	Ref [31]
Co-Co exfoliated LDH	45	353	1 M	Ref [31]
Co-N-C precatalyst	72	495	1 M	Ref [14]

Laboratory of Materials for Renewable Energy (LMER)
Institute of Chemical Sciences and Engineering (ISIC)
Basic Science Faculty (SB)

148

Figure S3.30. Activity for OER of the in situ Co catalyst compared with other reported Co-based catalyst. The details of the catalysts and electrolyte are summarized in Table S3.6.

Laboratory of Materials for Renewable Energy (LMER)
Institute of Chemical Sciences and Engineering (ISIC)
Basic Science Faculty (SB)

149
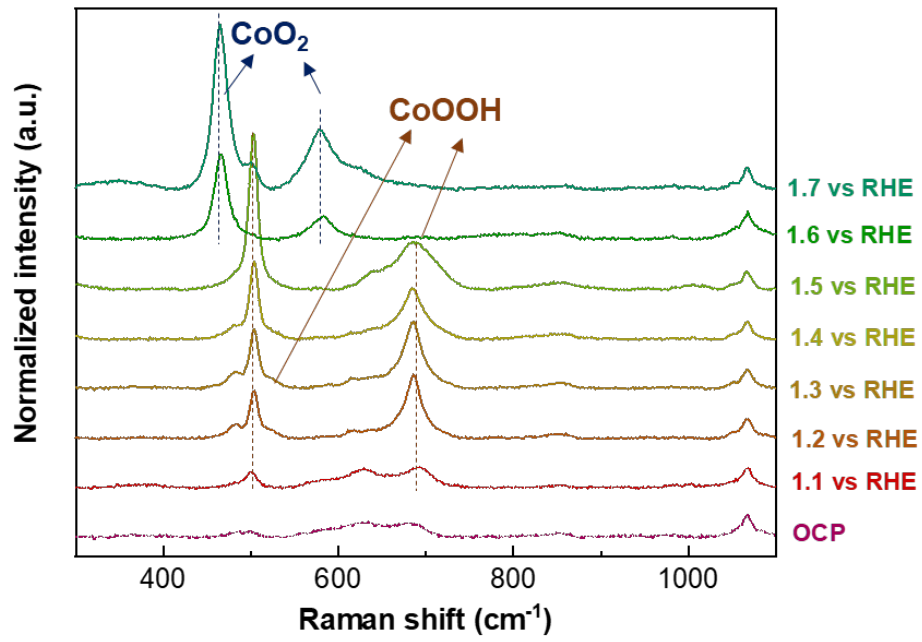
Figure S3.31. Operando Raman measurements acquired on GC plate in KOH-Co.

Laboratory of Materials for Renewable Energy (LMER)
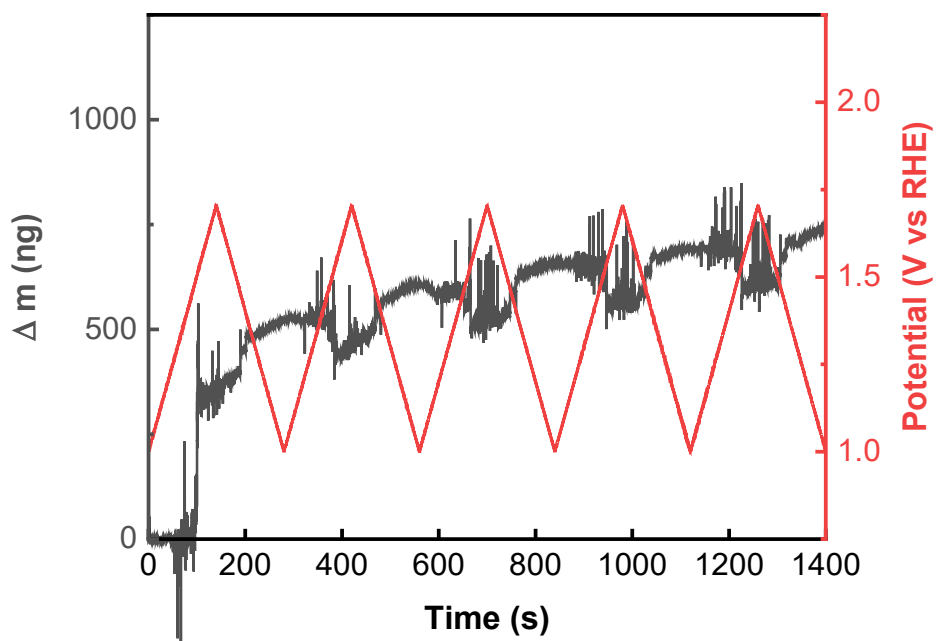Institute of Chemical Sciences and Engineering (ISIC)
Basic Science Faculty (SB)

150

Table S3.7. Summary of the reported Raman peak positions for CoOOH and OER-active phase CoO_2.

References	CoOOH (cm^{-1})	CoO$_2$ (cm^{-1})
Mechanism of Oxygen Evolution Catalyzed by Cobalt Oxyhydroxide: Cobalt Superoxide Species as a Key Intermediate and Dioxygen Release as a Rate-Determining Step[23]	500	474 (E_g), 581 (A_{1g})
Electrochemical Construction of Low-Crystalline CoOOH Nanosheets with Short-Range Ordered Grains to Improve Oxygen Evolution Activity[32]	502, 684	
Reversible Structural Evolution of NiCoO$_x$H$_y$ during the Oxygen Evolution Reaction and Identification of the Catalytically Active Phase[35]		467 (E_g), 572 (A_{1g})
Understanding the Roles of Electrogenerated Co^{3+} and Co^{4+} in Selectivity-Tuned 5-Hydroxymethylfurfural Oxidation[33]	503 (E_g)	474 (E_g), 560 (A_{1g})
Raman Study of Layered Rock-Salt LiCoO$_2$ and Its Electrochemical Lithium Deintercalation[36]		460 (E_g), 570 (A_{1g}) (Li$_{0.4}$CoO$_2$)
Enhanced Activity of Gold-Supported Cobalt Oxide for the Electrochemical Evolution of Oxygen[11]	505, 565	

Laboratory of Materials for Renewable Energy (LMER)
Institute of Chemical Sciences and Engineering (ISIC)
Basic Science Faculty (SB)

151
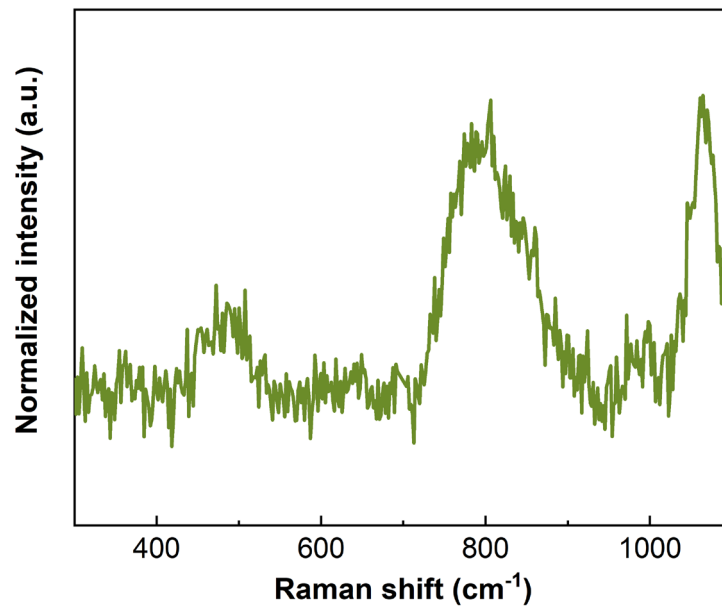
Figure S3.32. Raman spectrum of bare GC plate surface.

Laboratory of Materials for Renewable Energy (LMER)
Institute of Chemical Sciences and Engineering (ISIC)
Basic Science Faculty (SB)

152

Figure S3.33. Change in mass of in situ Co catalyst over 5 CVs. The drop of mass occurred when the potential went up from 1.55 to 1.7 then down to 1.55 vs RHE.

Laboratory of Materials for Renewable Energy (LMER)
Institute of Chemical Sciences and Engineering (ISIC)
Basic Science Faculty (SB)

153
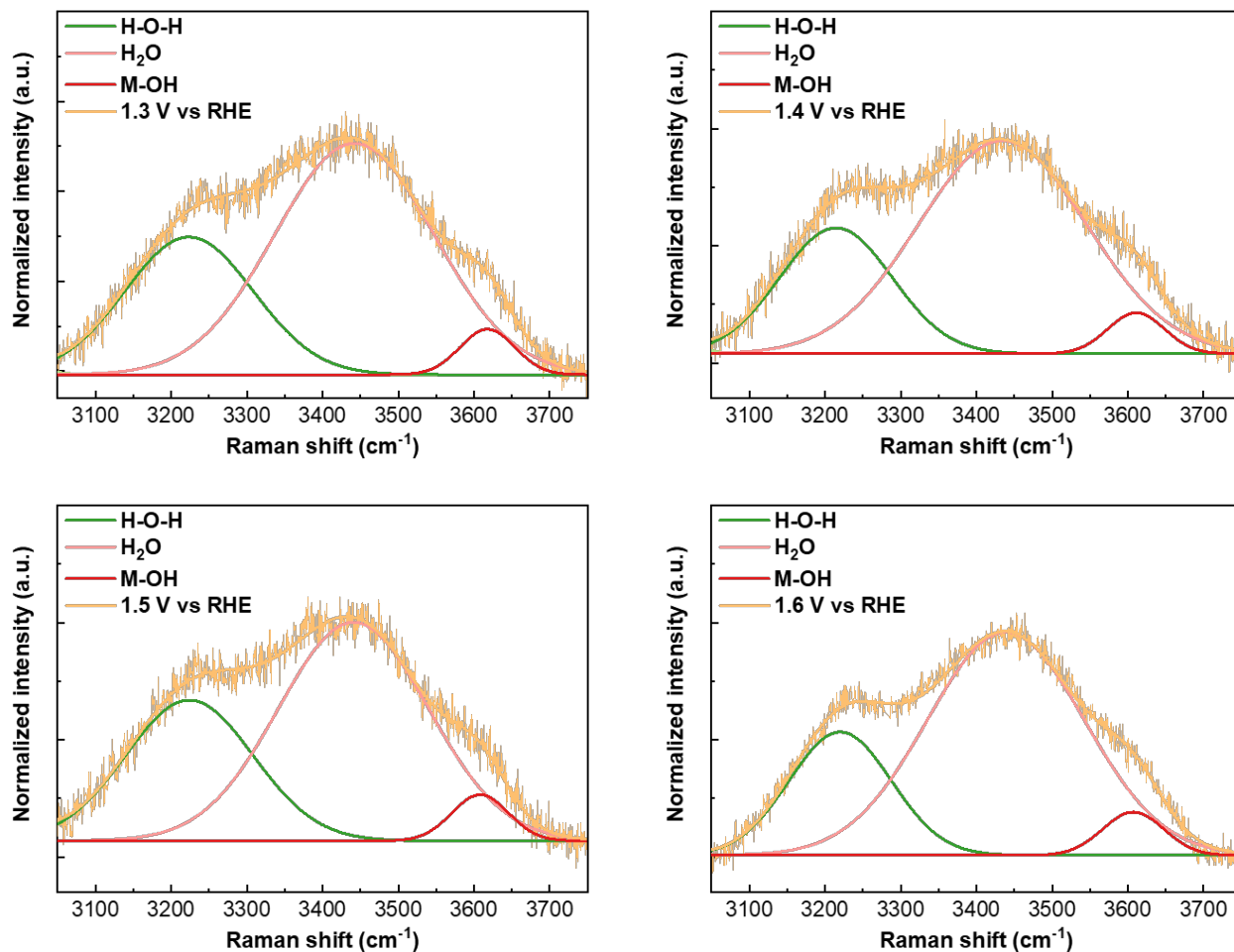
Figure S3.34. Operando Raman spectroscopy and the deconvoluted peaks of the GC plate activated in KOH-Co in the range of 3050 to 3750 cm^{-1}. The applied potentials were from 1.3 to 1.6 V vs RHE.

Laboratory of Materials for Renewable Energy (LMER)
Institute of Chemical Sciences and Engineering (ISIC)
Basic Science Faculty (SB)

154
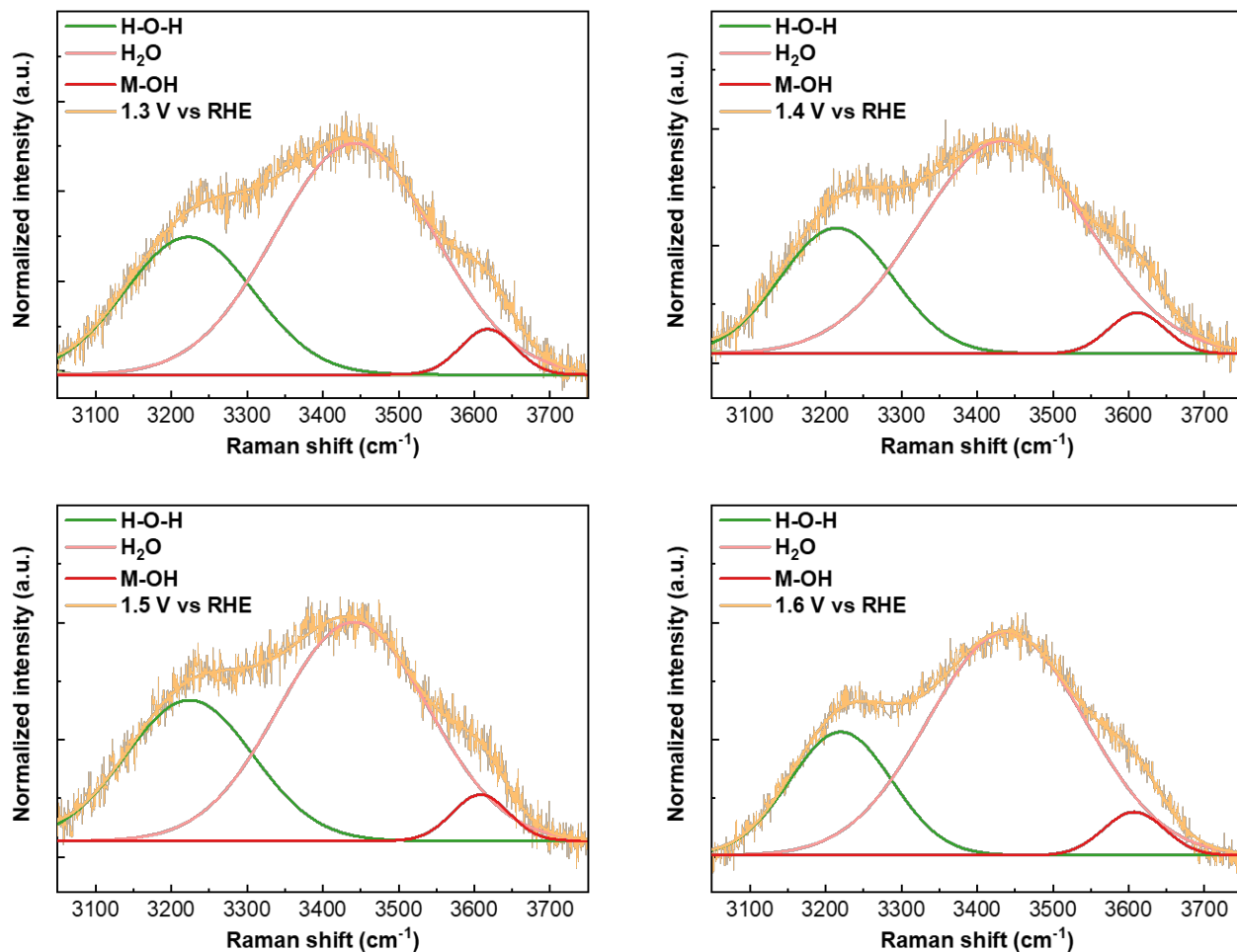
Figure S3.35. Operando Raman spectroscopy and the deconvoluted peaks of the GC plate activated in KOH-CoFe in the range of 3050 to 3750 cm^{-1}. The applied potentials were from 1.3 to 1.6 V vs RHE.

Laboratory of Materials for Renewable Energy (LMER)
Institute of Chemical Sciences and Engineering (ISIC)
Basic Science Faculty (SB)

155
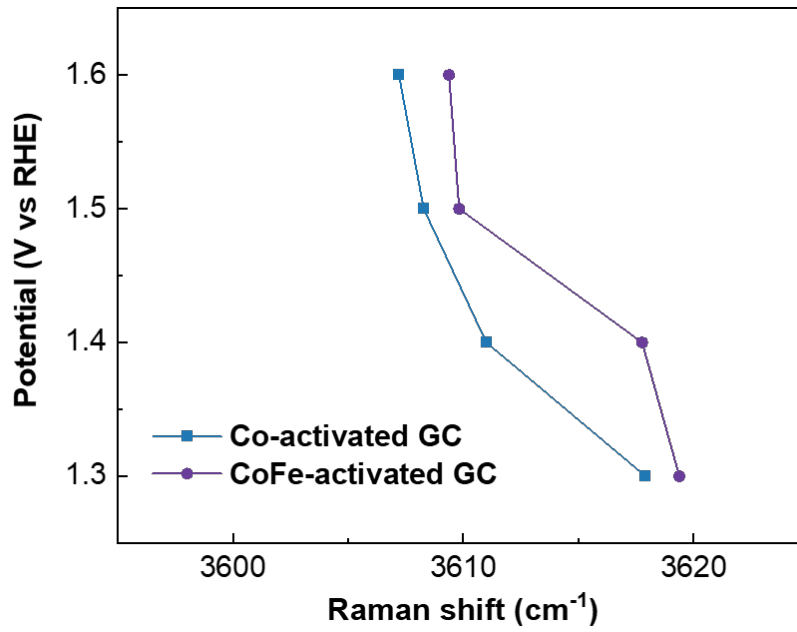
Figure S3.36. Position of the M-OH bond peak at different applied potentials for GC plate activated in KOH-Co and in KOH-CoFe.

Laboratory of Materials for Renewable Energy (LMER)
Institute of Chemical Sciences and Engineering (ISIC)
Basic Science Faculty (SB)

156
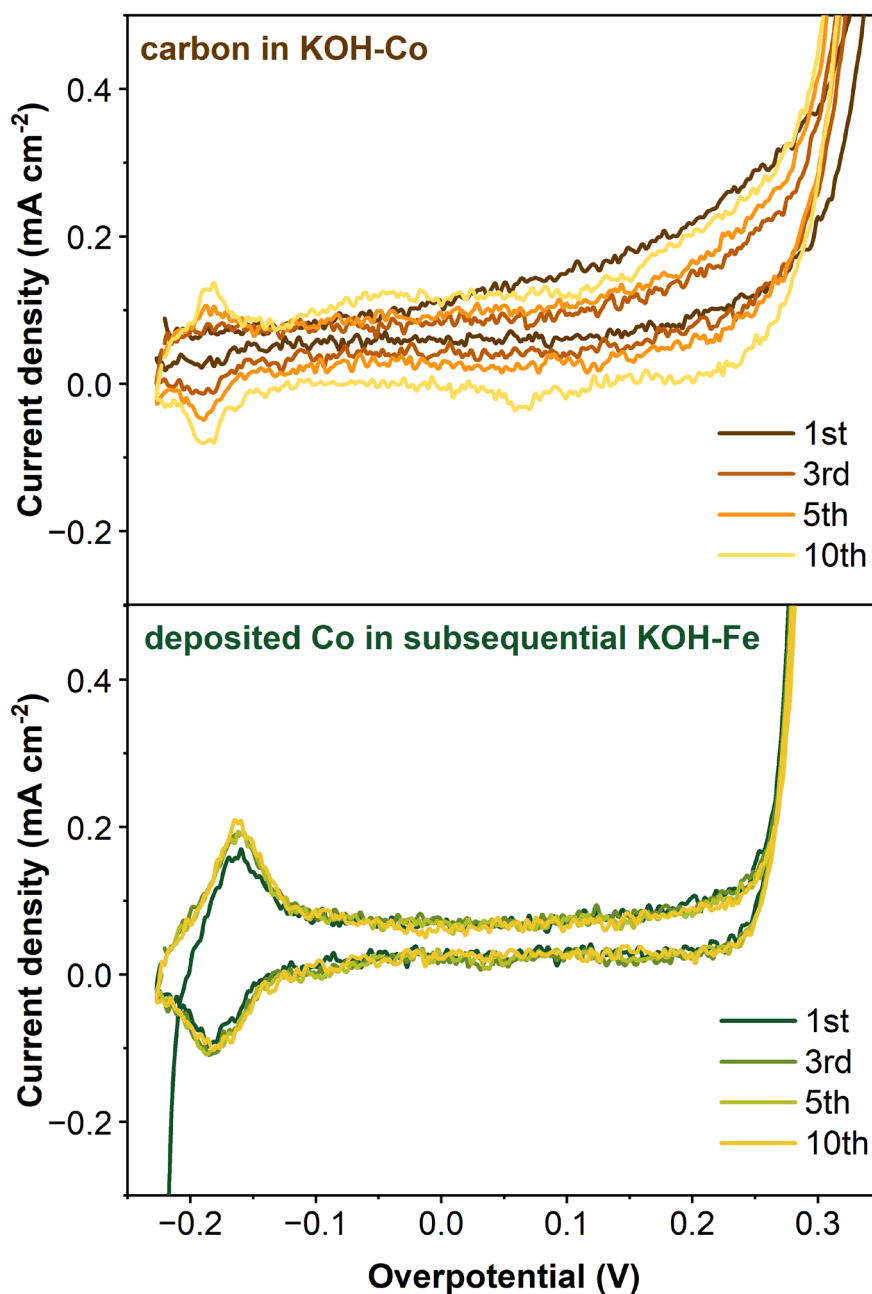
Figure S3.37. CV curve of GC-RDE cycled in KOH-Co, and that of deposited Co cycled in KOH-Fe, in the potential range prior to OER. The 1st, 3rd, 5th and 10th CV curves were presented to follow to evolution of electrochemical profile upon cycling.

Laboratory of Materials for Renewable Energy (LMER)
Institute of Chemical Sciences and Engineering (ISIC)
Basic Science Faculty (SB)

157
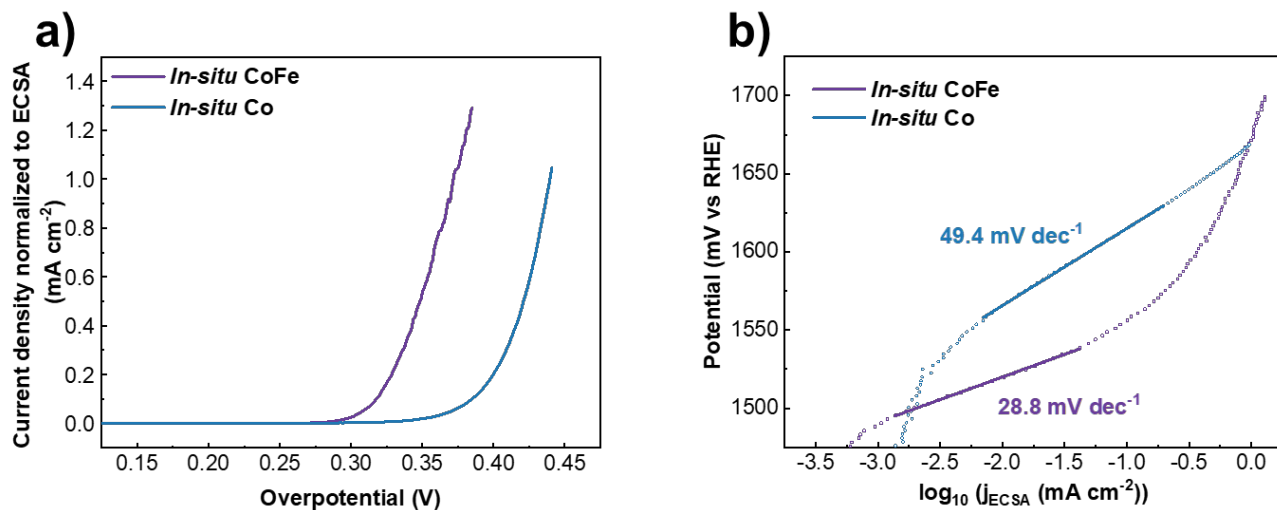
Figure S3.38. a) ECSA-normalized current density as a function of overpotential of in situ Co and Co-Fe catalysts. **b)** and the corresponding Tafel slopes.

Laboratory of Materials for Renewable Energy (LMER)
Institute of Chemical Sciences and Engineering (ISIC)
Basic Science Faculty (SB)

158

Table S3.8. Summary of Tafel slope, overpotential at 10 mA cm^{-2} and concentration of KOH from a variety of Co-Fe-based catalyst, IrO$_2$ and RuO$_2$.

Co-Fe-based catalyst	Tafel slope (mV dec^{-1})	Overpotential at 10 mA cm^{-2} (mV)	c_{KOH}	Ref
In situ Co-Fe	28.6	320	1 M	This work
Fe$_{0.33}$Co$_{0.67}$OOH PNSAs/CFC	30	266	1 M	Ref [28]
Co/Fe 32 red	41	339	1 M	Ref [51]
Co/Fe 32	55	378	1M	Ref [25]
Co$_{0.46}$Fe$_{0.54}$OOH	29	330	1 M	Ref [8]
Co$_3$Fe$_7$	70.8	440	0.1 M	Ref [27]
Co disk activated in Fe^{3+}	33	345	1 M	Ref [52]
Fe adsorbed CoO$_x$	27.6	309	1 M	Ref [43]
Co-Fe-N-C on carbon cloth	40	321	1 M	Ref [30]
Co-Fe-N-C on glassy carbon	44	360	1 M	Ref [14]
Co(Fe)OOH	55	300	0.1 M	Ref [24]
Fe-CoOOH/G	37	330	1 M	Ref [44]
FeCo$_2$O$_4$	83.2	470	0.1 M	Ref [45]
Co(Fe)OOH$_x$ nanoparticles (2.8%Fe)	43	556	1 M	Ref [46]
Fe$_1$Co$_3$Ox@C-800	40	272	1 M	Ref [53]
Co$_x$Fe$_{1-x}$P/NC	44	299	1 M	Ref [47]
CoFe-7.5	58	294	1 M	Ref [6]
BSCF	60	360	0.1 M	Ref [5]
CoFe$_2$O$_4$	82.15	403	0.1 M	Ref [48]
RuO$_2$ || C	52.7	328	1M	This work
IrO$_2$ || C	72.8	491	1M	This work

Laboratory of Materials for Renewable Energy (LMER)
Institute of Chemical Sciences and Engineering (ISIC)
Basic Science Faculty (SB)

159

REFERENCES

[1]   C. C. L. McCrory, S. Jung, J. C. Peters, T. F. Jaramillo, *J. Am. Chem. Soc.* **2013**, *135*, 16977.

[2]   C. Wei, R. R. Rao, J. Peng, B. Huang, I. E. L. Stephens, M. Risch, Z. J. Xu, Y. Shao-Horn, *Adv. Mater.* **2019**, *31*, 1.

[3]   M. Gong, H. Dai, *Nano Res.* **2014**, *8*, 23.

[4]   E. Fabbri, T. J. Schmidt, *ACS Catal.* **2018**, *8*, 9765.

[5]   J. Suntivich, K. J. May, H. A. Gasteiger, J. B. Goodenough, Y. Shao-Horn, *Science (80-.).* **2011**, *334*, 1383.

[6]   X. Gao, J. Liu, Y. Sun, X. Wang, Z. Geng, F. Shi, X. Wang, W. Zhang, S. Feng, Y. Wang, K. Huang, *Inorg. Chem. Front.* **2019**, *6*, 3295.

[7]   D. Friebel, M. W. Louie, M. Bajdich, K. E. Sanwald, Y. Cai, A. M. Wise, M. J. Cheng, D. Sokaras, T. C. Weng, R. Alonso-Mori, R. C. Davis, J. R. Bargar, J. K. Nørskov, A. Nilsson, A. T. Bell, *J. Am. Chem. Soc.* **2015**, *137*, 1305.

[8]   M. S. Burke, M. G. Kast, L. Trotochaud, A. M. Smith, S. W. Boettcher, *J. Am. Chem. Soc.* **2015**, *137*, 3638.

[9]   S. Jung, C. C. L. McCrory, I. M. Ferrer, J. C. Peters, T. F. Jaramillo, *J. Mater. Chem. A* **2016**, *4*, 3068.

[10]   W. H. Lee, M. H. Han, Y. J. Ko, B. K. Min, K. H. Chae, H. S. Oh, *Nat. Commun.* **2022**, *13*, 1.

[11]   B. S. Yeo, A. T. Bell, *J. Am. Chem. Soc.* **2011**, *133*, 5587.

[12]   L. Trotochaud, S. L. Young, J. K. Ranney, S. W. Boettcher, *J. Am. Chem. Soc.* **2014**, *136*, 6744.

[13]   M. B. Stevens, C. D. M. Trang, L. J. Enman, J. Deng, S. W. Boettcher, *J. Am. Chem. Soc.* **2017**, *139*, 11361.

[14]   L. Bai, C.-S. Hsu, D. T. L. Alexander, H. M. Chen, X. Hu, *J. Am. Chem. Soc.* **2019**, *141*, 14190.

[15]   J. Deng, M. R. Nellist, M. B. Stevens, C. Dette, Y. Wang, S. W. Boettcher, *Nano Lett.* **2017**, *17*, 6922.

[16]   T. Zhang, M. R. Nellist, L. J. Enman, J. Xiang, S. W. Boettcher, *ChemSusChem* **2019**, *12*, 2015.

[17]   J. T. Mefford, A. R. Akbashev, M. Kang, C. L. Bentley, W. E. Gent, H. D. Deng, D. H. Alsem, Y. S. Yu, N. J. Salmon, D. A. Shapiro, P. R. Unwin, W. C. Chueh, *Nature* **2021**, *593*, 67.

[18]   S. Jung, C. C. L. McCrory, I. M. Ferrer, J. C. Peters, T. F. Jaramillo, *J. Mater. Chem. A* **2016**, *4*, 3068.

[19]   L. Zhong, M. Barreau, D. Chen, V. Caps, M. Haevecker, D. Teschner, D. H. Simonne, E. Borfecchia, W. Baaziz, B. Šmíd, S. Zafeiratos, *Appl. Catal. B Environ.* **2021**, *297*, DOI 10.1016/j.apcatb.2021.120397.

Laboratory of Materials for Renewable Energy (LMER)
Institute of Chemical Sciences and Engineering (ISIC)
Basic Science Faculty (SB)

160

[20]   L. Zhong, M. Barreau, V. Caps, V. Papaefthimiou, M. Haevecker, D. Teschner, W. Baaziz, E. Borfecchia, L. Braglia, S. Zafeiratos, *ACS Catal.* **2021**, *11*, 5369.

[21]   H. Yu, Y. Wang, C. Zhu, Y. Jing, Q. Song, C. Guan, C.-F. Du, H. Yu, Y. Wang, Y. Jing, Q. Song, C. Du, C. Zhu, C. Guan, *Adv. Mater. Interfaces* **2021**, *8*, 2001310.

[22]   M. W. Louie, A. T. Bell, *J. Am. Chem. Soc.* **2013**, *135*, 12329.

[23]   A. Moysiadou, S. Lee, C. S. Hsu, H. M. Chen, X. Hu, *J. Am. Chem. Soc.* **2020**, *142*, 11901.

[24]   X. Cheng, B. J. Kim, E. Fabbri, T. J. Schmidt, *ACS Appl. Mater. Interfaces* **2019**, *11*, 34787.

[25]   E. Budiyanto, M. Yu, M. Chen, S. Debeer, O. Rüdiger, H. Tüysüz, *ACS Appl. Energy Mater.* **2020**, *3*, 8583.

[26]   Y. Liang, Y. Li, H. Wang, J. Zhou, J. Wang, T. Regier, H. Dai, *Nat. Mater.* **2011**, *10*, 780.

[27]   J. Meng, Z. Cui, X. Yang, S. Zhu, Z. Li, K. Qi, L. Zheng, Y. Liang, *J. Catal.* **2018**, *365*, 227.

[28]   S. H. Ye, Z. X. Shi, J. X. Feng, Y. X. Tong, G. R. Li, *Angew. Chemie - Int. Ed.* **2018**, *57*, 2672.

[29]   C. Alex, S. C. Sarma, S. C. Peter, N. S. John, *ACS Appl. Energy Mater.* **2020**, *3*, 5439.

[30]   L. Bai, C. S. Hsu, D. T. L. Alexander, H. M. Chen, X. Hu, *Nat. Energy* **2021**, *6*, 1054.

[31]   F. Song, X. Hu, *Nat. Commun.* **2014**, *5*, 4477.

[32]   S. Ye, J. Wang, J. Hu, Z. Chen, L. Zheng, Y. Fu, Y. Lei, X. Ren, C. He, Q. Zhang, J. Liu, *ACS Catal.* **2021**, *11*, 6104.

[33]   X. Deng, G. Y. Xu, Y. J. Zhang, L. Wang, J. Zhang, J. F. Li, X. Z. Fu, J. L. Luo, *Angew. Chemie - Int. Ed.* **2021**, *60*, 20535.

[34]   J. Li, G. Lu, G. Wu, D. Mao, Y. Guo, Y. Wang, Y. Guo, *RSC Adv.* **2013**, *3*, 12409.

[35]   Z. Chen, L. Cai, X. Yang, C. Kronawitter, L. Guo, S. Shen, B. E. Koel, *ACS Catal.* **2018**, *8*, 1238.

[36]   M. Inaba, Y. Iriyama, Z. Ogumi, Y. Todzuka, A. Tasaka, **1997**, *28*, 613.

[37]   J. Quiño, T. Hellwig, M. Griesing, W. Pauer, H. U. Moritz, S. Will, A. Braeuer, *Int. J. Heat Mass Transf.* **2015**, *89*, 406.

[38]   J.-W. Zhao, C.-F. Li, Z.-X. Shi, J.-L. Guan, G.-R. Li, *Research* **2020**, *2020*, 1.

[39]   R. L. Frost, M. L. Weier, J. T. Kloprogge, *J. Raman Spectrosc.* **2003**, *34*, 760.

[40]   C. G. Morales-Guio, L. Liardet, X. Hu, *J. Am. Chem. Soc.* **2016**, *138*, 8946.

[41]   P. Rüetschi, P. Delahay, *J. Chem. Phys.* **1955**, *23*, 556.

[42]   S. Trasatti, *J. Electroanal. Chem.* **1980**, *111*, 125.

[43]   L. Gong, X. Y. E. Chng, Y. Du, S. Xi, B. S. Yeo, *ACS Catal.* **2017**, *8*, 807.

[44]   X. Han, C. Yu, S. Zhou, C. Zhao, H. Huang, J. Yang, Z. Liu, J. Zhao, J. Qiu, *Adv. Energy Mater.* **2017**, *7*, 1602148.

Laboratory of Materials for Renewable Energy (LMER)
Institute of Chemical Sciences and Engineering (ISIC)
Basic Science Faculty (SB)

161

[45]   M. Harada, F. Kotegawa, M. Kuwa, *ACS Appl. Energy Mater.* **2022**, *5*, 278.

[46]   Z. Sun, A. Curto, J. Rodríguez-Fernández, Z. Wang, A. Parikh, J. Fester, M. Dong, A. Vojvodic, J. V. Lauritsen, *ACS Nano* **2021**, *15*, 18226.

[47]   J. Chen, Y. Zhang, H. Ye, J. Q. Xie, Y. Li, C. Yan, R. Sun, C. P. Wong, *ACS Appl. Energy Mater.* **2019**, *2*, 2734.

[48]   M. Li, Y. Xiong, X. Liu, X. Bo, Y. Zhang, C. Han, L. Guo, *Nanoscale* **2015**, *7*, 8920.

[49]   L. Gong, J. Koh, B. S. Yeo, *ChemSusChem* **2018**, *11*, 3790.

[50]   E. Budiyanto, S. Salamon, Y. Wang, H. Wende, H. Tüysüz, *JACS Au* **2022**, *2*, 697.

[51]   E. Budiyanto, S. Salamon, Y. Wang, H. Wende, H. Tü Ysü, *JACS Au* **2022**, *2*, 697.

[52]   L. Gong, J. Koh, B. S. Yeo, *ChemSusChem* **2018**, *11*, 3790.

[53]   X. Bai, Q. Wang, J. Guan, *ACS Appl. Nano Mater.* **2021**, *4*, 12663.

Laboratory of Materials for Renewable Energy (LMER)
Institute of Chemical Sciences and Engineering (ISIC)
Basic Science Faculty (SB)

162

CHAPTER 4:
Enhanced electrocatalytic CO₂ reduction to C₂₊ products by adjusting the local reaction environment with polymer binders

Thi Ha My Pham,[a,b] Jie Zhang,[a,b] Mo Li,[a,b] Tzu-Hsien Shen,[c] Youngdon Ko,[a,b] Vasiliki Tileli,[c] Wen Luo,[a,b,d],* Andreas Züttel[a,b]

[a]Laboratory of Materials for Renewable Energy (LMER), Institute of Chemical Sciences and Engineering (ISIC), Basic Science Faculty (SB), Ecole Polytechnique Fédérale de Lausanne (EPFL) Valis/Wallis, Energypolis, Rue de l'Industrie 17, CH-1951 Sion, Switzerland

[b]EMPA Materials & Technology, CH-8600 Dübendorf, Switzerland

[c]Institute of Materials (IMX), Ecole Polytechnique Fédérale de Lausanne (EPFL), CH-1015 Lausanne, Switzerland

[d]School of Environmental and Chemical Engineering, Shanghai University, 99 Shangda Road, Shanghai 200444, China

*Corresponding author: wenluo@shu.edu.cn, wen.luo@epfl.ch

Chapter 4 is reproduced with permission from John Wiley & Sons

Summary: Powder catalysts coated with polymer binder for enhanced electrochemical CO₂ reduction to multi-carbon products were developed, inspired by water-repulsive surfaces in the nature. The use of hydrophobic binders increases the local concentration of gas reactants and intermediates, suppressing the hydrogen evolution reaction.

Laboratory of Materials for Renewable Energy (LMER)
Institute of Chemical Sciences and Engineering (ISIC)
Basic Science Faculty (SB)

163
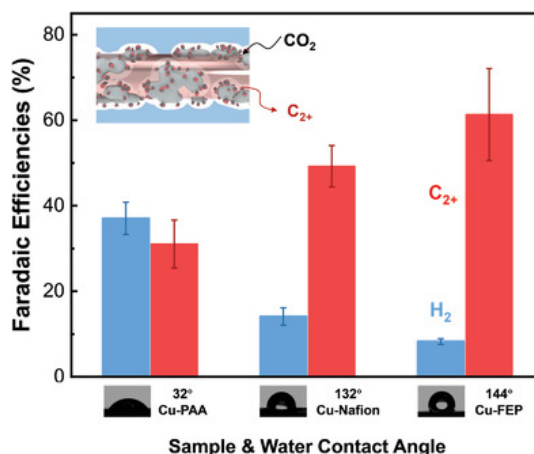
Abstract

The activity and selectivity of the electrochemical CO_2 reduction reaction (CO_2RR) are often hindered by the limited access of CO_2 to the catalyst surface and overtaken by the competing hydrogen evolution reaction. Herein, it is revealed that polymers used as catalyst binders can effectively modulate the accessibility of CO_2 relative to H_2O at the vicinity of the catalyst and thus the performance of CO_2RR. Three polymers with different hydrophilicities (i.e., polyacrylic acid (PAA), Nafion, and fluorinated ethylene propylene (FEP)) were selected as binders for Cu catalysts. At a thickness of only ~1.2 nm, these binders strongly affected the activity and selectivity towards multi-carbon (C_{2+}) products. The FEP coated catalyst exhibits a C_{2+} partial current density of over 600 mA cm^{-2} with ~77% faradaic efficiency at −0.76 V vs. RHE. This high performance is benefitted from the hydrophobic (aerophilic) property of FEP, which reduces the local concentration of H_2O and enhance that of the reactant (i.e., CO_2) and the reaction intermediates (i.e., CO). These findings suggest that tuning the hydrophobicity of electrocatalysts with polymer binders can be a promising pathway to regulate the performance of electrochemical reactions involving gas-solid-liquid interfaces.

Keywords: electrocatalysis, CO_2 reduction, polymer binder, copper catalyst, hydrophobicity

Laboratory of Materials for Renewable Energy (LMER)
Institute of Chemical Sciences and Engineering (ISIC)
Basic Science Faculty (SB)

164

1. Introduction

Over the past century, an excessive amount of CO_2 has been released into the atmosphere due to the consumption of fossil fuels, giving rise to climate change and other environmental problems [1,2]. A zero-emission energy economy is no longer sufficient; the discharged carbon in the atmosphere must be sequestrated. Recently, electrochemical CO_2 reduction reactions (CO2RR) enabled by renewable energy have been suggested as a promising strategy to solve these problems, sequestrating discharged CO_2 into chemical feedstocks and downscaling the use of fossil fuels in the chemical production industry. In addition, CO2RR is an efficient way to store electricity generated from intermittent renewable energies in the form of liquid fuels for transport and other applications [3–5].

Copper-based materials are the most investigated class of catalysts for CO2RR due to their unique ability to reduce CO_2 molecules to carbonaceous compounds containing more than two carbon atoms (C_{2+} products). However, the high overpotential required and the low product selectivity over the pristine Cu surface have motivated researchers to develop more efficient strategies to overcome these challenges. Most previous publications have focused on engineering the properties of Cu-based catalysts, such as optimizing the size and shape of Cu nanomaterials [6–10], introducing grain boundaries [11], and creating alloys with other metals [12–15] to increase the number of active sites and/or to improve the intrinsic catalytic activities of Cu towards the desired products. Despite the tremendous progress that has been made, CO2RR is still not viable at an industrial scale.

The performance of a catalytic reaction, however, is not only affected by the catalyst. It is also influenced by reaction pressure, temperature, ratio of reactants, etc. In the case of CO2RR, the reaction is mostly carried out at room temperature and at ambient pressure conditions; hence, tuning the ratio of reactants becomes a practical and attractive strategy to improve the performance of CO2RR. Since H_2O and CO_2 are the reactants for aqueous CO2RR, and the hydrogen evolution reaction (HER) from H_2O is the competitive reaction that limits the CO2RR selectivity, it is reasonable to optimize the ratio of H_2O and CO_2 to suppress H_2 evolution and enhance the electrolysis of CO_2. In a conventional H-cell reactor, the electrode is immersed in the electrolyte, and CO_2 molecules dissolve in the electrolyte and diffuse to the surface of the electrode. Thus, the ratio of CO_2 to H_2O is always limited by the low solubility and slow diffusion of CO_2, particularly at high current densities [16]. Using a flow reactor can overcome this limitation, as the supply of CO_2 and H_2O is separated by the gas diffusion electrode (GDE) [17,18]. However, GDEs tend to lose their hydrophobicity during CO2RR, leading to the flooding of the electrodes and, consequently, a decrease in CO_2 mass transport [19,20]. To maintain a higher CO_2 to H_2O ratio, researchers have tried to coat Cu surfaces with a relatively thick layer of polymer or ionomer[21–23]. This strategy, however, may decrease the conductivity of the electrode and block the active sites of the catalyst[21].

On the other hand, polymers are often used to bind catalyst powders onto the supporting material (e.g., carbon paper), and Nafion is an almost universal binder selection for catalysts used in CO2RR due to its good proton conductivity. However, little attention has been paid to whether Nafion is the most suitable binder for Cu catalysts used in CO2RR, and how the hydrophobicity of polymer binders affects the catalytic performance. Here, we used three types of polymers, such as polyacrylic acid (PAA) and fluorinated

Laboratory of Materials for Renewable Energy (LMER)
Institute of Chemical Sciences and Engineering (ISIC)
Basic Science Faculty (SB)

165

ethylene propylene (FEP), as binders for Cu catalysts, and revealed that their distinct hydrophobic properties can change the transport of H_2O and CO_2 to the electrode surface, thus greatly affecting the activity and selectivity of CO_2RR. We observed an enhanced selectivity towards carbonaceous products, particularly in C_{2+} products, induced by the hydrophobicity of the FEP binder. We also observed an increased H_2 selectivity induced by a hydrophilic binder (PAA). Specifically, with FEP as a binder, we achieved ~50% Faradaic efficiency (FE) for C_{2+} at -1.1 V vs RHE in a conventional H-cell and ~77% C_{2+} FE at -0.76 V vs RHE in a flow cell. In addition, we confirmed the important role of polymer binders in tuning the local environment through ex-situ and in situ characterizations. Since polymer binders are widely used in electrochemical reactions, including CO_2, CO and N_2 reduction reactions, we believe that this work is of great importance to researchers from these fields and we anticipate that screening of polymer binders will be an important step in future studies.

2. Results & Discussions

2.1. Characterization of the copper electrode

CuO was synthesized from $Cu(NO_3)_2$ and NaOH through a simple precipitation method and used as a representative Cu catalyst in this work. The X-ray diffraction (XRD) spectrum confirmed that the obtained material was pure polycrystalline CuO (Figure 4.1a). The morphology of CuO was studied using scanning electron microscopy (SEM), and a highly porous structure was revealed (Figure S4.1). Close-up analysis of the CuO material reveals that the porous structure was built out of CuO needles, which have a length of several hundred nanometers and a width of 10 to 20 nm (Figure 4.1b). The high-resolution transmission electron microscopy (HR-TEM) images acquired at the edge of a CuO needle indicates that the needle was composed of small grains with a well-defined crystal structure (Figure S4.2a) and rich in grain boundaries (Figure S4.2b). Figure 4.1c shows HR-TEM images of particles with grains corresponding to various crystalline planes. Figure 4.1d is composed of four representative grains with well-defined d-spacings between the crystalline planes, which can be attributed to the exposure of (002), (111), and ($\bar{1}$13) facets (Figure S4.2c), verifying the polycrystalline nature of the as-synthesized CuO catalyst.

Laboratory of Materials for Renewable Energy (LMER)
Institute of Chemical Sciences and Engineering (ISIC)
Basic Science Faculty (SB)

166
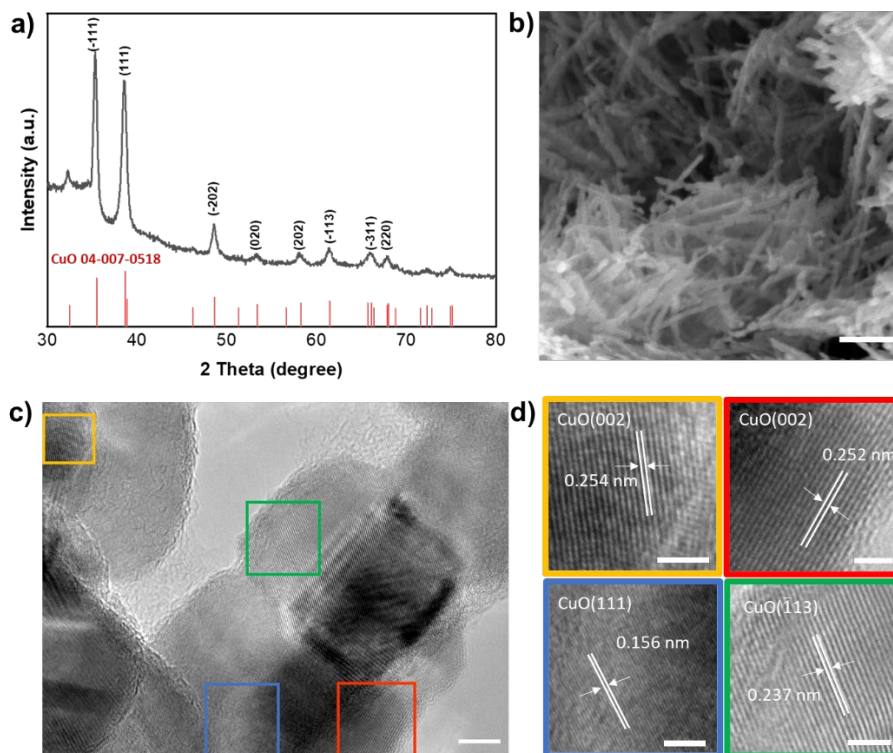
Figure 4.1. Physical characterizations of the as-synthesized powder catalysts. a) XRD pattern of the as-synthesized catalyst including the diffraction lines of CuO from the Powder Diffraction File database. b) Needle like structure of the as-synthesized CuO with an aspect ratio of 6 to 10. (SEM image, Scale bar: 200 nm). c) Selected grains of as-synthesized CuO (HR-TEM image, Scale bar: 10 nm). d) Magnified image of the areas outlined in Figure 4.1c. (HR-TEM images, Scale bar: 2 nm).

For preparing the working electrode, we chose three types of polymers that have different hydrophobicities as binders: (1) PAA, which only has hydrophilic functional groups; (2) Nafion, which has both hydrophobic and hydrophilic functionalities; and (3) FEP, which only has hydrophobic functional groups (chemical formulae shown in Figure S4.3). The CuO powder and the polymer binder (0.2 mg/mg catalyst) were simply mixed in iso-propanol, sonicated for dispersing, and drop-casted to prepare the electrode. The distribution of the polymer binder on the powder catalyst was first studied using SEM energy-dispersive X-ray spectroscopy (SEM-EDX). Figure 4.2a shows a SEM image and its corresponding EDX map of the Cu-PAA sample, where the map of carbon present in PAA strongly overlaps with that of Cu, indicating that PAA is uniformly distributed on the CuO needles. Similar results were also obtained for Cu-Nafion and Cu-FEP, as indicated by the overlap of the elemental map of F and those of Cu and O (Figure S4.4). In addition, energy-filtered TEM (EF-TEM) was used to investigate the coverage of the polymer layer on the powder catalyst. Figure 4.2b shows the bright-field TEM image of CuO particles coated with the PAA polymer. The corresponding EF-TEM carbon elemental map in Figure 4.2c using core-loss carbon K edge electron energy-loss spectra (EELS) corroborates the fact that the carbonaceous polymer layer was homogeneously coated on the surface of the CuO particles. The TEM images in Figure S4.5 also show that the coating layer had a thickness of around 1.2 nm for all three samples. Thus, these results demonstrate that a simple method involving physical mixing and ultrasonication is sufficient to coat the surface of the CuO powder with a thin layer of polymer binder.

Laboratory of Materials for Renewable Energy (LMER)
Institute of Chemical Sciences and Engineering (ISIC)
Basic Science Faculty (SB)

167

The surface properties of polymer coated CuO samples were studied using X-ray photoelectron spectroscopy (XPS). For this measurement, the three dispersions were drop-casted on clean Au foils to ensure good conductivity and to avoid the influence of other elements. On all three samples, the presence of polymer binder on the CuO surface was confirmed, with C-O, C=O, and C-F peaks clearly observable in the C 1s and O 1s region in the XPS spectra (Figure 4.2d). All samples show typical Cu 2p spectra of CuO, indicated by the presence of Cu $2p_{3/2}$ peak at ~933.6 eV as well as high intensity satellite peaks. In addition, no peaks related to Cu-F or Cu-S bonding were detected, demonstrating that coating of polymer binder did not change the chemical properties of CuO.
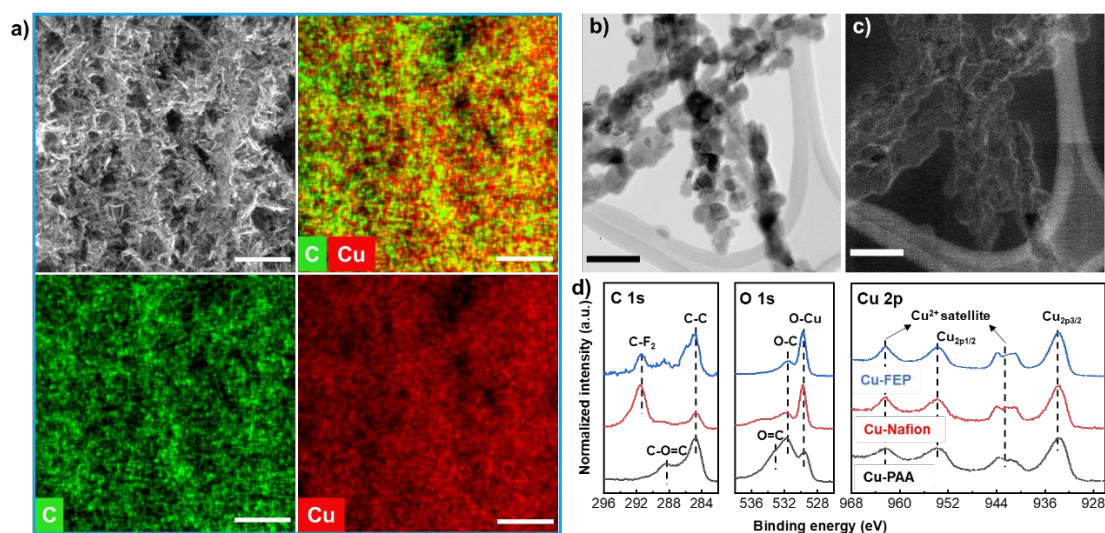
Figure 4.2. Morphology and chemical composition of the Cu-polymer catalysts. a) Cu-PAA drop-casted on a Ni foil (SEM image and the corresponding elemental map of Cu and C, Scale bar: 1 µm). A clean Ni foil was used as substrate to avoid the influence of other elements. b) Morphology of CuO (bright-field TEM image, Scale bar: 50 nm) and c) The corresponding carbon distribution of the Cu-PAA catalyst (EF-TEM carbon elemental map, Scale bar: 50 nm). d) Surface chemistry of the three Cu-polymer catalysts (XPS spectra for C 1s, O 1s, and Cu 2p, respectively); a clean Au foil was used for good conductivity and to avoid the influence of other elements.

To evaluate the effect of different polymer binders on the hydrophobicity of Cu-based electrodes, we performed the water contact angle (WCA) and the captive bubble contact angle (CBCA) measurements. Figure 4.3 shows that the WCA for Cu-PAA, Cu-Nafion, and Cu-FEP were 32°, 132°, and 144°, respectively, corresponding to an increasing trend in hydrophobicity. On the other hand, the measured CBCA followed an opposite trend compared to the WCA (Figure 4.3): the contact angle for the CO_2 bubble increased from Cu-FEP (47°) to Cu-Nafion (73°) and Cu-PAA (117°). These results indicate that a thin layer of polymer binder can successfully change the hydrophobicity of the electrode. With PAA as a binder, the electrode surface is highly hydrophilic, hindering the access of CO_2 towards the surface of the catalyst during CO_2RR. In contrast, for Cu-FEP electrodes, the hydrophobic nature of FEP favors the accumulation of CO_2 gas, thus can increase its local concentration near the catalyst. Overall, from the comprehensive characterizations above, we can conclude that Cu-based catalysts coated with a thin layer of three different polymer binders were successfully synthesized. The hydrophobicity of the electrode was effectively tuned by the hydrophilic

Laboratory of Materials for Renewable Energy (LMER)
Institute of Chemical Sciences and Engineering (ISIC)
Basic Science Faculty (SB)

168

or hydrophobic properties of the polymer binder, which is expected to change the ratio of reactants (H_2O and CO_2) near the surface of the electrode.
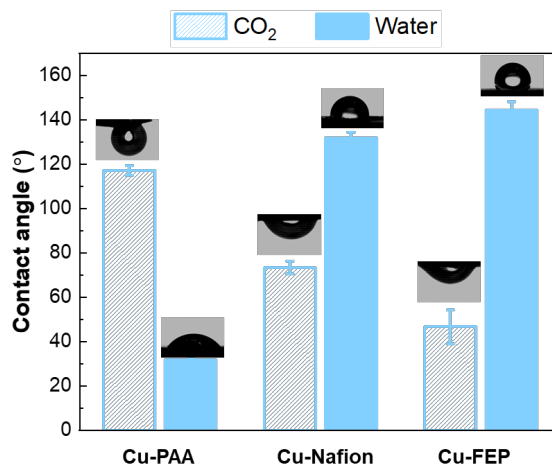
Figure 4.3. Characterization of the hydrophilicity and CO_2-philicity of the Cu-polymer catalysts. The water- and CO_2-contact angles of each catalyst were determined by the tangent method. Water contact angle: filled, CO_2 captive contact angle: striped.
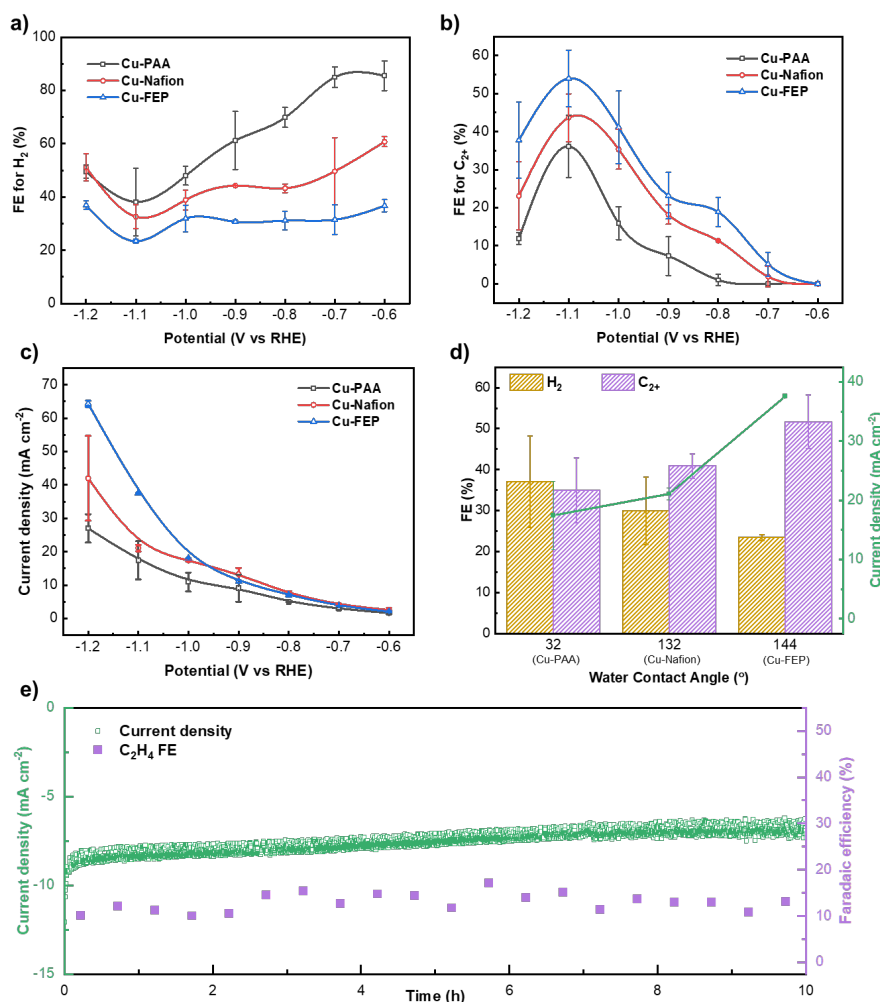
2.2. CO₂RR performance

To evaluate the effect of the polymer binder on the catalytic performance of the as-synthesized Cu-based catalysts, we first performed CO_2RR tests in a conventional H-cell in CO_2-saturated 0.1 M $KHCO_3$ at potentials ranging from -0.6 to -1.2 V vs RHE (product distributions are shown in Figure S4.7, with bare Cu sample as reference). The FEs of H_2 on CuO-derived catalysts with three different binders were plotted against the applied potential (Figure 4.4a). The H_2 selectivity was significantly suppressed in the entire potential range by the hydrophobic polymer, compared to a hydrophilic polymer such as PAA. Consequently, the total FEs for CO_2RR (FEs for CO, formate, CH_4, C_2H_4, n-propanol, ethanol, and acetate) increased with the polymer's hydrophobicity and aerophilicity (Figure S4.8a). We further analyzed the product distribution of CO_2RR and plotted the FEs for C_{2+} products (C_2H_4, n-propanol, ethanol, and acetate) and C_1 products (CO, HCOOH, and CH_4) in Figure 4.4b and Figure S4.8b, respectively. As shown in Figure 4.4b, C_{2+} products can be detected at potentials from -0.7 V vs RHE for all three samples, and the FEs increased with the hydrophobicity of the surface: Cu-FEP > Cu-Nafion > Cu-PAA. The highest FE of C_{2+} products ($\sim$ 52%) was reached on the CuO-FEP electrode at -1.1 V vs RHE at a partial current density of 37.4 mA cm^{-2}. In addition, the enhancement of the CO_2RR selectivity by the hydrophobic polymer is more significant for C_{2+} than that for C_1 products, especially at high overpotentials. As shown in Figure S4.8c, the maximum ratio of C_{2+} FE to C_1 FE for the Cu-FEP electrode was 5.5, while the ratio for the Cu-PAA sample was only 2. These results suggest that the polymer binder plays a significant role in enhancing the selectivity of CO_2RR, especially for C_{2+} products, while suppressing the selectivity of H_2.

In addition to product selectivity, the current density of CO_2RR was also affected by the polymer binder. As shown in Figure 4.4c, at a high overpotential range (-1.0 to -1.2 V vs RHE), the overall current density of Cu-FEP was higher than that of Cu-Nafion and Cu-PAA. The high current density of Cu-FEP was mainly

Laboratory of Materials for Renewable Energy (LMER)
Institute of Chemical Sciences and Engineering (ISIC)
Basic Science Faculty (SB)

169

attributable to the increased partial current density for CO_2RR rather than HER (Figure S4.9 a,b). This indicates that even with a thin hydrophobic polymer layer on the catalyst surface, the H_2O supply in the H-cell was still sufficient for HER, and the enhanced CO_2 local concentration was the key to improved CO_2RR activity and C_{2+} selectivity. Further, we evaluated the effect of binder content on the catalytic performance. As shown in Figure S4.10, a low level of FEP (0.05 mg/mg-catalyst) could not effectively promote the reduction of CO_2 to C_{2+} products, while an excessive amount of FEP (0.8 mg/mg-catalyst) led to thick coatings that block the active surface of the catalyst, again demonstrating the important role of polymer binders in electrocatalysis.

After the performance tests, the morphology and the hydrophobicity of the used catalysts were studied. The highly porous network and the needle-like structure of CuO remained intact for all three samples, as demonstrated in the SEM images (Figure S4.11). Also, the polymer layers coated on the CuO needles are preserved (Figure S4.11 c,f,i). In consequence, the WCAs of the three used samples are very similar to that of the fresh sample, indicating that the initial CuO reduction and the following CO_2 electrolysis process did not change the hydrophobicity of the catalysts (Figure S4.12). During long-term test, the current density and FE for C_2H_4 remained stable for Cu-FEP (Figure 4.4e) and Cu-Nafion (Figure S4.13a), while a decrease of FE for C_2H_4 and fluctuations in current density were observed due to the wetting of the Cu-PAA electrode (Figure S4.13b). Overall, a good correlation between the CO_2RR performance and the surface hydrophobicity can be established (Figure 4.4d), and this correlation can be further extended to other polymer binders (Figure S4.14).
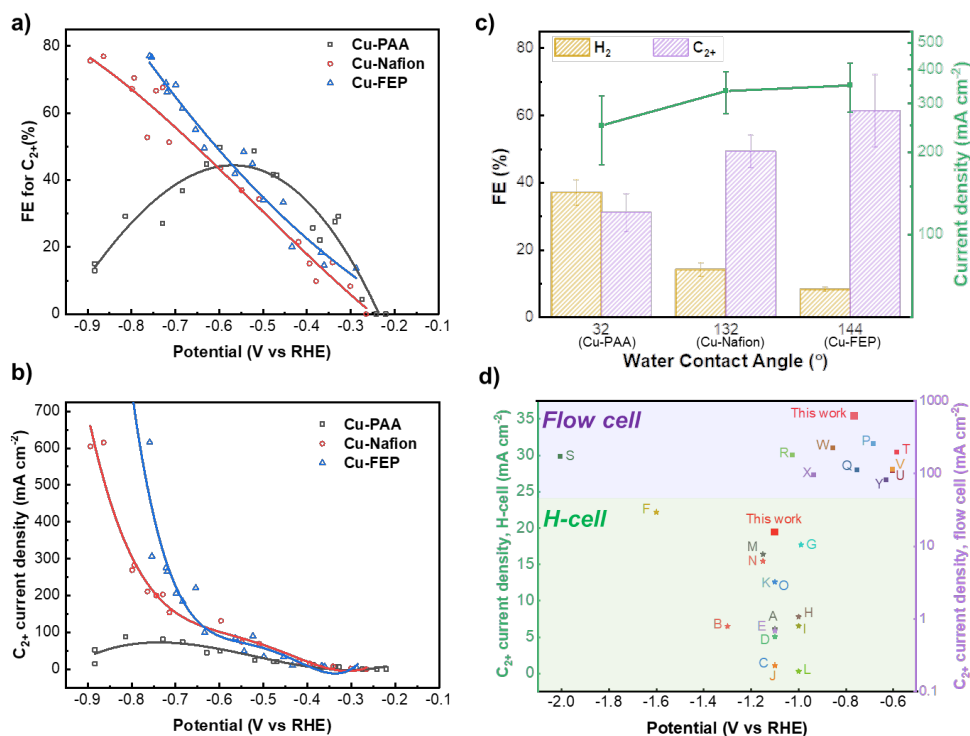
Laboratory of Materials for Renewable Energy (LMER)
Institute of Chemical Sciences and Engineering (ISIC)
Basic Science Faculty (SB)

170

Figure 4.4. (a) Faradaic efficiency of H_2, (b) faradaic efficiency C_{2+} products, and (c) Total current density for Cu-PAA, Cu-Nafion and Cu-FEP. (d) Activity and product selectivity of the CO_2RR towards H_2 and C_{2+} products as a function of the hydrophilicity, acquired in H-cell at -1.1 V vs RHE. (e) Current density and C_2H_4 selectivity for Cu-FEP over 10 h of CO_2RR, acquired in H-cell at -0.8 V vs RHE.

As we have shown above, although the hydrophobic layer can dramatically improve the performance of CO_2RR in the H-cell, both the current density and C_{2+} selectivity are still limited by the low CO_2 concentration (~34 mM L^{-1}). To overcome the limitations of CO_2-solubility, we performed CO_2 electrolysis in a flow cell where the CO_2 supply and H_2O supply were decoupled by a gas diffusion electrode (GDE). The experiments were performed at constant current densities of 50, 100, 200, 300, 400, and 800 mA cm^{-2} using 1.0 M KOH as an electrolyte, and product distributions are shown in Figure S4.15. Similar to the H-cell, the use of hydrophobic bonder suppressed significantly the HER over the whole range of overpotential (Figure S4.16). Figure 4.5a shows the FEs of C_{2+} products for the Cu-FEP, Cu-Nafion, and Cu-PAA samples. The C_{2+} selectivity of Cu-FEP and Cu-Nafion increased continuously with a decrease in the applied potential, unlike in the H-cell where volcano-shaped curves were observed. This trend can be explained by the absence of the limitation of CO_2 mass transport in the flow reactor even at much higher current densities. However, the volcano-shaped C_{2+} FE curve was still observed for Cu-PAA, where the C_{2+} FE reached a maximum of 49% between -0.5 and -0.6 V vs RHE, and then dropped down to only 13% at -0.88 V vs RHE. This was mainly due to the low hydrophobicity of the Cu-PAA electrode which led to severe flooding, and hence

Laboratory of Materials for Renewable Energy (LMER)
Institute of Chemical Sciences and Engineering (ISIC)
Basic Science Faculty (SB)

171

limited CO_2 transport at higher overpotential ranges, as salt crystals were clearly observed on the CO_2-gas side of the GDE after only a few minutes of reaction (Figure S4.17). Notably, at -0.76 V vs RHE, Cu-FEP showed the highest C_{2+} FE of ~77% towards C_{2+} products and a partial current density of more than 600 mA.cm^{-2} (Figure 4.5b). Cu-Nafion also reached similar FE and current density but at a more negative potential (-0.86 V vs RHE). In the case of the hydrophilic Cu-PAA sample, the best partial current density for C_{2+} was 87.6 mA cm^{-2} at -0.81 V vs RHE, approximately eight times lower than that of the Cu-FEP and Cu-Nafion samples. Thus, similar to that of the H-cell, the binder's hydrophobicity correlates well to the activity and selectivity of the Cu catalysts in the flow reactor, as summarized in Figure 4.5c and Figure S4.14b. By performing additional control experiments using the spray-coating method to prepare GDE[24], we further confirm that this hydrophobicity-performance correlation is also applicable for electrodes prepared by other methods (Figure S4.18).

Previous studies have shown that electrodes are much less stable in flow cells than that in H-cells due to the flooding issue. However, we find that the stability of the GDE can be significantly improved with a hydrophobic binder. For the Cu-FEP electrode, no flooding was observed after 16 h of stability test at 200 mA cm^{-2} in 1.0 M KOH, and the FE for C_2H_4 even increased slightly with the reaction time (Figure S4.19a). In comparison, after 10 h test, the Cu-Nafion electrode became less stable at 200 mA cm^{-2} and the Cu-PAA electrode was completely flooded at only 50 mA cm^{-2}. Notably, the morphology of Cu nanowires changed during the reaction, which is similar to previous observations that Cu catalysts undergo reconstruction[25]. The reconstruction is more obvious for the Cu-PAA sample, as the needle-like structure of Cu changed to a particle structure after 15 min of CO_2 electrolysis at 50 mA cm^{-2} (Figure S4.20). After longer reaction time, the morphology reconstruction takes place for all three samples (Figure S4.21). However, EDX maps showed that polymer binders remained on the electrode and their signals overlapped with that of Cu (Figure S4.21b,c), explaining the high stability of the Cu-FEP sample.

Laboratory of Materials for Renewable Energy (LMER)
Institute of Chemical Sciences and Engineering (ISIC)
Basic Science Faculty (SB)

172

Figure 4.5. (a) Faradaic efficiency for C_{2+} products, (b) Partial current density for C_{2+} products, and (c) Activity and product selectivity of the CO_2RR towards H_2 and C_{2+} products as a function of the hydrophilicity, acquired in flow cell at -0.71 V vs RHE, with aqueous 1.0 M KOH as electrolyte. (d) C_{2+} production rate (represented as partial current density) as a function of the potential. The Cu-FEP catalyst compared with other reported CO_2RR catalysts obtained in H-cells (star) and flow cells (square). Details of each catalyst and the reported reactions conditions are provided in Table S4.2 and Table S4.3.

We also compared the performance of the Cu-FEP sample with the reported state-of-the-art Cu-based catalysts in H-cells [8,21,33–36,22,26–32] and flow cells [18,24,37–41] (Figure 4.5d), in terms of the partial current density and the applied potential. It is clear that in both the H-cell and flow cell reactors, our Cu-FEP sample is among the best Cu-based catalysts documented in the literature, showcasing high C_{2+} selectivity and current density at relatively low overpotentials. These results demonstrate that optimizing the hydrophobicity of the electrode with a polymer binder is a simple yet highly effective way of enhancing the CO_2RR performance of Cu-based catalysts.
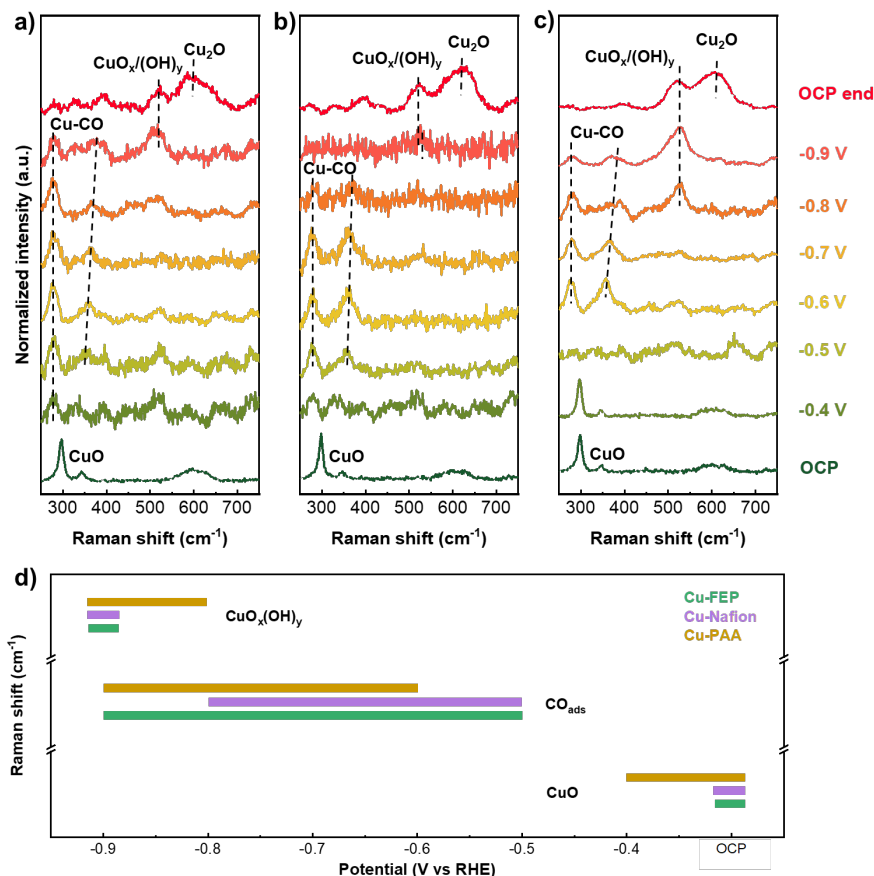
2.3. Investigation into the mechanism of C_{2+} enhancement

To gain insight into the enhanced C_{2+} selectivity observed on the hydrophobic electrode, we monitored the reduction process of the CuO and intermediates of CO_2RR using operando surface-enhanced Raman spectroscopy (SERS). As shown in Figure 4.6, for all three samples, two distinct peaks at 298 and 340 cm⁻¹ and one broad peak ranging between 570–650 cm⁻¹ were observed at open circuit potential (OCP), which are originated from cupric oxide (CuO) [42,43]. When -0.4 V vs RHE was applied, all of the above peaks disappeared from the Cu-Nafion and Cu-FEP spectra, indicating that the Cu samples were completely reduced to Cu. In the case of Cu-PAA, these peaks disappeared at -0.5 V vs RHE, suggesting that the

Laboratory of Materials for Renewable Energy (LMER)
Institute of Chemical Sciences and Engineering (ISIC)
Basic Science Faculty (SB)

173

reduction of Cu to metallic Cu is more sluggish compared to the other two cases. This may be attributed to the slightly denser and thicker layer of PAA coating around the powder catalyst due to its higher solubility (Figure S4.5).

After the complete reduction of Cu, several Raman peaks related to the adsorbed CO appeared. Two peaks at 280 and 367 cm^{-1} were attributed to the rotation of CO_{ads} on Cu and the stretching of metal-molecular bond, respectively [14,30,44,45] (Figure 4.6); a broad band ranging between 2000–2093 cm^{-1} was attributed to the internal stretching of CO molecule (Figure S4.22). This broad peak was composed of two adjacent peaks: the first peak at 2000 cm^{-1} corresponded to the CO_{atop} configuration, and the second peak at 2093 cm^{-1} arose from the CO_{bridge} configuration [45]. These peaks became more clearly defined at moderate overpotentials (-0.6 and -0.7 V vs RHE), indicative of a greater degree of CO coverage at this potential range. We also observed a blueshift in the metal-molecular stretching as the potential became more negative, which had been previously attributed to the electrochemical Stark effect [46,47]. Starting from -0.9 V vs RHE for Cu-FEP and Cu-Nafion, and from -0.8 V vs RHE for Cu-PAA, a new peak at 520 cm^{-1} appeared. This was reported to be from adsorbed OH_{ads} on the Cu surface, originating from the high local pH near the catalyst surface due to the consumption of protons by CO_2RR and HER [48]. After removing the potential, no intermediate peaks were detected, but a new broad peak indicative of cuprous oxide appeared at 610–625 cm^{-1}[45]. Thus, we can conclude that metallic copper is the active site for CO_2RR, and is responsible for adsorbing the key reaction intermediate, CO, for C_{2+} products.

The results above can be correlated with the electrochemical performance of the catalysts. Figure 4.6d summarized the presence of adsorbed species on the catalyst surface at various applied potentials. The CO adsorption peaks were observed in a wider potential range (-0.5 to -0.9 V vs RHE) for Cu-FEP compared to that for Cu-Nafion (-0.5 to -0.8 V vs RHE) and Cu-PAA (-0.6 to -0.9 V vs RHE). The enhanced CO chemisorption can be attributed to the high production rate of CO (Figure S4.23) induced by the high local concentration of CO_2 on the surface, as well as to the accumulation of CO on the catalyst surface thanks to the hydrophobicity of the polymer binder. As CO is the key intermediate for C_{2+} products, the presence of these CO chemisorption peaks at low overpotentials, as well as over a wide potential range, explains why Cu-FEP produced more C_{2+} products over the entire potential range compared to Cu-Nafion and Cu-PAA.

Laboratory of Materials for Renewable Energy (LMER)
Institute of Chemical Sciences and Engineering (ISIC)
Basic Science Faculty (SB)

174

Figure 4.6. Operando Raman spectra of (a) Cu-FEP, (b) Cu-Nafion, (c) Cu-PAA. From bottom to top: initial OCP, -0.4 to -0.9 V vs RHE, final OCP. (d) Adsorbed species ($CuO_x(OH)_y$, CO_{ads}, CuO) present at the surface of the three working electrode (Cu-FEP, Cu-Nafion, Cu-PAA) during the CO_2RR, identified by operando Raman. The detection of each surface species at their characteristic Raman shifts was presented with respect to the applied potential.

While the contact angle measurements shed light on how the ratio between CO_2 and H_2O was responsible for the enhanced CO_2RR selectivity, the operando Raman measurements suggest that the ratio between CO and H_2O plays a key role in tuning the C_{2+} selectivity. To further verify these results, we carried out control experiments on a catalyst with better CO selectivity (Figure S4.24): the Au-nanoparticle-decorated CuO catalyst (Figure S4.24a, b). Catalysts with the three different polymer binders were denoted as Au@Cu-PAA, Au@Cu-Nafion, and Au@Cu-FEP. We also evaluated these samples in an H-cell using 0.1 M $KHCO_3$ as the electrolyte. As expected, the Au@Cu-FEP catalyst, which contains the most hydrophobic polymer binder, exhibited the highest CO_2RR selectivity due to the highest local CO_2 concentration (Figure S4.24c). However, its C_{2+} selectivity was lower than that of Au@Cu-Nafion (Figure S4.24d). Since Au is highly selective for CO but not active for HER, the Au@Cu surface was expected to require more protons to further reduce the adsorbed CO towards C_{2+} products compared to a pure Cu catalyst. Consequently, when the binder is partially hydrophilic, as is the case of Au@Cu-Nafion, the reduction of CO is more efficient, resulting in greater C_{2+} selectivity. These results, together with those observed from Cu-polymer catalysts, allows us to conclude that the hydrophobicity of polymer binders can effectively regulate the activity and selectivity of CO_2RR by tuning the local concentrations of reactants (i.e., CO_2 and H_2O) and intermediates (i.e., CO).

Laboratory of Materials for Renewable Energy (LMER)   175
Institute of Chemical Sciences and Engineering (ISIC)
Basic Science Faculty (SB)

Based on the results described above, the mechanism of CO_2RR over Cu-polymer binder catalysts is illustrated in Figure 4.7. In an H-cell, Cu particles are coated with a layer of binder, the electrolyte is CO_2-saturated, and both protons and CO_2 have to access the catalyst surface through the electrolyte. In the case of Cu-PAA, due to the hydrophilic nature of the binder, the surface of the catalyst is covered by the electrolyte such that the CO_2 concentration is much lower than H_2O (33 mmol L^{-1} for CO_2 compared to 55 mol L^{-1} for H_2O) (Figure 7a). For Cu-FEP, due to the high hydrophobicity of FEP, there exist local channels around the catalyst where only CO_2-vapor can access the electrode, thus increasing the local concentration of CO_2 and enhancing CO_2RR (Figure 4.7b). In a flow cell, the catalyst is drop-casted on the microporous layer (MPL) side of the GDE, and CO_2 is introduced from the other side. The reaction takes place at the triple-phase boundary where the catalyst is in contact with both the electrolyte and CO_2. With a hydrophilic binder, these boundaries are located only at the electrolyte-MPL interface, because the surface of the catalyst is covered by the electrolyte (Figure 4.7c). When a hydrophobic binder such as FEP is used, the catalyst is only partially in contact with the electrolyte due to the water-repellent properties of the binder. A micro-hydrophobic environment is created around the FEP molecules and allows CO_2 to access surfaces of the catalyst that are located far away from the electrolyte-MPL interface, thus enhancing CO_2RR (Figure 4.7d). Furthermore, in both configurations, a high concentration of CO_2 near FEP can result in a high production rate of CO; this, combined with the enhanced accessibility of CO to the catalyst surface, improves the selectivity of C_{2+}.
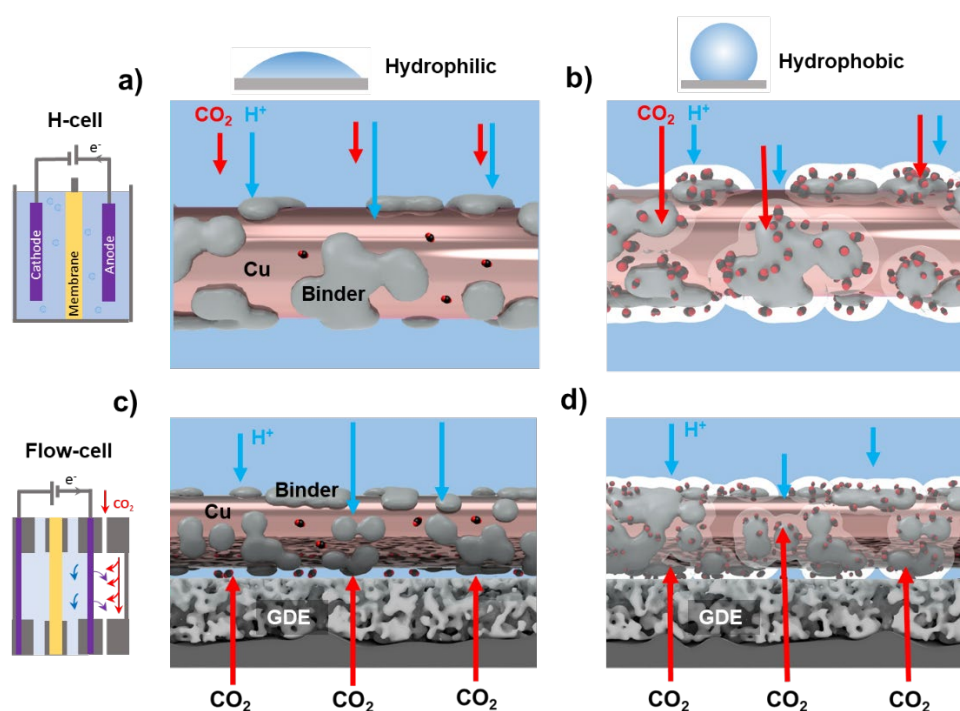
Figure 4.7. Proposed mechanism of water and CO_2 transports to the Cu surface in hydrophilic (a, c) and hydrophobic (b, d) environments in an H-cell (a, b) and flow cell (c, d). Electrolyte (light blue), Cu (brownish red), polymer binder (gray), trapped CO_2 in hydrophobic samples (white), CO_2 pathway (red arrow), H^+ pathway (blue arrow).

Laboratory of Materials for Renewable Energy (LMER)
Institute of Chemical Sciences and Engineering (ISIC)
Basic Science Faculty (SB)

176

3. Conclusions

In summary, we show that coating the surface of Cu catalysts with a thin layer of polymer binder is a simple but effective method for tuning the CO_2RR activity and selectivity. This is because polymer binders not only bond catalyst powders on the support but also change the local concentration of reactants (i.e., CO_2 and H_2O) near the catalyst surface, thus altering the CO_2RR performance. Specifically, a hydrophobic polymer binder (i.e., FEP) can facilitate the access of CO_2 to the Cu surface, thereby promoting the production and accumulation of the key reaction intermediate CO, and resulting in an increase in the production of C_{2+} products. Our results show that a Cu catalyst coated with an FEP binder achieved ~52 % faradaic efficiency toward C_{2+} products in an H-cell. In a flow reactor, a partial current density of more than 600 mA cm^{-2} was obtained for C_{2+} products with ~77% faradaic efficiency. Therefore, our findings highlight that, in addition to modifying the intrinsic properties of the catalyst, controlling the local concentration of the reactants by tuning the hydrophobicity of the catalyst with a proper polymer binder can also greatly improve the performance of CO_2RR.

4. Methodology

4.1. Synthesis of the CuO catalyst

The CuO catalyst was synthesized using a precipitation method adapted from a previous publication [49]. 1.3 g of $Cu(NO_3)_2 \cdot 3H_2O$ (Sigma-Aldrich) was dissolved in 100 mL of Milli-Q water, followed by the addition of 30 mL of 0.15 M NH_4OH prepared from ammonium hydroxide, 28% NH_3 (Alfa Aesar). Following this, 10 mL of 1.0 M NaOH (Reactolab SA) was introduced at a rate of 2 mL/min. The precipitation reaction was carried out for 30 min while being continuously stirred with a magnetic agitator. The obtained $Cu(OH)_2$ precipitate was then washed thoroughly with deionized water and ethanol in a centrifuge. Finally, the $Cu(OH)_2$ precipitate was freeze-dried for 72 h and calcined in air for 1 h at 300°C to obtain the CuO catalyst.

4.2. Working electrode preparation

The catalyst ink was prepared by dispersing the as-synthesized CuO catalyst in isopropanol (IPA, $\geq$ 99.8%, analytical reagent grade, Fisher Scientific). Polyacrylic acid (PAA, 63 wt.% solution in water, Fisher Scientific), Nafion (5 wt.% in a mixture of lower aliphatic alcohols and water, Sigma-Aldrich), and fluorinated ethylene propylene (FEP, 50 wt.% dispersion in water, FuelCellStore) were used as binders across three separate samples. The chemical formulae of the three polymers are shown in Figure S4.3. The dispersion (containing 0.2 mg of polymer binder and 0.25 mL of solvent for every mg of catalyst) was sonicated for 10 min, then drop-casted onto the carbon paper (H-cell: Toray Carbon Paper, TGP-H-60, Alfa Aesar; Flow cell: YLS-35, Suzhou Sinero Technology Co.) with a loading of 0.4 mg/cm^2. The obtained working electrodes were denoted as Cu-PAA, Cu-Nafion, and Cu-FEP, respectively.

Laboratory of Materials for Renewable Energy (LMER)
Institute of Chemical Sciences and Engineering (ISIC)
Basic Science Faculty (SB)

177

4.3. Performance test

A potentiostat (Metrohm Autolab PGSTAT302N) was used to perform electrochemical measurements. The gas products were quantified using an on-line gas chromatograph (GC, SRI instruments 8610C), which was equipped with a thermal conductivity detector (TCD) and a flame ionization detector (FID). A series of standard gases with different concentrations of CO, CH_4, C_2H_4, and C_2H_6 were used to calibrate the GC (Equation S4.1). The electrolyte was collected after the chronoamperometric measurement, and ^1H nuclear magnetic resonance (NMR) was used to quantify liquid products (Bruker 400 MHz AVIII HD. A mixture of methanol, ethanol, n-propanol, acetic acid, acetone, and formic acid with a pre-defined concentration was used to construct a calibration curve. The concentrations of the liquid mixtures used for calibration ranged from 0.067 to 10 mM (Equation S4.2, Figure S4.6, Table S4.1).

The electrochemical cell was an H-shaped, gas-tight cell composed of two compartments: one for the oxygen evolution reaction (OER), and one for the CO_2RR. An ion-exchange membrane (Nafion 212, Dupont) was used to separate the two compartments. The cathode compartment was composed of an Ag/AgCl reference electrode and a working electrode with the catalyst of interest. CO_2 was continuously bubbled into the 0.1 M $KHCO_3$ catholyte both before and during the CO_2RR. A Pt wire was used as a counter electrode in the anode compartment. The electrochemical measurements in the flow reactor were performed using a previously reported system [17]. The CO_2 flow rate was kept at 110 mL/min. The constant potential mode was used for H-cell measurements and the constant current mode was used for flow-cell measurements. All potentials were reported after iR correction.

4.4. Materials characterization

Scanning electron microscopy (SEM) images were acquired on a Thermofisher Teneo FE-SEM, and high-resolution transmission electron microscopy (HR-TEM) images were obtained with a Thermofisher Tecnai Osiris 200kV TEM. The energy-filtered TEM (EF-TEM) images were acquired using a JEOL 2200FS TEM. EFTEM carbon elemental maps were performed using the three window-method on the carbon K edge in electron energy-loss spectra (EELS). The X-ray diffraction (XRD) spectra were acquired using a Bruker D8 Advance system using Cu Kα (λ = 1.54 Å) radiation. X-ray photoelectron spectroscopy (XPS) was performed with a Kratos Axis Supra XPS system, using a monochromated Al Ka (1486.61eV) X-ray source at a nominal power of 225W. A pass energy of 20 eV was used for acquiring the C 1s, O 1s, and Cu 2p core-level spectra. The Water Contact Angle (WCA) and the Captive Bubble Contact Angle (CBCA) were measured with a Kruss EasyDrop Drop Shape Analyzer.

4.5. Operando Raman measurements

Surface-enhanced operando Raman spectroscopy was performed using a home-built Raman cell. The incident and scattered beams were sent to the sample and collected through an immersion objective, respectively (Leica, 63x). A red light with a wavelength of 632 nm was used as the laser beam. 0.1 M $KHCO_3$ was used as the electrolyte and CO_2 was purged continuously to the cathodic compartment both before and during the Raman measurements.

Laboratory of Materials for Renewable Energy (LMER)   178
Institute of Chemical Sciences and Engineering (ISIC)
Basic Science Faculty (SB)

Supporting Information

Acknowledgments

Conflict of interest
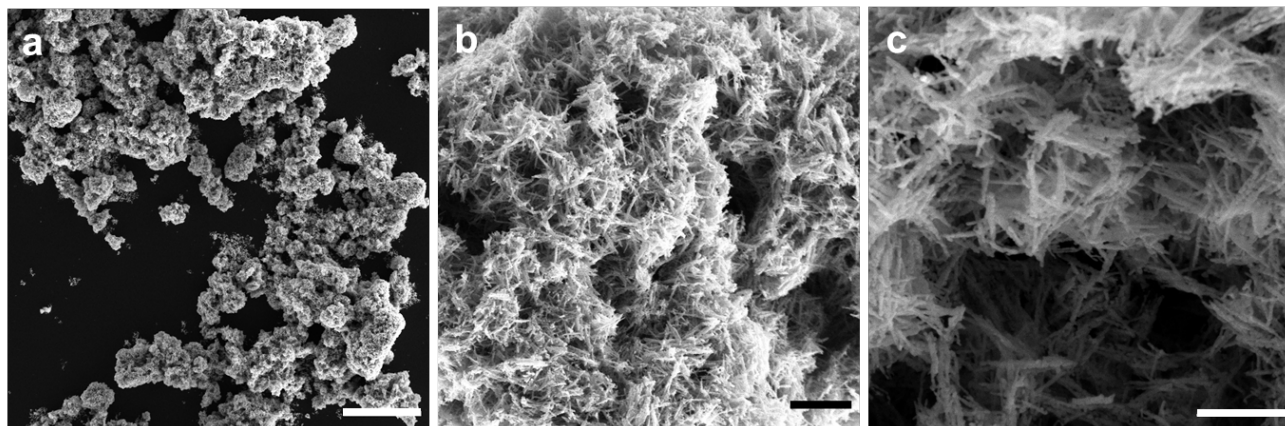
The authors declare no conflict of interest.

References

[1] N. S. Lewis, D. G. Nocera, *Proc. Natl. Acad. Sci. U. S. A.* **2006**, *103*, 15729.

[2] T. R. Cook, D. K. Dogutan, S. Y. Reece, Y. Surendranath, T. S. Teets, D. G. Nocera, *Chem. Rev.* **2010**, *110*, 6474.

[3] P. De Luna, C. Hahn, D. Higgins, S. A. Jaffer, T. F. Jaramillo, E. H. Sargent, *Science (80-.).* **2019**, *364*, DOI 10.1126/science.aav3506.

[4] H. B. Gray, *Nat. Chem.* **2009**, *1*, 7.

[5] L. Schlapbach, A. Züttel, *Nature* **2001**, *414*, 353.

[6] R. Reske, H. Mistry, F. Behafarid, B. Roldan Cuenya, P. Strasser, *J. Am. Chem. Soc.* **2014**, *136*, 6978.

[7] F. S. Roberts, K. P. Kuhl, A. Nilsson, *Angew. Chemie Int. Ed.* **2015**, *54*, 5179.

[8] A. Loiudice, P. Lobaccaro, E. A. Kamali, T. Thao, B. H. Huang, J. W. Ager, R. Buonsanti, *Angew. Chemie Int. Ed.* **2016**, *55*, 5789.

[9] W. Luo, J. Zhang, M. Li, A. Züttel, *ACS Catal.* **2019**, *9*, 3783.

[10] W. Luo, W. Xie, M. Li, J. Zhang, A. Züttel, *J. Mater. Chem. A* **2019**, *7*, 4505.

[11] X. Feng, K. Jiang, S. Fan, M. W. Kanan, *ACS Cent. Sci.* **2016**, *2*, 169.

[12] C. G. Morales-Guio, E. R. Cave, S. A. Nitopi, J. T. Feaster, L. Wang, K. P. Kuhl, A. Jackson, N. C. Johnson, D. N. Abram, T. Hatsukade, C. Hahn, T. F. Jaramillo, *Nat. Catal.* **2018**, *1*, 764.

[13] D. Ren, B. S. H. Ang, B. S. Yeo, *ACS Catal.* **2016**, *6*, 8239.

[14] J. Gao, H. Zhang, X. Guo, J. Luo, S. M. Zakeeruddin, D. Ren, M. Grätzel, *J. Am. Chem. Soc.* **2019**, *141*, 18704.

[15] W. Luo, W. Xie, R. Mutschler, E. Oveisi, G. L. De Gregorio, R. Buonsanti, A. Züttel, *ACS Catal.*

Laboratory of Materials for Renewable Energy (LMER)
Institute of Chemical Sciences and Engineering (ISIC)
Basic Science Faculty (SB)

179

2018, *8*, 6571.

[16]   L.-C. Weng, A. T. Bell, A. Z. Weber, *Phys. Chem. Chem. Phys.* **2018**, *20*, 16973.

[17]   J. Zhang, W. Luo, A. Züttel, *J. Catal.* **2020**, *385*, 140.

[18]   J. Zhang, W. Luo, A. Züttel, *J. Mater. Chem. A* **2019**, *7*, 26285.

[19]   K. Yang, R. Kas, W. A. Smith, T. Burdyny, *ACS Energy Lett.* **2021**, *6*, 33.

[20]   N. T. Nesbitt, T. Burdyny, H. Simonson, D. Salvatore, D. Bohra, R. Kas, W. A. Smith, *ACS Catal.* **2020**, *10*, 14093.

[21]   D. Wakerley, S. Lamaison, F. Ozanam, N. Menguy, D. Mercier, P. Marcus, M. Fontecave, V. Mougel, *Nat. Mater.* **2019**, *18*, 1222.

[22]   Z. Cai, Y. Zhang, Y. Zhao, Y. Wu, W. Xu, X. Wen, Y. Zhong, Y. Zhang, W. Liu, H. Wang, Y. Kuang, X. Sun, *Nano Res. 2018 122* **2018**, *12*, 345.

[23]   F. P. García de Arquer, C. T. Dinh, A. Ozden, J. Wicks, C. McCallum, A. R. Kirmani, D. H. Nam, C. Gabardo, A. Seifitokaldani, X. Wang, Y. C. Li, F. Li, J. Edwards, L. J. Richter, S. J. Thorpe, D. Sinton, E. H. Sargent, *Science (80-.).* **2020**, *367*, 661.

[24]   Y. C. Tan, K. B. Lee, H. Song, J. Oh, *Joule* **2020**, *4*, 1104.

[25]   G. H. Simon, C. S. Kley, B. Roldan Cuenya, *Angew. Chemie Int. Ed.* **2021**, *60*, 2561.

[26]   D. Ren, Y. Deng, D. Handoko, C. S. Chen, S. Malkhandi, B. S. Yeo, **2015**, DOI 10.1021/cs502128q.

[27]   S. Khan, J. Hwang, Y. S. Horn, K. K. Varanasi, *Cell Reports Phys. Sci.* **2021**, *2*, 100318.

[28]   M. Ma, K. Djanashvili, W. A. Smith, *Angew. Chemie Int. Ed.* **2016**, *55*, 6680.

[29]   M. Wang, L. Wan, J. Luo, *Nanoscale* **2021**, *13*, 3588.

[30]   A. Herzog, A. Bergmann, H. S. Jeon, J. Timoshenko, S. Kühl, C. Rettenmaier, M. Lopez Luna, F. T. Haase, B. Roldan Cuenya, *Angew. Chemie Int. Ed.* **2021**, *60*, 7426.

[31]   Y. Lum, J. W. Ager, *Angew. Chemie Int. Ed.* **2018**, *57*, 551.

[32]   A. Dutta, I. Z. Montiel, R. Erni, K. Kiran, M. Rahaman, J. Drnec, P. Broekmann, *Nano Energy* **2020**, *68*, 104331.

[33]   F. Scholten, K. L. C. Nguyen, J. P. Bruce, M. Heyde, B. Roldan Cuenya, *Angew. Chemie Int. Ed.* **2021**, *60*, 19169.

[34]   C. Kim, J. C. Bui, X. Luo, J. K. Cooper, A. Kusoglu, A. Z. Weber, A. T. Bell, *Nat. Energy 2021 611* **2021**, *6*, 1026.

[35]   D. Ren, J. Gao, L. Pan, Z. Wang, J. Luo, S. M. Zakeeruddin, A. Hagfeldt, M. Grätzel, *Angew. Chemie* **2019**, *131*, 15178.

[36]   H. Jung, S. Y. Lee, C. W. Lee, M. K. Cho, D. H. Won, C. Kim, H. S. Oh, B. K. Min, Y. J. Hwang, *J. Am. Chem. Soc.* **2019**, *141*, 4624.

Laboratory of Materials for Renewable Energy (LMER)   180
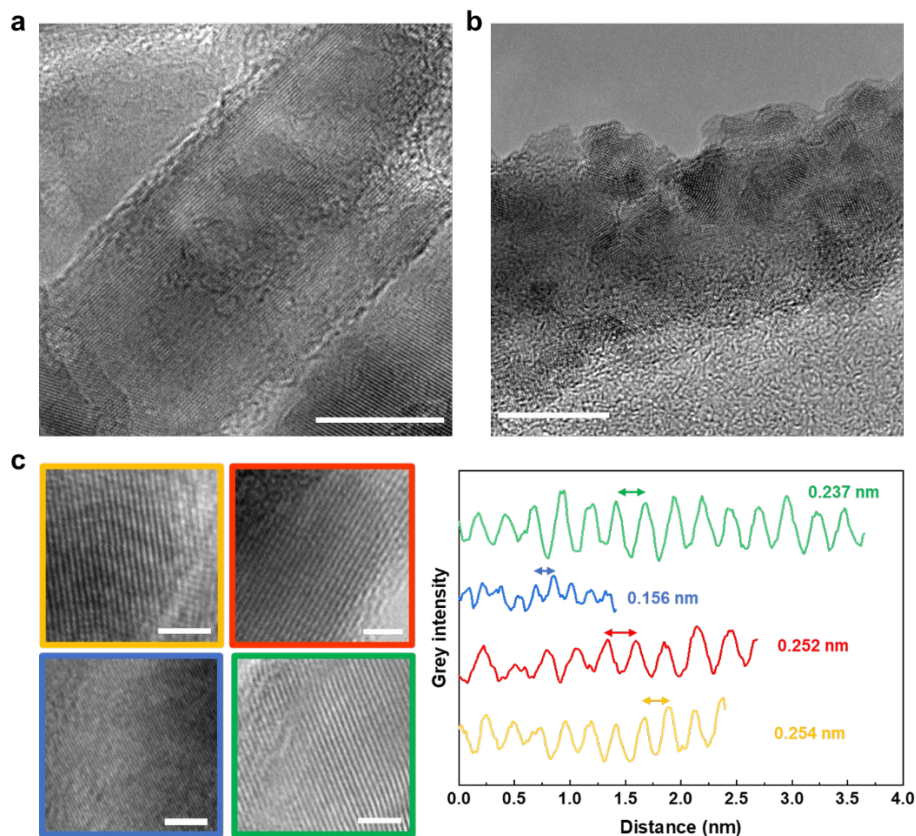Institute of Chemical Sciences and Engineering (ISIC)
Basic Science Faculty (SB)

[37]   T. Möller, F. Scholten, T. N. Thanh, I. Sinev, J. Timoshenko, X. Wang, Z. Jovanov, M. Gliech, B. Roldan Cuenya, A. S. Varela, P. Strasser, *Angew. Chemie* **2020**, *132*, 18130.

[38]   Z.-Z. Niu, F.-Y. Gao, X.-L. Zhang, P.-P. Yang, R. Liu, L.-P. Chi, Z.-Z. Wu, S. Qin, X. Yu, M.-R. Gao, *J. Am. Chem. Soc.* **2021**, *143*, 8011.

[39]   S. Ma, M. Sadakiyo, R. Luo, M. Heima, M. Yamauchi, P. J. A. Kenis, *J. Power Sources* **2016**, *301*, 219.

[40]   C. Reller, R. Krause, E. Volkova, B. Schmid, S. Neubauer, A. Rucki, M. Schuster, G. Schmid, *Adv. Energy Mater.* **2017**, *7*, 1602114.

[41]   K. K. Patra, S. Park, H. Song, B. Kim, W. Kim, J. Oh, *ACS Appl. Energy Mater.* **2020**, *3*, 11343.

[42]   P. O. Larsson, A. Andersson, *J. Catal.* **1998**, *179*, 72.

[43]   L. Debbichi, M. C. Marco De Lucas, J. F. Pierson, P. Krü, **2012**, DOI 10.1021/jp303096m.

[44]   S. Jiang, K. Klingan, C. Pasquini, H. Dau, *J. Chem. Phys* **2019**, *150*, 41718.

[45]   X. Chang, Y. Zhao, B. Xu, *ACS Catal.* **2020**, *10*, 13737.

[46]   C. Zhan, F. Dattila, C. Rettenmaier, A. Bergmann, S. Kühl, R. García-Muelas, N. López, B. R. Cuenya, *ACS Catal.* **2021**, 7694.

[47]   P. Zhang, J. Cai, Y. X. Chen, Z. Q. Tang, D. Chen, J. Yang, D. Y. Wu, B. Ren, Z. Q. Tian, *J. Phys. Chem. C* **2010**, *114*, 403.

[48]   M. Moradzaman, G. Mul, *ChemElectroChem* **2021**, *8*, 1478.

[49]   J. J. Lv, M. Jouny, W. Luc, W. Zhu, J. J. Zhu, F. Jiao, *Adv. Mater.* **2018**, *30*, 1803111.

Laboratory of Materials for Renewable Energy (LMER)
Institute of Chemical Sciences and Engineering (ISIC)
Basic Science Faculty (SB)

181

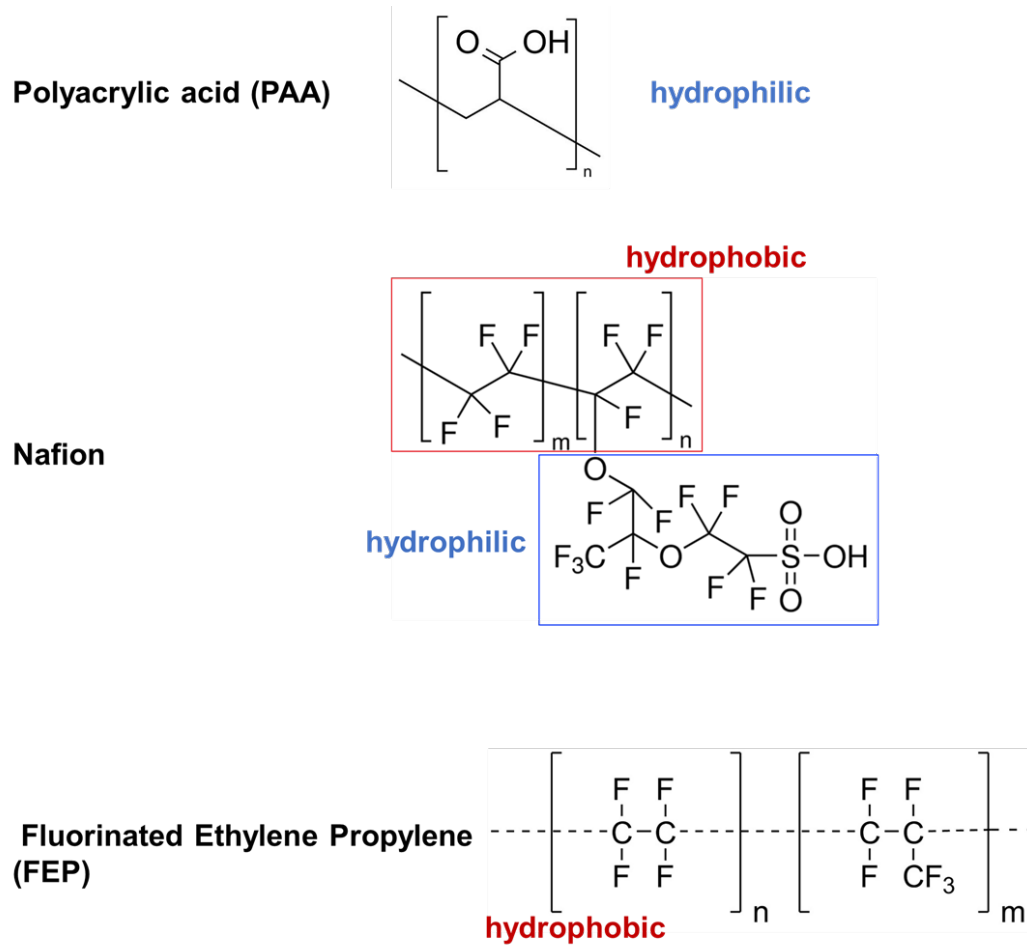## 5. Supporting Information

Characterization of the oxide catalyst

Figure S4.1. SEM images of the highly porous catalyst copper oxide, acquired at different magnifications. Scale bar for **a)** 20 µm **b)** 1 µm **c)** 500 nm.

Laboratory of Materials for Renewable Energy (LMER)
Institute of Chemical Sciences and Engineering (ISIC)
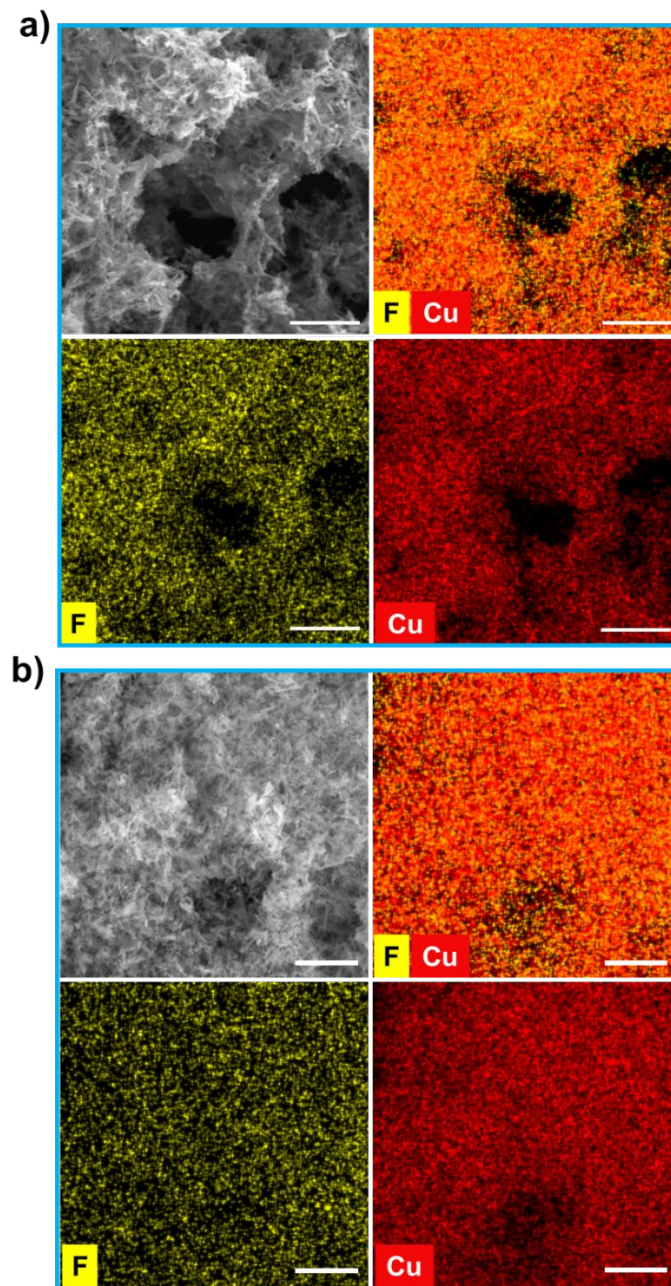Basic Science Faculty (SB)

182

Figure S4.2. HR-TEM images of different grains and analysis of their d-spacing. Scale bar: 2 nm. A line was drawn perpendicularly to the crystal plane and a profile plot of the grey scale is shown. The d-spacing was determined by analyzing the distance between two adjacent grey intensity peaks. Determination of d-spacing base on grey intensity level of the crystal planes and **d)** the corresponding HR-TEM images of different grains of as-synthesized CuO. Scale bar: 2 nm.
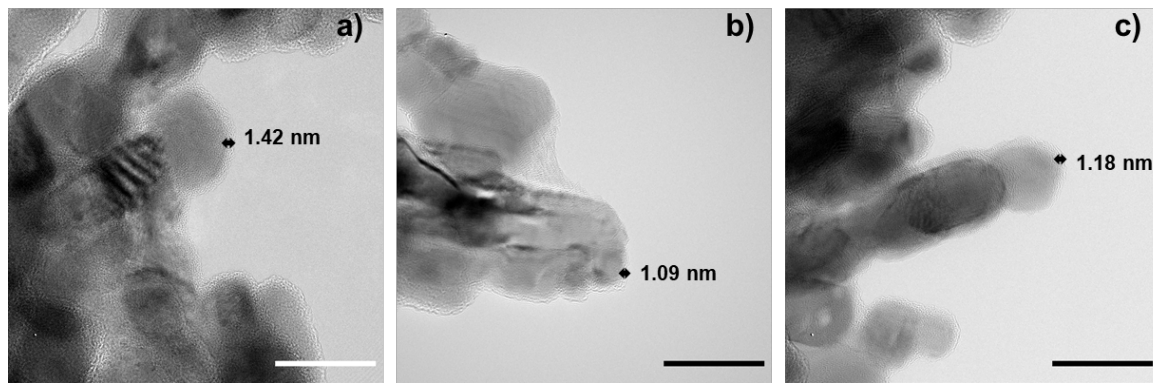
Laboratory of Materials for Renewable Energy (LMER)
Institute of Chemical Sciences and Engineering (ISIC)
Basic Science Faculty (SB)

183

Figure S4.3. Chemical formula of PAA, Nafion and FEP.

Laboratory of Materials for Renewable Energy (LMER)
Institute of Chemical Sciences and Engineering (ISIC)
Basic Science Faculty (SB)

184

Figure S4.4. SEM image and elemental maps of **a)** Cu-Nafion and **b)** Cu-FEP. The dispersions of Cu-Nafion and Cu-FEP were drop-casted onto a glassy carbon surface. The distribution of the polymer can be well indicated by the elemental map of Cu and F.

Laboratory of Materials for Renewable Energy (LMER)
Institute of Chemical Sciences and Engineering (ISIC)
Basic Science Faculty (SB)

185

Figure S4.5. TEM images of the polymer layer coated on the CuO surface. **a)** Cu-PAA. **b)** Cu-Nafion. **c)** Cu-FEP. Scale bar: 20 nm.

Laboratory of Materials for Renewable Energy (LMER)
Institute of Chemical Sciences and Engineering (ISIC)
Basic Science Faculty (SB)

186

Electrochemical performance

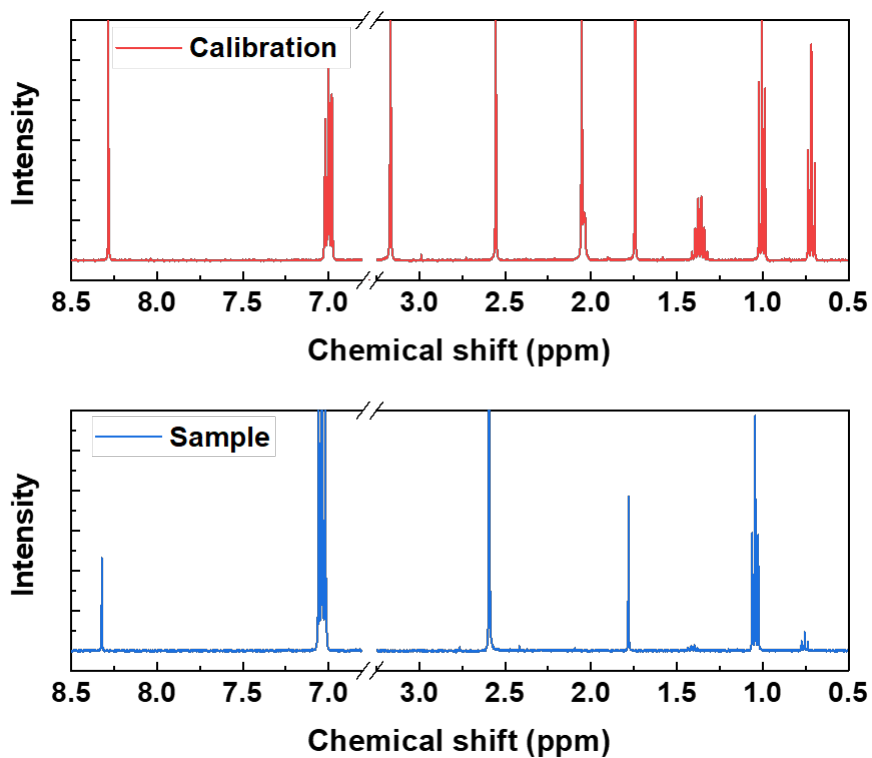**Equation S4.1** Calculations of the partial current density and the faradaic efficiency (FE) for gas products

$$\text{Partial current density} = \frac{\text{measured concentration} \times F \times z \times \text{pressure} \times CO_2 \text{ flow rate}}{R \times T}$$

$$FE = \frac{\text{measured concentration} \times F \times z \times \text{pressure} \times CO_2 \text{ flow rate}}{I_{total} \times R \times T}$$

Equation S4.2 Calculations of the partial current density and the faradaic efficiency (FE) for liquid products

$$\text{Partial current density} = \frac{\text{measured molarity} \times F \times z \times \text{pressure} \times CO_2 \text{ flow rate}}{t}$$
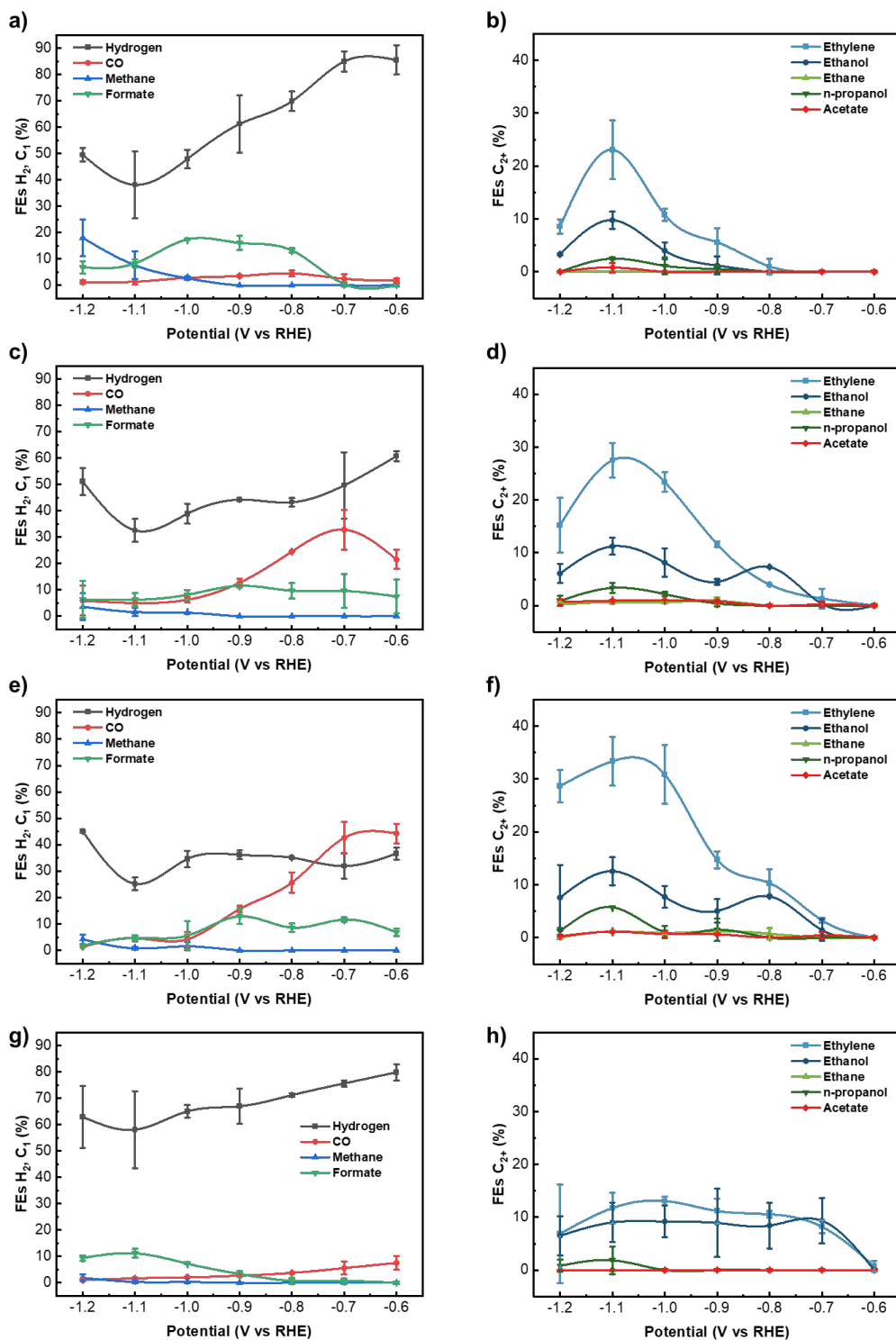
$$FE = \frac{\text{measured molarity} \times F \times z \times \text{pressure} \times CO_2 \text{ flow rate}}{I_{total} \times t}$$

Laboratory of Materials for Renewable Energy (LMER)
Institute of Chemical Sciences and Engineering (ISIC)
Basic Science Faculty (SB)

187
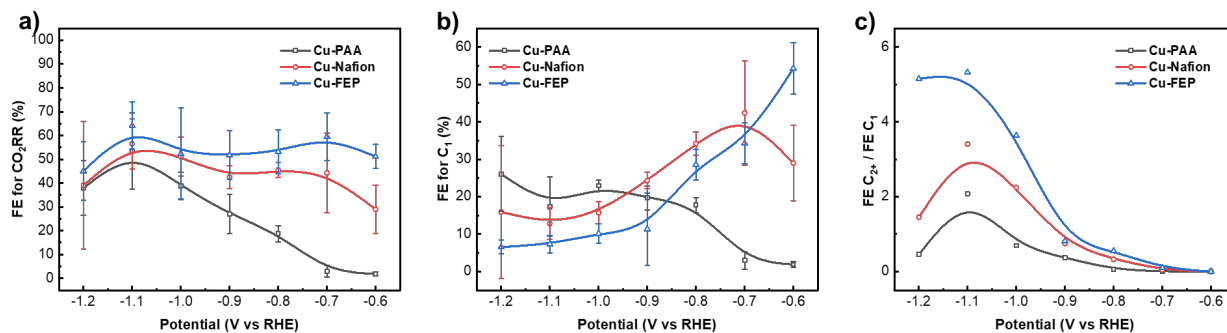
Figure S4.6. ^{1}H NMR spectrum for of **a)** a prepared solution used for calibration curve and **b)** a sample from CuO-FEP after 800 s of reaction under –400 mA.cm^{-2}.

Laboratory of Materials for Renewable Energy (LMER)
Institute of Chemical Sciences and Engineering (ISIC)
Basic Science Faculty (SB)

188

Table S4.1. Chemical shift of the liquid products in NMR measurements

Product	Chemical shift
n-propanol	0.77
Ethanol	1.06
Acetate	1.87
Acetone	2.1
Methanol	3.23
Formate	8.33

Laboratory of Materials for Renewable Energy (LMER)   189
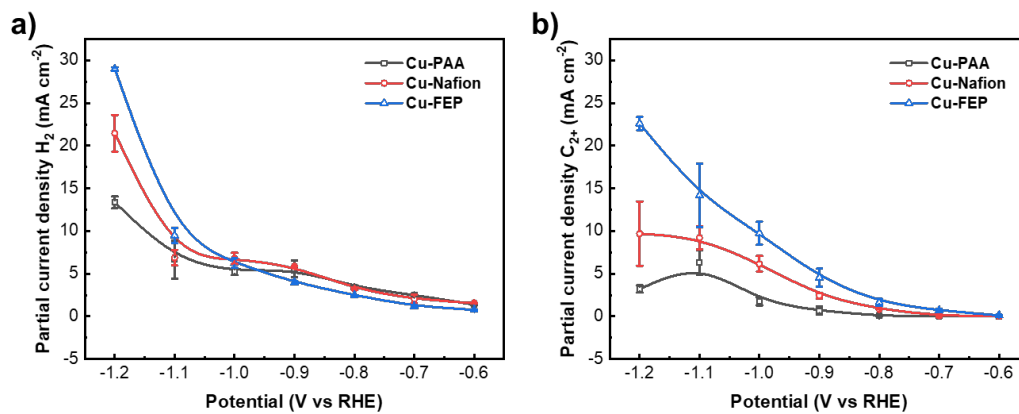Institute of Chemical Sciences and Engineering (ISIC)
Basic Science Faculty (SB)

Figure S4.7. Faradaic efficiencies towards all CO$_2$RR products of (a)(b) Cu-PAA, (c)(d) Cu-Nafion, and (e)(f) Cu-FEP. (g)(h) Bare Cu.
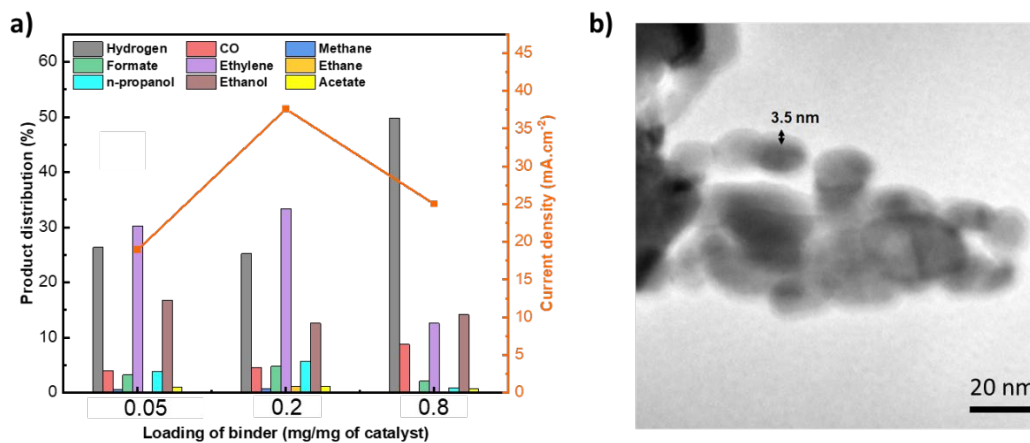
Laboratory of Materials for Renewable Energy (LMER)
Institute of Chemical Sciences and Engineering (ISIC)
Basic Science Faculty (SB)

190

Figure S4.8. Faradaic efficiencies towards a) C_1 and C_{2+} products, b) C_1 products and c) Ratio of FE for C_{2+}/C_1 products of the Cu-polymer catalysts with respect to the potential, in the H-cell, with 0.1 M KHCO$_3$ as the electrolyte.

Laboratory of Materials for Renewable Energy (LMER)
Institute of Chemical Sciences and Engineering (ISIC)
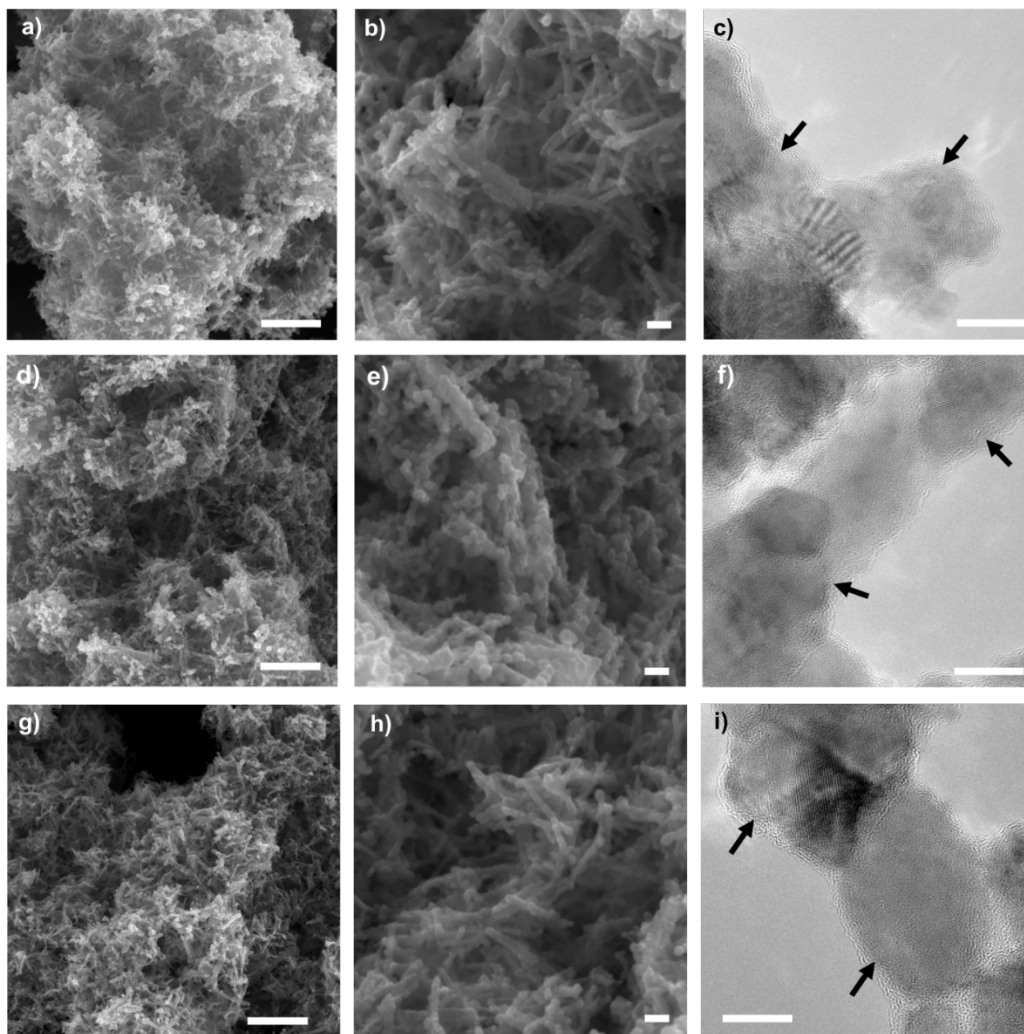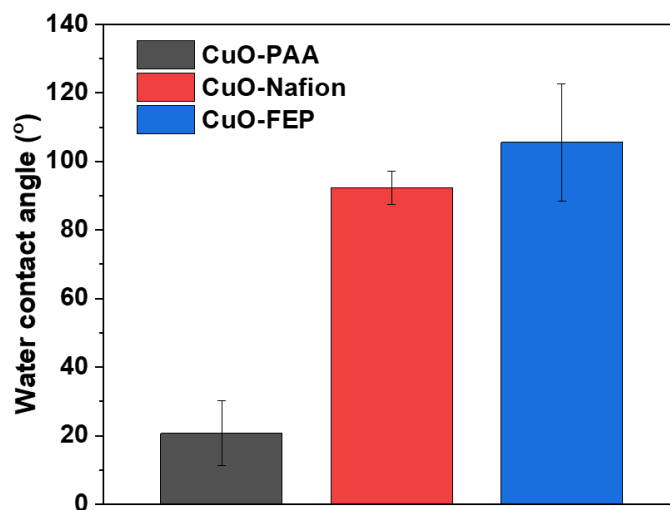*Basic Science Faculty (SB)*

191

a)

b)

Figure S4.9. a) Partial current densities of H_2 and b) C_{2+} of the three Cu-polymer catalysts with respect to the potential, obtained in the H-cell, with 0.1 M $KHCO_3$ as the electrolyte.

Laboratory of Materials for Renewable Energy (LMER)
Institute of Chemical Sciences and Engineering (ISIC)
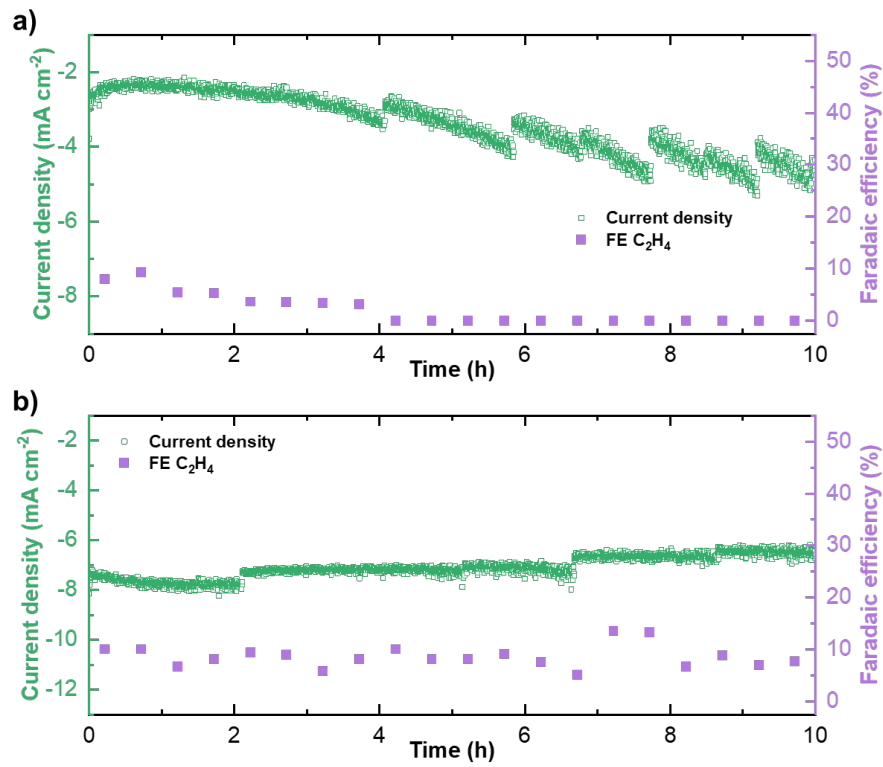Basic Science Faculty (SB)

192

Figure S4.10. (a) Product distribution and current density of Cu-FEP at three different loadings of FEP. Obtained in H-cell, at -1.1 V vs RHE, in 0.1 M KHCO$_3$. (c) A typical TEM image of the Cu-FEP sample with 0.8 mg FEP/ mg catalyst.
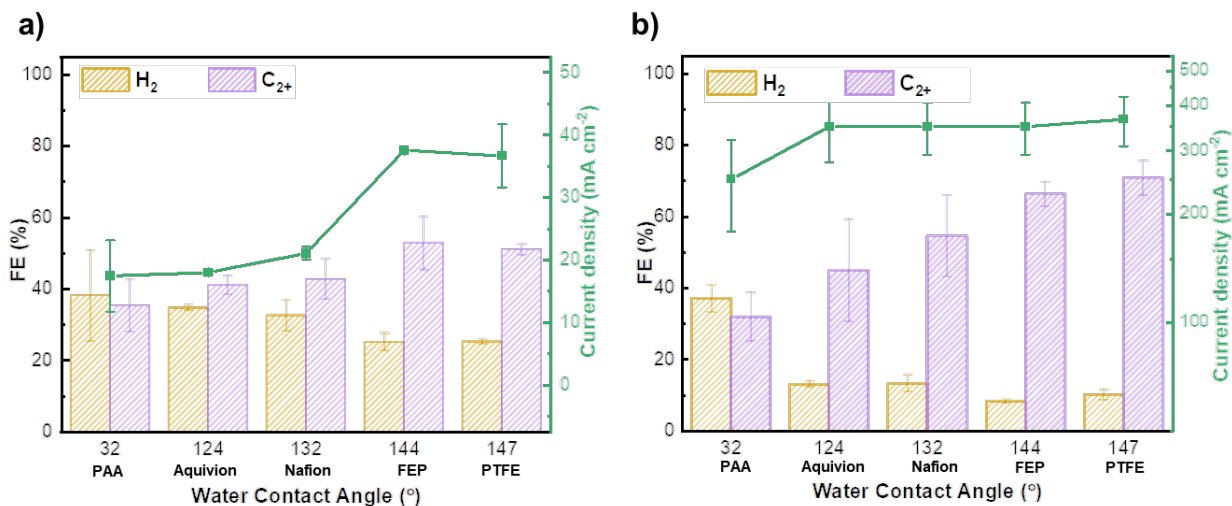
Laboratory of Materials for Renewable Energy (LMER)
Institute of Chemical Sciences and Engineering (ISIC)
Basic Science Faculty (SB)

193

Figure S4.11. Morphology of the catalyst after 1 h electrolysis of CO_2, at -1.1 V vs RHE, in 0.1 M $KHCO_3$. (a-c) Cu-PAA, (d-f) Cu-Nafion, (g-i) Cu-FEP. Scale bar: (a)(d)(g) 1 µm, (b)(e)(h) 100 nm, (c)(f)(i) 10 nm.

Laboratory of Materials for Renewable Energy (LMER)
Institute of Chemical Sciences and Engineering (ISIC)
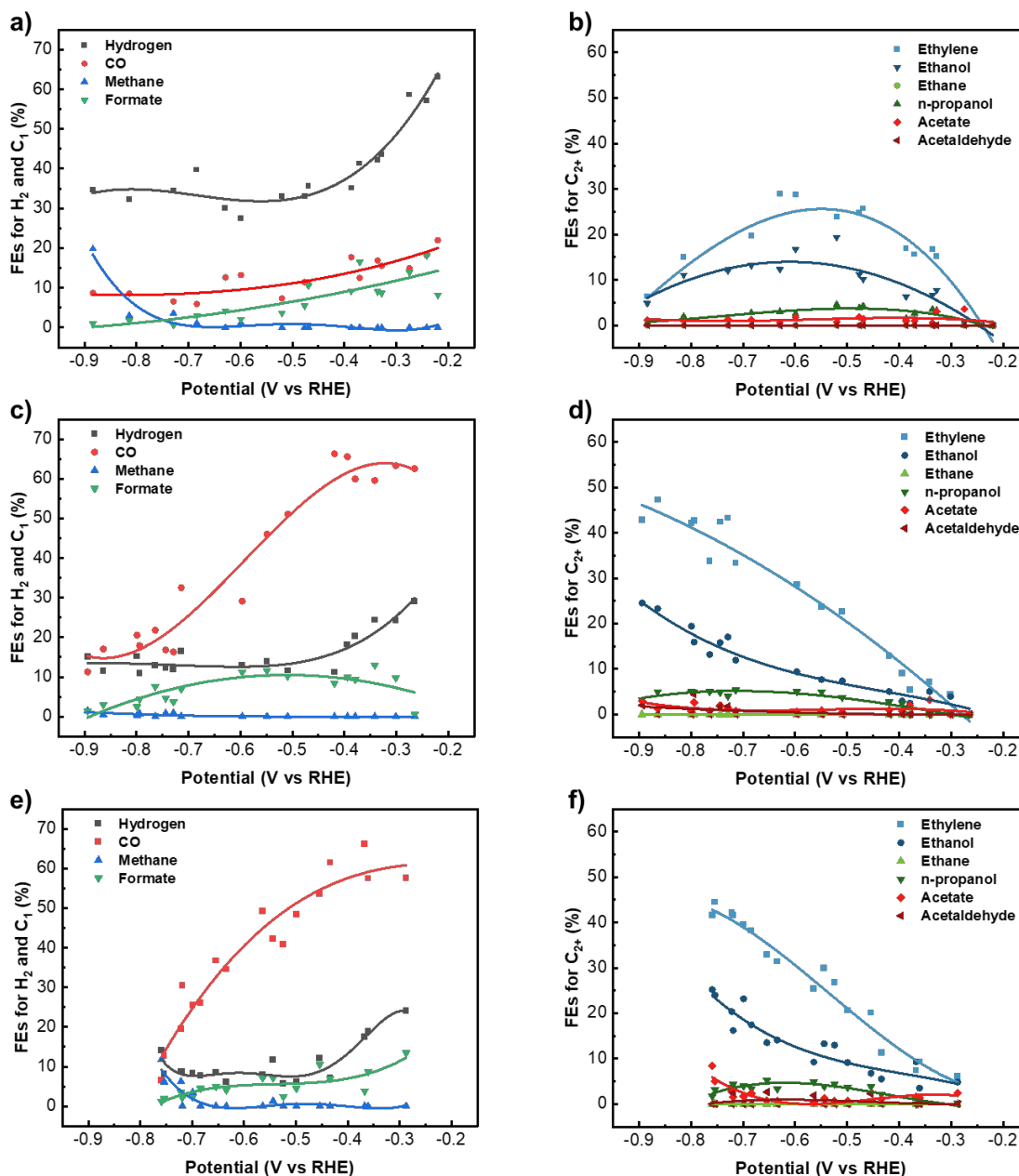Basic Science Faculty (SB)

194

Figure S4.12. Water contact angle (CA) measurements of the three coated surfaces after 1 h electrolysis of CO_2, at -1.0 V vs RHE, in 0.1 M $KHCO_3$.
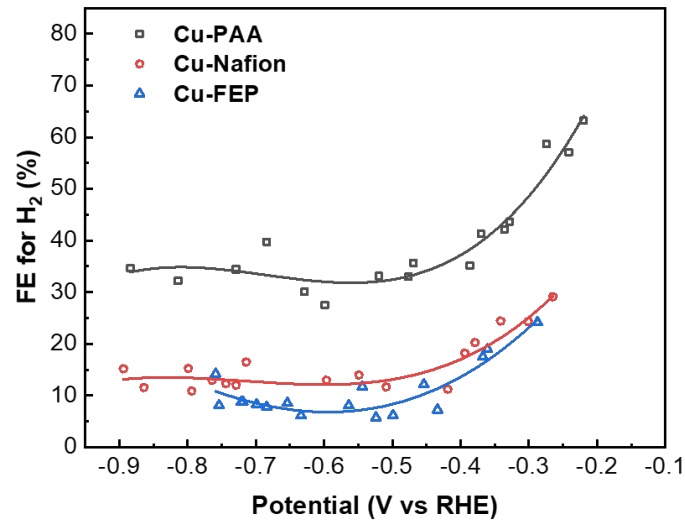
Laboratory of Materials for Renewable Energy (LMER)
Institute of Chemical Sciences and Engineering (ISIC)
Basic Science Faculty (SB)

195

Figure S4.13. Stability of a) Cu-PAA and b) Cu-Nafion over 10 h of electrolysis of CO_2, at -0.8 V vs RHE, in 0.1 M $KHCO_3$.

Laboratory of Materials for Renewable Energy (LMER)
Institute of Chemical Sciences and Engineering (ISIC)
Basic Science Faculty (SB)

196

Figure S4.14. Activity and product selectivity of the CO_2RR towards H_2 and C_{2+} products as a function of the hydrophilicity for 5 polymers, acquired in **a)** H-cell at -1.1 V vs RHE in 0.1 M $KHCO_3$, and b) flow cell at -0.71 V vs RHE in 0.1 M KOH.

Laboratory of Materials for Renewable Energy (LMER)
Institute of Chemical Sciences and Engineering (ISIC)
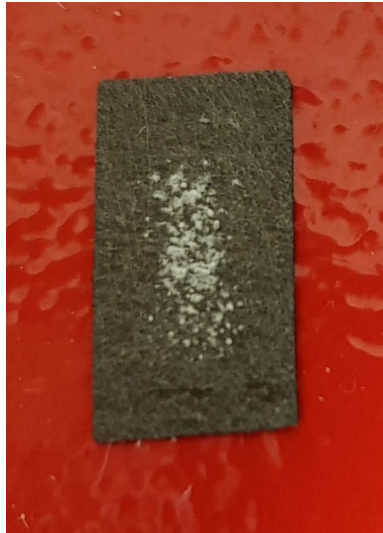Basic Science Faculty (SB)

197

Figure S4.15. Product distributions of the Cu-polymer catalysts in a flow cell, with 1.0 M KOH as an electrolyte at a CO_2 flow rate of 110 mL/min. (a)(b) Cu-PAA, (c)(f) Cu-Nafion, and (e)(f) Cu-FEP. Lines are added to guide the eyes.

Laboratory of Materials for Renewable Energy (LMER)
Institute of Chemical Sciences and Engineering (ISIC)
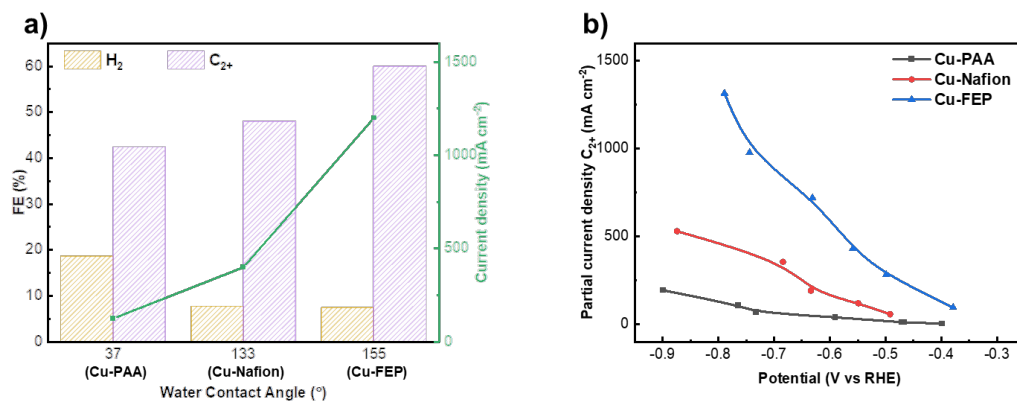Basic Science Faculty (SB)

198

Figure S4.16. FE of H_2 of the three Cu-polymer catalysts with respect to the potential, obtained in the flow cell, with 1.0 M KOH as the electrolyte.
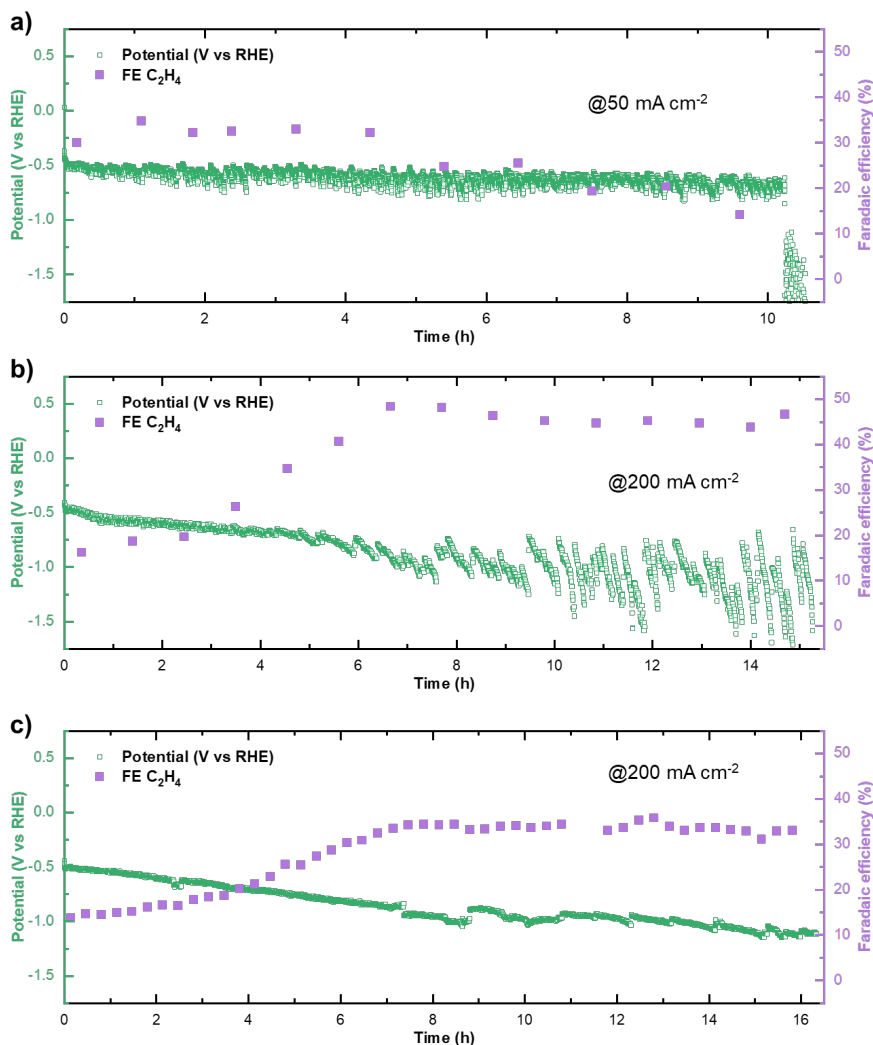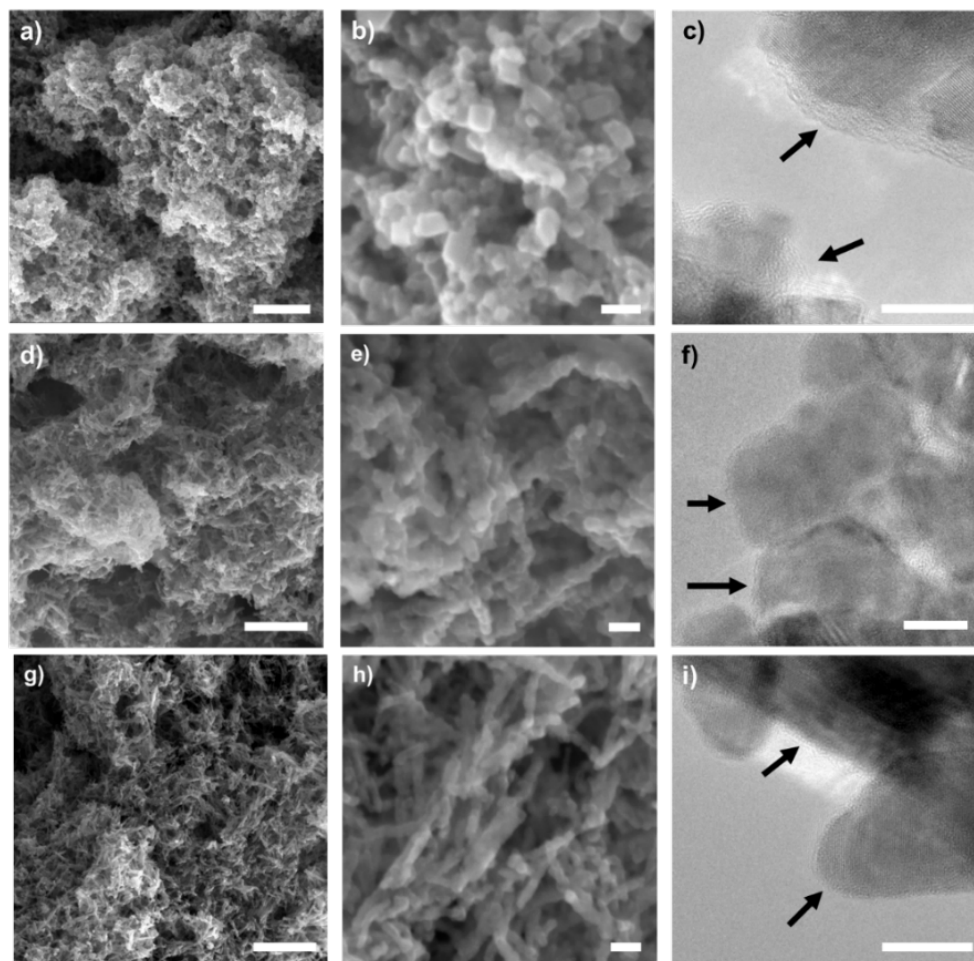
Laboratory of Materials for Renewable Energy (LMER)
Institute of Chemical Sciences and Engineering (ISIC)
Basic Science Faculty (SB)

199

Figure S4.17. K_2CO_3 accumulates at the backside of the GDE of Cu-PAA after CO_2 electrolysis reaction.

Laboratory of Materials for Renewable Energy (LMER)
Institute of Chemical Sciences and Engineering (ISIC)
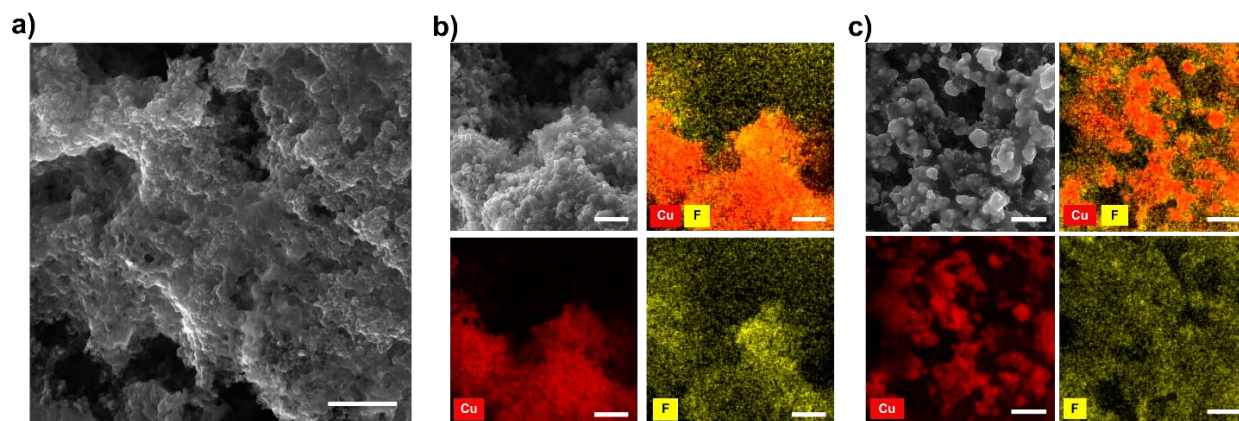Basic Science Faculty (SB)

200

Figure S4.18. a) Activity and product selectivity of the CO_2RR towards H_2 and C_{2+} products as a function of the hydrophilicity, acquired at around -0.64 V vs RHE, for spray-coated Cu-PAA, Cu-Nafion and Cu-FEP. **b)** Partial current densities for C_{2+} products of the three Cu-polymer catalysts with respect to the potential, obtained in the flow cell, with 1.0 M KOH as the electrolyte.

Laboratory of Materials for Renewable Energy (LMER)
Institute of Chemical Sciences and Engineering (ISIC)
Basic Science Faculty (SB)

201

Figure S4.19. Stability of **a)** Cu-PAA over 10 h of electrolysis of CO_2, at 50 mA.cm^{-2} in 1.0 M KOH and **b)** Cu-Nafion, and **c)** Cu-FEP over 15 h of electrolysis of CO_2, at 200 mA.cm^{-2} in 1.0 M KOH. The increasing trend of C_2H_4 FE for Cu-Nafion and Cu-FEP can be due to the decrease of potential. And the decreased potential may originate from the change of Cu structure, electrode conductivity, or accumulation of K_2CO_3.

Laboratory of Materials for Renewable Energy (LMER)
Institute of Chemical Sciences and Engineering (ISIC)
Basic Science Faculty (SB)

202

Figure S4.20. Morphology of the catalyst after 15 min electrolysis of CO_2, at 50 mA.cm^{-2}, in 1.0 M KOH. (a-c) Cu-PAA, (d-f) Cu-Nafion, (g-i) Cu-FEP. Scale bar: (a)(d)(g) 1 µm, (b)(e)(h) 100 nm, (c)(f)(i) 10 nm.

Laboratory of Materials for Renewable Energy (LMER)
Institute of Chemical Sciences and Engineering (ISIC)
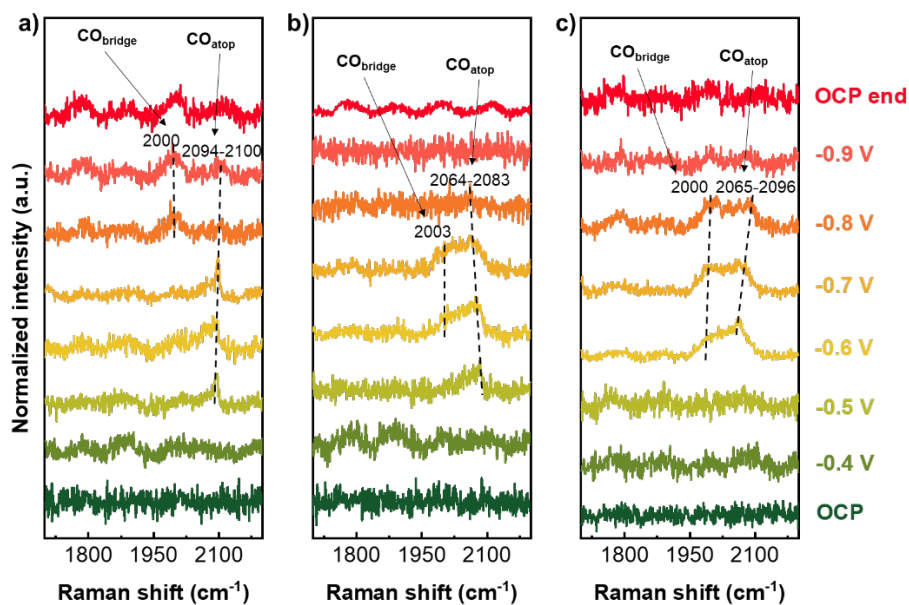Basic Science Faculty (SB)

203

Figure S4.21. Morphology of the Cu-binder catalysts after stability test in the flow cell. a) SEM image of Cu-PAA (the signal of C from the microporous layer does not allow to interpret the elemental maps of Cu and C for Cu-PAA). b) SEM image and its corresponding elemental maps of Cu and F for Cu-Nafion, and c) Cu-FEP. Scale bar: 1μm.

Laboratory of Materials for Renewable Energy (LMER)
Institute of Chemical Sciences and Engineering (ISIC)
Basic Science Faculty (SB)

204

Table S4.2. Comparison of the catalysts, electrochemical performance and reactions conditions between this work and previous publications in H-cell

Position in Figure 4.6	References	FE C$_{2+}$ (%)	Current density (mA.cm^{-2})	Potential (V vs RHE)	Electrolyte
A	5wt%-PTFE-coated Cu nanoarrays[1]	34	18	-1.1	0.1M KHCO$_3$
B	Nafion-coated CuO nanowires[2]	26	25	-1.3	0.1M KHCO$_3$
C	8.1-μm-length Cu NW arrays[3]	28	4	-1.1	0.1M KHCO$_3$
D	Electropolished Cu wire[4]	40	12.6	-1.1	0.1M KHCO$_3$
E	Oxide-derived nanostructured Cu wire[4]	49	12	-1.1	0.1M KHCO$_3$
F	Alkanethiol-treated Cu dendrites[5]	74	30	-1.6	0.1M CsHCO$_3$
G	3.6 um Cu$_2$O film deposited on Cu[6]	50.6	35	-0.99	0.1M KHCO$_3$
H	Cu$_2$O nanocubes decorated with 3 at% Ag[7]	60	13	-1	0.1M KHCO$_3$
I	^{18}O enriched OD Cu catalysts[8]	60	10.9	-1	0.1M KHCO$_3$
J	44 nm-Cu nanocubes[9]	55	2	-1.1	0.1M KHCO$_3$
K	Ag$_{15}$Cu$_{85}$ foam[10]	41.2	30.5	-1.1	0.5M KHCO$_3$
L	Electropolished Cu(111)[11]	10	3	-1	0.1M KHCO$_3$
M	Cu-Sustainion covered with Nafion[12]	80	20.5	-1.15	0.1 M CsHCO$_3$
N	ZnO/CuO[13]	31.8	48.6	-1.15	0.1M KHCO$_3$
O	Fragmented Cu-Based NP/C[14]	17	74	-1.1	0.1M KHCO$_3$
	CuO-FEP$^{this work}$	52	37.4	-1.1	0.1M KHCO$_3$

Laboratory of Materials for Renewable Energy (LMER)
Institute of Chemical Sciences and Engineering (ISIC)
Basic Science Faculty (SB)

205

Table S4.3. Comparison of the catalysts, electrochemical performance and reactions conditions between this work and previous publications in flow-cell

Position in Figure 4.6	References	FE C$_{2+}$ (%)	Current density (mA.cm^{-2})	Potential (V vs RHE)	Electrolyte
P	Electrodeposited hydrophobic Cu-nanoneedles electrode[15]	64	438	-0.68	1.0 M KOH
Q	Cu particles and Nafion[15]	25.3	398	-0.75	1.0 M KOH
R	Unsupported Cu$_2$O nanocubes[16]	59	300	-1.02	1.0 M KHCO$_3$
S	Cu nanodendrites[17]	57	298	-2	0.1M KBr
T	Cu nanoparticles, prepared by solvent-based method[18]	46	430	-0.58	1.0 M KOH
U	Thermal annealed Cu oxide nanowires[19]	36	300	-0.6	1M KOH
V	Wet chemical oxidized Cu oxide nanowires[19]	38	300	-0.6	1M KOH
W	Cu$_2$O nanoparticle, dropcasted GDE[20]	32	300	-0.93	1M KHCO$_3$
X	Cu$_2$O nanoparticle, airbrushed GDE[20]	75.5	300	-0.85	1M KHCO$_3$
Y	B-doped CuO[21]	60	137	-0.625	1.0 M KOH
	CuO-FEP[this work]	77	800	-0.76	1.0 M KOH

Laboratory of Materials for Renewable Energy (LMER)
Institute of Chemical Sciences and Engineering (ISIC)
Basic Science Faculty (SB)

206

Figure S4.22. Operando Raman spectrum of the three Cu-polymer catalysts, Raman shift ranges from 1700 to 2200 cm^{-1}. From bottom to top: initial OCP, -0.4 to -0.9 V vs RHE, final OCP. Raman spectrum is acquired at 60s after the chronoamperometric test starts. **a)** Cu-FEP. **b)** Cu-Nafion. **c)** Cu-PAA.

Laboratory of Materials for Renewable Energy (LMER)
Institute of Chemical Sciences and Engineering (ISIC)
Basic Science Faculty (SB)

207
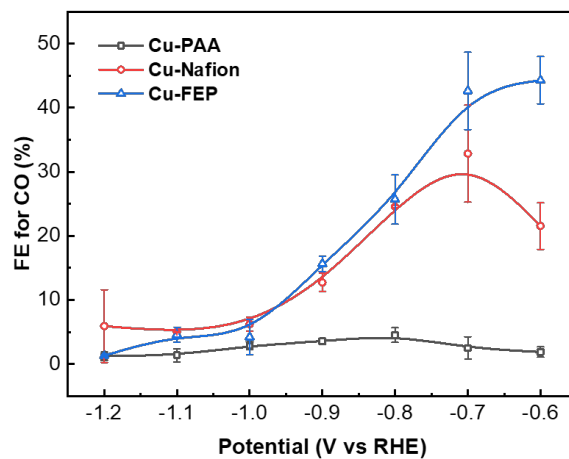
Figure S4.23. Faradaic efficiencies towards CO of Cu catalysts with the three binders with respect to the potential. Obtained in the H-cell, with 0.1 M KHCO$_3$ as the electrolyte.

Laboratory of Materials for Renewable Energy (LMER)
Institute of Chemical Sciences and Engineering (ISIC)
Basic Science Faculty (SB)

208

Synthesis of Au-nanoparticles-supported on Cu

On the as-synthesized CuO support, Au is precipitated and deposited to obtain the **Au@Cu** catalyst. The synthesis proceeds as following:

(1) Neutralization of the precursor: The precursor for Au deposition is $HAuCl_4 \cdot 3H_2O$, it is neutralized with NaOH to avoid dissolution of the CuO support. In 28.5 mL of H_2O, 1.5 mL of 0.02 M $HAuCl_4 \cdot 3H_2O$ is added. The solution is stirred and heated up to $70°C$ and 0.01 M NaOH is added to bring the pH up to 6.

(2) Precipitation deposition: 81 mg of CuO is added to the neutralized position and the pH is adjusted to approximately 7.5. The reaction is kept at 75°C under continuous stirring for 1h then cooled down to room temperature. The obtained solution is washed with deionized water twice, then ethanol, before freeze-fried for 72 hours,

(3) After freeze-drying, the powder CuO-Au is calcined in air for 1 h at 300°C.

Laboratory of Materials for Renewable Energy (LMER)   209
Institute of Chemical Sciences and Engineering (ISIC)
Basic Science Faculty (SB)
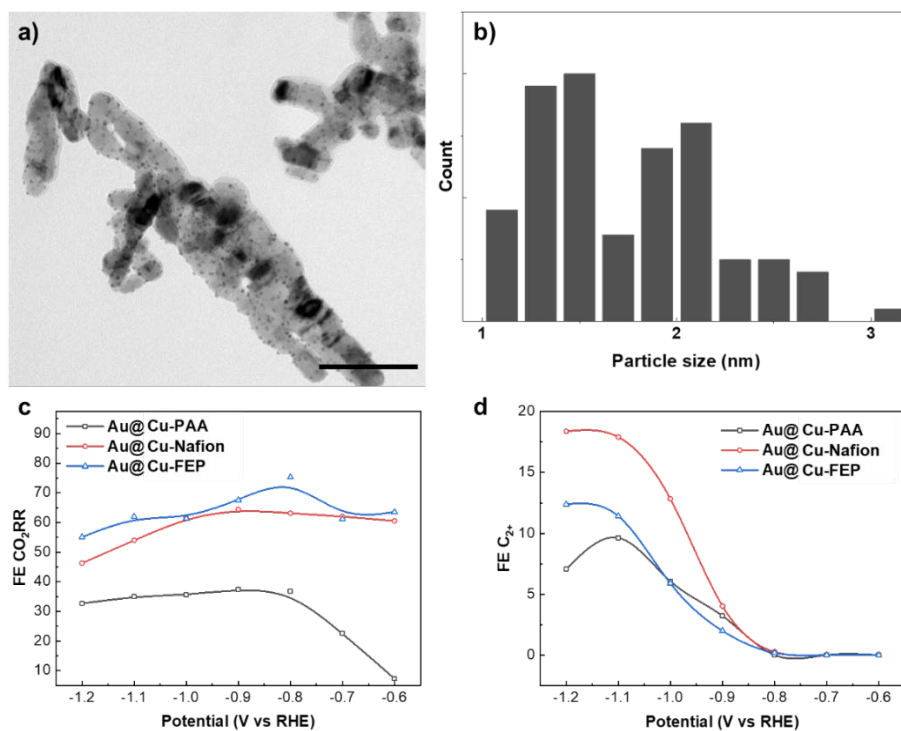
Figure S4.24. Performance of the as-synthesized Au@Cu-polymer catalysts. **a)** TEM image (Scale bar: 100 nm) and **b)** the particle size distribution of the Au@Cu sample without polymer binder. **c)** and **d)** Faradaic efficiency towards C_1 and C_{2+} products of the Au@Cu-polymer catalysts, 0.1 M $KHCO_3$ in H-cell.

Laboratory of Materials for Renewable Energy (LMER)
Institute of Chemical Sciences and Engineering (ISIC)
Basic Science Faculty (SB)

210

REFERENCES

[1]   Z. Cai, Y. Zhang, Y. Zhao, Y. Wu, W. Xu, X. Wen, Y. Zhong, Y. Zhang, W. Liu, H. Wang, Y. Kuang, X. Sun, *Nano Res. 2018 122* **2018**, *12*, 345.

[2]   M. Wang, L. Wan, J. Luo, *Nanoscale* **2021**, *13*, 3588.

[3]   M. Ma, K. Djanashvili, W. A. Smith, *Angew. Chemie Int. Ed.* **2016**, *55*, 6680.

[4]   S. Khan, J. Hwang, Y. S. Horn, K. K. Varanasi, *Cell Reports Phys. Sci.* **2021**, *2*, 100318.

[5]   D. Wakerley, S. Lamaison, F. Ozanam, N. Menguy, D. Mercier, P. Marcus, M. Fontecave, V. Mougel, *Nat. Mater.* **2019**, *18*, 1222.

[6]   D. Ren, Y. Deng, D. Handoko, C. S. Chen, S. Malkhandi, B. S. Yeo, **2015**, DOI 10.1021/cs502128q.

[7]   A. Herzog, A. Bergmann, H. S. Jeon, J. Timoshenko, S. Kühl, C. Rettenmaier, M. Lopez Luna, F. T. Haase, B. Roldan Cuenya, *Angew. Chemie Int. Ed.* **2021**, anie. 202017070.

[8]   Y. Lum, J. W. Ager, *Angew. Chemie Int. Ed.* **2018**, *57*, 551.

[9]   A. Loiudice, P. Lobaccaro, E. A. Kamali, T. Thao, B. H. Huang, J. W. Ager, R. Buonsanti, *Angew. Chemie Int. Ed.* **2016**, *55*, 5789.

[10]   A. Dutta, I. Z. Montiel, R. Erni, K. Kiran, M. Rahaman, J. Drnec, P. Broekmann, *Nano Energy* **2020**, *68*, 104331.

[11]   F. Scholten, K. L. C. Nguyen, J. P. Bruce, M. Heyde, B. Roldan Cuenya, *Angew. Chemie Int. Ed.* **2021**, *60*, 19169.

[12]   C. Kim, J. C. Bui, X. Luo, J. K. Cooper, A. Kusoglu, A. Z. Weber, A. T. Bell, *Nat. Energy 2021 611* **2021**, *6*, 1026.

[13]   D. Ren, J. Gao, L. Pan, Z. Wang, J. Luo, S. M. Zakeeruddin, A. Hagfeldt, M. Grätzel, *Angew. Chemie* **2019**, *131*, 15178.

[14]   H. Jung, S. Y. Lee, C. W. Lee, M. K. Cho, D. H. Won, C. Kim, H. S. Oh, B. K. Min, Y. J. Hwang, *J. Am. Chem. Soc.* **2019**, *141*, 4624.

[15]   Z.-Z. Niu, F.-Y. Gao, X.-L. Zhang, P.-P. Yang, R. Liu, L.-P. Chi, Z.-Z. Wu, S. Qin, X. Yu, M.-R. Gao, *J. Am. Chem. Soc.* **2021**, *143*, 8011.

[16]   T. Möller, F. Scholten, T. N. Thanh, I. Sinev, J. Timoshenko, X. Wang, Z. Jovanov, M. Gliech, B. Roldan Cuenya, A. S. Varela, P. Strasser, *Angew. Chemie* **2020**, *132*, 18130.

[17]   C. Reller, R. Krause, E. Volkova, B. Schmid, S. Neubauer, A. Rucki, M. Schuster, G. Schmid, *Adv. Energy Mater.* **2017**, *7*, 1602114.

[18]   S. Ma, M. Sadakiyo, R. Luo, M. Heima, M. Yamauchi, P. J. A. Kenis, *J. Power Sources* **2016**, *301*, 219.

[19]   J. Zhang, W. Luo, A. Züttel, *J. Mater. Chem. A* **2019**, *7*, 26285.

Laboratory of Materials for Renewable Energy (LMER)
Institute of Chemical Sciences and Engineering (ISIC)
Basic Science Faculty (SB)

211

[20]   Y. C. Tan, K. B. Lee, H. Song, J. Oh, *Joule* **2020**, *4*, 1104.

[21]   K. K. Patra, S. Park, H. Song, B. Kim, W. Kim, J. Oh, *ACS Appl. Energy Mater.* **2020**, *3*, 11343.

Laboratory of Materials for Renewable Energy (LMER)   212
Institute of Chemical Sciences and Engineering (ISIC)
Basic Science Faculty (SB)

CHAPTER 5:

Unveiling degradation mechanisms in gas diffusion electrodes towards enhancing the stability of CO₂ electrolysis in acidic environments

Thi Ha My Pham,[a,b] Jie Zhang,[c,*] Wen Luo,[d] Boon Siang Yeo,[c,*] Andreas Züttel[a,b]

[a]Laboratory of Materials for Renewable Energy (LMER), Institute of Chemical Sciences and Engineering (ISIC), Basic Science Faculty (SB), Ecole Polytechnique Fédérale de Lausanne (EPFL) Valais/Wallis, Energypolis, Rue de l'Industrie 17, CH-1951 Sion, Switzerland

[b]EMPA Materials & Technology, CH-8600 Dübendorf, Switzerland

[c] Department of Chemistry, Faculty of Science, National University of Singapore, 3 Science Drive 3, 117543 Singapore, Singapore

[d] School of Mechanical Engineering, Beijing Institute of Technology, Beijing 100081, P. R. China

*Corresponding author: to be discussed

Laboratory of Materials for Renewable Energy (LMER)
Institute of Chemical Sciences and Engineering (ISIC)
Basic Science Faculty (SB)

213

Abstract

CO_2 electrolysis in acidic environments is recognized for its capacity to enhance CO_2 utilisation via a buffering effect to convert carbonate formed at high local pH levels back into CO_2. Nevertheless, the process requires further exploration to improve its selectivity towards CO_2 reduction reaction (CO_2RR) products, particularly multicarbon (C_{2+}) ones, and enhance its overall stability. This study reveals that in a configuration where the catholyte is recycled to form a closed liquid cycle, the bulk pH increases throughout the reaction and the Cu-based catalyst undergoes dynamic evolution, involving initial dissolution at a low pH followed by redeposition under a negative overpotential. The observed shift in bulk pH was identified as the primary cause of flooding and the deactivation of the gas diffusion electrode (GDE). To address this, we proposed separating the inlet catholyte from the outlet liquid products to maintain a constant pH entering the cell. The continuous flow of the solution ensures that the pH near the catalyst is kept below a critical value, preventing flooding. Additionally, a rational design of the microporous and catalyst layers contributes to extending the lifetime of the GDE before flooding occurs, achieving stability for up to 8 hours at 600 mA cm^{-2}.

Keywords: electrocatalysis, CO_2 reduction, acidic environment, multicarbon product, stability.

Laboratory of Materials for Renewable Energy (LMER)   214
Institute of Chemical Sciences and Engineering (ISIC)
Basic Science Faculty (SB)

1   Introduction

The electrochemical carbon dioxide reduction reaction (eCO$_2$RR) represents a promising strategy for mitigating CO$_2$ emissions and storing renewable energy in the form of chemical feedstock[1–3]. However, this reaction faces challenges primarily due to the limited water solubility of CO$_2$ molecules and the high overpotential resulting from their stability. Additionally, the eCO$_2$RR typically operates at neutral pH to avoid the competing hydrogen evolution reaction (HER) in acidic environments and carbonate formation in alkaline solutions[4,5].

Flow cell reactors, in which CO$_2$ is fed from the rear of a gas diffusion electrode (GDE) coated with a microporous (MP) layer (where the catalyst is deposited and the electrolyte is supplied), effectively address the challenge of CO$_2$ solubility in aqueous electrolytes[6]. Since CO$_2$ is introduced from the rear of the GDE and comes into contact with the electrolyte in a very thin region – that is, the catalyst layer – this cell design allows for the utilisation of alkaline electrolytes, reducing the occurrence of the HER. Therefore, the partial current density for multicarbon (C$_{2+}$) products can be boosted to over 1 A cm^{-2} in a flow cell reactor employing an alkaline electrolyte[7].

CO$_2$ electrolysis in a flow cell is primarily performed in alkaline solutions to minimise hydrogen evolution. However, even when CO$_2$ is supplied from the rear of the GDE, it can still permeate the alkaline electrolyte, leading to carbonate formation. The supplied CO$_2$ is, thus, only partially converted into the desired products, resulting in low CO$_2$ utilisation[8–10]. Furthermore, once the alkaline electrolyte penetrates the MP layer and reaches the rear of the GDE, it can rapidly form carbonate salts, hindering CO$_2$ access to the catalyst layer and leading to the flooding of the GDE[11–14]. Scholars have reported that a moderately low-pH electrolyte can still lead to high selectivity towards C$_{2+}$ products due to localised high-pH levels at the catalyst surface[15]. Simultaneously, the low-pH bulk electrolyte can continuously diffuse towards the surface, converting the bicarbonate generated by the elevated local pH back into CO$_2$. This approach, involving an acidic electrolyte, not only yields a comparable amount of C$_{2+}$ products using less CO$_2$ but also protects the GDE from flooding. In CO$_2$ electrolysis, many strategies have been proposed to minimise the occurrence of the HER, increase the selectivity towards C$_{2+}$ products, and enhance the reaction stability in acidic environments. The C$_{2+}$ Faradaic efficiency (FE) can be improved via the suppression of proton access by increasing the cation concentration at the catalyst layers[16,17] and the hydrophobicity in the vicinity of the catalyst[18,19]. One can elevate the cation concentration near the catalyst by, for example, introducing a cation-enriched layer[9], utilising a functionalised adlayer[20,21], or employing a nanostructured catalyst to increase the localised K$^+$ concentration[22]. Improving the stability of CO$_2$ electrolysis in acidic settings involves altering the MP layer to prevent flooding, introducing cationic groups to regulate the water[16], or employing pulse electrolysis to self-remove salt formation[23].

Despite the successful development of numerous strategies to improve C$_{2+}$ selectivity in acidic environments, one still needs to consider the interplay between reaction activity and stability. High activity results in a significant release of hydroxide ions at the reaction sites, constituting the principal reason for GDE degradation[24]. In particular, the cationic concentrations typically used for the CO$_2$RR in acidic environments, such as 3 M, could induce a more critical deactivation of the GDE than the concentration

Laboratory of Materials for Renewable Energy (LMER)
Institute of Chemical Sciences and Engineering (ISIC)
Basic Science Faculty (SB)

215

employed in alkaline electrolytes, which is only 1 M. In this work, we confirmed that CO_2 electrolysis in acidic media exhibits a similar product distribution to that in alkaline media and that the surface pH is alkaline. The continuous generation of hydroxide ions from the reaction sites rapidly changes the bulk pH, leading to the deactivation of the GDE. By separating the inlet catholyte and the liquid products, the hydroxide ions are quickly neutralised, and the pH near the catalyst is kept constant, enhancing the stability of the GDE. Increasing the thickness of the MP and catalyst layers while ensuring sufficient porosity for CO_2 diffusion significantly extends the lifetime of the GDE before the onset of flooding.

2 Methodology

2.1 Synthesis of CuO catalysts

The CuO catalysts were synthesised following the same protocol reported in previous studies[18]. Specifically, 1.3 g of $Cu(NO_3)_2 \cdot 3H_2O$ (Sigma-Aldrich) was dissolved in 100 mL of Milli-Q water, followed by the addition of 30 mL of 0.15 M NH_4OH prepared from ammonium hydroxide, 28% NH_3 (Alfa Aesar). Subsequently, 10 mL of 1.0 M NaOH (Reactolab SA) was gradually added at a rate of 2 mL min^{-1}. The precipitation reaction was allowed to proceed for 30 minutes, with continuous stirring facilitated by a magnetic agitator. The $Cu(OH)_2$ precipitate was then centrifuged, filtered, and thoroughly washed with deionised water and ethanol. Subsequently, the precipitate was freeze-dried for 72 hours and then calcined in air for 1 hour at 300 °C to yield the CuO catalyst.

2.2 Preparation of the GDE

The GDE was prepared by spray-coating the as-received GDE (YLS-30T, Suzhou Sinero Technology Co.) with the catalyst ink, consisting of isopropanol as the solvent, the as-synthesised catalyst (4 mg mL_{IPA}^{-1}), and a 5% dispersion of PTFE (diluted from 65% PTFE, Fuel Cell Store) at 4 µL $mg_{catalyst}^{-1}$. After evaporating the solvent, the GDE was calcined at 300 °C for 30 minutes to melt the PTFE particles.

The Vulcan PTFE ink was prepared by mixing carbon black (CB; Vulcan XC-72R, Fuel Cell Store) with 5% PTFE (diluted from PTFE DISP 30, Fuel Cell Store) and IPA as the solvent. A loading of 4 mg mL_{IPA}^{-1} was used, and that of the 5% PTFE was 4 µL mg_{carbon}^{-1}.

The GNP-CuO catalysts were prepared using IPA and 5% PTFE with a powder loading – total mass of graphene nanoplatelets (GNPs; Sigma-Aldrich) and CuO – of 4 mg mL_{IPA}^{-1} and a PTFE loading of 4 µL mg_{powder}^{-1}.

2.3 Electrochemical characterisation

Electrochemical measurements were performed using a potentiostat (Metrohm Autolab PGSTAT302N). The gaseous products were quantified using an online gas chromatograph (GC, SRI Instruments 8610C) equipped with a thermal conductivity detector (TCD) and a flame ionisation detector (FID). The electrolyte was collected after the chronopotentiostatic measurements, and ^1H nuclear magnetic resonance (NMR; Bruker 400 MHz AVIII HD) spectroscopy was used to quantify the liquid products. The flow cell used for the electrochemical measurements is the same as that used in previous work[6], with a cation exchange

Laboratory of Materials for Renewable Energy (LMER)
Institute of Chemical Sciences and Engineering (ISIC)
Basic Science Faculty (SB)

216

membrane (CEM, Nafion 115, Ion Power) separating the cathode and anode chambers. A leakless Ag/AgCl (Metrohm) reference electrode was employed, and a Pt plate served as the counter electrode. The catholyte was composed of 3 M KCl (Sigma-Aldrich), and the pH of the solution was adjusted to acidic levels via the addition of 3 M H_3PO_4 (diluted from 85% H_3PO_4, Sigma-Aldrich). The anolyte comprised a solution of 3 M $KHCO_3$ (Thermo Scientific). The pH evolution was measured over time with a pH metre (Mettler Toledo).

2.4   Material characterisation

Scanning electron microscopy (SEM) images and corresponding energy-dispersive X-ray (EDX) spectroscopy elemental maps were acquired using a FE-SEM ThermoFisher Teneo device. High-angle annular dark field (HAADF) images and the corresponding EDX maps were obtained with a ThermoFisher Tecnai Osiris 200 kV TEM instrument. The water contact angle (WCA) was measured with a Kruss EasyDrop Drop Shape Analyzer, and inductively coupled plasma-optical emission spectrometry (ICP-OES) was performed with an Agilent 5110 instrument.
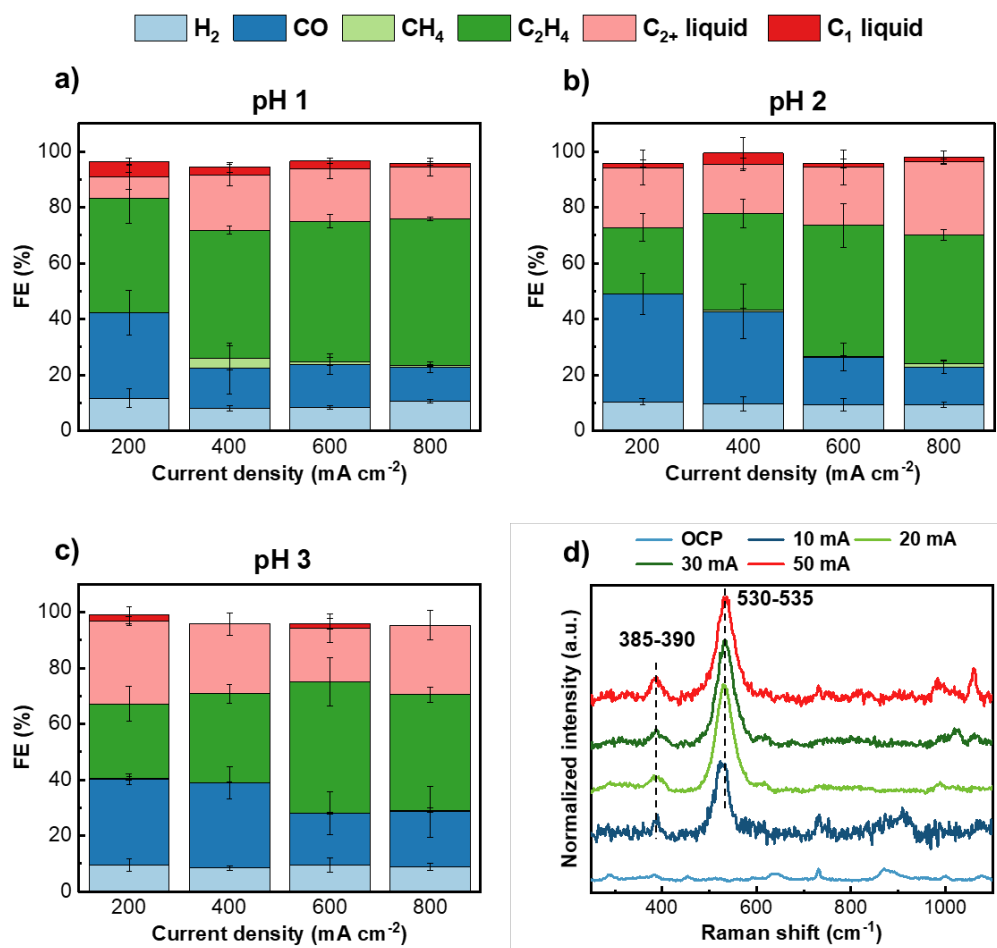
Operando Raman measurements were performed using an in situ Raman cell (Gaoss Union), with a continuous flow of CO_2 in the gas chamber (Figure S5.1). The catholyte comprised 3 M KCl adjusted with 3 M H_3PO_4 to the targeted pH, and the anolyte was 3 M $KHCO_3$. A noncontinuous flow was used for both since the catholyte chamber was open to the air to accommodate the immersion objective (Leica, 63x). The incident beam involved red light with a wavelength of 632 nm. Constant currents of 10, 20, 30, and 50 mA were applied and maintained for 2 minutes before the acquisition of Raman spectra.

3   Results and Discussion

3.1 CO_2 electrolysis using a CuO catalyst in an acidic environment

The Cu-based catalyst herein, synthesised using a similar protocol as in our previous work, involved Cu(II) oxide, showcasing a highly porous morphology. Since the selectivity of this catalyst towards H_2 exceeds 25% in 0.1 M $KHCO_3$ in an H-cell[18], using an acidic electrolyte was expected to result in a higher FE for H_2. Therefore, when using an acidic electrolyte, CO_2 electrolysis was only performed in a flow cell.

The product distribution of the eCO_2RR in an acidic electrolyte at a pH of 1, 2, and 3 is presented in Figures 5.1a–c. The FE was acquired over 20 minutes of CO_2 electrolysis with 90 mL of the catholyte being recycled; specifically, the outlet liquid from the cell was injected back into the inlet catholyte (Figure 5.2a). We observed a FE of approximately 10% for H_2 and around 90% for the CO_2RR at almost all current densities, indicating that the flow cell effectively suppresses H_2 evolution even in an acidic electrolyte. At every pH, while the FE for H_2 remains unchanged with an increasing current density, the product distribution shifts from CO to C_2H_4, most likely due to the increased overpotential with increasing current densities. Notably, there is no significant difference in the product distribution at different pH levels of the acidic electrolyte; the distribution is very similar to that obtained with 1 M KOH, using the same catalyst and experimental setup (Figure S5.2).

Laboratory of Materials for Renewable Energy (LMER)
Institute of Chemical Sciences and Engineering (ISIC)
Basic Science Faculty (SB)

217

Figure 5.1. Product distribution of CO_2 electrolysis at 600 mA cm^{-2} under different pH conditions: **a)** pH 1, **b)** pH 2, and **c)** pH 3. The feed CO_2 flow rate is approximately 50 mL min^{-1}, and the flow rates of the catholyte and anolyte are maintained at 1.5 mL min^{-1}. The outlet liquids from both chambers are reinjected into the inlet electrolytes for a closed liquid flow. **d)** Operando Raman spectra for CO_2 electrolysis at pH 2. From bottom to top: OCP and applied currents of 10, 20, 30, and 50 mA.

The selectivity towards C_{2+} products at the three pH values also exhibits an identical trend. The FE for C_{2+} products ranges from 45–55% at 200 mA cm^{-2} and increases to 65–75% at 800 mA cm^{-2} (Figure S5.3). When the cell is performing optimally – for instance, at 600 and 800 mA cm^{-2} at pH 1, and at 800 mA cm^{-2} at pH 2 – the FE for C_{2+} products exceeds 70% and approaches the value of 76% achieved with a flow cell using 1 M KOH[18]. This demonstrates that the added cations function efficiently as competing actors to reduce the access of protons to the catalyst.

The post-corrected potentials measured as a function of the current density at different bulk pH levels (Figure S5.4a) indicate that more acidic environments result in a more negative potential versus RHE, as determined by the correction according to the Nernst equation using the bulk pH. However, the recorded potentials versus the Ag/AgCl reference electrode are similar regardless of the bulk pH (Figure S5.4b). Additionally, the product distribution of the CO_2RR on the CuO catalyst exhibits a similar profile at the three different acidic pH values; this distribution also closely resembles that obtained with an alkaline pH of 14 (Figure S5.2), suggesting that even in a bulk acidic electrolyte, the local pH in the vicinity of the catalyst might be alkaline. Indeed, the hydroxide species of Cu was observed on the catalyst surface in an

Laboratory of Materials for Renewable Energy (LMER)
Institute of Chemical Sciences and Engineering (ISIC)
Basic Science Faculty (SB)

218

acidic electrolyte with operando Raman spectroscopy[25–27] (Raman shifts ranging from 385–390 cm^{-1} and 530–535 cm^{-1}), confirming the alkaline environment at the surface (Figure 5.1d).

The CO_2 flow rate has no significant influence on the distribution of the gaseous products: the FEs of H_2 and C_{2+} are almost equal at inlet CO_2 flow rates of 50 and 15 mL min^{-1} (Figure S5.5). Upon examining the final catholyte, we noted not only the presence of liquid products from the eCO_2RR but also dissolved Cu. The amount of dissolved Cu exceeds 15% of that initially spray-coated on the GDE after the reaction at pH 1; is approximately 3.5% and 2% at pH 2 and 3, respectively; and is negligible (under 1%) at pH 14 (Figure S5.6). The pre-electroreduction of the oxide catalyst (to form EC-Cu) in a neutral electrolyte at a low current density prior to CO_2 electrolysis in acidic media, as conducted in some reported works[10,28], does not reduce the amount of dissolved Cu (Figure S5.7). This might arise from the dissolution of the oxide shell that has been re-oxidised during the sample-transfer step of the EC-Cu. Therefore, in our work, CuO was directly employed (as-synthesised) in CO_2 electrolysis.

3.2 Evolution of product distribution under two system configurations

The CO_2 electrolysis setup, schematically illustrated in Figure 5.2a, features a closed electrolyte flow, aligning with numerous previous studies on CO_2 electrolysis in an acidic environment[9,10,22,29,30]. When transitioning from an alkaline to an acidic electrolyte, we anticipated a trade-off between flooding mitigation and proton concentration. Specifically, the acidic electrolyte was expected to prevent flooding due to the buffering capacity of the acid, neutralising hydroxide ions. Concurrently, however, it introduces an excessive amount of protons to the catalyst. Despite successfully managing the proton concentration by introducing cations through the high CO_2RR and C_{2+} selectivity, we did not observe any improvement in the stability of the electrode (Figures 5.2b–d and S5.8). The changes in the liquid C_1 and C_{2+} products are also negligible (Figure S5.9); therefore, tracking the evolution of gaseous products is sufficient to evaluate the degree of flooding in the GDE. In our case, the deactivation of the electrode was predominantly observed through the evolution of gaseous products, specifically H_2 (via the HER) and C_2H_4. After 1 hour of CO_2 electrolysis, the FE of H_2 increases to more than 30%, while that of C_2H_4 drops from more than 50% to 30%, regardless of the bulk pH (Figures 5.2b–d). Such deactivation of the electrode could be induced by the degradation of the catalyst or the GDE; to further investigate whether it arose from the evolution of the CuO catalyst in acidic bulk electrolyte or from the flooding of the electrode, we monitored the former over 1 hour of CO_2 electrolysis via ICP-OES. The evolution of the amount of Cu in the catholyte as a function of time indicates initial dissolution percentages of approximately 2.6, 3.2, and 8.0% of the CuO catalyst at pH 3, 2, and 1, respectively (Figure S5.10). This aligns with the Pourbaix diagram, indicating that CuO dissolves in an acidic environment[31]. Once the CuO had been completely reduced to the metallic Cu phase by the negative overpotential, the catalyst ceased to dissolve. Additionally, the amount of Cu in the catholyte started to decrease after 1500 s, suggesting a redeposition process of ionic Cu^{2+} in the catholyte onto the electrode. We concluded that during CO_2 electrolysis, the CuO catalysts evolve dynamically under the effects of low pH and a negative overpotential, leading to the formation of newly deposited Cu-based catalysts that might differ from the as-synthesised catalysts.

Laboratory of Materials for Renewable Energy (LMER)
Institute of Chemical Sciences and Engineering (ISIC)
Basic Science Faculty (SB)

219
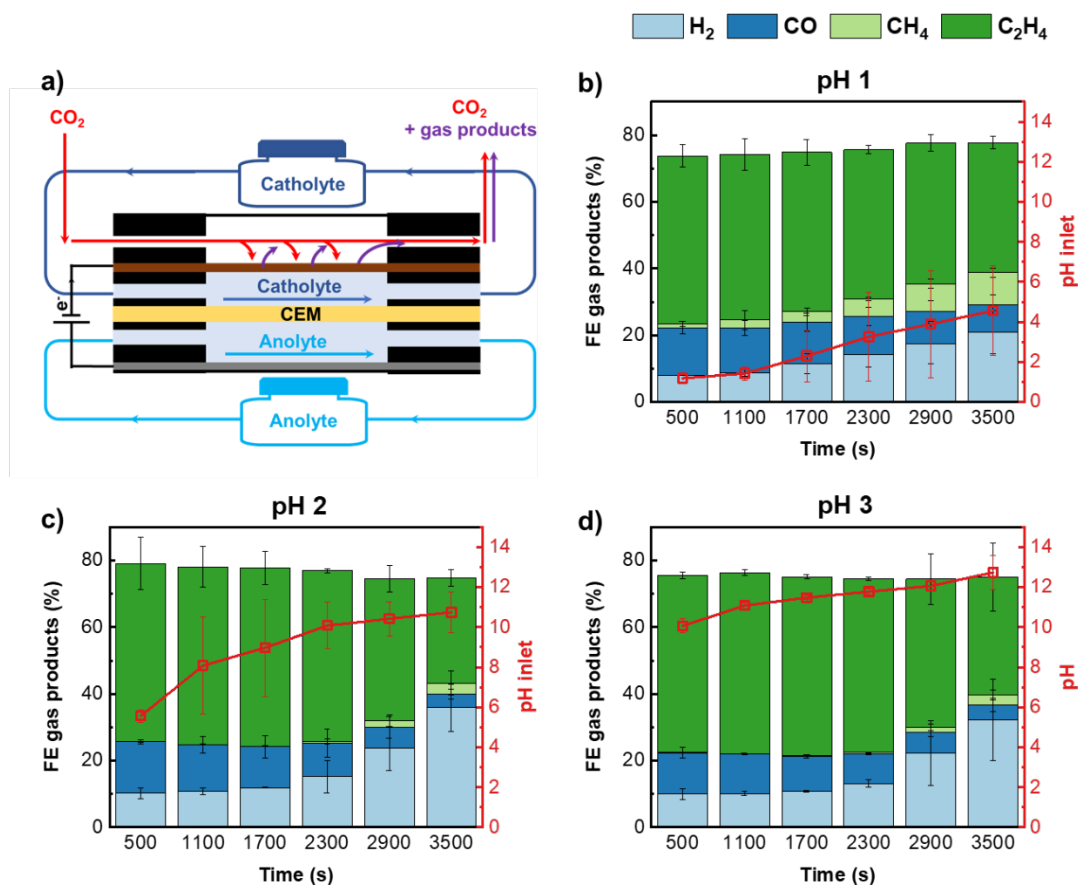
Figure 5.2. "Recycling" configuration of CO_2 electrolysis. **a)** Schematic illustration of the "recycling" configuration, where the outlet catholyte flowing out of the flow cell is injected back into the catholyte reservoir (the volume of the catholyte is 90 mL). Evolution of the product distribution and the pH of the catholyte reservoir over 1 hour of CO_2 electrolysis with a "recycling" configuration at **b)** pH 1, **c)** pH 2, and **d)** pH 3. The feed CO_2 flow rate is approximately 15 mL min^{-1}, and the flow rates of the catholyte and anolyte are maintained at 1.5 mL min^{-1}.

GDE flooding was indeed identified as the origin of electrode deactivation in an acidic electrolyte, as evidenced by salt formation on the rear of the GDE after 1 hour of electrolysis (Figure S5.11). The source of GDE flooding can be traced to the pH evolution of the catholyte. With a bulk pH of 3, the pH rapidly rises to 10.3 after 300 s and 12.1 after 1 hour of CO_2 electrolysis due to the formation of hydroxide ions (Figure 5.2d). Therefore, the electrolyte transforms rapidly into an alkaline state, explaining the similar product distribution between pH 3 and 14 as well as the rapid flooding phenomenon. Similarly, an initial bulk pH of 2 increases quickly to 5.8 after 300 s and then to 10.5 after 1 hour of CO_2 electrolysis (Figure 5.2c). On the other hand, the highly acidic catholyte at pH 1 only increases to a pH of approximately 5 after 1 hour of CO_2 electrolysis (Figure 5.2b). From these observations, one can anticipate the possibility that the local pH at the reaction sites, where hydroxide ions are released, is significantly higher than the measured bulk pH. The bulk pH, which evolves rapidly, is not sufficient to neutralise the local pH levels and prevent flooding.

The GDE was reused with the same catalyst after removing the salts on its rear, with a partial recovery in its CO_2RR performance, as evidenced by reduced hydrogen evolution and an increase in the FEs of CO and C_2H_4 (Figure S5.12). This confirms that the GDE is one factor causing electrode degradation. However, the CO_2RR selectivity does not reach the initial level of the freshly prepared GDE and also degrades rapidly

Laboratory of Materials for Renewable Energy (LMER)
Institute of Chemical Sciences and Engineering (ISIC)
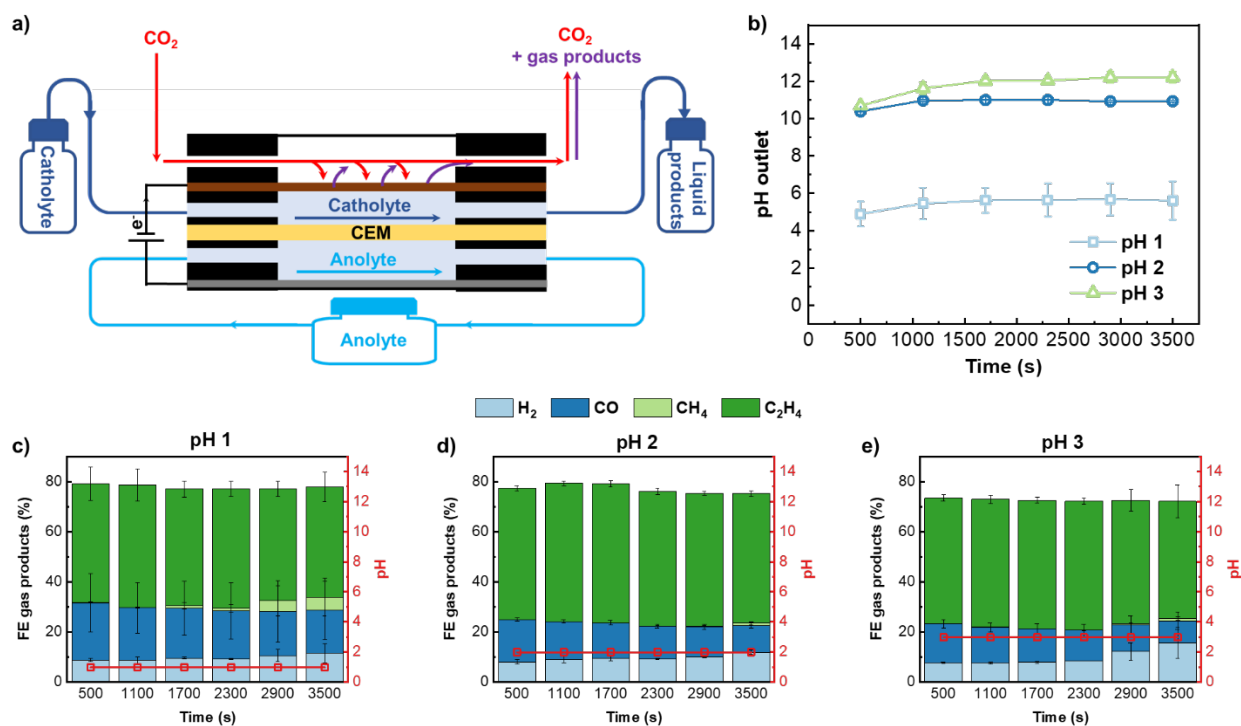Basic Science Faculty (SB)

220

after 1500 s. This irreversible loss in performance could arise from the dissolved and redeposited CuO catalyst or the loss in GDE hydrophobicity, as indicated by a reduction in the WCA from 135° to 75° (Figure S5.13), which cannot be recovered by simply cleaning the rear of the GDE.

To avoid the effects of the dynamic redeposition of the Cu-based catalysts and pH changes in the bulk electrolyte, we proposed a modification to the reaction system. Rather than injecting the outlet catholyte back into the initial catholyte reservoir (herein referred to as the "recycling" configuration), the outlet catholyte containing liquid products was collected in a separate container (herein termed the "separating" configuration), as shown in Figure 5.3a. In this setup, the inlet catholyte is consistently maintained at its bulk pH, and the redeposition of dissolved Cu ions onto the GDE is avoided.

As expected, in measuring the amount of Cu in the outlet catholyte (collected immediately after every GC injection), dissolved Cu was only observed in the catholyte collected after 500 s (Figure S5.14). This dissolution represents a loss fraction of 1.1, 1.8, and 9.6% at pH 3, 2, and 1, respectively. No dissolved Cu was noted thereafter, indicating that the dissolution occurred only during immersion and before the CuO was completely reduced to metallic Cu. Therefore, one can conclude that this change in the design of the reaction system can successfully prevent the effect of Cu redeposition.

Tracking the pH of the outlet electrolyte aided in evaluating the pH at the reaction site. While the latter might be higher than the value measured at the outlet, the continuous flow of inlet acidic catholyte allows for the immediate neutralisation of the excess basicity. Therefore, the measured pH of the outlet liquid products is expected to correspond to that in the vicinity of the catalyst. In the "separating" configuration, the measured pH of the outlet liquid products is significantly different from that of the inlet, with values of 5, 10.5, and 12 for inlet pH values of 1, 2, and 3, respectively (Figure 5.3b). For all three inlet pH values, the measured pH of the outlet liquids remains stable over time, except for the initial values, which are slightly lower since they involve introducing the acidic electrolyte to wet the GDE before applying the current density of 600 mA cm^{-2}.

The evolution of gaseous products in this modified system is presented in Figures 5.3c–e. Unlike the case of the "recycling" configuration, where changes are observed in the bulk pH and product selectivity, in the "separating" configuration, the pH of the inlet liquid flow is fixed, and the reaction exhibits significantly greater stability. Over 1 hour, the HER remains stable at approximately 10% for all three pH values, and no major changes were observed in the FE of C_2H_4, which is consistently maintained at approximately 50%. Therefore, with this change in the reaction system configuration, one can successfully monitor the pH of the catholyte entering the cell, ensuring sufficient inlet protons to recombine with the hydroxide ions generated from the reaction.

Laboratory of Materials for Renewable Energy (LMER)
Institute of Chemical Sciences and Engineering (ISIC)
Basic Science Faculty (SB)

221

Figure 5.3. "Separating" configuration of CO_2 electrolysis. **a)** Schematic illustration of the "separating" configuration, where the outlet catholyte flowing out from the flow cell is collected separately (the pH of the catholyte flowing into the flow cell is kept at the value of the catholyte reservoir). **b)** Evolution of the pH of the outlet liquid products flowing out of the cathode chamber over 1 hour. Evolution of the product distribution and pH of the catholyte reservoir over 1 hour of CO_2 electrolysis in a "separating" configuration at **c)** pH 1, **d)** pH 2, and **e)** pH 3. The feed CO_2 flow rate is approximately 15 mL min^{-1}, and the flow rates of the catholyte and anolyte are maintained at 1.5 mL min^{-1}.

3.3 GDE design for enhanced stability

3.3.1 Catalyst surface loading

The initial dissolution of CuO before reduction to metallic Cu is rather significant in the case of a CuO loading of 0.4 mg cm^{-2}, especially in a highly acidic environment (pH 1). This loss of the catalyst not only decreases the number of active sites for the CO_2RR but also weakens the GDE since the catalyst layer itself prevents liquid penetration to the rear of the GDE. Increasing the catalyst loading undoubtedly reduces the loss fraction and creates a thicker catalyst layer that can improve the resistance of the electrode against flooding. After increasing the catalyst loading to 2 and 4 mg cm^{-2}, the values of the FE of CO almost double, while those of C_2H_4 are slightly lower compared to the values at loadings of 0.4 and 1 mg cm^{-2}, probably due to the lower overpotential at a similar current density (Figures 5.4a and S5.15b).

After increasing the catalyst loading from 0.4 to 1.0 mg cm^{-2}, we observed an improvement in the stability of the GDE: the time for the FE of C_{2+} to drop below 40% and, correspondingly, for the HER to exceed 20% is extended to 5000 s (Figures 5.4a and S5.15b). At a higher loading of 2 mg cm^{-2}, the lifetime of the GDE before the onset of flooding is further improved. The HER is kept under 20% for 5000 s before increasing to 40% at 8000 s, indicating a gradual flooding of the GDE. The FE of C_2H_4 gradually increases from 38 to 55% in the first 4000 s, likely due to the wetting of the thick catalyst layer. Even in the presence of flooding, the FE of C_2H_4 remains above 40% after 8000 s, and the increased hydrogen evolution is compensated for

Laboratory of Materials for Renewable Energy (LMER)
Institute of Chemical Sciences and Engineering (ISIC)
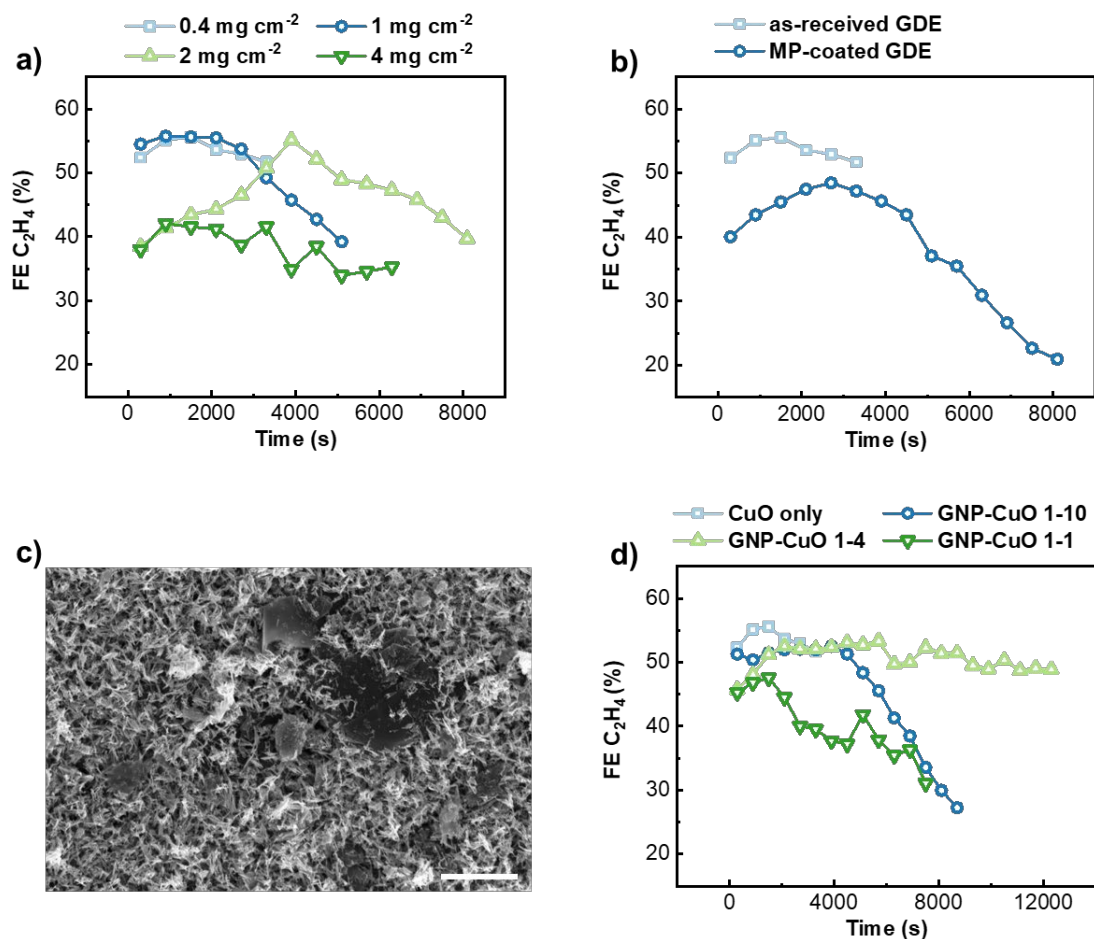Basic Science Faculty (SB)

222

by the decrease in the FE of CO (Figure S5.15). Therefore, a thicker catalyst layer protects the GDE from abrupt flooding, as in the case of a loading of 0.4 mg cm^{-2}. When the catalyst loading is excessively high – at, for example, 4 mg cm^{-2} – the catalyst might become too thick and dense, potentially blocking CO_2 diffusion within the catalyst layer and leading to an overall higher degree of hydrogen evolution (Figure S5.15a). The decrease in hydrophobicity after the reaction involving the GDE with a CuO loading of 2 mg cm^{-2} is also the smallest among the samples (Figure S5.16). In brief, increasing the thickness of the catalyst layer could enhance the barrier against flooding to a certain degree, though the layer must always allow for the diffusion of CO_2 through it.

3.3.2 Microporous layer

As a thicker catalyst layer helps decelerate the flooding of the GDE, we introduced an additional MP layer by spray-coating an ink containing Vulcan carbon black and a PTFE binder onto the as-received GDE YSL-30T. This layer was expected to provide additional thickness to the GDE while maintaining the continued diffusion of CO_2 due to the porous carbon, without changing the product distribution of the reaction (Figure S5.17). Such a layer is unlike a dense catalyst layer, which could block the feed gas and reduce the transport of gaseous products to the gas outlet.

While the HER does not change with the addition of this layer (Figure S5.18a), the FE of C_2H_4 gradually increases within the first hour before reaching its maximum value, corresponding to the wetting process of the GDE (Figure 5.4b). The additional MP layer results in a slightly higher amount of CO and a lower quantity of C_2H_4 compared to the as-received GDE (Figure S5.18b). This is attributed to the additional hydrophobicity provided by the MP layer to the GDE, as indicated by the larger WCA of the GDE coated with the MP layer (Figure S5.19). The GDE might be "drier", reducing the amount of hydrogenated CO, which is one of the intermediates for C_2H_4. However, the additional MP layer effectively increases the lifetime of the GDE before flooding occurs.

Laboratory of Materials for Renewable Energy (LMER)
Institute of Chemical Sciences and Engineering (ISIC)
Basic Science Faculty (SB)   223

Figure 5.4. Rational design of the carbon GDE to improve its lifetime prior to flooding. **a)** FEs of C_{2+} achieved at different surface loadings of the catalyst and **b)** those obtained with an additional MP layer, generated by spray-coating Vulcan PTFE ink onto the GDE at a surface loading of 0.8 mg cm^{-2} of Vulcan. **c)** SEM image of GDE spray-coated with GNP-CuO 1-4 (scale bar: 2 μm). **d)** FEs of C_{2+} obtained with different GNP:CuO mass ratios. The feed CO_2 flow rate is approximately 15 mL min^{-1}, and the flow rates of the catholyte and anolyte are maintained at 1.5 mL min^{-1}.

3.3.3 Dispersion of CuO catalysts

To increase the catalyst loading without creating a dense layer blocking CO_2 diffusion, we mixed the CuO catalyst with a nonactive compound acting as a scaffold to better disperse the powder catalyst. Inspired by the work of Kwon et al.[32], who used MgAl nanosheets to create "house-of-cards" scaffolds for their catalysts and to allow for catalyst loadings up to 5.82 mg cm^{-2}, we employed graphene nanoplatelets (GNPs), which also exhibit a nanosheet structure, as demonstrated in our previous work[33,34]. By physically mixing the GNPs and CuO catalysts, we observed that the nanosheet phase successfully generates channels separating the compact catalyst phase, ensuring CO_2 diffusion, as shown in the SEM images in Figures 5.4c and S5.20.

Different GNP:CuO mass ratios were tested to obtain the optimal ratio for enhanced resistance against flooding. The product distributions for the three mixtures – GNP-CuO 1-10, GNP-CuO 1-4, and GNP-CuO 1-1 – and that for CuO are presented in Figure S5.21. Upon the addition of GNPs to the catalyst layer, the GNP phase does not affect the CO$_2$RR selectivity, as opposed to the activity of tandem catalysts (e.g., Cu–Ag ones)[35,36]. At GNP:CuO mass ratios of 1:10 and 1:4, the product distribution profiles of the mixed systems are very similar to that of CuO used alone. At a 1:1 ratio, there is increased hydrogen evolution due

Laboratory of Materials for Renewable Energy (LMER)
Institute of Chemical Sciences and Engineering (ISIC)
Basic Science Faculty (SB)

224

to the excess amount of GNPs, but the profile of the CO_2RR products remains unchanged. Therefore, one can conclude that GNPs do not chemically contribute as an active phase or a coupled phase (for tandem catalysts) to CO_2RR catalytic activity.

While the addition of GNPs does not change the CO_2RR selectivity, it exerts a significant influence on the lifetime of the GDE. Using a GNP:CuO mass ratio of 1:10, the time point for the FE of H_2 to reach 20% and that of C_2H_4 to drop below 40% is 6000 s (Figures 5.4d and S5.22a). When this ratio is further increased to 1:4, the above-mentioned time point is extended to 12000 s. In addition, even though hydrogen evolution slowly increases over time due to gradual flooding, the FE of C_2H_4 remains stable and over 50%. This increasing trend of the HER is mostly compensated for by the decrease in CO (Figure S5.22b). However, when the GNP:CuO mass ratio is further increased to 1:1, with the molar concentration of the GNPs almost sevenfold higher than that of CuO, this time point is significantly reduced, most probably due to the excessive occurrence of the HER caused by the carbon (Figures 5.4d and S5.22). Furthermore, the WCA after the reaction indicates that the resistance of the GDE improves upon adding GNPs to the CuO catalyst since its loss in hydrophobicity is reduced (Figure S5.23). We determined that a GNP:CuO ratio of 1:4 offers the optimal layer thickness and morphology; this thickness is sufficient to enhance resistance against flooding, with channels dispersing the CuO to facilitate improved CO_2 diffusion. Importantly, this ratio ensures that the hydrogen evolution generated by the carbon is minimised.

Incorporating the optimized GDE composition in the "separating" configuration significantly improves the lifetime of the GDE prior to flooding. With a GDE comprising an additional MP layer and GNP-CuO 1-4 with a surface loading of 0.4 mg cm^{-2}, the FE of H_2 remains below 10% for almost 3 hours, with the corresponding FE of C_2H_4 remaining stable at approximately 50% (Figure S5.24). Higher loadings of 1 and 2 mg cm^{-2} aid in keeping the hydrogen evolution at 10% for approximately 5 hours (Figures S5.25 and S5.26). Additionally, once flooding begins, a higher surface loading with a thicker layer makes the deactivation less abrupt. The outlet pH remains stable when the GDE exhibits consistent performance but increases once flooding starts. With a bulk pH of 2, the outlet pH remains stable at around 10.5 but surges to over 11.5 at the point of flooding; this increase may result from salt crystals blocking CO_2 access to the catalyst layer. Consequently, the absorption of hydroxide ions by CO_2 is significantly reduced, leading to a higher pH in the outlet liquid.

Upon transitioning to a bulk pH of 1, the outlet liquid is maintained at a pH between 6 and 6.5, and no flooding occurs for almost 8 hours of CO_2 electrolysis. The FE of H_2 is maintained under 10%, accompanied by a transition from CO to C_2H_4 over time, as evidenced by the gradual increase in the FE of C_2H_4 and the gradual decrease in the FE of CO (Figure 5.5a). In brief, the "separating" system configuration utilising GNP-CuO 1-4 on a carbon GDE modified with an additional MP layer leads to stability for up to 8 hours (Figure 5.5b). Even though the lifetime of our GDE was shorter than the long-term longevity achieved with carbon-based GDEs at low current density in other works[19,37], we emphasize that our relatively high current density of 0.6 A cm^{-2} shows a good tradeoff between lifetime and current density[19,24,37–42] (Figure 5.5c and Table S5.1). Additionally, this stability falls within the range obtained for CO_2 electrolysis achieved with the PTFE GDE, commonly used in acids [9,10,20,22,28–30,43], and known for its high hydrophobicity and stability (Figure S5.28 and Table S5.2).

Laboratory of Materials for Renewable Energy (LMER)
Institute of Chemical Sciences and Engineering (ISIC)
Basic Science Faculty (SB)

225
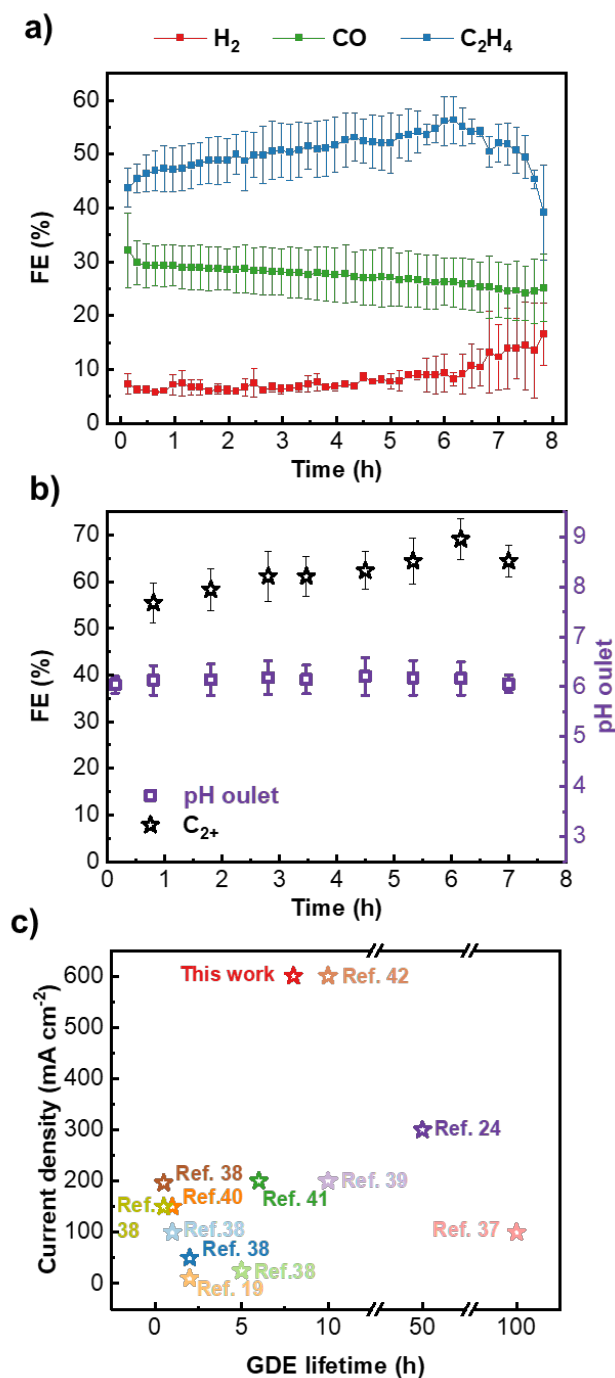
Figure 5.5. a) Gaseous product distribution of CO_2 electrolysis, **b)** FEs of C_{2+} and pH of the outlet liquids using "separating" configuration, in 3 M KCl adjusted to pH 1 with H_3PO_4, over time. The feed CO_2 flow rate is approximately 15 mL min^{-1}, and the flow rates of the catholyte and anolyte are maintained at 1.5 mL min^{-1}. **c)** Plot of the current densities versus lifetime of the carbon-based GDEs for CO_2-electrolysis in flow-cell. The details of the catalysts and electrolytes are summarized in Table S5.1.

4   Conclusion

In conclusion, we have demonstrated that CO_2 electrolysis in acidic environments, while expected to exhibit better stability than in alkaline environments, still suffers from flooding due to high local pH levels. Operando Raman spectroscopy revealed an alkaline catalyst surface, evidenced by the presence of oxyhydroxide species when examining the catalyst surface in acidic environments. Additionally, in a system

Laboratory of Materials for Renewable Energy (LMER)
Institute of Chemical Sciences and Engineering (ISIC)
Basic Science Faculty (SB)

226

configuration where the catholyte is recycled to form a closed liquid flow, the oxide catalyst undergoes a reconstruction process, including dissolution and redeposition. Furthermore, the bulk pH increases over time and leads to insufficient neutralisation of the hydroxide ions generated at the reaction sites, causing GDE flooding. By collecting the outlet liquid separately in a "separating" configuration, one can avoid the dynamic evolution of the Cu-based catalyst while maintaining the pH of the catholyte entering the cell constant. This inlet flow at a constant pH provides sufficient acidity to neutralise the hydroxide ions, keeping the pH near the catalyst below the critical range for carbonate formation upon combination with CO_2. The rational design of the GDE, including increasing the thicknesses of the MP and catalyst layers while ensuring the continued diffusion of CO_2 through them, contributes to creating a more resistant barrier against flooding, thereby increasing the lifetime of the carbon GDE.

Laboratory of Materials for Renewable Energy (LMER)
Institute of Chemical Sciences and Engineering (ISIC)
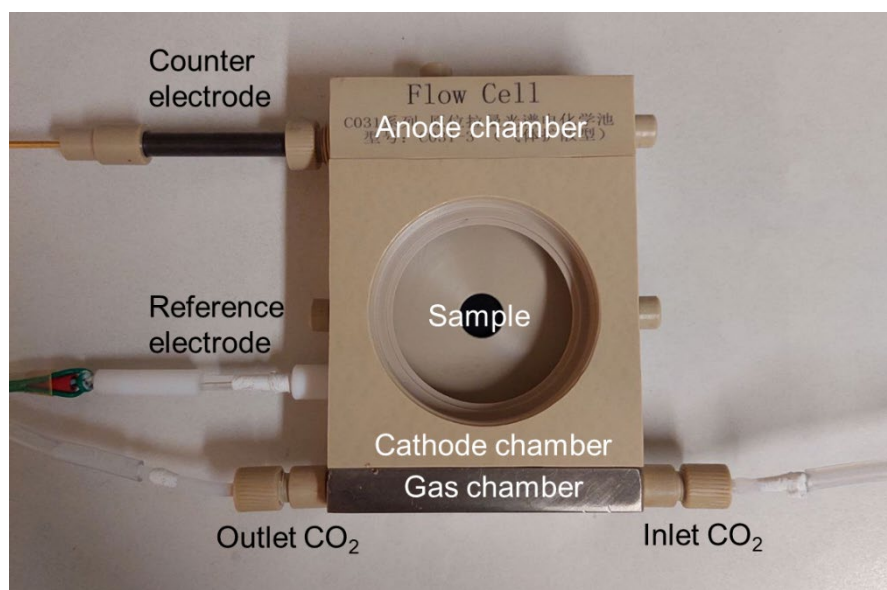Basic Science Faculty (SB)

227

References

[1]   A. Anzai, M. Higashi, M. Yamauchi, *Chem. Commun.* **2023**, *59*, 11188.

[2]   S. Vesztergom, A. Dutta, M. Rahaman, K. Kiran, I. Zelocualtecatl Montiel, P. Broekmann, *ChemCatChem* **2021**, *13*, 1039.

[3]   C. Kim, J. C. Bui, X. Luo, J. K. Cooper, A. Kusoglu, A. Z. Weber, A. T. Bell, *Nat. Energy* **2022**, *7*, 116.

[4]   Y. Hori, *Mod. Asp. Electrochem.* **2008**, *42*, 89.

[5]   S. Nitopi, E. Bertheussen, S. B. Scott, X. Liu, A. K. Engstfeld, S. Horch, B. Seger, I. E. L. Stephens, K. Chan, C. Hahn, J. K. Nørskov, T. F. Jaramillo, I. Chorkendorff, *Chem. Rev.* **2019**, *119*, 7610.

[6]   J. Zhang, W. Luo, A. Züttel, *J. Catal.* **2020**, *385*, 140.

[7]   F. P. García de Arquer, C. T. Dinh, A. Ozden, J. Wicks, C. McCallum, A. R. Kirmani, D. H. Nam, C. Gabardo, A. Seifitokaldani, X. Wang, Y. C. Li, F. Li, J. Edwards, L. J. Richter, S. J. Thorpe, D. Sinton, E. H. Sargent, *Science (80-.).* **2020**, *367*, 661.

[8]   T. Zhang, J. Zhou, T. Luo, J. Q. Lu, Z. Li, X. Weng, F. Yang, *Chem. - A Eur. J.* **2023**, *29*, DOI 10.1002/chem.202301455.

[9]   J. E. Huang, F. Li, A. Ozden, A. S. Rasouli, F. P. G. de Arquer, S. Liu, S. Zhang, M. Luo, X. Wang, Y. Lum, Y. Xu, K. Bertens, R. K. Miao, C. T. Dinh, D. Sinton, E. H. Sargent, *Science (80-.).* **2021**, *372*, 1074.

[10]   A. Perazio, C. E. Creissen, J. G. Rivera de la Cruz, M. W. Schreiber, M. Fontecave, *ACS Energy Lett.* **2023**, *8*, 2979.

[11]   Y. Kong, H. Hu, M. Liu, Y. Hou, V. Kolivoška, S. Vesztergom, P. Broekmann, *J. Catal.* **2022**, *408*, 1.

[12]   D. Wakerley, S. Lamaison, J. Wicks, A. Clemens, J. Feaster, D. Corral, S. A. Jaffer, A. Sarkar, M. Fontecave, E. B. Duoss, S. Baker, E. H. Sargent, T. F. Jaramillo, C. Hahn, *Nat. Energy* **2022**, *7*, 130.

[13]   E. W. Lees, B. A. W. Mowbray, F. G. L. Parlane, C. P. Berlinguette, *Nat. Rev. Mater.* **2022**, *7*, 55.

[14]   T. N. Nguyen, C. T. Dinh, *Chem. Soc. Rev.* **2020**, *49*, 7488.

[15]   Q. Hao, D. X. Liu, H. X. Zhong, Q. Tang, J. M. Yan, *Chem Catal.* **2023**, *3*, 100542.

[16]   M. C. O. Monteiro, F. Dattila, B. Hagedoorn, R. García-Muelas, N. López, M. T. M. Koper, *Nat. Catal.* **2021**, *4*, 654.

[17]   J. Gu, S. Liu, W. Ni, W. Ren, S. Haussener, X. Hu, *Nat. Catal.* **2022**, *5*, 268.

[18]   T. H. M. Pham, J. Zhang, M. Li, T. H. Shen, Y. Ko, V. Tileli, W. Luo, A. Züttel, *Adv. Energy Mater.* **2022**, *12*, DOI 10.1002/aenm.202103663.

[19]   Z. Yao, R. Lin, *Small* **2023**, *2306686*, 1.

Laboratory of Materials for Renewable Energy (LMER)
Institute of Chemical Sciences and Engineering (ISIC)
Basic Science Faculty (SB)

228

[20] Y. Zhao, L. Hao, A. Ozden, S. Liu, R. K. Miao, P. Ou, T. Alkayyali, S. Zhang, J. Ning, Y. Liang, Y. Xu, M. Fan, Y. Chen, J. E. Huang, K. Xie, J. Zhang, C. P. O'Brien, F. Li, E. H. Sargent, D. Sinton, *Nat. Synth.* **2023**, *2*, 403.

[21] M. Fan, J. E. Huang, R. K. Miao, Y. Mao, P. Ou, F. Li, X. Y. Li, Y. Cao, Z. Zhang, J. Zhang, Y. Yan, A. Ozden, W. Ni, Y. Wang, Y. Zhao, Z. Chen, B. Khatir, C. P. O'Brien, Y. Xu, Y. C. Xiao, G. I. N. Waterhouse, K. Golovin, Z. Wang, E. H. Sargent, D. Sinton, *Nat. Catal.* **2023**, *6*, 763.

[22] X. Zi, Y. Zhou, L. Zhu, Q. Chen, Y. Tan, X. Wang, M. Sayed, E. Pensa, R. A. Geioushy, K. Liu, J. Fu, E. Cortés, M. Liu, *Angew. Chemie - Int. Ed.* **2023**, *62*, 1.

[23] Y. Xu, J. P. Edwards, S. Liu, R. K. Miao, J. E. Huang, C. M. Gabardo, C. P. O'Brien, J. Li, E. H. Sargent, D. Sinton, *ACS Energy Lett.* **2021**, *6*, 809.

[24] K. Yang, R. Kas, W. A. Smith, T. Burdyny, *ACS Energy Lett.* **2021**, *6*, 33.

[25] Y. Cao, Z. Chen, P. Li, A. Ozden, P. Ou, W. Ni, J. Abed, E. Shirzadi, J. Zhang, D. Sinton, J. Ge, E. H. Sargent, *Nat. Commun.* **2023**, *14*, DOI 10.1038/s41467-023-37898-8.

[26] H. Ma, E. Ibáñez-Alé, R. Ganganahalli, J. Pérez-Ramírez, N. López, B. S. Yeo, *J. Am. Chem. Soc.* **2023**, DOI 10.1021/jacs.3c08079.

[27] Y. Zhao, X. Chang, A. S. Malkani, X. Yang, L. Thompson, F. Jiao, B. Xu, *J. Am. Chem. Soc.* **2020**, *142*, 9735.

[28] Z. Ma, Z. Yang, W. Lai, Q. Wang, Y. Qiao, H. Tao, C. Lian, M. Liu, C. Ma, A. Pan, H. Huang, *Nat. Commun.* **2022**, *13*, 1.

[29] W. Nie, G. P. Heim, N. B. Watkins, T. Agapie, J. C. Peters, *Angew. Chemie* **2023**, *135*, 1.

[30] Y. Xie, P. Ou, X. Wang, Z. Xu, Y. C. Li, Z. Wang, J. E. Huang, J. Wicks, C. McCallum, N. Wang, Y. Wang, T. Chen, B. T. W. Lo, D. Sinton, J. C. Yu, Y. Wang, E. H. Sargent, *Nat. Catal.* **2022**, *5*, 564.

[31] J. Zhang, C. Guo, S. Fang, X. Zhao, L. Li, H. Jiang, Z. Liu, Z. Fan, W. Xu, J. Xiao, M. Zhong, *Nat. Commun.* **2023**, *14*, 1.

[32] S. Kwon, J. Zhang, R. Ganganahalli, S. Verma, B. S. Yeo, *Angew. Chemie - Int. Ed.* **2023**, *62*, 1.

[33] T. H. M. Pham, Y. Ko, M. Wei, K. Zhao, L. Zhong, A. Züttel, *J. Mater. Chem. A* **2023**, *11*, 21066.

[34] L. Zhong, T. H. M. Pham, Y. Ko, A. Züttel, *Front. Chem. Eng.* **2023**, *5*, 1.

[35] J. Zhang, T. H. M. Pham, Y. Ko, M. Li, S. Yang, C. D. Koolen, L. Zhong, W. Luo, A. Züttel, *Cell Reports Phys. Sci.* **2022**, *3*, 100949.

[36] C. Chen, Y. Li, S. Yu, S. Louisia, J. Jin, M. Li, M. B. Ross, P. Yang, *Joule* **2020**, *4*, 1688.

[37] Y. Wu, L. Charlesworth, I. Maglaya, M. N. Idros, M. Li, T. Burdyny, G. Wang, T. E. Rufford, *ACS Energy Lett.* **2022**, *7*, 2884.

[38] M. E. Leonard, L. E. Clarke, A. Forner-Cuenca, S. M. Brown, F. R. Brushett, *ChemSusChem* **2020**,

Laboratory of Materials for Renewable Energy (LMER)
Institute of Chemical Sciences and Engineering (ISIC)
Basic Science Faculty (SB)

229

13, 400.
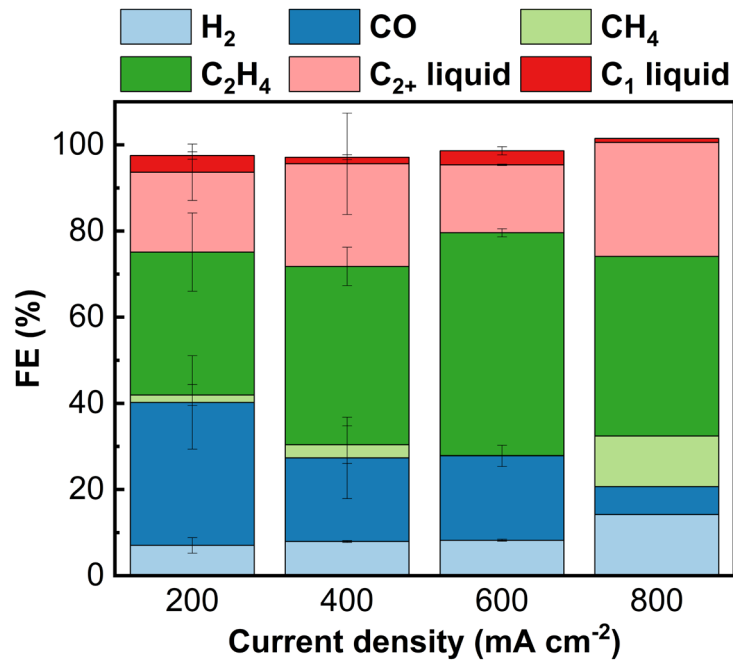
[39]   Y. C. Tan, K. B. Lee, H. Song, J. Oh, *Joule* **2020**, *4*, 1104.

[40]   Y. Wu, S. Garg, M. Li, M. N. Idros, Z. Li, R. Lin, J. Chen, G. Wang, T. E. Rufford, *J. Power Sources* **2022**, *522*, 230998.

[41]   E. R. Cofell, U. O. Nwabara, S. S. Bhargava, D. E. Henckel, P. J. A. Kenis, *ACS Appl. Mater. Interfaces* **2021**, *13*, 15132.

[42]   M. Sun, J. Cheng, M. Yamauchi, *Nat. Commun.* **2024**, *15*, 1.

[43]   Y. Chen, X. Y. Li, Z. Chen, A. Ozden, J. E. Huang, P. Ou, J. Dong, J. Zhang, C. Tian, B. H. Lee, X. Wang, S. Liu, Q. Qu, S. Wang, Y. Xu, R. K. Miao, Y. Zhao, Y. Liu, C. Qiu, J. Abed, H. Liu, H. Shin, D. Wang, Y. Li, D. Sinton, E. H. Sargent, *Nat. Nanotechnol.* **2023**, DOI 10.1038/s41565-023-01543-8.

Laboratory of Materials for Renewable Energy (LMER)
Institute of Chemical Sciences and Engineering (ISIC)
Basic Science Faculty (SB)

230
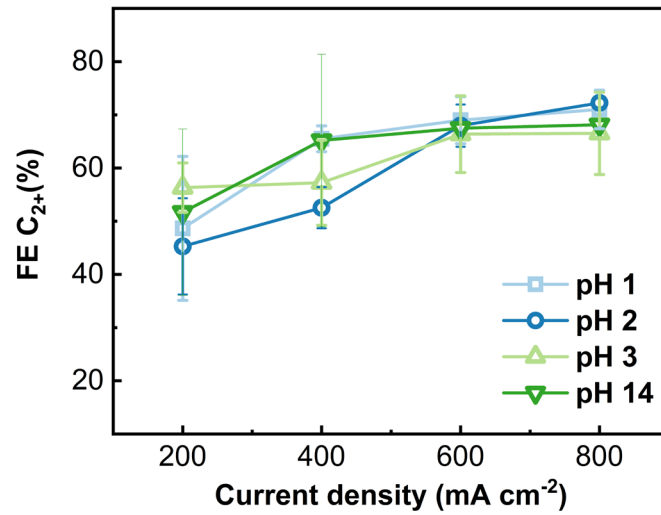
5   Supporting Information

Figure S5.1. Photograph of the cell used for operando Raman measurements. CO_2 flows through the gas chamber while the anode chamber is closed, and the cathode chamber is open to the air to accommodate the immersion objective.
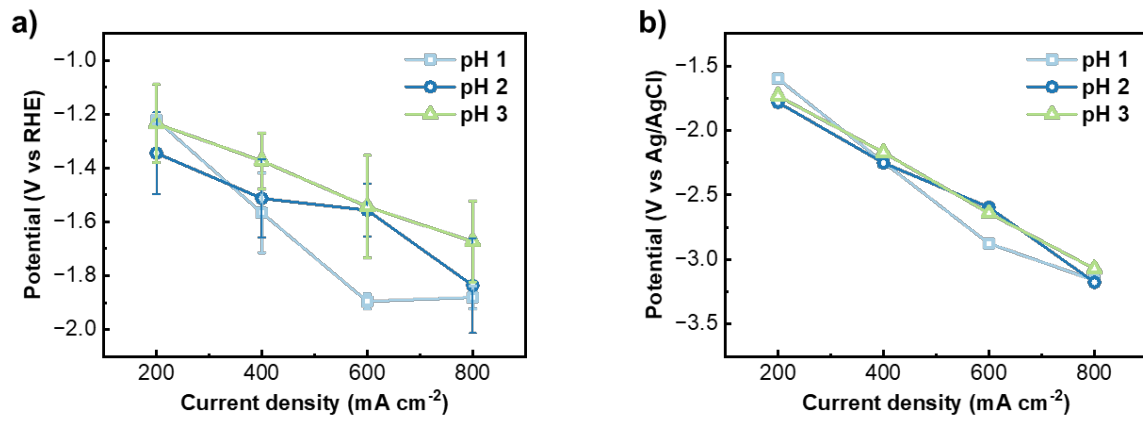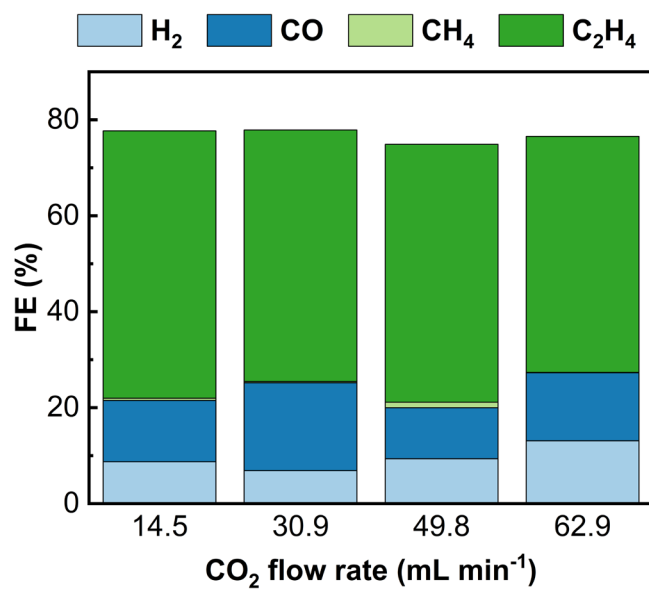
Laboratory of Materials for Renewable Energy (LMER)
Institute of Chemical Sciences and Engineering (ISIC)
Basic Science Faculty (SB)

231

Figure S5.2. Product distribution of CO_2 electrolysis in 1 M KOH at a constant current density of 600 mA cm^{-2} and a CO_2 flow rate of 100 mL min^{-1}.

Laboratory of Materials for Renewable Energy (LMER)
Institute of Chemical Sciences and Engineering (ISIC)
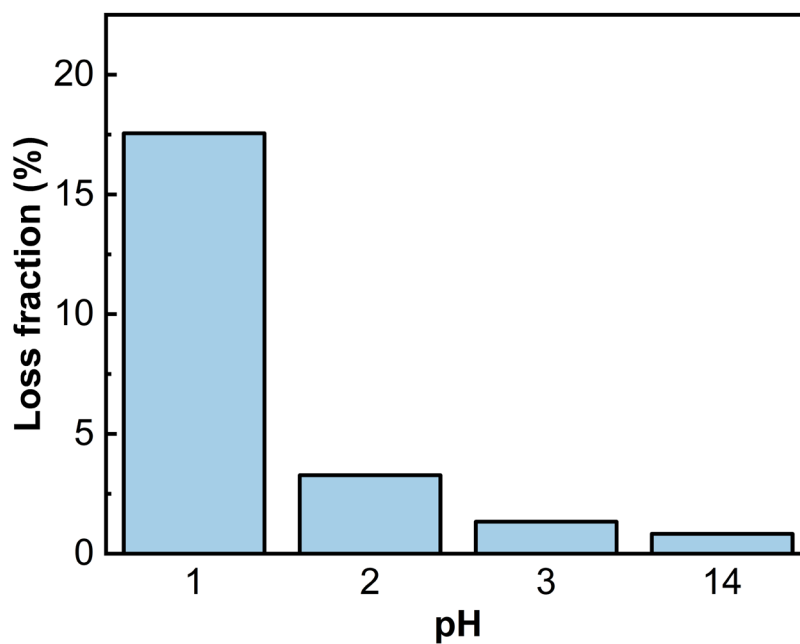Basic Science Faculty (SB)

232

Figure S5.3. Selectivity of the eCO$_2$RR towards C$_{2+}$ measured in electrolytes of different pH values at a constant current density of 600 mA cm^{-2}.

Laboratory of Materials for Renewable Energy (LMER)
Institute of Chemical Sciences and Engineering (ISIC)
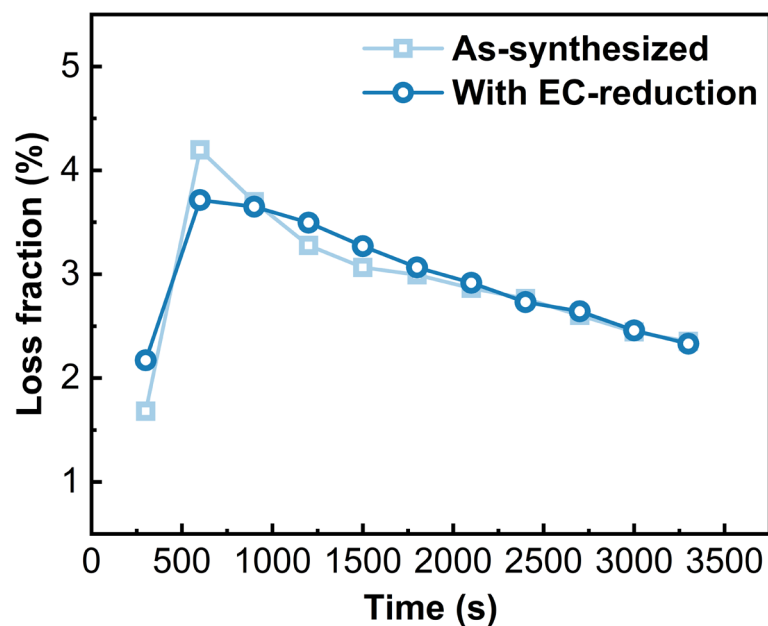Basic Science Faculty (SB)

233

Figure S5.4. Potentials recorded at a constant current density of 600 mA cm^{-2}: **a)** calculated, iR-corrected potentials versus RHE and **b)** measured potentials versus the Ag/AgCl electrode.
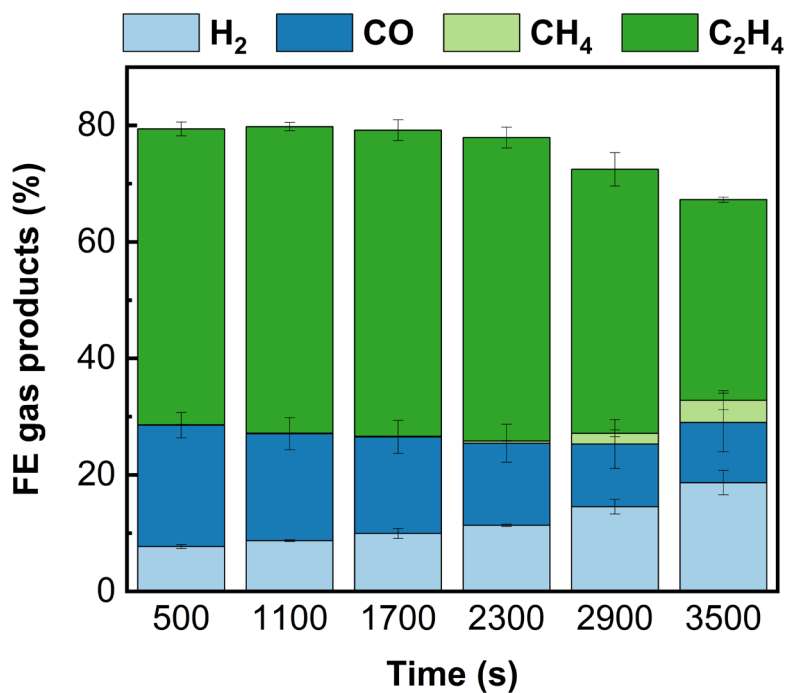
Laboratory of Materials for Renewable Energy (LMER)
Institute of Chemical Sciences and Engineering (ISIC)
Basic Science Faculty (SB)

234

Figure S5.5. Gaseous product distribution at various CO_2 flow rates and a constant current density of 600 mA cm^{-2}.

Laboratory of Materials for Renewable Energy (LMER)
Institute of Chemical Sciences and Engineering (ISIC)
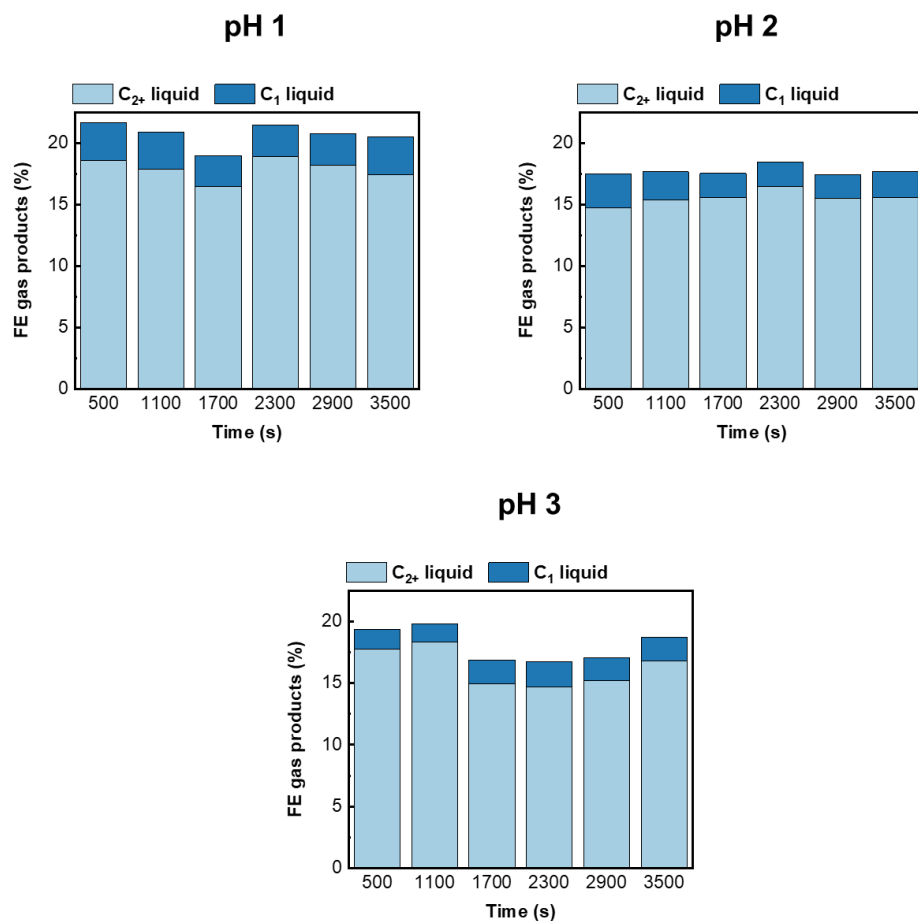Basic Science Faculty (SB)

235

Figure S5.6. Calculated fraction of Cu dissolved in the catholyte at different pH levels of the catholyte. The dissolved Cu was measured from the catholyte collected after 1 hour of CO_2 electrolysis at a constant current density of 600 mA cm^{-2}. The mass of dissolved Cu is normalised against the mass of CuO initially spray-coated onto the GDE.

Laboratory of Materials for Renewable Energy (LMER)
Institute of Chemical Sciences and Engineering (ISIC)
Basic Science Faculty (SB)

236

Figure S5.7. Calculated fraction of Cu dissolved in the catholyte over 1 hour of CO_2 electrolysis at pH 2 and a constant current density of 600 mA cm^{-2}. The Cu dissolution was examined for both the as-synthesised CuO and the EC-Cu, which was reduced for 20 minutes at 20 mA cm^{-2} in 0.1 M $KHCO_3$ before CO_2 electrolysis. The mass of dissolved Cu is normalised against the initially spray-coated mass of CuO on the GDE.
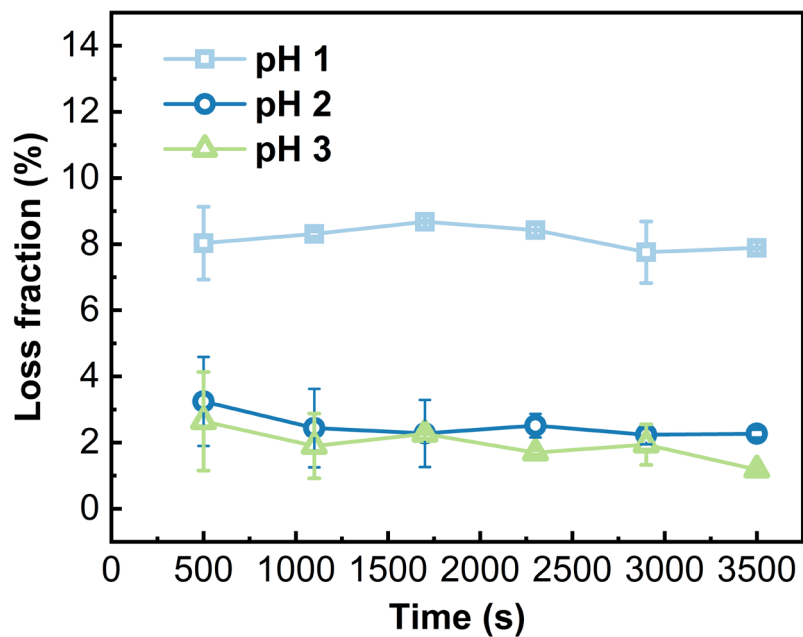
Laboratory of Materials for Renewable Energy (LMER)
Institute of Chemical Sciences and Engineering (ISIC)
Basic Science Faculty (SB)

237

Figure S5.8. Evolution of gaseous products over 1 hour of CO_2 electrolysis at pH 14 and a constant current density of 600 mA cm^{-2}, utilising the "recycling" configuration.

Laboratory of Materials for Renewable Energy (LMER)
Institute of Chemical Sciences and Engineering (ISIC)
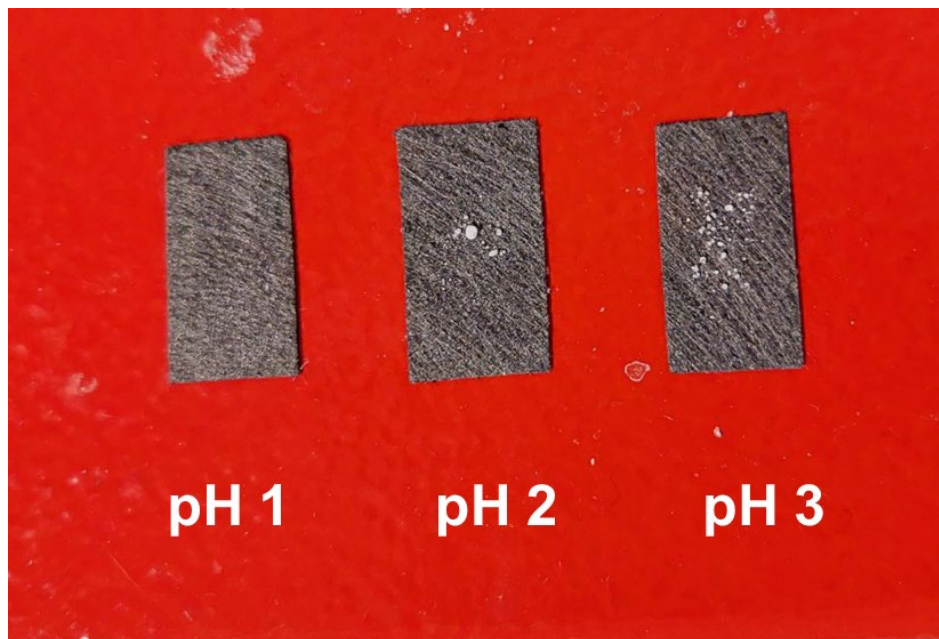Basic Science Faculty (SB)

238

Figure S5.9. Evolution of liquid products over 1 hour of CO_2 electrolysis in acidic electrolytes of pH 1, 2, and 3 at a constant current density of 600 mA cm^{-2}.

Laboratory of Materials for Renewable Energy (LMER)
Institute of Chemical Sciences and Engineering (ISIC)
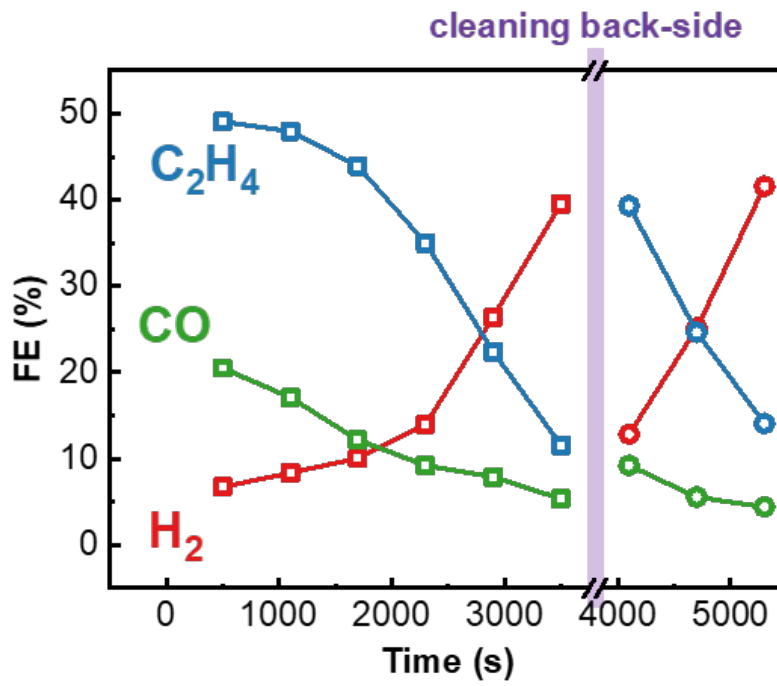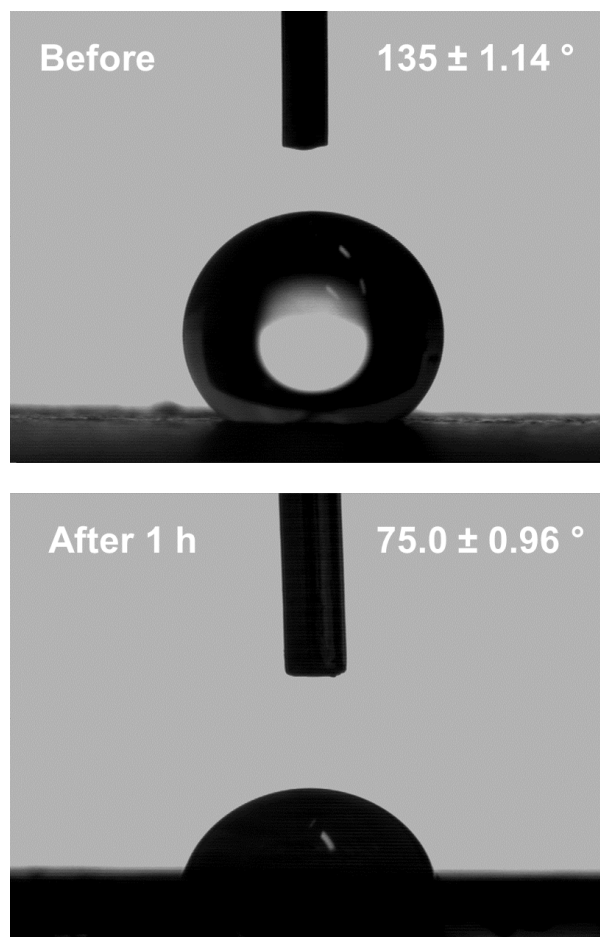Basic Science Faculty (SB)

239

Figure S5.10. Calculated fraction of Cu dissolved in the catholyte over 1 hour of CO_2 electrolysis at pH 1, 2, and 3, utilising the "recycling" configuration at a constant current density of 600 mA cm^{-2}. The mass of dissolved Cu is normalised against the initially spray-coated mass of CuO on the GDE.

Laboratory of Materials for Renewable Energy (LMER)   **240**
Institute of Chemical Sciences and Engineering (ISIC)
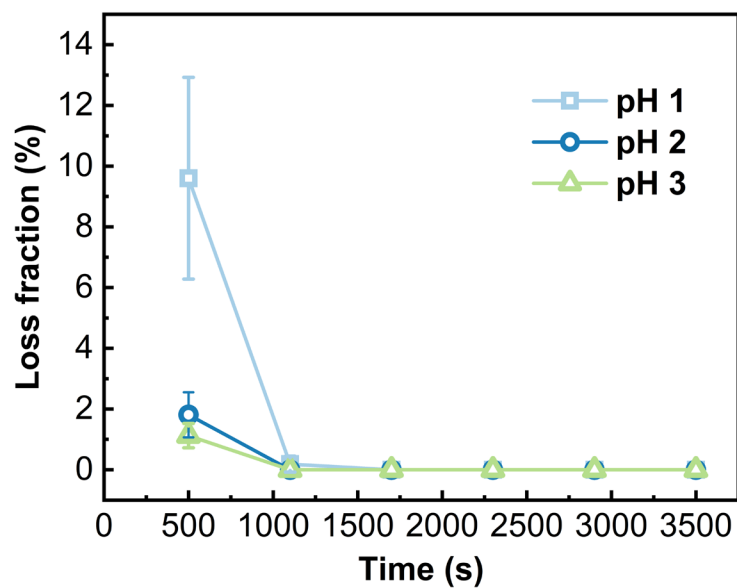Basic Science Faculty (SB)

Figure S5.11. Photographs of the rear of the carbon GDE after 1 hour of CO_2 electrolysis at pH 1, 2, and 3 and a constant current density of 600 mA cm^{-2}.
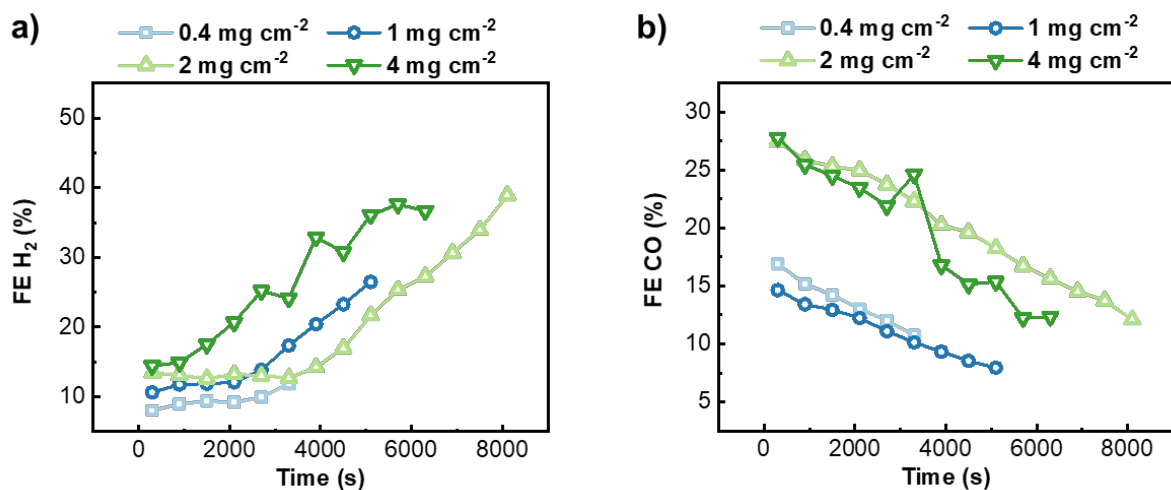
Laboratory of Materials for Renewable Energy (LMER)
Institute of Chemical Sciences and Engineering (ISIC)
Basic Science Faculty (SB)

241

Figure S5.12. Evolution of gaseous products over 1 hour of CO_2 electrolysis at a constant current density of 600 mA cm^{-2} and pH 2, and that in a new catholyte of pH 2 after cleaning the rear (back side) of the GDE.

Laboratory of Materials for Renewable Energy (LMER)
Institute of Chemical Sciences and Engineering (ISIC)
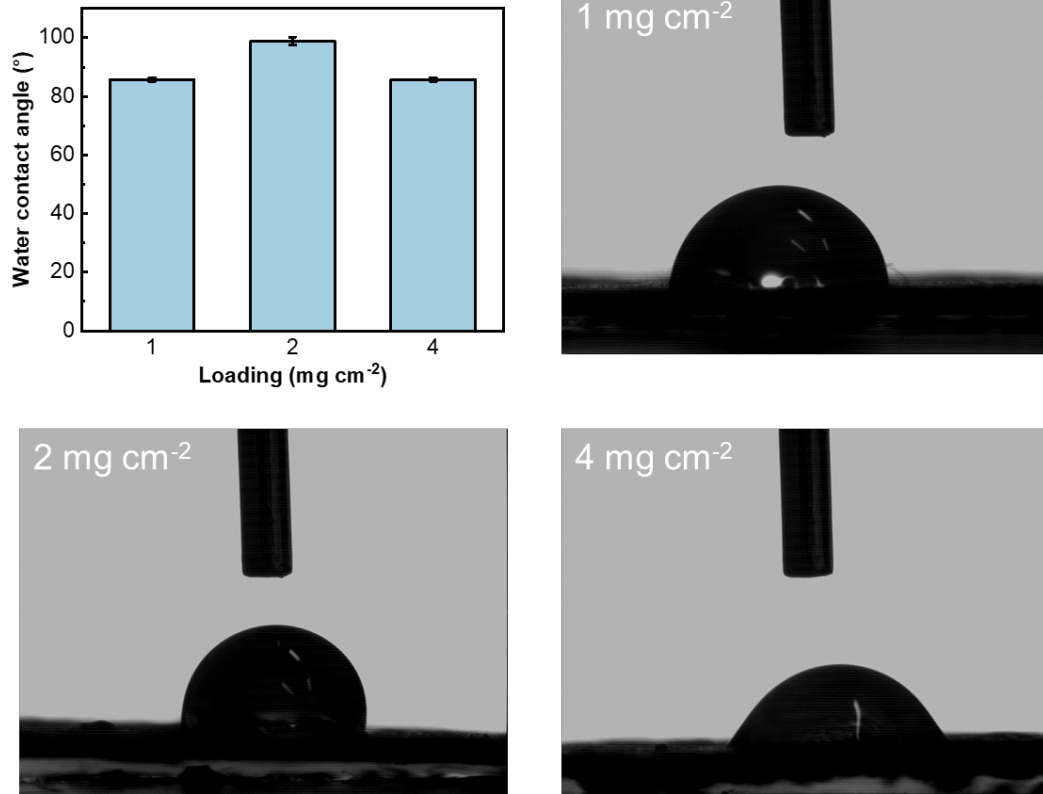Basic Science Faculty (SB)

242

243

Figure S5.13. WCA of the CuO catalyst initially spray-coated onto the carbon GDE and that after 1 hour of CO_2 electrolysis at pH 2 and a constant current density of 600 mA cm^{-2}.
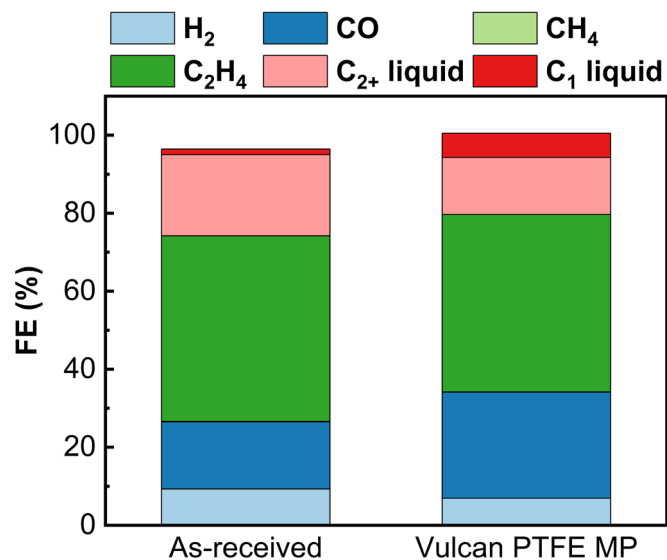
Laboratory of Materials for Renewable Energy (LMER)
Institute of Chemical Sciences and Engineering (ISIC)
Basic Science Faculty (SB)

243

Figure S5.14. Calculated fraction of Cu dissolved in the catholyte over 1 hour of CO_2 electrolysis at pH 1, 2, and 3, using the "separating" configuration at a constant current density of 600 mA cm^{-2}. The mass of dissolved Cu is normalised against the initially spray-coated mass of CuO on the GDE.

Laboratory of Materials for Renewable Energy (LMER)
Institute of Chemical Sciences and Engineering (ISIC)
Basic Science Faculty (SB)

244

Figure S5.15. Evolution of gaseous products over 1 hour of CO_2 electrolysis at pH 2 and a constant current density of 600 mA cm^{-2}, with different CuO surface loadings: **a)** FE of H_2 and **b)** FE of CO.

Laboratory of Materials for Renewable Energy (LMER)
Institute of Chemical Sciences and Engineering (ISIC)
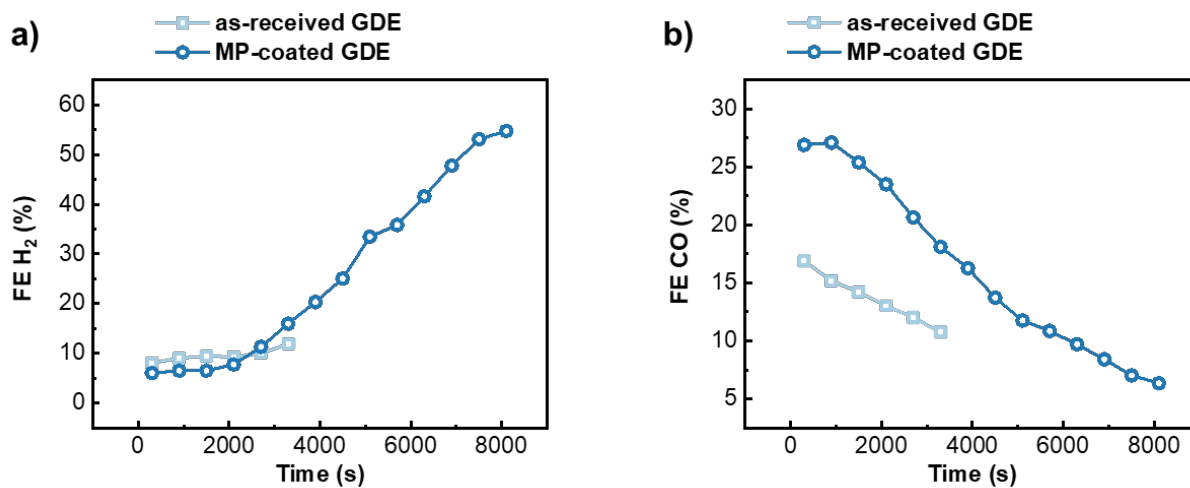Basic Science Faculty (SB)

245

Figure S5.16. WCA of the carbon GDE with different CuO loadings at pH 2 and a constant current density of 600 mA cm^{-2}, after CO$_2$ electrolysis until the onset of flooding.

Laboratory of Materials for Renewable Energy (LMER)
Institute of Chemical Sciences and Engineering (ISIC)
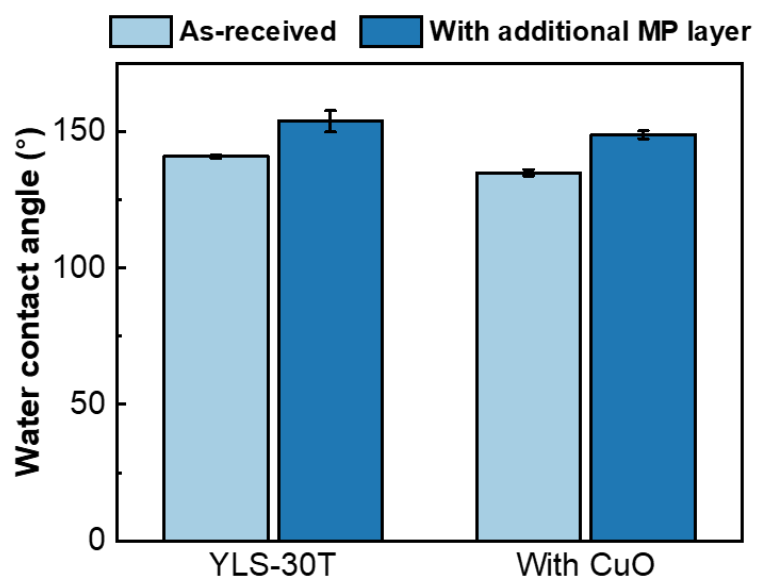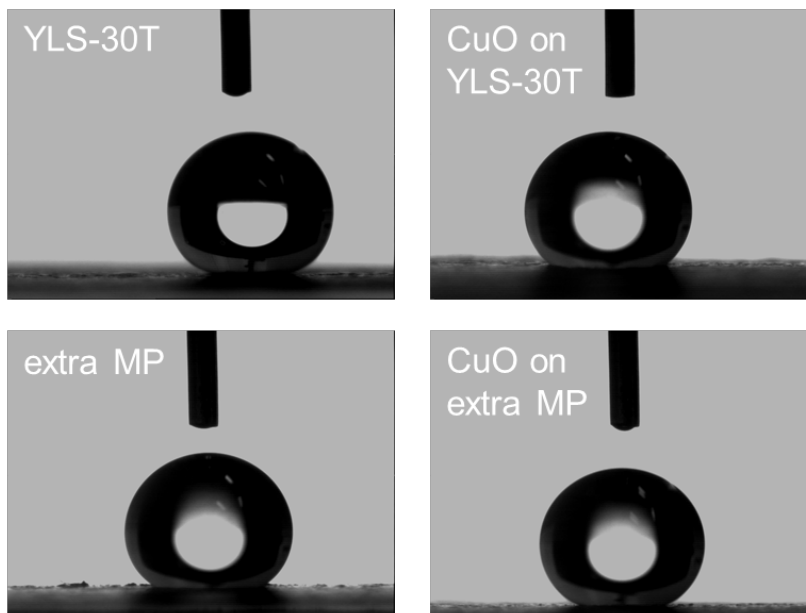Basic Science Faculty (SB)

246

Figure S5.17. Product distribution of CO_2 electrolysis at a current density of 600 mA cm^{-2} and pH 2 for the as-received YLS-30T GDE spray-coated with CuO and the GDE with an additional MP layer. The CuO loading is 0.4 mg cm^{-2}.
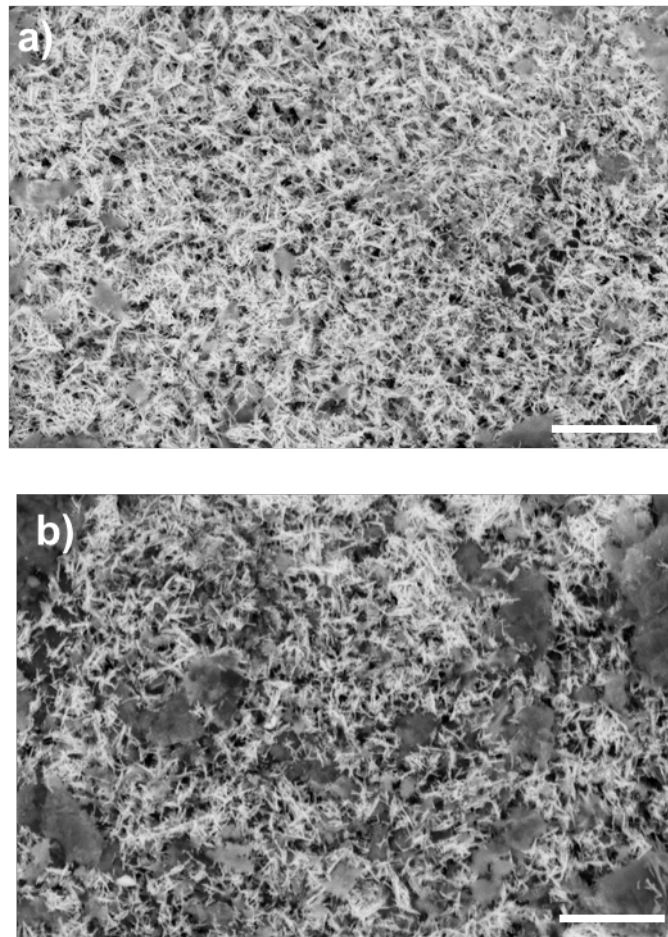
Laboratory of Materials for Renewable Energy (LMER)
Institute of Chemical Sciences and Engineering (ISIC)
Basic Science Faculty (SB)

247

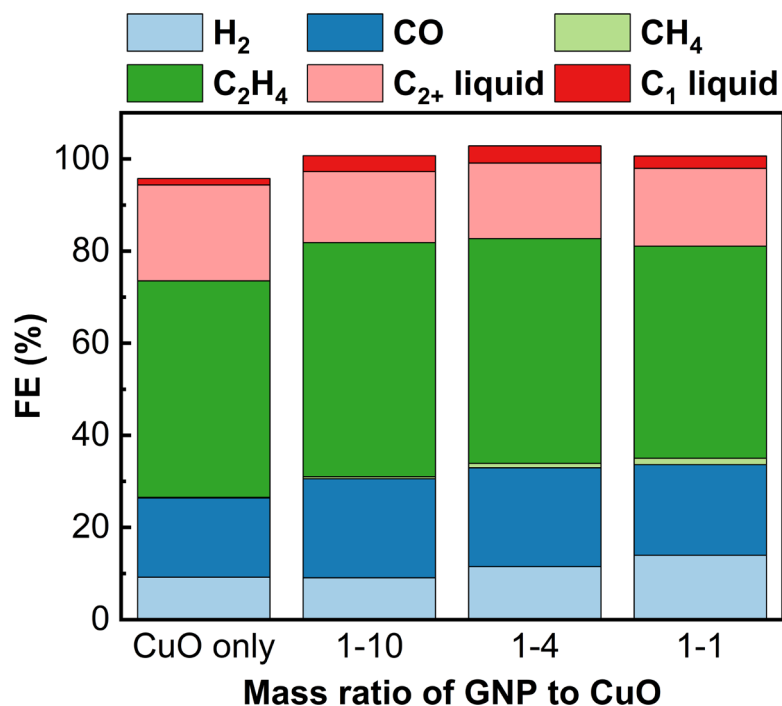**Figure S5.18.** Evolution of gaseous products over 1 hour of CO_2 electrolysis at pH 2 and a constant current density of 600 mA cm^{-2} for the as-received YLS-30T GDE spray-coated with CuO and the GDE with an additional MP layer: **a)** FE of H_2 and **b)** FE of CO.

Laboratory of Materials for Renewable Energy (LMER)
Institute of Chemical Sciences and Engineering (ISIC)
Basic Science Faculty (SB)

248

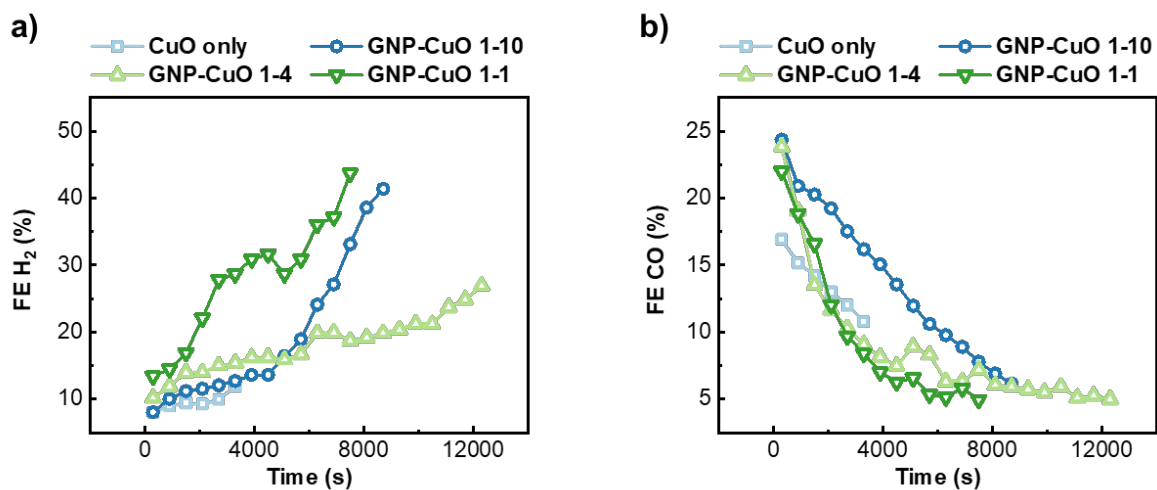**Figure S5.19.** WCAs of different freshly prepared GDEs: as-received YLS-30T GDE, as-received YLS-30T GDE spray-coated with CuO, YLS-30T GDE spray-coated with additional MP layer, and GDE with CuO spray-coated onto YLS-30T modified with an additional MP layer.

Laboratory of Materials for Renewable Energy (LMER)
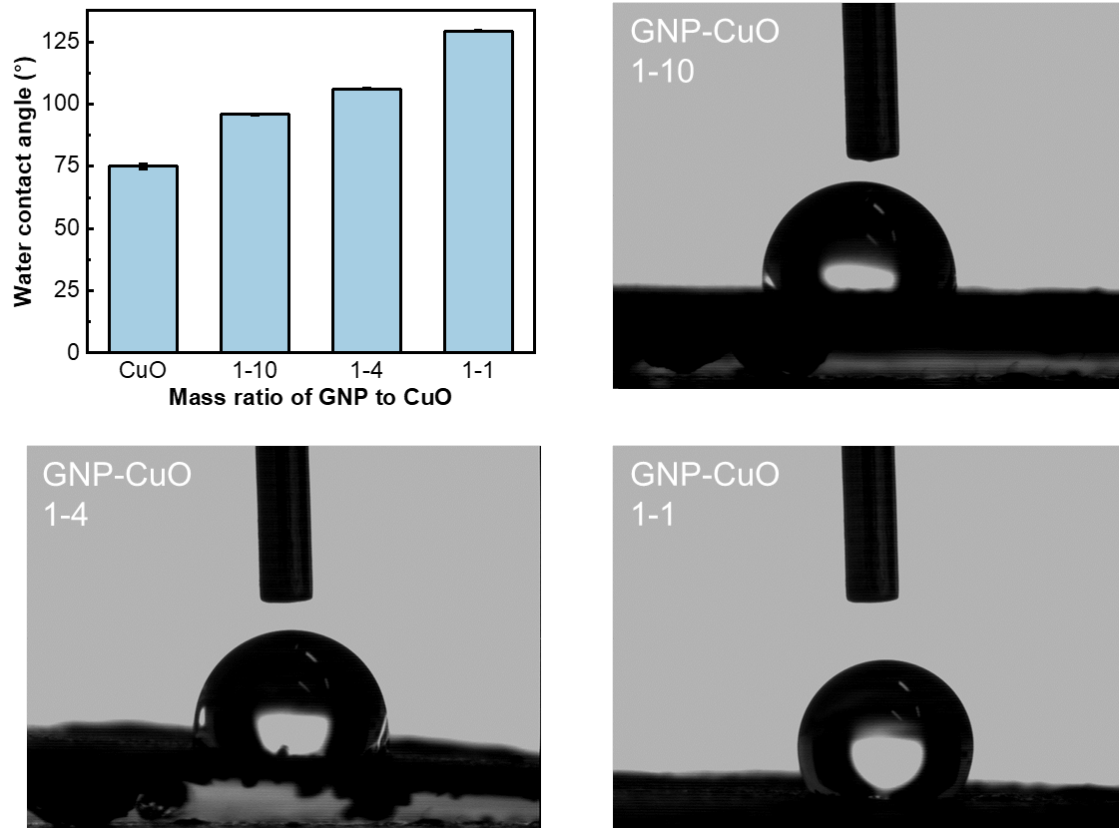Institute of Chemical Sciences and Engineering (ISIC)
Basic Science Faculty (SB)

249

Figure S5.20. SEM images of the GDE spray-coated with **a)** GNP-CuO 1-10 and **b)** GNP-CuO 1-1. Scale bar: 2 µm.

Laboratory of Materials for Renewable Energy (LMER)
Institute of Chemical Sciences and Engineering (ISIC)
Basic Science Faculty (SB)
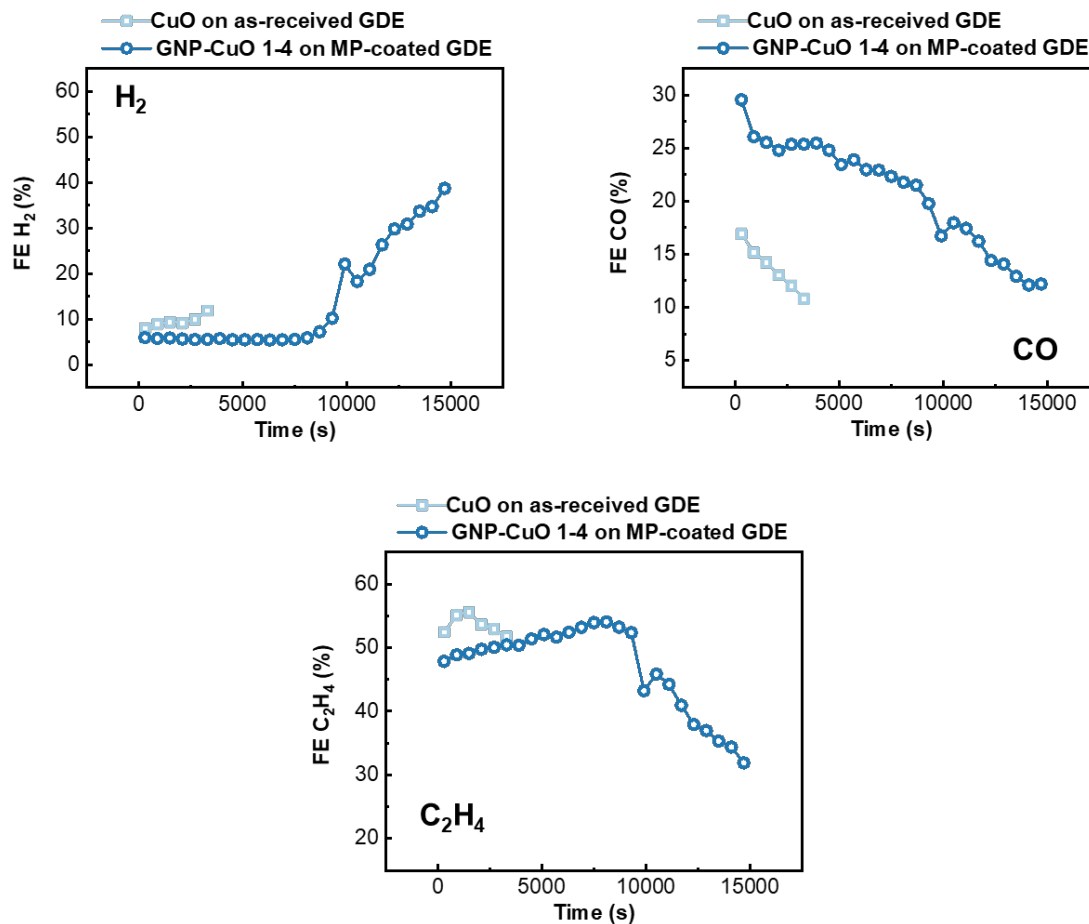
250

Figure S5.21. Product distribution of CO_2 electrolysis at a current density of 600 mA cm^{-2} and pH 2, using GNP/CuO mixtures of different ratios spray-coated onto the as-received YLS-30T GDE. The CuO loading is 0.4 mg cm^{-2}.

Laboratory of Materials for Renewable Energy (LMER)
Institute of Chemical Sciences and Engineering (ISIC)
Basic Science Faculty (SB)

251

a)

b)

Figure S5.22. Evolution of gaseous products over 1 hour of CO_2 electrolysis at pH 2 and a constant current density of 600 mA cm^{-2} for mixtures of different GNP:CuO ratios spray-coated onto the as-received YLS-30T GDE. The CuO loading is 0.4 mg cm^{-2}. **a)** FE of H_2 and **b)** FE of CO.

Laboratory of Materials for Renewable Energy (LMER)
Institute of Chemical Sciences and Engineering (ISIC)
Basic Science Faculty (SB)

252

Figure S5.23. WCA of the as-received YLS-30T GDE spray-coated with mixtures of different GNP:CuO ratios at pH 2 and a constant current density of 600 mA cm^{-2}, after CO$_2$ electrolysis until the onset of flooding.

Laboratory of Materials for Renewable Energy (LMER)
Institute of Chemical Sciences and Engineering (ISIC)
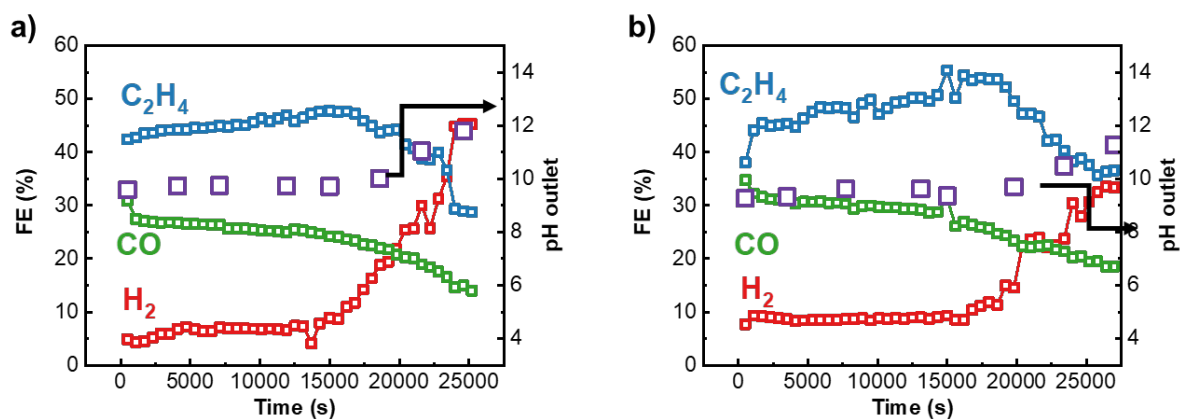Basic Science Faculty (SB)

253

Figure S5.24. FEs of H_2, CO, and C_2H_4 in extended CO_2 electrolysis on the MP-coated GDE spray-coated with GNP-CuO 1-4 at pH 2 and a constant current density of 600 mA cm^{-2}. The CuO loading is 0.4 mg cm^{-2}.

Laboratory of Materials for Renewable Energy (LMER)
Institute of Chemical Sciences and Engineering (ISIC)
Basic Science Faculty (SB)

254
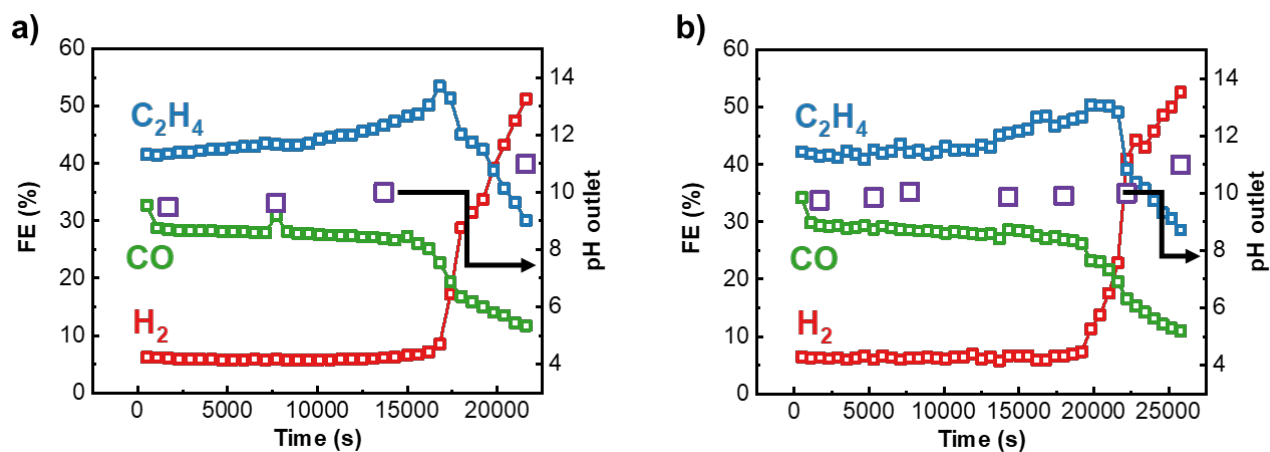
Figure S5.25. FEs of H_2, CO, and C_2H_4 and the pH evolution of the outlet liquid in extended CO_2 electrolysis on the MP-coated GDE spray-coated with GNP-CuO 1-4 at pH 2 and a constant current density of 600 mA cm^{-2}. The CuO loading is 1 mg cm^{-2}. **a)** 1st sample and **b)** 2nd sample.

Laboratory of Materials for Renewable Energy (LMER)
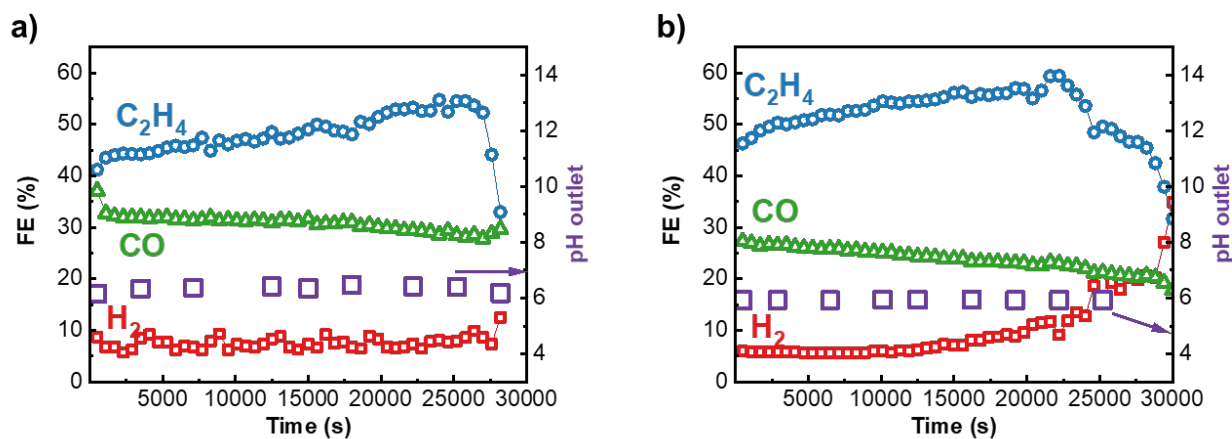Institute of Chemical Sciences and Engineering (ISIC)
Basic Science Faculty (SB)

255

Figure S5.26. FEs of H_2, CO, and C_2H_4 and the pH evolution of the outlet liquid in extended CO_2 electrolysis on the MP-coated GDE spray-coated with GNP-CuO 1-4 at pH 2 and a constant current density of 600 mA cm^{-2}. The CuO loading is 2 mg cm^{-2}. **a)** 1st sample and **b)** 2nd sample.

Laboratory of Materials for Renewable Energy (LMER)
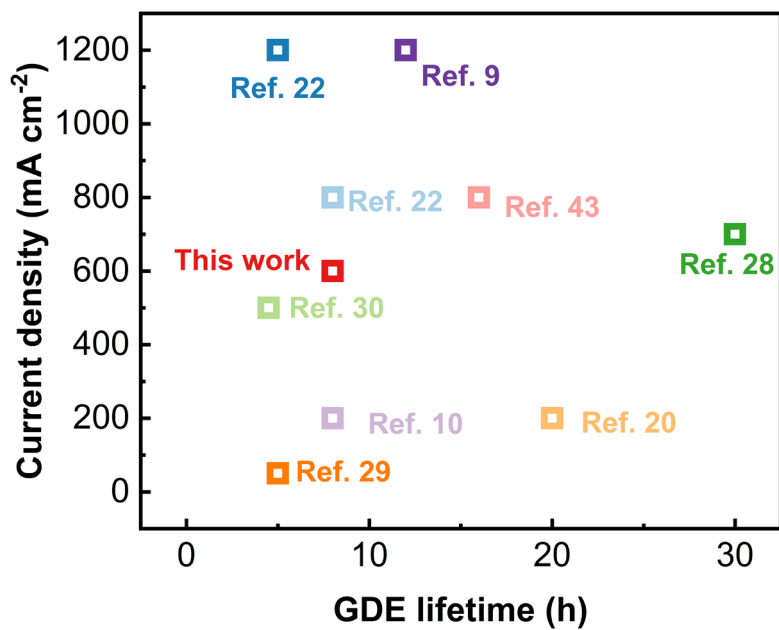Institute of Chemical Sciences and Engineering (ISIC)
Basic Science Faculty (SB)

256

Figure S5.27. FEs of H_2, CO, and C_2H_4 and the pH evolution of the outlet liquid in extended CO_2 electrolysis on the MP-coated GDE spray-coated with GNP-CuO 1-4 at pH 1 and a constant current density of 600 mA cm^{-2}. The CuO loading is 2 mg cm^{-2}. **a)** 1st sample and **b)** 2nd sample.

Laboratory of Materials for Renewable Energy (LMER)
Institute of Chemical Sciences and Engineering (ISIC)
Basic Science Faculty (SB)

257

Table S5.1. Summary of catalysts, pH of electrolytes and partial current density for C_{2+} products from a variety of carbon-based GDEs.

pH	Catalysts	Current density (mA cm^{-2})	Lifetime (h)	j_{C2+}	References
7	Cu/GDL	10	2		Role of the Carbon-Based Gas Diffusion Layer on Flooding in a Gas Diffusion Electrode Cell for Electrochemical CO_2 Reduction
7	AgNPs	150	1		Effects of microporous layer on electrolyte flooding in gas diffusion electrodes and selectivity of CO_2 electrolysis to CO
7	Cu2O	200	10	138	Modulating Local CO_2 Concentration as a General Strategy for Enhancing C−C Coupling in CO_2 Electroreduction
2	Cu/PTFE/C	300	50	186	Overcoming Low C_{2+} Yield in Acidic CO_2 Electroreduction: Modulating Local Hydrophobicity for Enhanced Performance
1	Cu nanoneedles	600	10	468	Gas diffusion enhanced electrode with ultrathin superhydrophobic macropore structure for acidic CO_2 electroreduction
14	Ag	196	0.5		Investigating Electrode Flooding in a Flowing Electrolyte, Gas-Fed Carbon Dioxide Electrolyzer
14	Ag	150	0.5		Investigating Electrode Flooding in a Flowing Electrolyte, Gas-Fed Carbon Dioxide Electrolyzer
14	Ag	100	1		Investigating Electrode Flooding in a Flowing Electrolyte, Gas-Fed Carbon Dioxide Electrolyzer
14	Ag	50	2		Investigating Electrode Flooding in a Flowing Electrolyte, Gas-Fed Carbon Dioxide Electrolyzer
14	Ag	25	5		Investigating Electrode Flooding in a Flowing Electrolyte, Gas-Fed Carbon Dioxide Electrolyzer
14	Ag	200	6		Investigation of Electrolyte-Dependent Carbonate Formation on Gas Diffusion Electrodes for CO_2 Electrolysis
14	Ag NPs	100	100		Mitigating Electrolyte Flooding for Electrochemical CO_2 Reduction via Infiltration of Hydrophobic Particles in a Gas Diffusion Layer

Laboratory of Materials for Renewable Energy (LMER)
Institute of Chemical Sciences and Engineering (ISIC)
Basic Science Faculty (SB)

258

Figure S5.28. Plot of the current densities versus lifetime of the PTFE GDEs for CO_2-electrolysis in flow-cell, and that of the carbon-based GDE used in this work. The reference numbers in the graph follow the numbering order in the main manuscript. The details of the catalysts and electrolytes are summarized in Table S5.2.

Laboratory of Materials for Renewable Energy (LMER)   259
Institute of Chemical Sciences and Engineering (ISIC)
Basic Science Faculty (SB)

Table S5.2. Summary of catalysts, electrolytes and partial current density for C_{2+} products from a variety of PTFE GDEs.

pH	Catalyst	Current density (mA cm^{-2})	Lifetime (h)	j_{C2+}	References
1	CuNNs	800	8	500	Breaking K$^+$ Concentration Limit on Cu Nanoneedles for Acidic Electrocatalytic CO_2 Reduction to Multi-Carbon Products
1	CuNNs	1200	5	700	Breaking K$^+$ Concentration Limit on Cu Nanoneedles for Acidic Electrocatalytic CO_2 Reduction to Multi-Carbon Products
2	6.2% Pd–Cu	500	4.5	350	High carbon utilization in CO_2 reduction to multi-carbon products in acidic media
≤ 1	ER-CuNS	700	30	525	CO_2 electroreduction to multicarbon products in strongly acidic electrolyte via synergistically modulating the local microenvironment
0.5 M H$_3$PO$_4$, 0.5 M KH$_2$PO$_4$, 2.5 M KCl	CoPc@HC/Cu	800	16	640	Efficient multicarbon formation in acidic CO_2 reduction via tandem electrocatalysis
1	COF:PFSA-modified PTFE–Cu electrodes	200	20	150	Conversion of CO_2 to multicarbon products in strong acid by controlling the catalyst microenvironment
1.0 M H$_3$PO$_4$ ([K+]=0.1 M), 1.5 mM tolyl-pyr	Modified-Cu/PTFE	50	5	14	Organic Additive-derived Films on Cu Electrodes Promote Electrochemical CO_2 Reduction to C_{2+} Products Under Strongly Acidic Conditions
1	Cu catalyst, reduced from CuO precatalyst	200	8	120	Acidic Electroreduction of CO_2 to Multi-Carbon Products with CO_2 Recovery and Recycling from Carbonate
1	CAL-modified Cu	1200	12	300	CO_2 electrolysis to multicarbon products in strong acid

Laboratory of Materials for Renewable Energy (LMER)
Institute of Chemical Sciences and Engineering (ISIC)
Basic Science Faculty (SB)

260

CHAPTER 6: Conclusion

In this thesis, we conducted an in-depth exploration of two sluggish reactions: water electrolysis and CO_2-electrolysis. The first reaction is the OER, which occurs at the anode side of the electrochemical cell in both water and CO_2-electrolysis, producing oxygen from an alkaline electrolyte. The second reaction involves the eCO₂RR, converting CO_2 into carbon-containing compounds. Both of these reactions involve multi-electron processes with complex pathways, necessitating the development of catalysts to reduce overpotential and enhance selectivity toward specific target products.

The enhancement of electrochemical reaction performance has been explored from various angles. This improvement can be achieved through the modification of the catalyst's activity, involving both its intrinsic activity via alloying and its active surface area through dispersion onto a high surface-area support. Additionally, the activity and stability of a reaction can be improved by adjusting the micro-environment in the vicinity of the catalyst, such as increasing hydrophobicity or controlling the local pH to prevent an excessively high concentration of hydroxide ions.

To be precise, we initially synthesized and investigated highly-dispersed Co-based nanoparticles on a high surface area carbon-based support for the OER. Our study not only successfully dispersed Co nanoparticles and sub-nanoparticles to achieve high mass activity, but also provided insights into the role of s-OFGs in the dispersion of the nanocatalysts. We have demonstrated that a high concentration of acidic s-OFGs enhanced the adsorption of cations from the precursor onto the support surface. Additionally, our work has shown that the finely dispersed and strongly anchored nanoparticles introduced additional defects to the carbon structure, as well as COOH groups to the surface which serves as sites for oxygen spillover. This process enhanced the overall OER activity of the supported Co-based catalysts.

Furthermore, we incorporated Fe in situ into the Co-based catalysts to enhance their activity toward OER. In-depth studies on the crystalline and chemical structures of the CoFe catalyst, as well as the local placement and incorporation mechanism of Fe, were conducted using ex-situ surface characterizations and electron microscopy techniques. Furthermore, we investigated the role of Fe in improving OER activity through operando Raman spectroscopy and electrochemical quartz-crystal microbalance. Initially, we demonstrated that the in situ synthesis of CoFe-catalyst is initiated by the anodic deposition of the Co-based phase, followed by the incorporation of Fe into this host-structure. Fe is homogeneously incorporated into the Co-based mixed oxides without forming a separate Fe-rich phase. This incorporation occurs through the replacement of Fe^{3+} in Co^{3+} sites, resulting in a slight increase in the Co lattice spacing of approximately 3%. The CoFe catalyst exhibited a Tafel slope of 28.3 mV dec^{-1} and an overpotential of 319 mV at 10 mA cm^{-2}, making it among the best CoFe-based materials for OER. Operando mass- and phase-tracking indicated that Fe reduced the transition potential from the in situ CoFe-catalyst to the OER-active phase.

On the cathode side of CO_2-electrolysis reaction, where CO_2 is electrochemically reduced to multicarbon products on a Cu-based catalyst, we managed water accessibility through the use of different polymer binders. Since the solubility of CO_2 in water is limited, the FE toward CO₂RR products is often hindered by the HER. By coating the catalyst with a thin layer of a hydrophobic binder, FEP, we successfully repel water

Laboratory of Materials for Renewable Energy (LMER)
Institute of Chemical Sciences and Engineering (ISIC)
Basic Science Faculty (SB)

261

and promote CO_2 access to the vicinity of the catalyst, thereby reducing HER and enhancing the selectivity toward CO_2RR products. Furthermore, through operando Raman spectroscopy, we observed that the CO surface intermediate is present over a wider potential range with a hydrophobic polymer binder compared to a hydrophilic one. This observation reveals that employing a hydrophobic binder retains not only CO_2 but also CO, which can be further reduced to C_{2+} products, explaining the enhanced selectivity toward C_{2+} products observed in both the H-cell and flow cell.

Finally, we performed CO_2-electrolysis in an acidic electrolyte with a flow cell to enhance the CO_2 utilization of the reaction. With the addition of cations, we successfully minimized the HER and achieved a selectivity towards C_{2+} products similar to that in alkaline media. By separating the inlet catholyte and the liquid products, we eliminated the effects from bulk pH changes and the dynamic restructuring of the catalysts, which typically reduce the electrode's lifetime. The resistance of the GDE against flooding could be further improved by modulating its composition, such as the thickness of MP layer, the loading of catalyst and the CO_2 diffusion within the catalyst layer. The implementation of the modified reaction system's design combined with optimal conditions of the GDE allowed us to mitigate flooding of the GDE and achieve stability for up to 7 hours at 600 mA cm^{-2}.

Laboratory of Materials for Renewable Energy (LMER)
Institute of Chemical Sciences and Engineering (ISIC)
Basic Science Faculty (SB)

262

CHAPTER 7: Perspectives

1. **Application of the in situ CoFe catalyst in operando XAS electrochemical cell:**

Since the CoFe catalyst can be directly deposited onto carbon, studying its operando oxidation state and local structure in an electrochemical cell becomes possible by spray-coating carbon powder onto a gold-coated Kapton film. Operando XAS performed on such catalysts will provide further insights into the Co-Fe interaction, enhancing and complementing our understanding of the role of Fe in promoting OER activity in Co-based catalysts.

2. **Investigation on polymers with limited proton conductivity and high anion conductivity for application in acidic eCO$_2$RR:**

High cation concentration is often used to reduce proton access to the catalyst, lowering the HER. However, in regions with high pH during the reaction, this can combine with CO_2 and the anion to form carbonate, potentially blocking CO_2 access. New approaches for managing proton access without high cation concentrations are necessary. Coating the catalyst layer with an ionomer or polymer exhibiting limited proton conductivity and high anion conductivity might offer a solution. This approach could minimize proton access while promoting anion transfer from the reaction site to the bulk electrolyte, enhancing buffering near the catalyst.

3. **Application of the FEP-coated CuO and the CoFe catalyst in a zero-gap flow cell to reduce cell voltage:**

While the FEP-coated CuO demonstrated enhanced current density and selectivity toward C_{2+} products in the CO$_2$RR in a flow cell, the in situ CoFe catalyst also exhibited superior activity for OER. Integrating the CoFe catalyst and the FEP-coated CuO into a zero-gap cell aims to reduce cell voltage. Other components involved in the reaction, such as the GDE and the membrane, will also be studied to lower the cell voltage, achieving a specific partial current density for C_{2+} products.

4. **Integration of Polydimethylsiloxane (PDMS) in the CO$_2$-electrolyzer:**

PDMS is commonly used for direct-air capture of CO_2 due to its CO_2-philicity. Therefore, integrating this polymer into the system, either as a binder or an additional layer near the catalyst, might allow for CO_2 electrolysis at lower CO_2 partial pressure.

Laboratory of Materials for Renewable Energy (LMER)
Institute of Chemical Sciences and Engineering (ISIC)
Basic Science Faculty (SB)

263

Curriculum Vitae

Work Experience

Intern (Novelis Switzerland SA, Sierre)   02.2019 - 06.2019

Development of screening methods for corrosion evaluation.

Education

05.2020 - present	PhD candidate in Chemistry (LMER-EPFL, Lausanne)
09.2022 - 02.2023	Exchange PhD (EPFL Doc.Mobility grant - NUS, Singapore)
09.2017 - 02.2020	Master in Materials Science & Engineering, EPFL, Lausanne
09.2012 - 07.2017	Bachelor in Materials Science & Engineering, EPFL, Lausanne
09.2010 - 06.2012	Baccalauréat français, Lycée français Alexandre Yersin, Vietnam

Software & Instruments

Microsoft Office, Wolfram Mathematica, ImageJ, Origin.

Electron microscopes (TEM, HR-TEM, STEM, SEM, EDX), Potentiostat (Metrohm, Gamry, Biologic), GC, ICP-OES, Raman spectroscope, XRD.

Projects

05.2020 – present   PhD thesis, LMER-EPFL

Exploring catalysts for Oxygen evolution reaction and CO_2 Electroreduction in energy applications.

10.2019 – 02.2020   Master thesis, INE-EPFL

Effects of iron impurities and ferroelectrics on the activity of cobalt-based oxide catalysts for Oxygen Evolution Reaction.

09.2018 – 01.2019   Semester project, INE-EPFL

Synthesis of highly active Ni(Fe)OOH electrocatalysts by electrochemical methods.

09.2018 – 01.2019   Semester project, TIC-EPFL

Effect of Surface Chemical Treatments on Friction in Silicon Oxide Tribocontacts.

02.2018 – 06.2018   Semester project, GEM-EPFL

High temperature corrosion investigation of metals for energy conversion devices.

02.2017 – 06.2017   Semester project, TIC-EPFL

Influence of storage temperature on the degradation of lacquered tinplate cans and on the corrosivity of the foodstuffs.

Publications (https://scholar.google.com/citations?user=u5GtQYQAAAAJ&hl=de&oi=ao)

Pham, T.H.M. et al. Elucidating the Mechanism of Fe Incorporation in In Situ Synthesized Co–Fe Oxygen-Evolving Nanocatalysts, J. Am. Chem. Soc. 2023, 145, 43, 23691–23701.

Pham, T.H.M. et al. Understanding the role of surface oxygen-containing functional groups on carbon-supported cobalt catalysts for oxygen evolution reaction, J. Mater. Chem. A 2023, 11 (39), 21066-21077.

Pham, T.H.M. et al. Enhanced Electrocatalytic CO_2 Reduction to C_{2+} Products by Adjusting the Local Reaction Environment with Polymer Binders, Adv. Energy Mater. 2022, 12 (9), 2103663.

Conferences

International Hydrogen Symposium 2023	Talk: Oxygen Evolution Reaction.
Global Young Scientist Summit 2023	Nominated participant by EPFL.
International Conference on Materials for Humanity 2022	Talk: CO_2 electrolysis.
European Young Chemists' Meeting 2022	Best Oral Presentation Award.

Thi Ha My Pham

19/10/1993

PERMIS B

Contact

thi.pham@epfl.ch

+41 787 99 55 30

Rue de l'Industrie 6, 1950 Sion

Skills

Data analysis and visualization, Written communication, Presentation skills, Analytical thinking, Critical reasoning, Creative problem-solving, Collaboration, Planning and organizing, Information gathering, Literature review, Experimental design, Report writing.

Keywords

Materials synthesis and analysis, Electrochemistry, Corrosion, Materials selection, Material Chemistry, Surface characterization, Catalysis, Renewable Energy.

Languages

Vietnamese (mother tongue), French (Mother tongue), English (C1), German (A1), Chinese (A1)

Activities and Interest

Baking, Board games, Travel, Yoga, Going to concerts, Classical music

Laboratory of Materials for Renewable Energy (LMER)
Institute of Chemical Sciences and Engineering (ISIC)
Basic Science Faculty (SB)

264

CHAPTER 8: Publications & Conferences

As first author:

T. H. M. Pham, J. Zhang, W. Luo, B.S. Yeo, A. Züttel. Unveiling degradation mechanisms in gas diffusion electrodes towards enhancing stability of the CO_2 electrolysis in acidic environments. *In preparation*.

T. H. M. Pham, T.-H. Shen, Y. Ko, L. Zhong, L. Lombardo, W. Luo, S. Horike, V. Tileli, A. Züttel, Elucidating the Mechanism of Fe Incorporation in In Situ Synthesized Co–Fe Oxygen-Evolving Nanocatalysts. *J. Am. Chem. Soc.* **2023**, *145*, 23691.

T. H. M. Pham, Y. Ko, M. Wei, K. Zhao, L. Zhong, A. Züttel, Understanding the role of surface oxygen-containing functional groups on carbon-supported cobalt catalysts for the oxygen evolution reaction. *J. Mater. Chem. A* **2023**, *11*, 21066.

T. H. M. Pham, J. Zhang, M. Li, T. H. Shen, Y. Ko, V. Tileli, W. Luo, A. Züttel, Enhanced Electrocatalytic CO2 Reduction to C_{2+} Products by Adjusting the Local Reaction Environment with Polymer Binders. *Adv. Energy Mater.* **2022**, *12*, DOI 10.1002/aenm.202103663.

As co-author:

J. Zhang, **T. H. M. Pham**, S. Xi, L. Zhong, D. Liem, A. Züttel, B. Rowley, R. Ganganahalli, F. Calle-Vallejo, B. S. Yeo. Low CO_2 Mass Transfer Promotes Methanol Electrosynthesis on Cobalt Phthalocyanine. *Submitted.*

L. Zhong, **T. H. M. Pham**, Z. Akbari, Y. Ko, S. Mohamad, Y. Kuddusi, N. Gallandat, A. Züttel. Highly-dispersed and active Ru supported catalyst for CO_2 methanation: the effects of synthesis parameters. *To be sumitted.*

Y. Ko, J. Park, X. Zhang, L. Kang, **T. H. M. Pham**, V. Boureau, C. Pham-Huu, J. Kim, L. Zhong, A. Züttel, All Platinum Group Metal-Free and Durable Catalysts for Direct Borohydride Fuel Cells. *ACS Appl. Energy Mater.* **2023**, xxxx, DOI 10.1021/acsaem.3c02578.

M. Wei, K. Wang, P. Pei, L. Zhong, A. Züttel, **T. H. M. Pham**, N. Shang, Y. Zuo, H. Wang, S. Zhao, Zinc carboxylate optimization strategy for extending Al-air battery system's lifetime. *Appl. Energy* **2023**, *350*, 121804.

J. Zhang, **T. H. M. Pham**, Z. Gao, M. Li, Y. Ko, L. Lombardo, W. Zhao, W. Luo, A. Züttel, Electrochemical CO2 Reduction over Copper Phthalocyanine Derived Catalysts with Enhanced Selectivity for Multicarbon Products. *ACS Catal.* **2023**, *13*, 9326.

M. Wei, K. Wang, L. Zhong, **T. H. M. Pham**, Y. Zuo, H. Wang, P. Zhang, Z. Chen, S. Zhao, P. Pei, F− competitive attack decomposing parasitic product $Al(OH)_3$ of hydrogel-based Al-air battery. *Energy Storage Mater.* **2023**, *60*, 102812.

Laboratory of Materials for Renewable Energy (LMER)
Institute of Chemical Sciences and Engineering (ISIC)
Basic Science Faculty (SB)

265

L. Zhong, T. H. M. Pham, Y. Ko, A. Züttel, Graphene nanoplatelets promoted CoO-based catalyst for low temperature CO2 methanation reaction. *Front. Chem. Eng.* **2023**, *5*, 1.

M. Wei, K. Wang, **T. H. M. Pham**, M. Zhang, D. Zhong, H. Wang, L. Zhong, D. Liu, P. Pei, A. Züttel, A fluoropolymer bifunctional solid membrane interface for improving the discharge duration in aqueous Al-air batteries. *Chem. Commun.* **2023**, *59*, 11121.

J. Zhang, **T. H. M. Pham**, Y. Ko, M. Li, S. Yang, C. D. Koolen, L. Zhong, W. Luo, A. Züttel, Tandem effect of Ag@C@Cu catalysts enhances ethanol selectivity for electrochemical CO2 reduction in flow reactors. *Cell Reports Phys. Sci.* **2022**, *3*, 100949.

Y. Ko, L. Lombardo, M. Li, **T. H. M. Pham**, H. Yang, A. Züttel, Selective Borohydride Oxidation Reaction on Nickel Catalyst with Anion and Cation Exchange Ionomer for High-Performance Direct Borohydride Fuel Cells. *Adv. Energy Mater.* **2022**, *12*, DOI 10.1002/aenm.202103539.

M. Li, **T. H. M. Pham**, Y. Ko, K. Zhao, L. Zhong, W. Luo, A. Züttel, Support-Dependent Cu-In Bimetallic Catalysts for Tailoring the Activity of Reverse Water Gas Shift Reaction. *ACS Sustain. Chem. Eng.* **2022**, *10*, 1524.

M. Li, **T. H. M. Pham**, E. Oveisi, Y. Ko, W. Luo, A. Züttel, Revealing the Surface Chemistry for CO2 Hydrogenation on Cu/CeO2-x Using Near-Ambient-Pressure X-ray Photoelectron Spectroscopy. *ACS Appl. Energy Mater.* **2021**, *4*, 12326.

T. H. Shen, L. Spillane, J. Vavra, **T. H. M. Pham**, J. Peng, Y. Shao-Horn, V. Tileli, Oxygen Evolution Reaction in Ba0.5Sr0.5Co0.8Fe0.2O3- Aided by Intrinsic Co/Fe Spinel-Like Surface. *J. Am. Chem. Soc.* **2020**, *142*, 15876.

Laboratory of Materials for Renewable Energy (LMER)
Institute of Chemical Sciences and Engineering (ISIC)
Basic Science Faculty (SB)

266

Conferences:

1. Oral presentation: **In situ Synthesis Of Highly Active Fe-doped Co-based Oxygen Evolving Catalysts** (*Advanced Materials Research Grand Meeting MRM2023/IUMRS-ICA2023, Kyoto 2023*)

2. Oral presentation: **Enhanced Electrocatalytic CO2 Reduction To C$_{2+}$ Products By Adjusting The Local Reaction Environment With Polymer Binders** (*Advanced Materials Research Grand Meeting MRM2023/IUMRS-ICA2023, Kyoto 2023*)

3. Oral presentation: **In situ synthesis of highly active Fe-doped Co-based catalyst for Oxygen Evolution Reaction** (*15th International Symposium Hydrogen & Energy, Emmetten 2023*)

4. Oral presentation: **Enhanced Electrocatalytic CO2 Reduction To C$_{2+}$ Products By Adjusting The Local Reaction Environment With Polymer Binders** (*International Conference on Materials for Humanity 2022, Singapore 2022*)

5. Oral presentation: **Enhanced Electrocatalytic CO2 Reduction To C$_{2+}$ Products By Adjusting The Local Reaction Environment With Polymer Binders** (*European Young Chemists' Meeting 2022, Switzerland 2022*)

Laboratory of Materials for Renewable Energy (LMER)
Institute of Chemical Sciences and Engineering (ISIC)
Basic Science Faculty (SB)

267

Teaching Activities

1. Advanced general chemistry (2020-2021): CH-160(a)
2. Experimental analytical chemistry (2020-2021): CH-309(a)
3. Advanced general chemistry (2021-2022): CH-160(a)
4. Analytical separation methods TP (for SFU) (2021-2022): UNIL-303
5. Analytical separation methods TP (for SFU) (2022-2023): UNIL-303

Laboratory of Materials for Renewable Energy (LMER)
Institute of Chemical Sciences and Engineering (ISIC)
Basic Science Faculty (SB)

268